National Technical University of Athens
School of Mechanical Engineering
Thermal Energy Sector
Laboratory of Steam Boilers and Thermal Plants

PhD Thesis:

EXPERIMENTAL INVESTIGATION AND ECONOMIC ASSESSMENT OF A FULLY AUTOMATED ORGANIC RANKINE CYCLE FOR WASTE HEAT RECOVERY FROM MARINE ENGINE JACKET COOLING WATER

Platon Pallis

MSc. Mechanical Engineer

Supervisor: Prof. Sotirios Karellas

Athens, June 2020

Επιβλέπων Καθηγητής

Δρ. Σ. Καρέλλας

Καθηγητής ΕΜΠ

Τριμελής Συμβουλευτική Επιτροπή

Δρ. Ε. Κακαράς

Καθηγητής Σ.Μ.Μ. ΕΜΠ

Δρ. Σ. Καρέλλας

Καθηγητής Σ.Μ.Μ. ΕΜΠ

Δρ. Δ. Χουντάλας

Καθηγητής Σ.Μ.Μ. ΕΜΠ

Επταμελής Εξεταστική Επιτροπή

Δρ. Ευάγγελος Γιακουμής	Καθηγητής Σ.Μ.Μ. ΕΜΠ
Δρ. Εμμανουήλ Κακαράς	Καθηγητής Σ.Μ.Μ. ΕΜΠ
Δρ. Σωτήριος Καρέλλας	Καθηγητής Σ.Μ.Μ. ΕΜΠ
Δρ. Ιωάννης Προυσαλίδης	Καθηγητής Σ.Ν.Μ.Μ. ΕΜΠ
Δρ. Εμμανουήλ Ρογδάκης	Καθηγητής Σ.Μ.Μ. ΕΜΠ
Δρ. Δημήτριος Χουντάλας	Καθηγητής Σ.Μ.Μ. ΕΜΠ
Δρ. Ειρήνη Κορωνάκη	Αναπληρώτρια Καθηγήτρια Σ.Μ.Μ. ΕΜΠ

Acknowledgements

I would like to deeply thank Professor S. Karellas & Professor E. Kakaras for the opportunity provided to broaden my knowledge and expertise over the years. I am also thankful to many other people whose assistance was definitely valuable. Namely, Dr. P. Vourliotis, Dr. A. Nikoglou, Dr. K. Braimakis, Dipl-Ing. Aris Leontaritis, Dipl-Ing. Tryfon Roumpedakis and Eythimios Dimitriadis. Last but not least, I wish to thank Dipl-Ing. Stratis Varvagiannis. His assistance and commitment was more than anyone could ask for.

This dissertation is dedicated to my beloved wife and my two daughters. It was a team work, after all.

Special Acknowledgement

The evolution and development of the experimental ORC test rig, as described in respective Chapters, was co funded by DNV GL, Strategic Research & Innovation East Med., Black & Caspian Seas/ Piraeus Hub in the frames of the “Marine-ORC project”.

Summary

The energetic consumption of a commercial ship mainly consists of propulsion and internal consumption electricity needs, which are entirely covered by specially designed marine diesel engines (main and auxiliary respectively). For large ships, the fuel expenses constitute about 30-55 % of the total operational costs, depending on the type of vessel. Strong motivation exists within the marine sector to reduce fuel expenses and to comply with even stricter efficiency regulations. Although, the Diesel process is highly efficient, large marine diesel engines are particularly well suited to be coupled with a WHR system, as the engine loses a large part of the fuel energy to the environment, mainly with the exhaust gases (up to 27 % of the input energy) and the jacket water (up to 25 % of the input energy). In this perspective, the present work focused on the recovery of heat from the internal combustion marine engines and more specifically from their jacket water cooling circuit. This research focused on the construction, experimental evaluation and full automation of an ORC WHR system, specially designed for the jacket water of a marine auxiliary diesel engine.

In Chapter 1, a general overview of the ship industry is presented. In addition, the existing and future regulatory framework is described, since it is crucial to have a clear view in order to assist stakeholders to make the right business decisions. All major global and regional regulations that will impact on shipping in the coming decades are also presented. Furthermore, special reference is made on the status of emissions from shipping. Finally, a comprehensive description of technological developments is made, in order to mitigate energy losses and improve overall performance. In light of all previous mentioned, the scope and objectives of the present study are discussed which is the recovery of heat from the internal combustion marine engines and more specifically from their jacket water cooling circuit.

In Chapter 2, the description of all components consisting the first version of the experimental Organic Rankine Cycle test rig is given. The selection of all components, compiling the experimental ORC system, is justified in regards to capacity /power, performance, material or any other special conditions / restrictions. All technical characteristics are presented, for each component.

In Chapter 3, the results of the two experimental campaigns are presented. Significant knowledge on the behavior, influencing parameters (i.e. cavitation phenomena on the ORC feed pump, the performance of the scroll expanders and the effect of superheating and subcooling) and improvements that would increase the overall performance of the ORC system are highlighted. The importance of the feed pump performance and free cavitation operation is justified, especially for small scale ORC units. As a result of the 2nd experimental campaign, several important conclusions are summarized. Specific cavitation tests revealed that a $NPSH_a > 7$ mH_2O at partial load and a $NPSH_a > 9$ mH_2O at full load are necessary to guarantee operation stability. Another important conclusion is, in order to maximize expander's isentropic efficiency, that the expander is required to operate at the highest possible rotational speeds. The results of experimental campaigns, played an important role in the evolution process of the automation & control strategy which was realized in the following chapter.

In Chapter 4, the final development of the WHR ORC prototype is presented. All required actions so as to operate the experimental ORC prototype in a real engine room as a standalone facility without any physical supervision are described. Namely, hazard / risk assessment, extensive reconstruction of all three circuits (hot water, working fluid, sea water), fully functional automation & control, Human Machine Interface in corporation, certificate of compliance to DNVGL rules for ships Pt.4 Cp.6 piping systems, are the most important ones. Finally, marine ORC prototype's impressive operational features such as autonomous startup and shut down and a successful rump down and rump up behavior during the HT temperature variation (ICE load variation) are

demonstrated. Finally, the current status of Organic Rankine Cycle marine applications is presented. A theoretical, research and market based review is described, briefly.

In Chapter 5, the economic performance and viability of a jacket water WHR ORC unit is assessed. A show case is examined which consists of a 13,600 TEU containership, which is powered by a two-stroke marine Diesel engine with a Maximum Continuous Rating (MCR) of a 72,240 kW. Two alternative sea routes are evaluated and the electrical output and the total net electrical energy over the year are estimated, respectively. Ultimately, several economic indexes, such as Net Present Value of investment, Internal Rate of Return, Levelized Cost of Energy (LCOE) of the WHR ORC unit are calculated. Finally, in the frames of a comprehensive sensitivity analysis, parameters affecting the economic indexes and thus the economic performance, such as running hours, interest rate and capital investment, are evaluated.

In final Chapter 6, the main conclusions and achievements of the present thesis are briefly mentioned, followed by its innovative aspects. In the last section of this chapter, some recommendations for future work are provided.

Περίληψη

Η χρήση ενέργειας σε ένα εμπορικό πλοίο καλύπτει τις ανάγκες κυρίως για την πρόωσή του και την παροχή ηλεκτρικής ενέργειας σε διάφορα συστήματά του, οι οποίες καλύπτονται εξ ολοκλήρου από ειδικά σχεδιασμένους ναυτικούς κινητήρες ντίζελ (κύριους και βοηθητικούς αντίστοιχα). Σε μεγάλα πλοία, το κόστος καυσίμου αποτελεί περίπου το 30-55 % του συνολικού λειτουργικού κόστους, ανάλογα με τον τύπο του πλοίου. Υπάρχουν ισχυρά κίνητρα στον τομέα της ναυτιλίας για τη μείωση του κόστους καυσίμου και τη συμμόρφωση με όλο και πιο αυστηρότερους κανονισμούς απόδοσης. Παρόλο που η τεχνολογία πετρελαιοκινητήρων είναι πολύ αποδοτική, οι μεγάλοι ναυτικοί κινητήρες ντίζελ θεωρούνται ιδιαίτερα κατάλληλοι για σύνδεσή τους με ένα σύστημα αξιοποίησης απορριπτόμενης θερμότητας (Waste Heat Recovery, WHR), καθώς ο κινητήρας απορρίπτει μεγάλο μέρος της χημικής ενέργειας καυσίμου στο περιβάλλον, κυρίως μέσω των καυσαερίων (έως 27 % της χημικής ενέργειας καυσίμου) και μέσω του νερού ψύξης του χιτωνίου του (έως και 25 % της χημικής ενέργειας καυσίμου). Λόγω των παραπάνω, η παρούσα διατριβή επικεντρώθηκε στην αξιοποίηση της απορριπτόμενης θερμότητας κινητήρων εσωτερικής καύσης και πιο συγκεκριμένα από το κύκλωμα νερού ψύξης του χιτωνίου. Η εργασία επικεντρώθηκε στην κατασκευή, την πειραματική αξιολόγηση και την πλήρη αυτοματοποίηση ενός συστήματος αξιοποίησης απορριπτόμενης θερμότητας με τη χρήση οργανικού κύκλου Rankine, ειδικά σχεδιασμένο για το κύκλωμα ψύξης του χιτωνίου ενός ναυτικού βοηθητικού πετρελαιοκινητήρα.

Στο Κεφάλαιο 1 (Chapter 1), παρουσιάζεται μια γενική επισκόπηση του κλάδου της ναυτιλίας. Επιπλέον, περιγράφεται το υφιστάμενο και το μελλοντικό κανονιστικό πλαίσιο, καθώς είναι ζωτικής σημασίας οι ενδιαφερόμενοι να έχουν μια σαφή άποψη προκειμένου να λάβουν τις σωστές επιχειρηματικές αποφάσεις. Στη συνέχεια, παρουσιάζονται όλοι οι σημαντικοί παγκόσμιοι και περιφερειακοί κανονισμοί που θα επηρεάσουν τη ναυτιλία τις επόμενες δεκαετίες. Επιπρόσθετα, γίνεται ειδική αναφορά στην κατάσταση των εκπομπών από τη ναυτιλία. Τέλος, γίνεται μια ολοκληρωμένη περιγραφή των τεχνολογικών εξελίξεων, προκειμένου να μετριαστούν οι απώλειες ενέργειας και να βελτιωθεί η συνολική απόδοση ενός πλοίου. Υπό το φως όλων των προαναφερθέντων, παρουσιάζεται ο σκοπός και οι στόχοι της παρούσας διατριβής, η οποία πραγματεύεται την ανάκτηση θερμότητας από κινητήρες εσωτερικής καύσης και πιο συγκεκριμένα από το κύκλωμα νερού ψύξης του χιτωνίου.

Στο Κεφάλαιο 2 (Chapter 2), δίδεται η περιγραφή όλου του επιμέρους εξοπλισμού που συνθέτει την πρώτη έκδοση της εργαστηριακής εγκατάστασης οργανικού κύκλου Rankine. Η επιλογή όλων των επιμέρους εξαρτημάτων, που συνθέτουν την εργαστηριακή εγκατάσταση οργανικού κύκλου Rankine, τεκμηριώνεται με βάση παραμέτρους όπως η χωρητικότητα / ισχύ, η απόδοση, το υλικό κατασκευής ή οποιουσδήποτε άλλος ειδικός όρος / περιορισμός. Παρουσιάζονται όλα τα τεχνικά χαρακτηριστικά για κάθε επιμέρους εξοπλισμό / εξάρτημα.

Στο Κεφάλαιο 3 (Chapter 3), παρουσιάζονται τα αποτελέσματα των πειραματικών μετρήσεων που διενεργήθηκαν σε δύο χρονικές περιόδους / καμπάνιες. Επίσης, επισημαίνονται, η σημαντική γνώση που αποκομίσθηκε σχετικά με τη συμπεριφορά, τις παραμέτρους που επηρεάζουν (π.χ. φαινόμενα σπηλαίωσης στην τροφοδοτική αντλία εργαζόμενου μέσου, την απόδοση των εκτονωτών και την επίδραση της υπερθέρμανσης και της υποψύξης) αλλά και βελτιώσεις που θα αυξήσουν τη συνολική απόδοση του συστήματος οργανικού κύκλου Rankine. Τεκμηριώνεται η σημασία της απόδοσης της τροφοδοτικής αντλίας και της λειτουργίας χωρίς φαινόμενα σπηλαίωσης, ειδικά για μονάδες οργανικού κύκλου Rankine μικρής κλίμακας. Ως αποτελέσματα της 2^{ης} πειραματικής εκστρατείας, συνοψίζονται αρκετά σημαντικά συμπεράσματα. Ειδικά σχεδιασμένες δοκιμές σπηλαίωσης αποκάλυψαν ότι ένα καθαρό ύψος κεφαλής αναρρόφησης (available Net Positive Suction Head, NPSHa) μεγαλύτερο από 7 mH_2O σε μερικό φορτίο και ένα καθαρό ύψος κεφαλής αναρρόφησης (available Net

Positive Suction Head, NPSHa) μεγαλύτερο από 9 mH_2O σε πλήρες φορτίο είναι απαραίτητα για τη διασφάλιση της σταθερότητας λειτουργίας της εγκατάστασης. Ένα άλλο σημαντικό συμπέρασμα είναι ότι, προκειμένου να μεγιστοποιηθεί ο ισεντροπικός βαθμός απόδοσης του εκτονωτή, ο εκτονωτής απαιτείται να λειτουργεί με τις υψηλότερες δυνατές ταχύτητες περιστροφής. Τα αποτελέσματα των πειραματικών εκστρατειών, έπαιξαν σημαντικό ρόλο στη διαδικασία εξέλιξης της στρατηγικής ελέγχου και αυτοματισμού της εγκατάστασης που πραγματοποιήθηκε στη συνέχεια και περιγράφεται στο επόμενο κεφάλαιο.

Στο Κεφάλαιο 4 (Chapter 4), παρουσιάζεται η τελική ανάπτυξη του πρωτοτύπου συστήματος αξιοποίησης απορριπτόμενης θερμότητας με τη χρήση οργανικού κύκλου Rankine. Περιγράφονται όλες οι απαιτούμενες ενέργειες για τη λειτουργία του πρωτοτύπου συστήματος αξιοποίησης απορριπτόμενης θερμότητας με τη χρήση οργανικού κύκλου Rankine σε πραγματικό μηχανοστάσιο ως αυτόνομη εγκατάσταση χωρίς φυσική επίβλεψη. Πιο συγκεκριμένα, η εκτίμηση επικινδυνότητας / κινδύνου, η εκτεταμένη ανακατασκευή και των τριών κυκλωμάτων (θερμό νερό, εργαζόμενο μέσο, θαλασσινό νερό), πλήρως λειτουργικός αυτοματισμός & έλεγχος, η εγκατάσταση πλατφόρμας διεπαφής ανθρώπου-μηχανής (Human Machine Interface, H.M.I.), πιστοποιητικό συμμόρφωσης με τους κανόνες του νηογνώμονα DNV GL για εγκατάσταση σε πλοία (DNVGL rules for ships Pt.4 Cp.6 piping systems), είναι τα πιο σημαντικά. Τέλος, επιδεικνύονται τα εντυπωσιακά λειτουργικά χαρακτηριστικά του ναυτικού πρωτοτύπου συστήματος αξιοποίησης απορριπτόμενης θερμότητας με τη χρήση οργανικού κύκλου Rankine, όπως η αυτόνομη εκκίνηση και τερματισμός λειτουργίας και η επιτυχημένη συμπεριφορά σε συνθήκες μεταβαλλόμενου φορτίου / θερμοκρασίας του νερού ψύξης του χιτωνίου (ως προσομοίωση της μεταβολής φορτίου μιας ναυτικής μηχανής εσωτερικής καύσης). Τέλος, παρουσιάζονται οι τρέχουσες εξελίξεις συστημάτων αξιοποίησης απορριπτόμενης θερμότητας με τη χρήση οργανικού κύκλου Rankine για ναυτικές εφαρμογές. Ενώ παρουσιάζεται συνοπτικά μια ανασκόπηση σε θεωρητικό, ερευνητικό και εμπορικό επίπεδο.

Στο Κεφάλαιο 5 (Chapter 5), αξιολογείται η οικονομική απόδοση και η βιωσιμότητα ενός συστήματος αξιοποίησης απορριπτόμενης θερμότητας με τη χρήση οργανικού κύκλου Rankine. Εξετάζεται μια επιδεικτική εφαρμογή που αποτελείται από ένα πλοίο μεταφοράς εμπορευματοκιβωτίων (13.6000 TEU, Twenty-foot Equivalent Unit), το οποίο κινείται από δίχρονο ναυτικό κινητήρα ντίζελ με μέγιστη ισχύς (Maximum Continuous Rating, MCR) 72,240 kW. Αξιολογούνται δύο εναλλακτικές θαλάσσιες διαδρομές και εκτιμάται η καθαρή ηλεκτρική ισχύς αλλά και η συνολική καθαρή ηλεκτρική ενέργεια κατά τη διάρκεια του έτους που παράγεται από το σύστημα αξιοποίησης απορριπτόμενης θερμότητας με τη χρήση οργανικού κύκλου Rankine. Επίσης, υπολογίζονται διάφοροι οικονομικοί δείκτες, όπως η καθαρή παρούσα αξία της επένδυσης, ο εσωτερικός βαθμός απόδοσης, το ισοσταθμισμένο κόστος ενέργειας (Levelized Cost of Energy, LCOE) του συστήματος αξιοποίησης απορριπτόμενης θερμότητας με τη χρήση οργανικού κύκλου Rankine. Τέλος, στο πλαίσιο μιας ολοκληρωμένης ανάλυσης ευαισθησίας, αξιολογούνται οι παράμετροι που επηρεάζουν τους οικονομικούς δείκτες και κατ' επέκταση τις οικονομικές επιδόσεις, όπως οι ώρες λειτουργίας, το επιτόκιο αναγωγής και το κεφάλαιο επένδυσης.

Στο τελευταίο κεφάλαιο 6 (Chapter 6) αναφέρονται τα κύρια συμπεράσματα και επιτεύγματα της παρούσας διατριβής, ακολουθούμενα από τις καινοτόμες πτυχές της. Στην τελευταία ενότητα αυτού του κεφαλαίου, παρέχονται ορισμένες προτάσεις για μελλοντική εργασία.

Contents

List of Figures

List of Tables

Nomenclature

BCR	Benefit to Cost Ratio
C	Relative error / Constant / Cost
CO_2	Carbon Dioxide
CEPCI	Chemical Engineering Price Cost Index
CFCs	Chlorofluorocarbons
CRF	Capital Recovery Factor
DPB	Depreciated Payback time
DWT	Dead Weight Tonnage
EEDI	Energy Efficiency Design Index
E	Energy
F.S.	Full Scale
ff	Filling Factor
f	Frequency, Hz
f	Year increase
GWP	Global Warming Potential
GHG	Green House Gas
GT	Gross Tonnage
G	Gravitational constant
h	Specific Enthalpy, J/kg
HCFCs	Hydrochlorofluorocarbons
HFEs	Hydrofluorethers
H.M.I.	Human Machine Interface
HT	High Temperature
Hz	Vertical distance from surface liquid to pump center line, mH_20
Ha	Acceleration head at pump suction, mH_2O
Hf	Friction losses in suction piping, mH_2O
ICE	Internal Combustion Engine
ICCT	International Council on Clean Transportation
IMO	International Maritime Organization
IRR	Internal Rate of Return
i	Interest rate
K	Compressibility constant
LT	Low Temperature
LCOE	Levelized Cost of Energy
L	Length, m
lpm	Liter per minute
$\dot{m}$	Mass flow rate, kg/s
MMT	Million Metric Tonnes
MCR	Maximum Continuous Rating
ME	Main Engine
NPV	Net Present Value
N	Rotational Speed, RPM
NPSHa	Available Net Positive Suction Head, mH_2O
NPSHr	Required Net Positive Suction Head, mH_2O
NO_x	Nitrogen Oxides
NO	Normally Open
NC	Normally Closed
ORC	Organic Rankine Cycle
ODP	Ozone Deplete Potential

p	Pressure, bar or mH_2O
Pvp	Absolute vapour pressure of liquid at pumping temperature, mH_2O
P&ID	Piping and Instrumentation Diagram
PVF	Present Value Factor
PLC	Programmable Logic Controller
Q	Heat transfer rate, W
rp	Specific pressure ratio
rpm / RPM	Revolutions per Minute
rv	Expansion ratio, -
R134a	1,1,1,2-Tetrafluoroethane
SO_x	Sulphur Oxides
SIC	Specific Investment Cost
SFOC	Specific fuel oil consumption
SPB	Simple Payback time
T	Temperature, K or °C
t	Year
TEU	Twenty-foot Equivalent Unit
VFD	Variable Frequency Driver
v	Specific volume, m^3/kg
$\dot{V}$	Volumetric flow rate, lt/min or m^3/s
V_{swept}	Swept volume, m^3
Visc	Dynamic Viscosity, cP
Vel	Velocity, m/s
$\dot{W}$ / P	Power, W
WHR	Waste Heat Recovery
WTH	Waste Thermal Heat

Greek letters

Δ	Difference, -
η	Efficiency, -
ρ	Density, kg/m^3
σ	Absolute error
ξ	Saturated vapor slope parameter, J/kgK^2
ϕ	Motor load,

Subscripts

a	Absolute
amb	Ambient
calc	Calculated
cond / cd	Condenser / Condensing
c	Cold
D	Demand
evap / ev	Evaporator / Evaporating
el / e	Electric
ex	Exhaust
exp	Expansion / Expander
el	Electrical
fd	Frequency driver
f	Fuel
FWG	Fresh Water Generator
gen	Generator

glob / global	Global
gross	Gross
h	Hot /High
hydr	Hydraulic
in	Inlet
is	Isentropic
JWC	Jacket Water Cooling
l	Low
mech	Mechanical
max	Maximum
min	Minimum
mot/m	Motor
net	Net
nom	Nominal
ncg	Non condensing gas
out	Outlet
OM	Operational & Maintenance
pump / p /pp	Pump
part	Partial
pr	Propulsion
rec	Receiver
su	Suction / Supply
s	Rotating magnetic flux / Synchronous speed
sat / s / vp	Saturation
sh	Shaft / Superheating
sc	Subcooling
sw	Sea water
th	Thermal / Thermodynamic
wf	Working fluid

Chapter 1. - Introduction

1.1 General overview

A global transition towards greater use of renewable energy and less use of fossil fuels is underway and will progress towards 2050. In addition, the ongoing digital transformation will — through automation, robotization, and adaptive manufacturing — have a large impact on global value chains. It will also advance the design and operation of ships, and create new business models. For shipping, there is increasing pressure to decarbonize and to reduce emissions to air. This will impact asset value and earning capacity more significantly than in the past. It will shape the future fleet in important ways, particularly in the choice of fuels and technologies.[1]

At the same time, it is crucial to understand the existing and future regulatory framework in order to make the right business decisions. Over the past decade, shipping has seen a surge of environmental regulations. Impact on shipping in the next five years will include:

— The global sulphur limit for ship fuels, as set by the International Maritime Organization (IMO)

— IMO Tier III requirements for limiting nitrogen oxides (NO_x) in Emission Control Areas (ECAs)

— The regulation of ballast-water management in accordance with The International Convention for the Control and Management of Ships' Ballast Water and Sediments.

— Greenhouse gas (GHG) emissions will be the main challenge for the next decades. In addition to global carbon dioxide (CO_2) requirements, many local, regional and national requirements are expected aiming at reducing harmful emissions of nitrogen oxides NO_x and sulphur oxides SO_x particles.

1.2 Shipping in context

The shipping industry is at the same time a major contributor to climate change and a relatively low- carbon mode of transporting freight. Shipping tends to have the lowest carbon footprint per unit of cargo transported, but ships carry more than half of international goods by tonne-mile, driving up the shipping industry's petroleum use and CO_2 emissions.[2],[3]&[4]

In Figure 1.1, the transportation's CO_2 emissions and petroleum use by transportation mode are summarized [5]. As shown, the largest shares of transportation energy use and climate impact come from the more than 1 billion on-road passenger and commercial vehicles. However, shipping, with just tens of thousands of vessels, is the next largest energy consumer and carbon emitter. Overall, the transportation sector consumes about half of the world's petroleum supply, amounting to about 47 million barrels of oil per day. Marine shipping uses about 11 % of the global transportation sector's petroleum, or about 5 million barrels per day. This energy use equates to 10 gigatonnes of CO_2 emissions annually from transportation, about 11 % of which is from marine shipping.

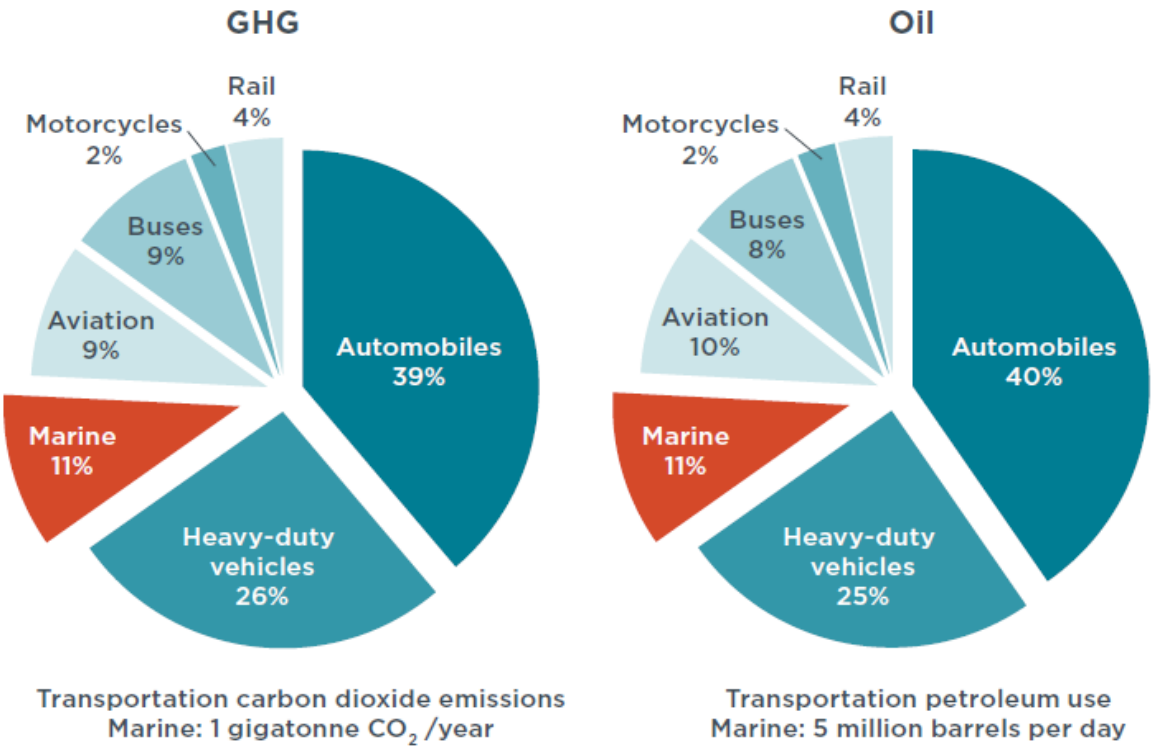

Figure 1.1: Marine shipping's contribution to global transportation climate emissions and petroleum consumption , reference year 2010. [5]

Shipping activity, and therefore its energy and carbon emissions, is closely intertwined with broader economic factors. Business-as-usual marine CO_2 emissions are expected to grow 50–250 % from 2007 to 2050 in the IMO's GHG assessment, due to the expansion of global trade. Shipping activity decreased during the 2008–2010 downturn but has now recovered to approximately pre-recession levels and is widely expected to resume its previous long-term growth trend.[1]

Furthermore, the expected rise of nearly a third (32 %) in seaborne trade measured in trillion tonne-nautical miles per year for 2016– 2030 (see Figure 1.2) and the increase in tonne- mileage over the forecast period for all trade segments except crude oil and oil products are underling the necessity of adequate actions and technological developments. The largest relative growth in trade is for gas and container cargo, for which a tripling and doubling, respectively, is foreseen by 2050. At least a 5 % growth in trade over the period 2030–2050 is predicted by DNV GL Energy Transportation Outlook 2018.[1]

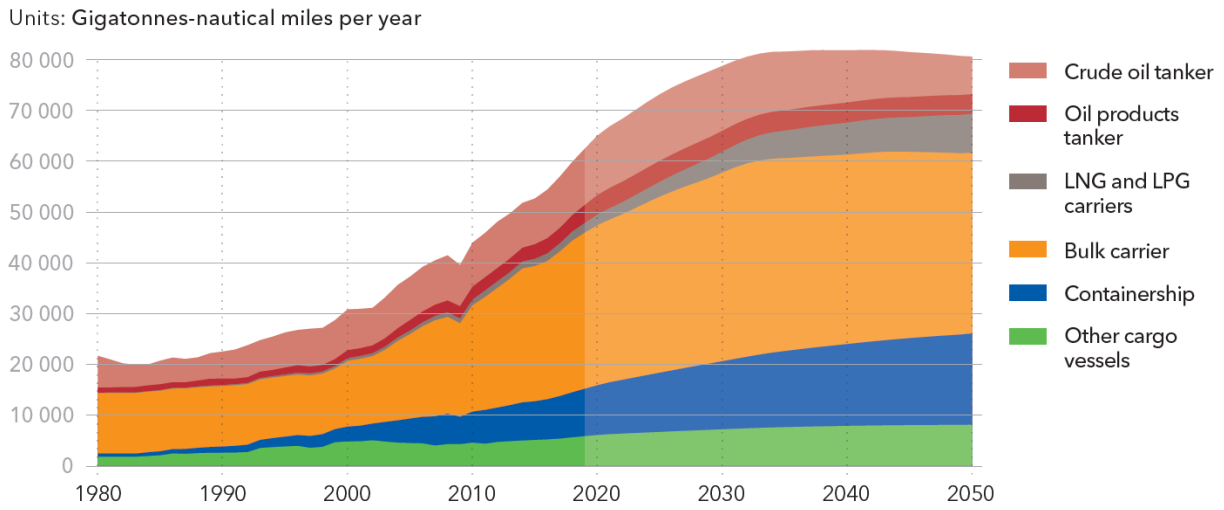

Figure 1.2: Evolution of World seaborne trade in tonne- miles. [15]

1.3 Regulatory timeline

Shipping has experienced a surge in environmental regulations over the past decade. Those emanating from agreements reached under the auspices of the International Maritime Organization (IMO) include the global sulphur limit on ship fuel, nitrogen oxides (NO_x) Tier III requirements in Emission Control Areas (ECAs) and the ballast water management regulation. All will impact on shipping in the next five years, while greenhouse gas (GHG) emissions will be the main challenge in the decades to 2050.

Hence, to ensure compliance and optimize business decisions in shipping, it is vital to understand existing and future regulatory frameworks and the expectations of external stakeholders. In this paragraph, all major global and regional regulations that will impact on shipping in the coming decades are presented in a timeline flowchart (Figure 1.3). In this timeline not all local regulations are included that have been adopted or may be in the future.

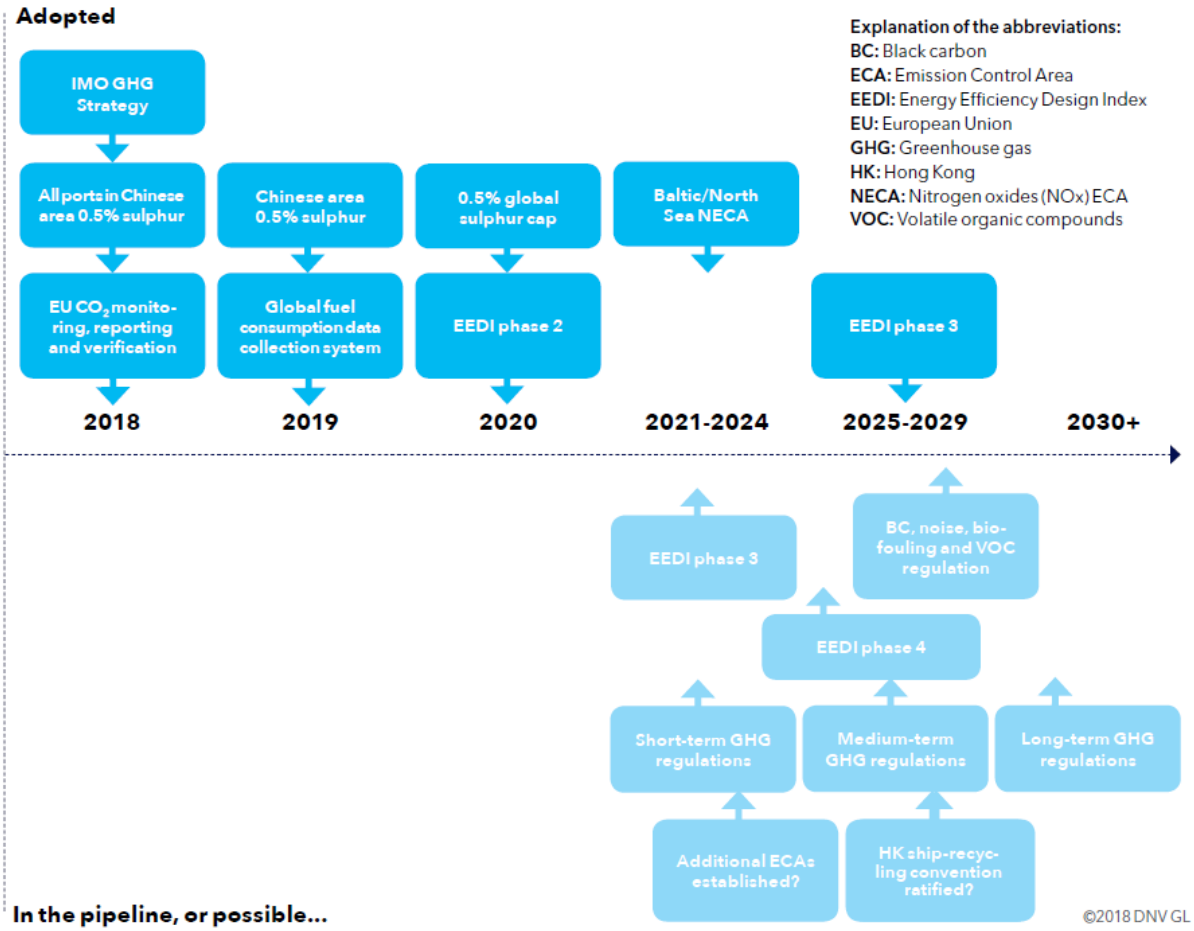

Figure 1.3: Timeline of adopted and possible environmental regulation towards 2030. [1]

1.3.1 EEDI definition& status

On July 2011, the MEPC62 adopted amendments for the prevention of air pollution from ships. These amendments focus on the energy efficiency of large ships and mandate an increasingly stringent EEDI score for the majority of new vessels. [6]

The EEDI regulation applies to new cargo ships greater than 400 gross tons (GT)[1] and varies with ship type, size, and function. The categories of ships covered include oil and gas tankers, bulk carriers, general cargo ships, refrigerated cargo carriers, container ships, passenger ships and roll-on roll-off [Ro-Ro] ships. Together, the included ship categories account for more than 72 % of CO_2 emissions from the new-build fleet (Passenger and Ro-Ro ships not included). [7]

The regulation currently does not apply to specialty vessels for which deadweight tonnage (DWT)[2] is not an adequate representation of transportation capacity. It also does not apply to vessels below 400 GT. The simplicity of the key variables in the EEDI equation also means that it cannot be applied to ships with alternative propulsion

[1] Gross tonnage (GT) is a nonlinear measure of a ship's overall internal volume. Gross tonnage is calculated based on "the moulded volume of all enclosed spaces of the ship" and is used to determine things such as a ship's manning regulations, safety rules, registration fees, and port dues.

[2] Deadweight Tonnage (DWT) is effectively a measure of a vessel's load-carrying capacity. For the EEDI equation, 100 % of DWT is used for all vessels, with the exception of containerships where 70 % is used.

systems such as diesel- electric because the installed power variable ($P_{ME(I)}$) cannot be determined in the straight-forward manner necessary for the Equation (1.4).

Future revisions of the regulation may seek to include additional ship and propulsion types by adjusting the formula or offering alternative formulations.

In simple words, EEDI estimates ship CO_2 emissions per ton-mile of goods transported relative to a reference average of similar ships.

$$EEDI = \frac{(CO_2 Emissions)}{(TransportWork)} \qquad (1.1)$$

In each ship, the following equation must be fulfilled,

$$Attained\ EEDI \leq Required\ EEDI = \left(1 - \frac{x}{100}\right) \times Reference\ Value \qquad (1.2)$$

Where:

- The calculated EEDI (Attained EEDI) based on design specifications and sea trials of new ships will have to be below a reference value (Required EEDI) that is based on a regression of EEDI values from existing ships built between 1999 and 2009 (Reference line).
- Reference Value as calculated in Equation (1.3)
- x is the reduction factor specified in *following* Table 1.2

$$Reference\ Value = a \times b^{-c} \qquad (1.3)$$

The values of parameters a, b and c are ship type dependent. In following Table 1.1, the respective values for various ships' types are presented.

***Table 1.1:** Respective values of parameters a, b and c for various ships' types.* **[6]**

Ship type	a	b	c
Bulk vessels	961.71	DWT	0.148
Oil tankers	1218.8	DWT	0.488
Gas carriers	1120	DWT	0.456
Container vessels	174.22	DWT	0.201
General Cargo vessels	107.48	DWT	0.216
Refrigerated cargo vessels	227.01	DWT	0.244

Table 1.2: Reduction factors (in %) for the EEDI relative to the EEDI Reference Value for various ships' types. **[6]**

Ship type	Size	Phase 1 1 Jan 2015-31 Dec 2019	Phase 2 1 Jan 2020-31 Dec 2024	Phase 3 1 Jan 2025 and onwards
Bulk vessels	*DWT* ≥ 20000	10	20	30
	10000 ≤ *DWT* ≤ 20000	0-10*	0-20*	0-30*
Oil tankers	DWT ≥ 20000	10	20	30
	4000 ≤ DWT ≤ 20000	0-10*	0-20*	0-30*
Gas carriers	*DWT* ≥ 10000	10	20	30
	2000 ≤ *DWT* ≤ 10000	0-10*	0-20*	0-30*
Container vessels	DWT ≥ 15000	10	20	30
	10000 ≤ DWT ≤ 15000	0-10*	0-20*	0-30*
General Cargo vessels	*DWT* ≥ 5000	10	15	30
	3000 ≤ *DWT* ≤ 5000	0-10*	0-15*	0-30*
Refrigerated cargo vessels	DWT ≥ 5000	10	15	30
	3000 ≤ DWT ≤ 5000	0-10*	0-15*	0-30*

*Reduction factor to be linearly interpolated between the two values dependent upon vessel size. The lower value of the reduction factor is to be applied to the smaller ship size.

An "on-time" deployment of the EEDI should had applied the design standards to ship orders placed on or after January 1, 2013 and to ships delivered after January 1, 2015 regardless of their order date. A three-step phase-in of the EEDI occurs in five-year increments: 10 % greater efficiency for ships delivered between 2015 and 2019, 20 % between 2020 and 2024, and 30 % after 2025 (please see Figure 1.3). Future ship efficiency improvements are determined relative to a baseline average efficiency of ships built between 1999 and 2009. Any country can elect to delay the EEDI implementation by up to 4 years without penalty. This clause was added to provide flexibility to developing countries that were concerned about upgrading their shipbuilding industry in time to provide ships that could satisfy EEDI requirements. The first guaranteed year for deployment of EEDI compliant ships would be 2019.The ICCT projected that up to 263 million tonnes (Mt) of CO_2 would be reduced annually by 2030. While the EEDI will add capital and implementation expense related to next-generation ship designs and technology, these costs are more than offset by projected savings up to 75 Mt and $52 billion of fuel annually.[8]

In the following Figure 1.4, the projected CO_2 emissions and cost savings through 2030 from the shipping fleet affected by EEDI Regulation is depicted.

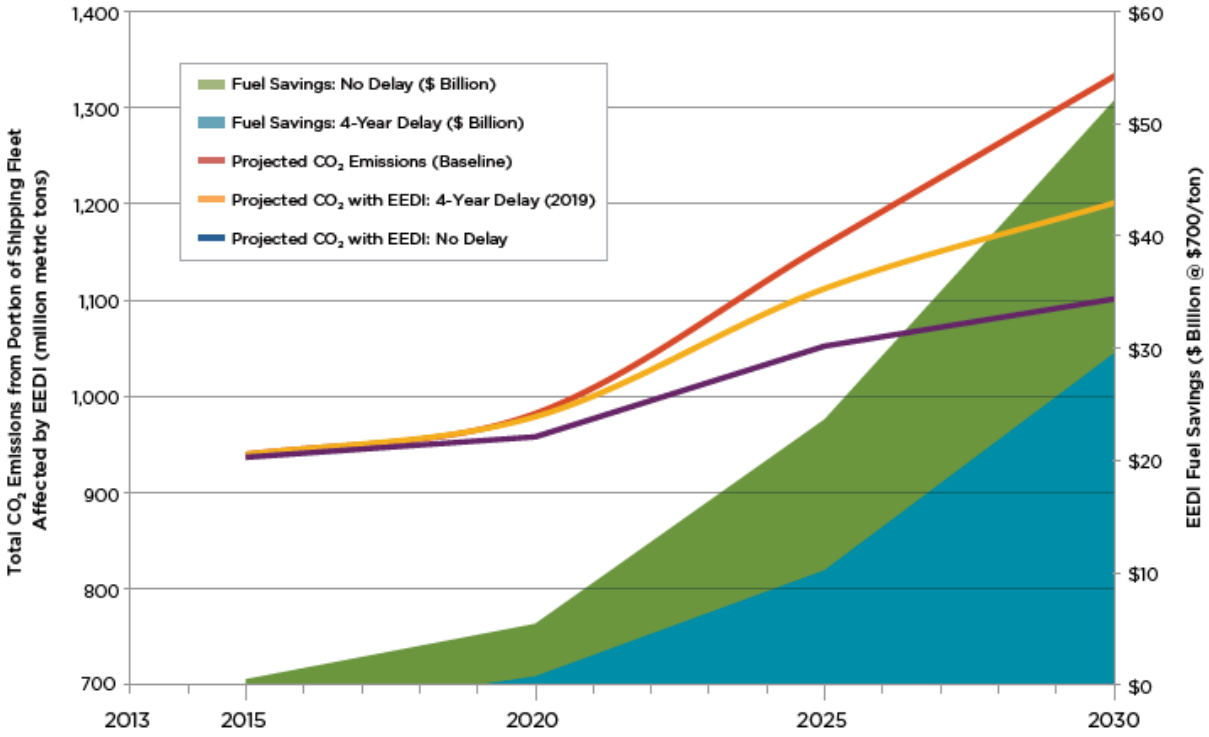

Figure 1.4: Projected CO_2 emissions and cost savings through 2030 from the shipping fleet affected by EEDI Regulation. IMO Scenario A2, with and without proposed 4-year delay.[8]

Furthermore, the full theoretical equation includes several adjustment and tailoring factors to suit specific classes of vessels and alternate configurations and operating conditions.[9]

MAIN ENGINES EMISSIONS | AUXILIARY ENGINES EMISSIONS | SHAFT GENERATORS/MOTORS EMISSIONS | EFFICIENCY TECHNOLOGIES

$$\frac{\left(\prod_{j=1}^{M} f_j\right)\left(\sum_{i=1}^{nME} P_{ME(i)} \cdot C_{FME(i)} \cdot SFC_{ME(i)}\right) + \left(P_{AE} \cdot C_{FAE} \cdot SFC_{AE}^{*}\right) + \left(\left(\prod_{j=1}^{M} f_j \cdot \sum_{i=1}^{nPTI} P_{PTI(i)} - \sum_{i=1}^{neff} f_{eff(i)} \cdot P_{AEeff(i)}\right) C_{FAE} \cdot SFC_{AE}\right) - \left(\sum_{i=1}^{neff} f_{eff(i)} \cdot P_{eff(i)} \cdot C_{FME} \cdot SFC_{ME}\right)}{f_i \cdot Capacity \cdot V_{ref} \cdot f_w}$$

TRANSPORT WORK

(1.4)

Where:

ENGINE POWER (P)

Individual engine power at 75% of Maximum Continuous Rating

- $P_{eff(i)}$ — Main engine power reduction due to individual technologies for mechanical energy efficiency
- $P_{AEeff(i)}$ — Auxilliary engine power reduction due to individual technologies for electrical energy efficiency
- $P_{PTI(i)}$ — Power of individual shaft motors divided by the efficiency of shaft generators
- P_{AE} — Combined installed power of auxilliary engines
- $P_{ME(i)}$ — Individual power of main engines

CO_2 EMISSIONS (C)

CO_2 emission factor based on type of fuel used by given engine

- C_{FME} — Main engine composite fuel factor
- C_{FAE} — Auxilliary engine fuel factor
- $C_{FME(i)}$ — Main engine individual fuel factors

SPECIFIC FUEL CONSUMPTION (SFC)

Fuel use per unit of engine power, as certified by manufacturer

- SFC_{ME} — Main engine (composite)
- SFC_{AE} — Auxilliary engine
- SFC_{AE}^{*} — Auxilliary engine (adjusted for shaft generators)
- $SFC_{ME(i)}$ — Main engine (individual)

CORRECTION AND ADJUSTMENT FACTORS (f)

Non-dimensional factors that were added to the EEDI equation to account for specific existing or anticipated conditions that would otherwise skew individual ships' rating

- $f_{eff(i)}$ — Availability factor of individual energy efficiency technologies (=1.0 if readily available)
- f_j — Correction factor for ship specific design elements. *E.g.* ice-classed ships which require extra weight for thicker hulls
- f_w — Coefficient indicating the decrease in ship speed due to weather and environmental conditions
- f_i — Capacity adjustment factor for any technical/regulatory limitation on capacity (=1.0 if none)

SHIP DESIGN PARAMETERS

- V_{ref} — Ship speed at maximum design load condition
- $Capacity$ — Deadweight Tonnage (DWT) rating for bulk ships and tankers; a per-centage of DWT for Containerships DWT indicates how much can be loaded onto a ship

icct THE INTERNATIONAL COUNCIL ON CLEAN TRANSPORTATION

[8]

The implementation of the EEDI, although a significant first step for ship efficiency, will slow, but not bring an absolute reduction in shipping CO_2 emissions (please see Figure 1.4). It will also do so only gradually over several decades as the entire fleet turns over and becomes EEDI- compliant. Older, less efficient ships that were built through the early 2000s, at times of lower fuel prices, higher profitability, and limited attention to efficiency and carbon emissions, will be in service well into the next decade and beyond.[5]

Therefore, the large remaining—and more near-term—opportunity for reducing CO_2 emissions in the industry therefore lies in the improvement of energy efficiency for in-use ships. Recent years have seen the emergence of highly cost-effective energy-saving technologies and maintenance routines, making such CO_2 savings a real possibility. To better reduce the risks inherent in the price of oil and its volatility, further energy-saving innovations continue to be developed in diesel engines, computerization, and operational practices among the most progressive ships and shipping lines.[16],[17]

1.4 Status on Emissions of Sulphur Oxides (SO_x)

Emissions of sulphur oxides (SO_x) from shipping are being regulated at global and regional levels (Table 1.3). The IMO has decided that the 0.5 % global sulphur cap for ship fuel will be implemented from 1 January 2020. The decision is final, will not be subject to re-negotiation, and has thus provided certainty to the maritime and bunker industries on regulatory conditions.

Table 1.3: Global and regional sulphur limit regulation and scrubber technology.

Area	Sulphur limit	Scrubbers
Global	0.5 % (2020)	Yes
Sulphur	0.1 % in all ports	Yes
EU	0.1 % in selected areas	Open-loop restricted in some countries
China	0.5 % in selected areas	Yes
California	0.1 % within 24 nm	No, only through research exemption

Uncertainty remains over the means of compliance, however. Ship operators will need to decide on their preferred compliance strategies, decisions that will have significant operational and financial implications. There is no one-size-fits-all solution on the table. Sulphur scrubbers, liquefied natural gas (LNG), and 'hybrid' fuels are all realistic options, but most vessels are expected, at least initially, to target 0.5 % sulphur fuel (distillates or low-sulphur fuel oil) as a default position. Local availability issues and price volatility are expected consequences of the unfamiliar fuel-demand picture that will materialize on 1 January 2020. Cases of non-compliance will likely be significant in number during a transitional period, due in particular to insufficient tank cleaning at bunker facilities and on ships.

On a regional and domestic level, the European Union's Water Framework Directive (2000/60/CE) is constraining the discharge of scrubber water. Belgium and Germany prohibit its discharge in most areas, allowing only closed-loop scrubbers. Similar restrictions apply in parts of the US, such as Connecticut.

In Asia, China is taking a staged approach to rolling out regulations governing domestic requirements for SO_x controls similar to emission control areas (ECAs). These apply to the sea areas off Hong Kong/Guangzhou and Shanghai, and in the Bohai Sea. The government is initially enforcing a maximum 0.5 % sulphur content for fuel burned in key ports in these areas, gradually expanding coverage, and culminating in applying the requirements to all fuel used in the sea areas from 2019 onwards. It is possible that the requirement for the sea areas will be tightened to no more than 0.1 % sulphur in 2020, and that a formal ECA application may be submitted to the IMO.

1.5 Status on Emissions of Nitrogen Oxides (NO_x)

The IMO's NO_x Tier III requirements are in force in the North American ECAs for ships constructed on or after 1 January 2016. Tier III also applies for engine retrofits (non-identical) and major conversions on existing ships from this date. Tier III requirements can be met by using LNG as fuel (depending on engine type) or by installing selective catalytic reactors (SCR) or exhaust gas recirculation systems (EGR).

Anyone constructing a ship today needs to consider whether operation in the North-American ECAs will be part of the operational pattern upon delivery, or might be at any time in the future. If so, NO_x-control technology will be required on board. When choosing such technology, operators should also consider how they intend to ensure compliance with the IMO's 2020 sulphur cap. Using LNG will ensure compliance with both NO_x and SO_x caps. EGR and SCR are NO_x-specific reduction technologies.

IMO has also placed NO_x Tier III requirements on ships operating in the North Sea and the Baltic ECAs. This will apply to ships constructed on or after 1 January 2021, and to engine retrofits and major conversions. There are presently no indications of other NO_x ECAs being in the pipeline, but China is considering requiring Tier II for their domestic fleet.

1.6 Status on Greenhouse Gas emissions (GHG)

When the COP 21 Paris Agreement on climate change mitigation was adopted in 2015 as a response to the global-warming threat, shipping was not included. Instead, the IMO was expected to come up with their own contributions to reducing GHG emissions.

In April 2018, the IMO adopted a strategy to achieve this in shipping. Taking 2008 as a baseline year, this aims to reduce total GHG emissions from shipping by at least 50 % by 2050, and to reduce the average carbon intensity (CO_2 per tonne-mile) by at least 40 % by 2030 while aiming for 70 % in 2050 (Figure 1.5). The IMO's ultimate vision is to phase out such emissions as soon as possible within this century. It will review strategy and targets in 2023, based on information gathered from its Data Collection System and from a fourth IMO GHG study, which is currently in ongoing status.

The EU has established general decarbonization goals suggesting a target of GHG emissions 80 % below 1990 levels by 2050. Along the way, there are milestones to achieve a binding target of 40 % cuts by 2030 and, indicatively, 60 % by 2040. All sectors are expected to contribute. For shipping this has, for example, led to the EU monitoring, reporting, and verification system, operational from 2018. It also means that shipping could

potentially be brought into the EU Emissions Trading System (ETS) unless the IMO establishes adequate measures by 2023. IMO actions are expected by then to be sufficient to avoid this.

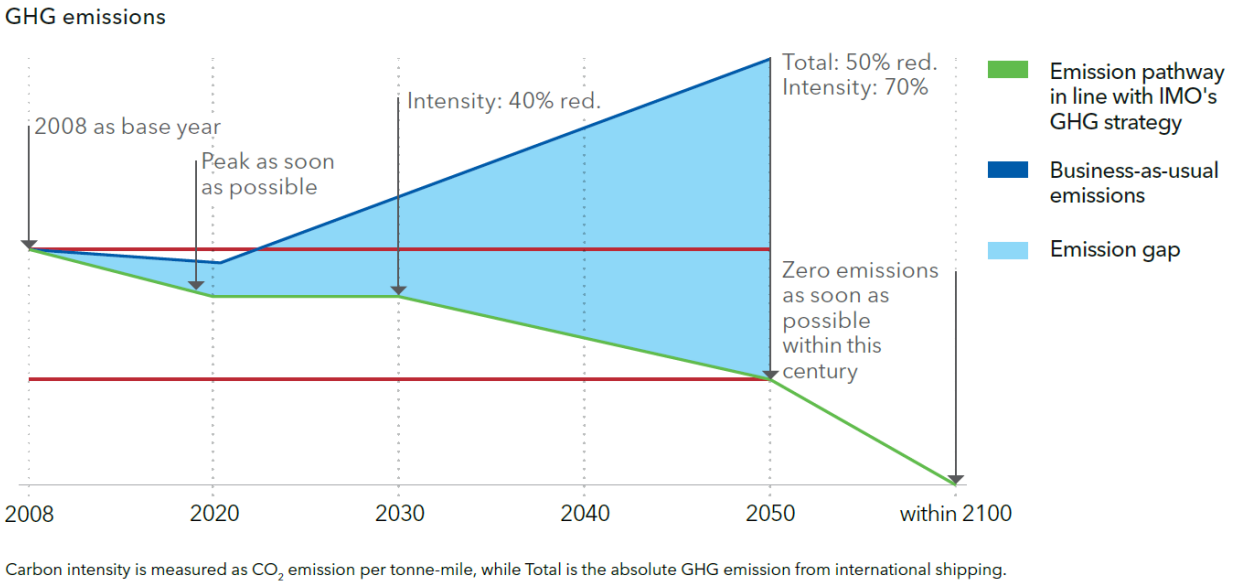

Figure 1.5: International Maritime Organization GHG strategy.

As shipping activity will continue to grow towards 2050, the IMO's 50 % reduction target is ambitious. It will require application of currently immature energy-efficiency technology and solutions, acceptance of lower speed, and deployment of large volumes of carbon-neutral sustainable fuels. Such fuels are presently unavailable in sufficient quantities. A concerted effort is needed to develop them and make them available in the necessary volumes and at acceptable prices.

Achieving its GHG ambitions will require the IMO to develop new policy measures and regulations. While nothing is yet agreed, its current strategy contains a long list of possible measures. They include, among others, strengthening the IMO's energy efficiency design index (EEDI), which is mandatory for new ships; application of operational indicators; speed optimization/reduction; market-based measures; and, development of carbon-neutral fuels. Such fuels will also be essential to achieve the IMO vision to fully decarbonize shipping somewhere between 2050 and 2100.

1.7 Status on Ships' technical and operational energy- efficiency measures

There are a number of energy loads and losses on ships, points at which energy is lost, consumed or dissipated. Near the point of combustion, these occur through thermodynamics, engine friction, thermal exhaust energy, and auxiliary loads within the engine compartment. Mechanical and friction losses in converting the engine torque and speed from the engine to the propeller are also important. In addition to the main engines, boilers and auxiliary engines have similar thermodynamic and friction losses. Many smaller energy demands—lighting, pumps, and fans—are also found on board ships. Each presents an opportunity for vessels to increase efficiency.

Several technical and operational measures are available for reducing shipping's energy use and emissions. Mitigation measures range from easily achievable operational measures to capital-intensive technical solutions.

This paragraph provides an overview of energy-efficiency measures, and points towards some next-generation energy- efficiency measures.

Technical measures generally aim at either reducing the power requirement to the engines or improving fuel efficiency. They are linked to the design and building of ships (e.g., hull design), to optimization of the propulsion system, to the control and efficient operation of the main and auxiliary engines, and to retrofits on existing ships. These measures generally have a substantial investment cost and potentially very significant emission reduction effects. Many technical measures are limited to application on new ships, due to the difficulties or high costs of retrofitting existing ships.

Operational measures relate to the way in which the ship is maintained and operated. They include measures such as optimized trim and ballasting, hull and propeller cleaning, better engine maintenance, and optimized weather routing and scheduling. Operational measures do not require significant investment in hard-ware and equipment. They generally have low investment costs and moderate operating costs. Implementation of many of these measures, many of which are attractive for purely economic reasons, requires execution of programs involving changes in management and training.

A recent literature review of 60 studies provides quantitative estimates of the CO_2 emission-reduction potential for different measures [10]. In Figure 1.6 the main results, indicating large variability, are presented.

In addition, as seen from a number of analyses by various research groups, available technologies and known operational approaches can significantly increase ship efficiency, often with low or negative overall cost—that is, the amortized investment has fuel-saving benefits that more than offset upfront costs. Numerous researches have demonstrated that available efficiency approaches have the ability to reduce fuel use and CO_2 from vessels by 20–40 % by 2020 and 30-55 % by 2030. ([11],[2],[12],[13]).

These studies are based upon bottom-up analyses of baseline ship technology and technologies that are available and emerging in the marketplace.

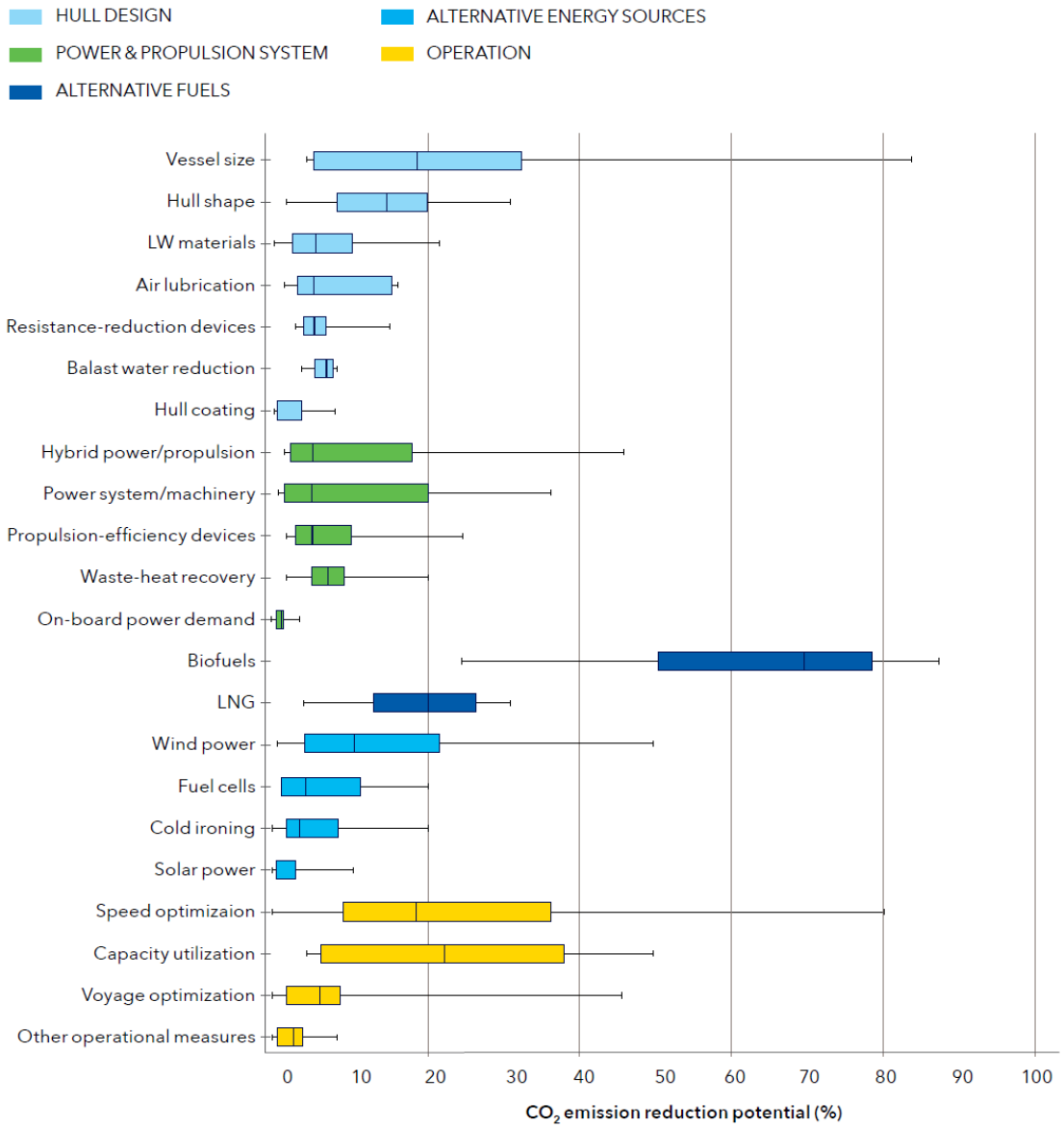

Figure 1.6: CO_2 emissions-reduction potential of individual measures within five main categories.[10]

Previous work by the ICCT [14] shows that a large percentage of the available technologies designed to increase ship efficiency are highly cost-effective. Figure 1.7 illustrates that, even with the application of conservative values for efficiency and CO_2 benefits, there are many "no regrets" approaches with energy savings far greater than the upfront capital costs of installing the technologies in the 2020 timeframe. For example, propeller polishing (a 4.0 % efficiency gain), water flow optimization (a 2.8 % efficiency gain), and hull cleaning (a 4.8 % efficiency gain) each have energy savings that far outweigh their upfront costs. These approaches, for example, result in at least $150 in net benefit for each associated tonnes of CO_2 emissions reduction. There are also technologies, i.e. Waste heat recovery, that not only exhibit significant CO_2 emissions reduction potential but at the same time there are very close to the "brake even line" in terms of economic feasibility. The ICCT study also indicates that, in the relatively near-term time frame until 2020, CO_2 emissions could be reduced by more than 400 million metric tonnes via shipping efficiency measures that each cost less than $75 per tonne and that, on average, deliver a net benefit.

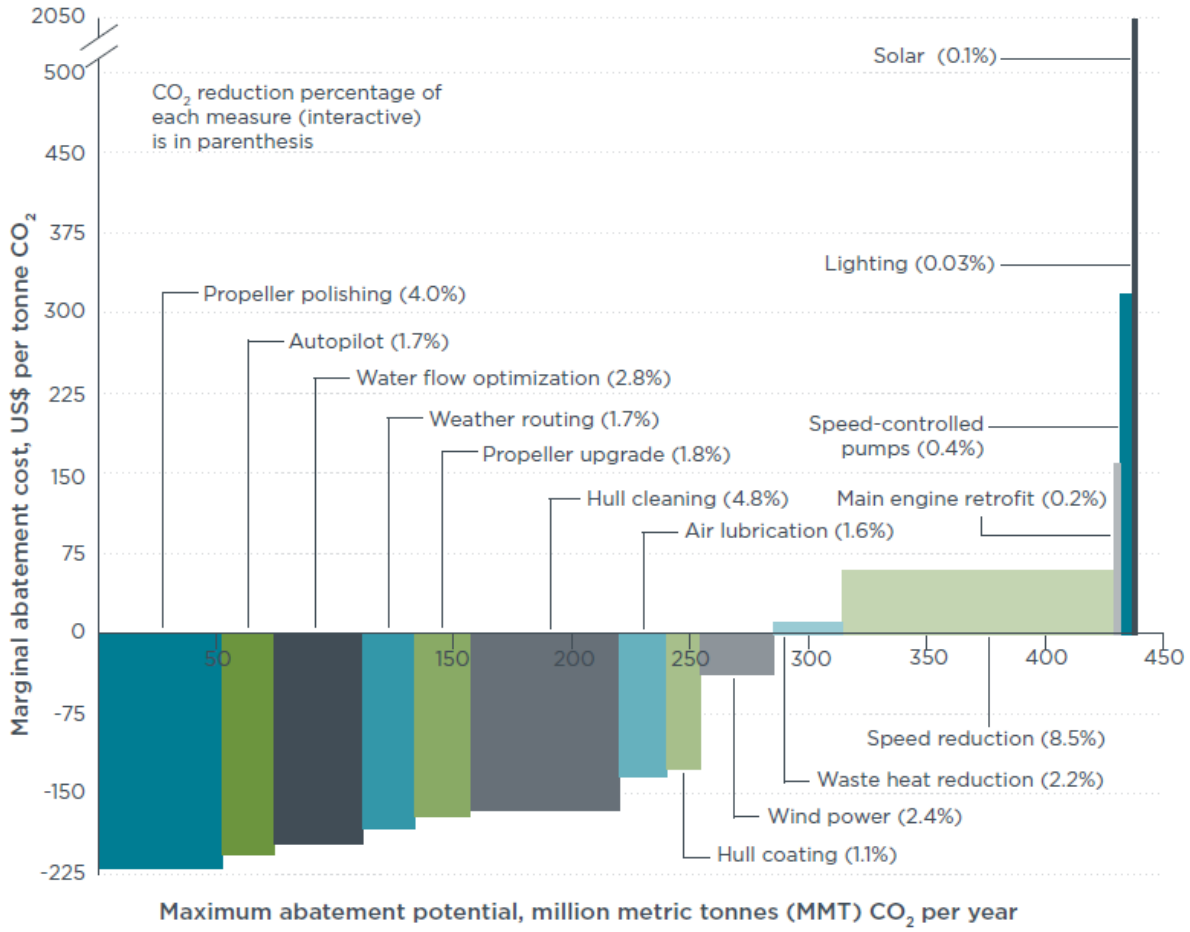

Figure 1.7: Marginal abatement potential, million metric tonnes (MMT) CO_2 per year.[14]

Supplementary to the above, in Table 1.4, the available technology and operational options for improving ship efficiency are summarized with an indication of whether EEDI and in-use efficiency policies promote their increased uptake. The options include engine efficiency approaches such as common rail and waste heat recovery to optimize engine efficiency under different operating conditions, propeller-related technologies such as propeller upgrade and propeller-rudder retrofit to reduce drag on the rudder and propeller and increase the efficiency of the transfer of the engine work to ship thrust and hydrodynamic and aerodynamic approaches that reduce the load on the ship that must be overcome by the propulsion system. In addition, there are auxiliary power efficiency options and a number of practices that can substantially reduce fuel use. Table 1.4 also itemizes the extent to which the efficiency practices might be promoted by the existing EEDI standards for new-build vessels and whether they could be promoted by an in-use ship efficiency policy. As presented in the table, a number of options not fully promoted by the IMO's EEDI standards, such as operational speed reduction, hull cleaning, or propeller polishing, would be under a company policy or IMO regulation that targeted in-use efficiency.

Table 1.4: Examples of ship efficiency measures that can be used to meet the EEDI and could be promoted by in-use efficiency policy. **[14]**

Area	Technology	Potential CO_2 and fuel use reduction	Improvements promoted by EEDI standards	Improvements promoted from in-use efficiency policy
Engine efficiency	Engine controls	0-1 %	✓	✓
	Engine common rail	0-1 %	✓	✓
	Waste heat recovery	6-8 %	✓	✓
	Design speed reduction*	10-30 %	✓	✓
Thrust efficiency	Propeller polishing	3-8 %		✓
	Propeller upgrade	1-3 %		✓
	Rudder	2-6 %	✓	✓
Hydrodynamics	Hull cleaning	1-10 %		✓
	Hull coating	1-5 %		✓
	Water flow optimization	1-4 %	✓	✓
Aerodynamics	Air lubrication	5-15 %	✓	✓
	Wind engine	3-12 %	✓	✓
	Kite	2-10 %	✓	✓
Auxiliary power	Auxiliary engine efficiency	1-2 %	✓	✓
	Efficient pumps, fans	0-1 %	✓	✓
	Efficient lighting	0-1 %	✓	✓
	Solar panels	0-3 %	✓	✓
Operational	Weather routing	1-4 %		✓
	Autopilot upgrade	1-3 %		✓
	Operational speed reduction*	10-30 %		✓

notes: "✓" = promotion of the practice/technology; percents in the table are not strictly additive

* CO_2 and fuel reduction rate depends upon the rate of speed reduction and extent to which engine design modifications, controls, design rating//tuning are included

1.7.1 Mitigating energy losses and improving overall performance

Technological developments in materials science, drag reduction, propulsion, and energy efficiency will provide the basis for the key specifications of new ship concepts. They will tackle energy losses and improve overall performance. Such losses are currently substantial. Only a fraction of the fuel energy entering a ship's main engines generates propulsion thrust. In a case study illustrated in Figure 1.8, 43 % of fuel energy is converted into shaft power, the rest being lost in the engine exhaust or as heat.[2] Further losses in the propeller and transmission mean only 28 % of the energy from the fuel is fed to the main engine and generates propulsion thrust. There is potential for improvement in the areas of greatest energy loss, for example, by reducing hull friction and recovering energy from the engine exhaust and cooling water.

A drive towards mapping energy losses and preventing them is a one-way road. Using advanced thermodynamics methods, such as exergy analysis, reveals insights about the potentially recoverable energy lost in a ship's energy cycle.

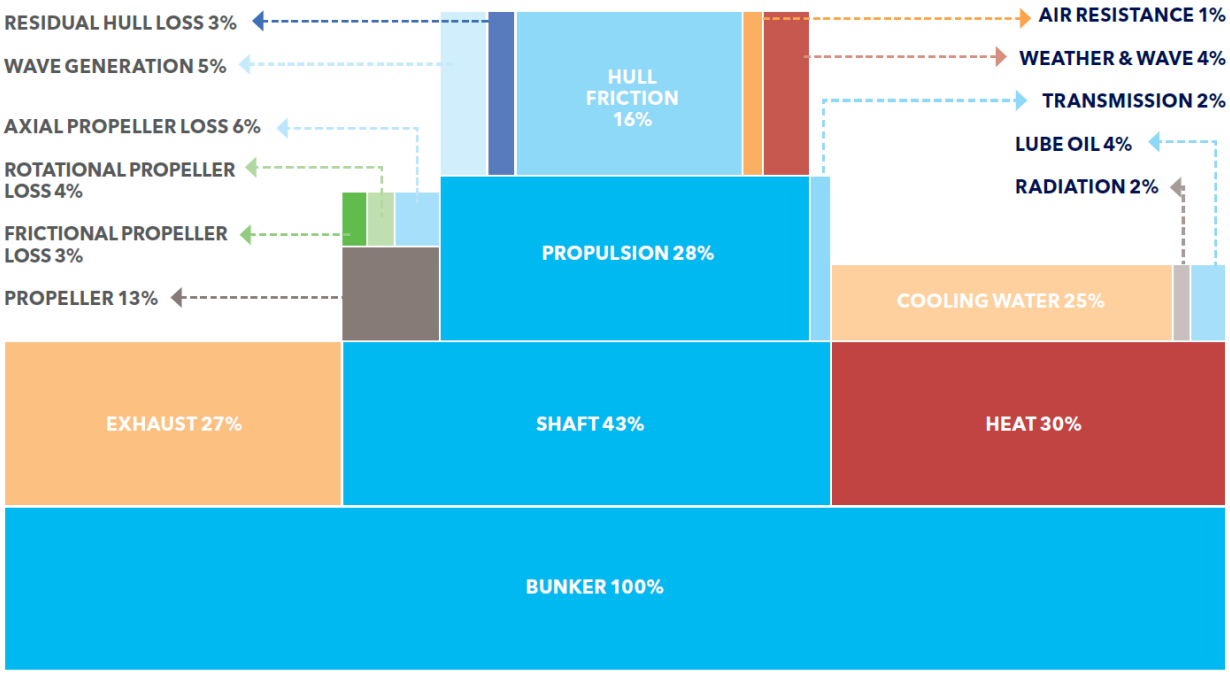

Figure 1.8: Use of propulsion energy on board the case of a small well maintained cargo ship.[2]

The bottom bar in the above Figure represents the energy input to the main engine from the fuel.

According to Smith et al.([18]), shipping emitted 921 megatonnes of carbon dioxide ($MtCO_2$) in 2008, and 870 $MtCO_2$ in 2018 ([15]). If emissions per tonne-mile remain the same, baseline emissions in 2050 would be 1,210 $MtCO_2$ based on the 39 % projected demand growth for seaborne trade (Figure 1.2).

The impact of energy-efficiency measures and speed reduction can be achieved to full effect early in the period up to 2035, as they can be implemented without renewing the fleet. It is projected that emissions will peak in mid-2020. Beyond 2035, the full impact of gradually improving the energy efficiency of new ships, and of the shift to carbon-neutral fuels for the pathways to achieve IMO ambitions will be evidenced.

According to DNV GL GHG pathway model, carbon emissions from international shipping could be significantly decreased to around 410 $MtCO_2$ in 2050. Figure 1.9 presents how various measures contribute to the emissions reduction for the pathway model. A tenth (10 %) of the emission reduction will be due to logistical improvements in the supply chain; 18 % from technical and operational energy-efficiency measures; 14 % from

speed reduction, taking into account the additional ships needed to cover the transport work, and, a further 22 % because of carbon-neutral fuels.

It is evident that the deployment of multi measure package solutions is a prerequisite in order to reach the IMO GHG targets. In addition, the energy efficiency solutions will be the corner stone of every strategy along with the usage of alternative fuels. Significant contribution within the energy efficiency matrix will be from the exploitation of the ICE Waste Heat potential.

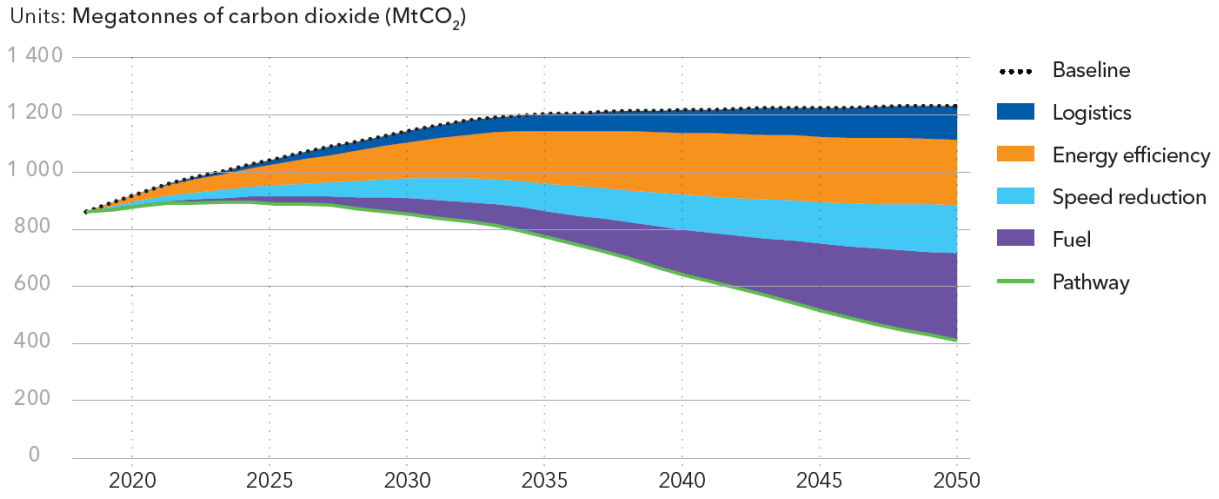

Figure 1.9: Shipping emissions reduction by measure (2018-2050) according to DNV GL GHG pathway model.

1.8 Scope and objectives of present study

As already pointed out, the energetic consumption of a commercial ship mainly consists of propulsion and internal consumption electricity needs, which are entirely covered by specially designed marine diesel engines (main and auxiliary respectively). For large ships, the fuel expenses constitute about 30-55 % of the total operational costs, depending on the type of vessel [19]. Strong motivation exists within the marine sector to reduce fuel expenses and to comply with even stricter efficiency regulations, e.g. the EEDI -Energy Efficiency Design Index [6]. Moreover, regarding emissions of CO_2, sulpfur and nitrogen oxides (SO_x and NO_x) the international regulations are changing towards stricter limits [6]. Hence, among others, emphasis is being put on the improvement of the thermal efficiency of engines by optimizing their configuration in order to achieve lower fuel consumption [20]-[21]. Also, research has been focused on advanced combustion technologies, such as the HCCI [22]-[23], lean combustion [24] and stratified combustion [25]-[26], in order to achieve a higher overall efficiency and reduce overall emissions. However, as these technologies have achieved quite a matured stage, it becomes harder to achieve further improvements via these methods, thus a valuable alternative approach to improve overall energy efficiency is to capture and reclaim the ‘‘waste heat’’ [27]. The latter is underlined by the necessity to increase as much as possible the overall energy efficiency in order to reach the IMO GHG targets by 2050 (see Figure 1.9).

Hence, to reduce the risks inherent in the price of oil and its volatility, further energy- saving innovations continue to be developed in diesel engines- such as waste heat recovery (WHR) systems-, computerization, and operational practices among the most progressive ships and shipping lines [16]-[17]. WHR systems for electrical

or mechanical power production can significantly contribute towards addressing these challenges, with the ORC (Organic Rankine Cycle), the Kalina cycle and the steam Rankine cycle receiving the majority of attention in the literature. The steam Rankine cycle is focused on higher temperature WHR mainly from the exhaust gases of the main engines of a ship, while the ORC/Kalina cycles are more suitable for smaller engines [28], like the marine auxiliary ones, while at the same time they can also be used for WHR from lower temperature heat sources (e.g. the jacket water of diesel engines). Because of the low boiling point of the working fluid, the ORC technology is well adapted to low temperature waste heat recovery, which cannot be accomplished with traditional water/steam Rankine systems. Moreover, the amount of thermal power discharged by a topping process can be of a magnitude order of some tens or hundreds of kW; these values are not compatible with superheated water-steam turbine cycles, which have a complex architecture and are typical of large-size power plants. Furthermore, optimization results suggest that the Kalina cycle possess no significant advantages compared to the ORC or the steam cycle [29].

Although the Diesel process is highly efficient, large marine diesel engines are particularly well suited to be coupled with a WHR system [32], as the engine loses a large part of the fuel energy to the environment, mainly with the exhaust gases (up to 27 % of the input energy) and the jacket water (up to 25 % of the input energy) [2]-[28]. However, both heat sources, originating from the main engine, are used -when needed- for covering the internal heating needs of a ship (e.g. heavy fuel oil pre-heating, fresh water generation, exhaust gas boiler), while the respective ones from the auxiliary engines remain unused. Several researchers have proposed WHR systems for main marine diesel engines ([29]-[30]-[31]-[32]) but no experimental study or even a theoretical analysis has ever been conducted regarding the jacket water of auxiliary engines. In this perspective, the present work focuses on the recovery of heat from the auxiliary engines and more specifically from their jacket water. For the scale and heat source temperature level considered, both the ORC and the Kalina could be used as bottoming cycles. Bombarda, et al. [33] compared the two processes applied for WHR on large marine engines and found that both cycles, when optimized, produced equal power outputs. This research focuses on the construction and experimental evaluation of an ORC WHR system, specially designed for the jacket water of a marine auxiliary diesel engine.

Chapter 2. - Description of laboratory ORC test rig

2.1 General overview& operating principle of ORC test rig

As already mentioned in Chapter 1, the experimental laboratory ORC test rig was designed to exploit 90 kW_{th} from a hot water circuit, thus, simulating the cooling circuit of the ship's auxiliary ICE (water jacket) and to produce 5 kW_e of electrical power. A typical value of the ICE's water jacket temperature outlet lays between 80 to 90 °C and there are no major variations for reasons to be explained below. Soft water was used for the condensation of the organic medium with a temperature of 15 °C. In real life ship operation, the condenser rejects the heat with the use of an open seawater circuit.

Hence, the experimental ORC prototype unit is based on a conventional low-temperature subcritical Organic Rankine Cycle. The organic working medium that was selected for the ORC cycle was the R134a refrigerant with a critical temperature of 100.1 °C and a saturation temperature at 25 bar equal to 77.7 °C (design point).

The operation principle of the experimental unit follows the philosophy of small scale ORC waste heat recovery systems: a pump raises the liquid refrigerant to the maximum cycle pressure, which is then evaporated by the waste heat source medium (water in this case) in a plate heat exchanger. Subsequently it is expanded in an expansion configuration (two open-drive scroll compressors in reverse operation, with swept volume ~ 121 cm3/rev, pressure ratio ~ 2.3, nominal power output: ~2.5 kW each, installed in parallel at the Marine-ORC unit) and is led to a condensing heat exchanger. The condensed refrigerant is fed to the ORC pump and the cycle is repeated. The main ORC components (ORC circuit with blue color), the heat transfer circuit (red color), and the cooling circuit (green color) are depicted in Figure 2.1.

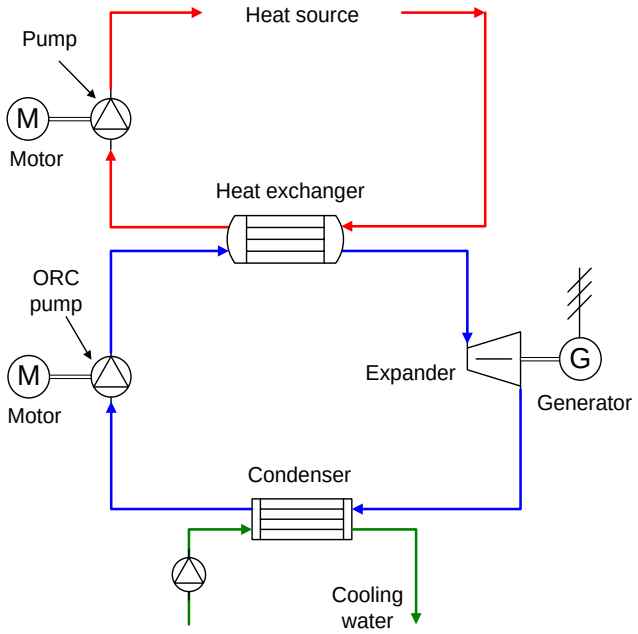

Figure 2.1: Simple configuration of an Organic Rankine Cycle set up, depicting main components.

Superheating of the medium is not necessary for the so-called "dry" organic media (that is, in which the saturated vapor curve has a positive slope on the T-s diagram), as it is impossible to generate a two-phase mixture during expansion. On the following Figure 2.2, the comparison of the saturated vapor curve for the three types of refrigerants ("Wet" refrigerant with a negative saturated vapor curve– "Isentropic" refrigerant with an almost vertical saturated vapor curve – and "Dry" refrigerants, which have a positive saturated vapor curve) is depicted. The 1,1,1,2 – Tetrafluoroethane (R134a), although designated as wet fluid, exhibits a value of (ξ) very close to

zero (-0.39 J/kgK^2). Thus, with a small superheating (less than 5^{o}C) the possibility of two phase mixture during expansion is minimized substantially.

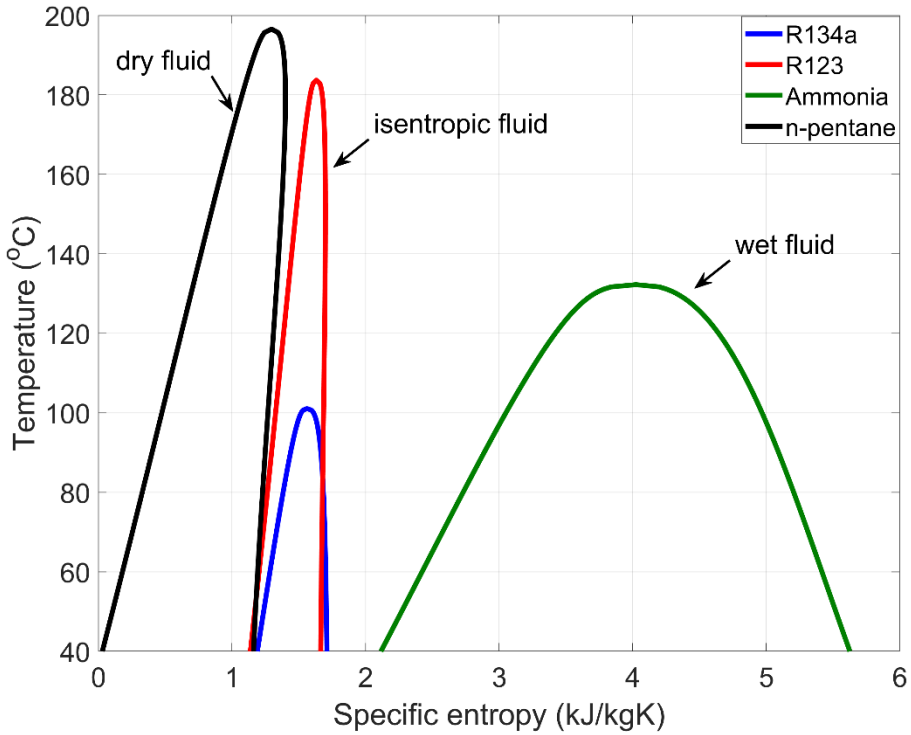

Figure 2.2: Comparison of the saturated vapor curve for the three types of refrigerants ("Wet" refrigerant – "Isentropic" refrigerant – and "Dry" refrigerants).

S. Quoilin documents [35] that from an energy point of view the increase in superheating results in a decrease in the thermodynamic efficiency of the cycle, although it is known that increases the specific mechanical output produced in the turbine, increasing the area enclosed in the T-s diagram. Since we are referring to a waste heat recovery application, where the increase in power produced is the ultimate target, a compromise between the two above phenomena must be realized. Hence, the evaporator was chosen so as to have a superheating of 4°C at the rated nominal operating conditions.

The process of the cycle is described as follows (Figure 2.3): the pump (1) continuously feeds the evaporator with a desired flow rate of the organic medium, in which the medium is preheated (2'), evaporated (2'') and superheated (2) and then driven to two identical expanders (3) (in parallel arrangement). The scroll expanders are coupled with belt to the asynchronous generators, respectively, equipped with frequency inverters. The existence of the two expanders allows the test rig to operate either in full or in part load with the possibility of isolating the second expander through the normally closed (NC) solenoid shown in the drawing of the test rig (Figure 2.4). The organic medium is then condensed in the condenser (4,4',4'') and ending up in the receiver. The cycle is closed after subcooling the medium to a subcooler (5), which ensures that the organic medium entering the pump is at a temperature well below that of saturation, thereby preventing the cavitation phenomena on the pump. The subcooler was installed at a later stage of the experimental investigation campaign, further details will be presented in section 3.1.

The thermodynamic states of the cycle described in the preceding paragraph are depicted in the diagram below. The values are indicative and present the theoretical rated design operating conditions of the specific experimental ORC test rig.

The thermodynamic efficiency of the cycle is defined as the ratio of the produced work of the expander to the heat absorbed by the evaporator:

$$\eta_{th} = \frac{h_2 - h_3}{h_2 - h_1} \qquad (2.1)$$

While in the electrical efficiency calculation, the net electrical power produced is considered

$$\eta_{el} = \frac{P_{net}}{m_{wf} \cdot (h_2 - h_1)} = \frac{P_{gen} - P_p}{m_{wf} \cdot (h_2 - h_1)} \qquad (2.2)$$

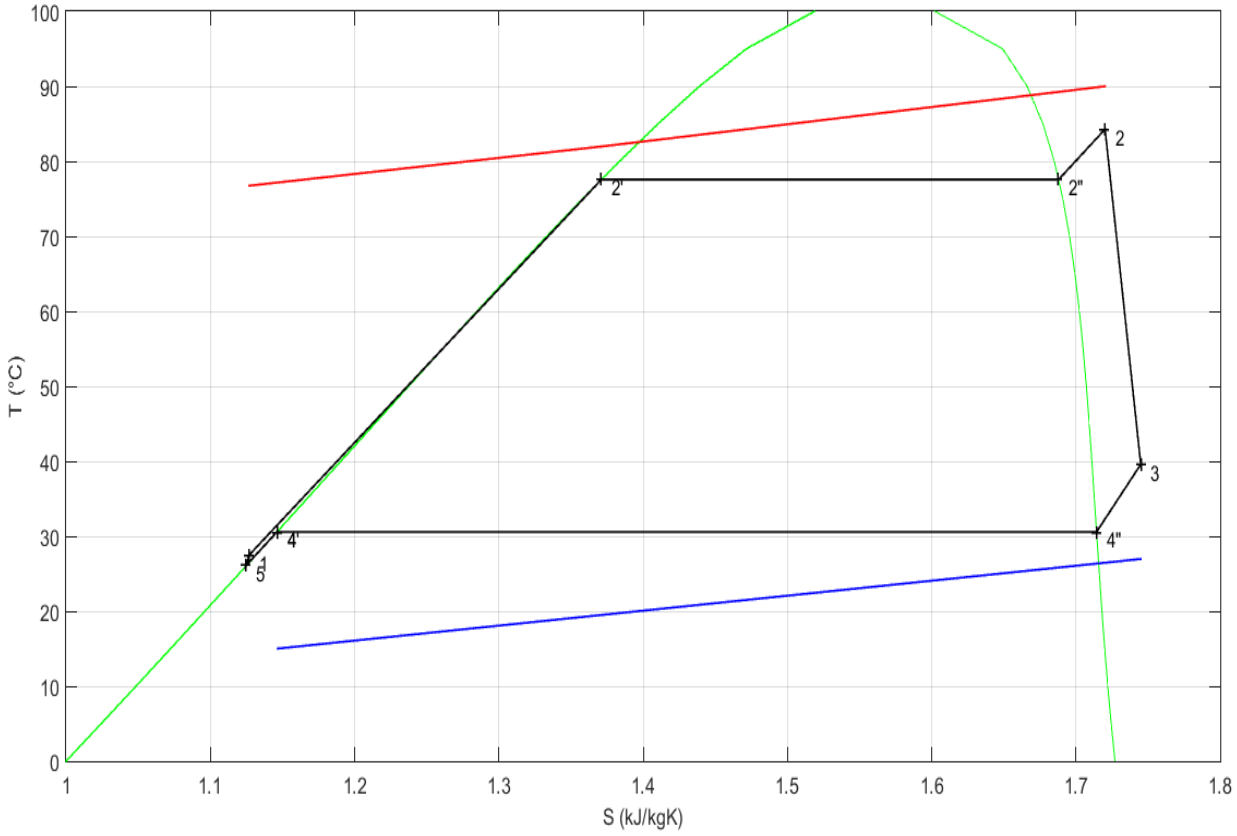

Figure 2.3: Thermodynamic Cycle's T-s diagram at nominal design conditions.

The P& ID schematic of the constructed experimental test rig is presented in Figure 2.4. Where all components are illustrated as built. The presented equipment and components are briefly described in the following paragraphs of the present Chapter 2.

[

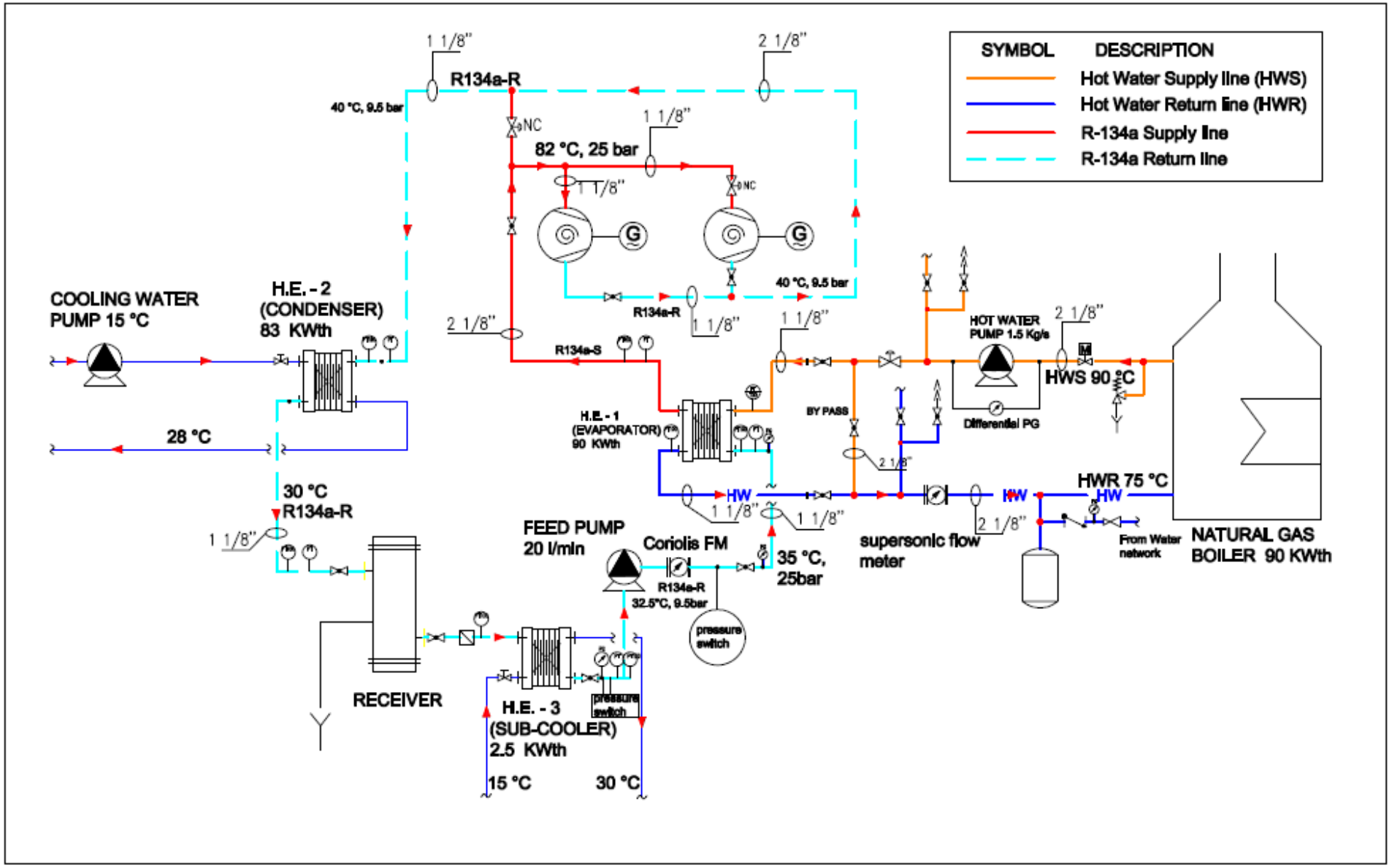

Figure 2.4: P&ID schematic (as built) of the laboratory experimental ORC test rig.

2.2 Pump

The pump selected is a multi-diaphragm pump manufactured by Wanner Engineering. The pump belongs to the product line Hydra-Cell and the model is D/G-10. Among the different types specified in Figure 2.5, the installed pump is the D-10-X and has a metallic head, so that it can withstand the 25 bar high pressure of the cycle. If the machine were in fact equipped with a non-metallic head, it could deal with a maximum pressure of only 17 bar. As far as the difference between types D and G are concerned, the choice of one of the two letters refers to two different types of threads for the inlet and outlet ports. D indicates NPT type (National Pipe Thread) and it is an American standard thread; letter G, instead, stands for BSPT type (British Standard Pipe – Tapered thread).

D/G-10 Specifications

Max Pressure	Metallic: 1000 psi (70 bar) Non-Metallic: 250 psi (17 bar) Slurry Duty (SD): 300 psi (21 bar)		
Capacity @ Max Pressure			
	rpm	gpm	l/min
D/G-10-X	1450	7.8	29.0
D/G-10-E	1750	8.0	30.3
D/G-10-S	1750	6.0	22.7
D/G-10-I	1750	3.9	14.9
Delivery @ Max Pressure			
	revs/gal	revs/liter	
D/G-10-X	185	50	
D/G-10-E	219	58	
D/G-10-S	292	77	
D/G-10-I	448	117	
Max Inlet Pressure			
Metallic:	250 psi (17 bar)		
Non-Metallic:	50 psi (3.5 bar)		
Slurry Duty (SD):	50 psi (3.5 bar)		
Max Temperature			
Metallic:	250°F (121°C) – consult factory for temperatures above 160°F (71°C)		
Non-Metallic:	Polypropylene: 120°F (49°C); Kynar, Celcon & Slurry Duty: 140°F (60°C) – consult factory for temperatures above 120°F (49°C)		
Inlet Port	D-10: 1 inch NPT G-10: 1 inch BSPT		
Discharge Port	D-10: 3/4 inch NPT G-10: 3/4 inch BSPT		
Shaft Diameter	7/8 inch (22.22 mm)		
Shaft Rotation	Bidirectional		
Bearings	Tapered roller		
Oil Capacity	1.1 US quarts (1.05 liters)		
Weight	Metallic Heads: 48 lbs (22 kg) Non-Metallic Heads: 35 lbs (16 kg)		

Calculating Required Horsepower (kW)*

$$\frac{15 \times rpm}{63{,}000} + \frac{gpm \times psi}{1{,}460} = \text{electric motor HP*}$$

$$\frac{15 \times rpm}{84{,}428} + \frac{lpm \times bar}{511} = \text{electric motor kW*}$$

* rpm equals pump shaft rpm. HP/kW is required application power. Use caution when sizing motors with variable speed drives.

Figure 2.5: Specifications of the pump as provided by the manufacturer.[36]

The multi diaphragm pump is considered as a positive displacement pump and its' basic operational principal is presented briefly below, with the help of Figure 2.6:

Rotating the pump shaft causes a piston to compress or decompress an oil-filled chamber. The diaphragm (membrane) transfers the compression / decompression caused by the piston to the main chamber of the pump through which the working medium passes. The inlet / outlet control of the fluid is controlled by means of non-return valves made of stainless steel beads. The general operating characteristics of the pump are summarized in the following Table 2.1*:*

Table 2.1: Technical characteristics of D10-X.

General characteristics	
Maximum inlet pressure (bar)	17
Inlet diameter (in)	1
Outlet diameter (in)	3/4
Nominal characteristics	
Rotational speed (rpm)	1450
Nominal flow rate (lpm)	30.6
Maximum outlet pressure	69

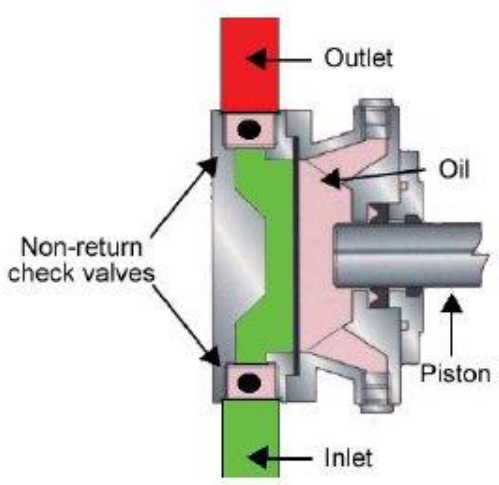

Figure 2.6: Schematic of a typical diaphragm pump.

One of the reasons that such a pump is preferable to the experimental ORC cycle test rig is that it allows the working medium to be separated from the moving mechanical parts, reducing the likelihood of leakage or contact of the medium with lubricants. Also, it is also ideal for applications where large manometric heads are required for relatively small volume deliveries (in our case 160 mH_20 for a flow rate of 20 l/min).[37]

As is known in positive displacement pumps, the supply flow rate is theoretically independent of its manometric head, although in practice it tends to decrease slightly with the increase of the latter, mainly due to volumetric losses. Thus, the volume flow rate of the pump in question is proportional to the rotational speed (with dependent constant the swept volume), and its pressure is determined solely by the hydraulic resistance of the pipeline, which is primarily determined by the expander for an ORC cycle. The following Figure 2.7 shows the characteristic curve provided by the pump manufacturer (volume flowrate vs. rotational speed):

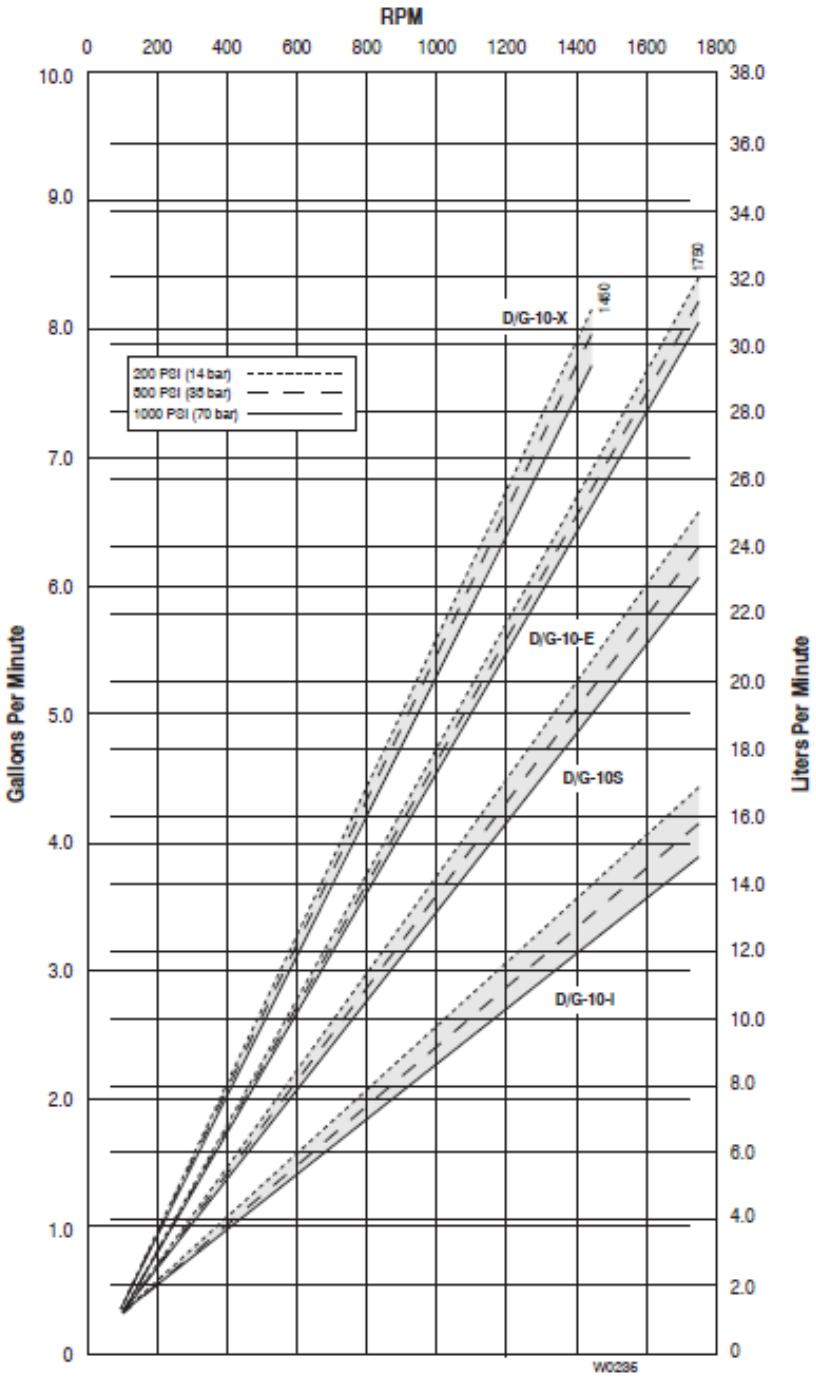

Figure 2.7: Volume flow rate [gpm], [l/min] vs. rotational speed [rpm] of Hydra-Cell D-10X multi diaphragm pump.[36]

From the above curves, a linear dependence is found between the delivered volume flowrate and rotational speed as it was expected. Only a slight decrease in the lines slope is registered when switching from a lower maximum pressure to a higher one. The good agreement between the manufacturer curves and the experimental values will be discussed in section 3.7. Furthermore, this dependence by linearly adjusting some of the points between the 14 bar and 35 bar lines (pump operating range) is as follows:

$$\dot{V}[lpm] = \frac{N_P[RPM] - 22.681}{46.705} \qquad (2.3)$$

Since the pump is directly connected to a six-pole three-phase induction motor of 3.0 kW nominal rated output, manufactured by Valliadis (model K123S-6), pump and motor have the same rotational speed and, naturally, the latter is imposed by the motor. The nominal speed of the motor is 960 rpm at 50Hz; therefore, when it is mentioned that that the pump is operating at its nominal speed, it is actually meant that the motor is operating at its nominal point since the pump has no nominal operational point. The specifications and the characteristic curves of the pump (Figure 2.5 and Figure 2.7) do not show, indeed, a nominal point where the machine should preferably operate. On the contrary, the volume flowrate curves attest that the machine can operate in the whole rpm range. The rotational speed of the motor is controlled by a Siemens inverter (see section 2.11.1). The characteristics of the pump motor are given in the table below:

Table 2.2: Technical characteristics of pump's motor Valliadis (model K123S-6).

Manufacturer	**VALIADIS**	**Power Factor**	**0.76 PF FL**
Family / Frame	**K132S**	**Efficiency FL**	**86.40**
Rated Power	**3.00kW / 4.00hp**	**Torque FL**	**30**
Rotational speed	**960 RPM**	**Locked rotor torque / Full load torque**	**2.10**
Mounting	**B35**	**Star delta torque / Full load torque**	**Y-MOTOR**
Voltage / Connection	**230-Δ / 400 - Y**	**Pull out torque / Full load torque**	**3.20**
Frequency	**50Hz**	**Star delta pull out torque / Full load torque**	**Y-MOTOR**
Enclose	**55IP**	**Locked rotor current / Full load current**	**6.4**
Full load current	**6.60A / 11.43A**	**Star delta locked current / Full load current**	**Y-MOTOR**
Insulation class	**F**	**Bearing DE**	**62008ZZC3**
Comment	**3 x PTC 150°C**	**Bearing NDE**	**62008ZZC3**
Feature	**Cast iron - motor**	**Code**	**21/6-004.00/6**
Weight	**63.0kg**		

The manufacturer also provides detailed measurements from tests performed to evaluate motor performance. The manufacturer suggests an equation for the calculation of the power required by the pump. It expresses the shaft power as a function of the pump rotational speed (rpm) and of the hydraulic power delivered to the fluid (lpm*bar). Since there is no torque meter between the motor and the pump, this equation has a key role in the determination of the mechanical power as pump input. It has also been used in the semi-empirical model of D'Amico, Pallis et.al [47] for the same pump and it was used during this study as well, in order to investigate the behaviour of the electric motor.

The equation is rewritten below with the nomenclature used:

$$\dot{W}_{sh,pump}[kW] = \frac{\dot{V}\Delta p}{511} + \frac{15 * rpm}{84428} \qquad (2.4)$$

where: $\dot{W}_{sh,pump}$ = the pump shaft power [kW]

$\dot{V}$ = volume flow rate [lt/min]

Δp = pressure difference [bar]

rpm = pump/motor rotational speed [rpm]

2.3 Organic medium (Refrigerant)

Organic media for ORC are common refrigerants with low boiling temperatures. Such may be chlorofluorocarbons (CFCs), hydrochlorofluorocarbons (HCFCs) and hydrofluorethers (HFEs). The selected refrigerant for the laboratory experimental test rig is R134a (1,1,1,2-Tetrafluoroethane) with a critical temperature of 100.1 °C and a saturation temperature at 25bar equal to 77.7 °C (design point). Further details of R134a are presented in Table 2.3.

Table 2.3: Characteristics of R134a (1,1,1,2-Tetrafluoroethane).

Critical Temperature T_c (°C)	Critical Pressure P_c (bar)	ODP	GWP	Latent heat (KJ/kg)	ASHRAE 34 classification
101.1	**40.6**	**0**	**1300**	**155.4**	**A1**

Where:

ODP (EU Directive 2037/2000). The initials refer to 'Ozone Deplete Potential' and refer to the relative degradation caused by this refrigerant in the ozone layer of the atmosphere, with trichlorofluoromethane (R-11 CFC-11) having the value of 1.0. The composition of the refrigerant is that which causes the ozone layer to degrade, which are denoted by the first C in the CFC and HCFC refrigerants. Gradually these refrigerants will be replaced by HFCs and HFEs which do not contain chlorine and therefore the ODP index

will be zero. R123 will be gradually replaced by HFE7000 hydrocarbons due to the zero ODP of the latter. Depending on the legislation, R123 will be withdrawn by the end of 2030.

GWP (EU Directive 842/2006). Originally referred to as "Global Warming Potential", it is a relative measure that shows how much heat a greenhouse gas traps in the atmosphere. Reference has been made to CO_2 with a GWP value of 1.0. Perfluorocarbons (PFCs) will be phased out and replaced by other potential refrigerants due to the large GWP index. HFC-134a) will gradually be replaced by R1234yf or R1234ze due to its high GWP.

ASHRAE 34 STANDARD "Designation and Safety Classification of Refrigerants". ASHRAE Standard 34 assigns the refrigerant numbers and determines the proper safety classification based on toxicity and flammability data. ASHRAE defines two safety classifications for toxicity: Class A signifies refrigerants that are of lower toxicity and Class B signifies refrigerants that are of higher toxicity. For flammability, there are three classifications and one sub-classification. The three main flammability classifications are: Class 1, for refrigerants that do not propagate a flame when tested as per the standard; Class 2, for refrigerants that are of lower flammability, and Class 3, for highly flammable refrigerants, like the hydrocarbons. The safety classification matrix (Table 2.4) was recently updated to include a new flammability Subclass 2L, for flammability Class 2 refrigerants that burn very slowly. Some HFOs, which have very low global warming potential, are mildly flammable and are classified as A2L. This indicates they are of lower toxicity and have a low burning velocity of ≤10 cm/sec.

Selecting the organic medium for each application is probably one of the most important processes in designing an ORC. Most often the choice of a working medium influences the choice of system expander and vice versa.

For positive displacement expanders, the constraints are derived from the expansion ratio and the built in volume per rotation. The maximum expansion ratio, depending on the machine, usually does not exceed 5, with the exception of reciprocating expanders whose expansion rates can be as high as 20. In the case of screws, the ratio is limited by the length of the rotor and in the scrolls by the number of coils. The built in volume rotation is related to the maximum rotor diameter on the helical coils and the maximum height and diameter of the coil on the coils.

Table 2.4: Safety Classification of Refrigerants in ASHRAE34 "Designation and Safety Classification of Refrigerants".

		Toxicity	
		Lower Toxicity	Higher Toxicity
Flammability	Higher Flammability	**A3** R-290 Propane R-600a Isobutane	**B3**
	Lower Flammability	**A2** R-152a	**B2**
		A2L* R-32 R-1234yf R-1234ze(E)	**B2L*** R-717 Ammonia
	No Flame Propagation	**A1** R-22 R-134a R-410A R-1233zd(E) R-404A R-407C R-507A R-744 Carbon Dioxide	**B1** R-123

*A2L and B2L are lower flammability refrigerants with a minimum burning velocity of ≤10 cm/sec

A combination of energetic and environmental /safety reasons led to the choice of the above organic medium. The high theoretical efficiency that can be achieved for the evaporation and condensation temperatures of that cycle, which are determined by the temperature of the jacket's cooling water (heat source) and the temperature of seawater (heat dissipation), based on simulations of similar cycles that have been done in the past [34]. In addition, the fact that the evaporation temperature is close to the critical for the organic medium in question allows for a reduction in the size of the equipment due to its higher density compared to other organic media with a higher critical temperature. Furthermore, based on the above temperature conditions and the use of positive displacement expander, it is possible to operate the test rig in a range of operating conditions according to the operating maps created by S. Quoilin in the framework of his doctoral thesis [35]. According to the latter research and for the case of scroll expander, the following Figure 2.8 depicts the adequacy of R134a as selected organic medium. Finally, given the restrictions imposed by the closed state nature of the ship's engine room, the organic working medium should be assigned as A1 according to ASHRAE 34 "Designation and Safety Classification of Refrigerants".

Using these constraints, S.Quoilin in his doctorate dissertation developed a map of the permitted operating conditions in a T_{ev} / T_{cd} diagram, as shown in Figure 2.8.

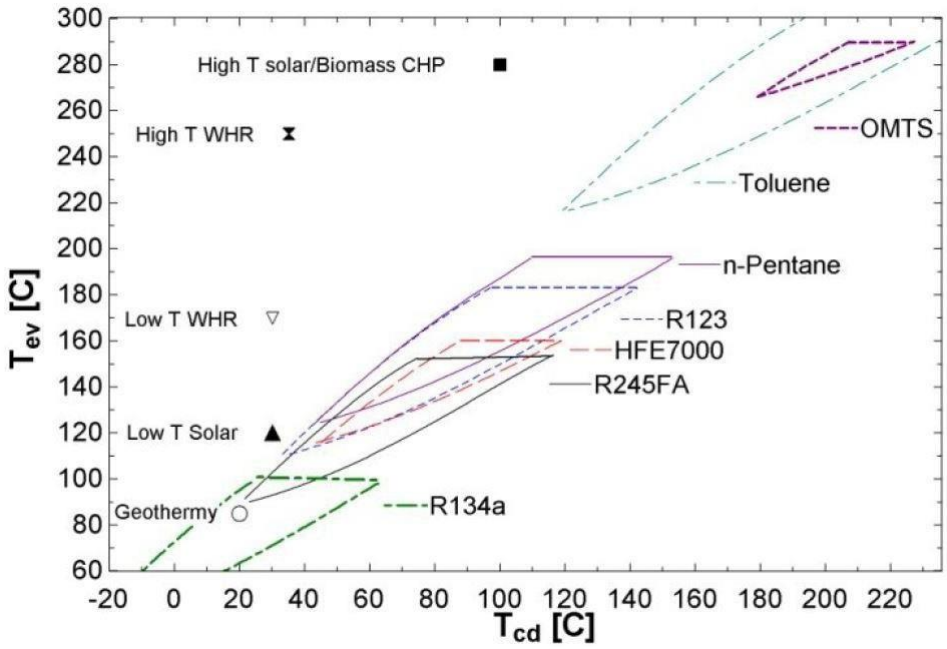

Figure 2.8: Scroll expanders operational map. [35]

The map has 5 points corresponding to specific ORC applications depending on evaporation and condensation temperatures. Each line sets the limits of the evaporation and condensation temperatures that can be achieved with every particular refrigerant, based on the limitations previously set. The upper line results from the critical temperature of the refrigerant. The upper left curve is given by the limitation of the over-expansion losses. The downer right curve is given by the limitation on the volume coefficient.

2.4 Evaporator / Condenser

The heat exchangers (H.E.) selected for the evaporation and condensation of the working medium are brazed plate stainless steel H.E. and belong to the range of Alfa Laval CBH60-XXHheat exchangers series. Plate exchangers consist of a series of very thin plates that are placed one after the other and are joined together either by tightening and inserting elastic gaskets between (gasketed plate heat exchangers) or by welding (brazed heat exchangers). Corrugations are formed in the plates following a particular arrangement (eg V or fishbone). The fluids pass through channels formed by the placement of two consecutive mirrored plates, due to the corrugations on each side. Thus on one side of each plate flows the first fluid and on the other side, counter flows the second fluid, as shown in the Figure 2.9. The fluids enter and exit the channels through holes at the corners of each plate (inlet and outlet). The result is a large heat transfer surface area and low thermal resistance due to the small thickness of the plates

and the sharp changes in the flow direction within each channel, which enhance heat transfer by convection.

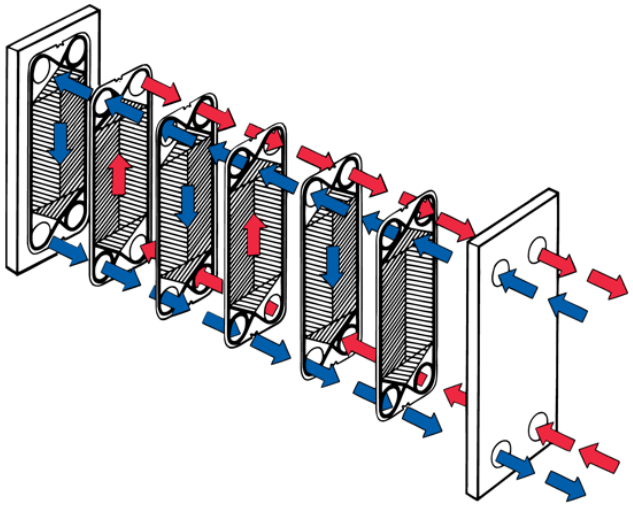

Figure 2.9: Schematic of a typical plate heat exchanger.

This type of heat exchanger is generally preferred because of its high specific heat transfer rate per surface, which therefore allows it to be significantly more compact, a parameter that is very important for installation of this scope and nature, like in a ship's engine room. In addition, the fluid volume inside the heat exchanger is relatively small, allowing for a faster response in dynamic conditions. On the other hand, it usually exhibits higher pressure drop values than other types of heat exchangers (i.e. shell and tube), which is largely determined by the channel arrangement and the chevron angle. Finally, it has relatively low resistance to high pressures, but this does not particularly affect in this type of applications.

The general characteristics of the two heat exchangers are summarized in the following tables:

Table 2.5: Characteristics of ORC test rig evaporator.

	Evaporator (Alfa Laval CBH60 -90H-F)
Number of plates	90
Heat transfer surface	3.881 m^2
Nominal heat transfer capacity	90 kW_{th}
Maximum pressure	32 bar (at 225 °C)
Volume (lt)	9.17

Table 2.6: Characteristics of ORC test rig condenser.

	Condenser (Alfa Laval CBH60 -60H-F)
Number of plates	60
Heat transfer surface	2.486 m^2
Nominal heat transfer capacity	83 kW_{th}
Maximum pressure	32 bar (at 225 °C)
Volume (lt)	5.90

The connections' arrangement of each heat exchanger was designed to facilitate phase change and reduce hydraulic losses inside them. This involves connecting the evaporator in such a way that the inlet of the working medium is at the bottom respective connection port and the outlet on the upper connection port, so as to facilitate the movement of the gas phase bubbles with natural circulation. On the other hand, the condenser connection arrangement is reversed, with the working medium coming in from the upper connection port and exiting from the bottom to favor condensate descent by its own weight.

2.5 Expander

The expander is the machine that produces the useful work of the cycle by expanding the high pressure and operating temperature medium to a lower pressure. The general term expander is used against the turbine because in contrast to the usual practice in steam cycles, where the expander is a steam turbine, in small-scale ORC applications (<1 MW_e) positive-displacement expanders are normally used such as the piston, screw or scroll.

2.5.1 Screening of the appropriate expander technology

The type of expander that can be used in a small-scale ORC application has some limitations. The following is a brief description of the selection procedure for the application under consideration.

The most common option could be the turbine. The turbines produce the useful work through the continuous interaction of the working fluid with the rotor blades. Although this is a proven and reliable technology, there are several reasons that ultimately lead to the choice of another type of expander, in the case of small-scale ORC applications.

For example, a typical axial turbine stage has pressure ratios of 1.5. This means that this application requires a two-stage axial turbine, since at the nominal operating point the pressure ratio is greater than 2.5 - which implies a specific manufacture of this machine and therefore an increased cost.

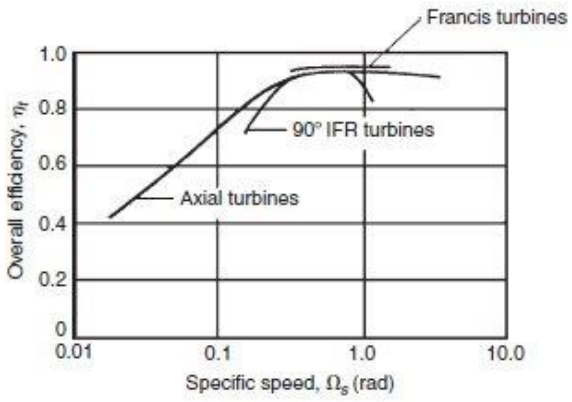

Figure 2.10: Schematic correlation of specific speed with efficiency for various types of turbines.[38]

Alternatively, the use of a radial turbine could solve the problems of high pressure ratios on one hand. On the other hand, radial turbines have a much narrower range of performance. Figure 2.10 shows a typical change in the efficiency of such a turbine as a function of the number of specific speed [38]:

$$N_s = \frac{N(rad/s)\sqrt{V_{ex}(m^3/s)}}{\Delta h(J/kg)^{0.75}} \quad (2.5)$$

Where $\dot{V}_{ex}$ is the volume flow at the turbine outlet and Δh the difference in specific enthalpy between the turbine inlet and outlet. It can be seen that the efficiency of a typical inward-flow radial turbine reaches satisfactory values when N_S ranges between [0.3-1].

Based on the lower limit of this interval and the nominal operating point of the ORC cycle, the turbine speed shall be at least:

$$N = 38800\ rpm \quad (2.6)$$

which means that a typical design of such a machine requires the use of a gearbox with a reduction ratio of about 1:10 for the use of a two pole generator, which increases the cost and complexity of the installation. In addition, the power scale of a few kW (5-6 kW for this cycle) imposes due to Euler's theorem the design of very small impellers, which is very difficult to construct, making the use of a radial turbine inappropriate for such application.

Finally, all turbine engines impose no liquid phase formation inside, due to the possible wear of the blades. Although in "wet" organic media, such as R134a (with ξ almost zero), this is unlikely to occur during

expansion, generally the fact that positive displacement expanders can operate even in two-phase flow gives them a manufacturing advantage.

In contrast, positive displacement expanders for a given volume flow rate exhibit a rotational speed proportional to their scan volume, which means that it is possible to choose a compact expansion machine that does not require the use of a gear unit. They also have the capability to operate at high pressures for relatively small flow rates. The pressure ratio of such an expander is determined by the ratio of the expansion volume to the suction volume and takes typical values from 2 (scroll) to 5 (screw). Lastly, since most of this type of expansion machines is manufactured by converting to similar compressors, they are readily available on the market and therefore quite economical.

Pistons, although providing a wide range of pressure ratios, are not preferred because of the inlet-outlet valve system, which increases the complexity of the system and eventually the capital cost.

Hence, the choice between the screw type and the scroll type is determined solely by the power scale.

Screw expanders are intended for larger flow rate applications (0.1–5 m^3/s at the expander output) and therefore higher power (> 20 kW), with their lower threshold being defined by the low efficiency performance based on current technology [7], as illustrated in the adjacent Figure 2.11. It is therefore obvious that for the scale and characteristics of this application (V = 0.01 m^3 / s and P_{th} = 5 kW) the only option was the scroll expander technology.

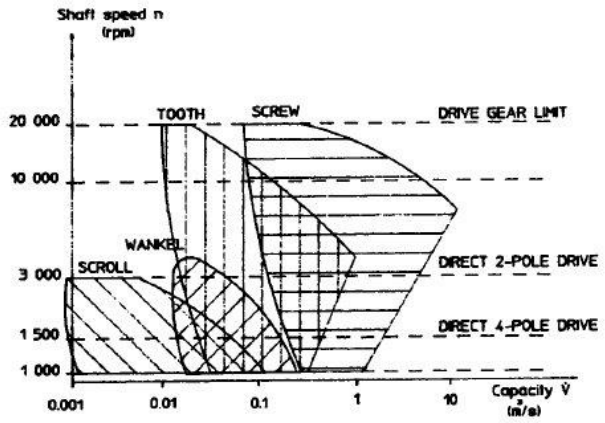

Figure 2.11: Range of acceptable efficiency versus the volume flow rate for various types of positive displacement expanders.[39]

Hence, the choice between the screw type and the scroll type is determined solely by the power scale.

In agreement with all above, are the results from various ORC cycle simulations performed by S. Quoilin [40]. These results show that for applications of power less than 10 kW, the scroll expander is the ideal choice, with screws and turbines being suitable for larger power plants.

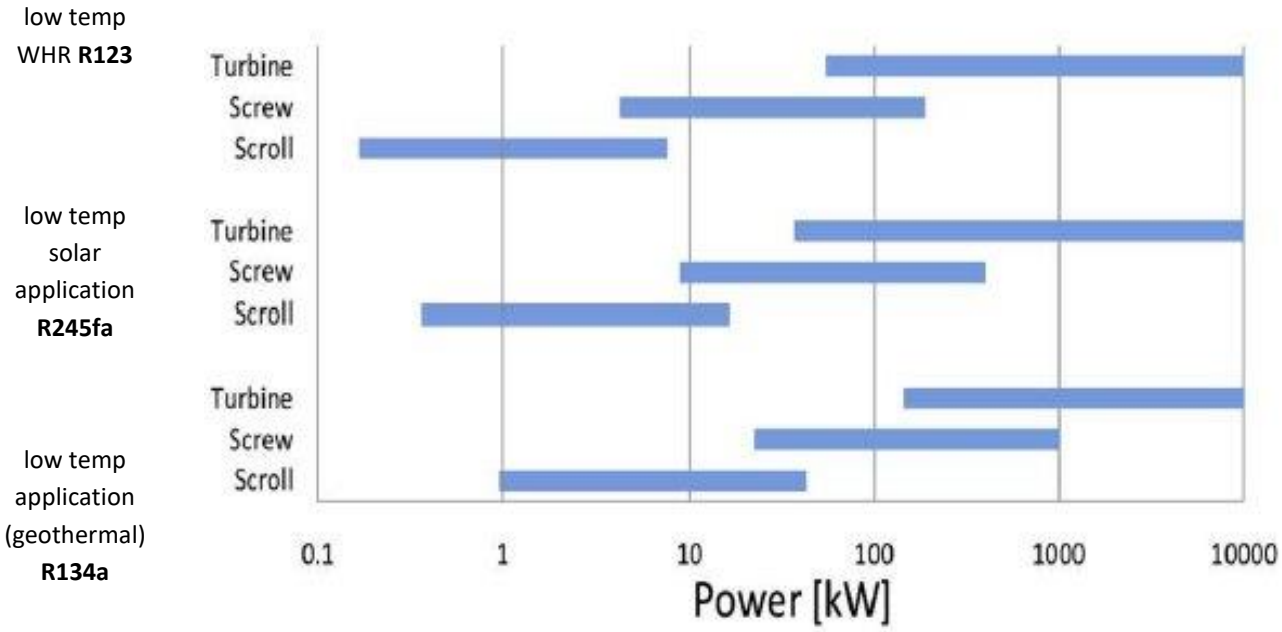

Figure 2.12: Range of acceptable efficiency versus the volume flow rate for various types of positive displacement expanders.[40]

2.5.2 Selection of helical expander (scroll)

The fact that the helical expander is the ideal choice for small-scale ORC applications has led to the development of research and the development of various prototype models by helical compressors in recent years. Experience so far has shown that helical expanders are an economical and reliable solution, and can have quite satisfactory isotropic efficiency. Recent experimental studies have shown that the efficiency of such a machine can reach up to 71 %.[41]

The operating principle of the helical expander is the opposite of that of the compressor. It consists of two scrolls, one orbiting and one fixed, which are cam mounted together. The fluid enters at high-pressure and temperature state at the center of the two scrolls and expands by pushing the orbiting scroll, leading to points where the volume enclosed by the two scrolls is larger. The eccentricity between the two scrolls results in the rotating motion of the orbiting scroll. The expansion pressure ratio is determined by the ratio of inlet-outlet volumes, or expansion ratio (r_v).

Figure 2.13: Operating principle& the scroll wraps of a typical helical expander (scroll).[42]

The expansion ratio is a structural parameter of the expander and hence for a given inlet pressure defines the pressure at the end of the expansion process. Since the pressure at the expander outlet is practically determined by the condensation temperature, the fluid exiting the last coil (State 9 in the Figure 2.13) makes an isochoric process in order to reach the externally imposed outlet pressure. If the condensation pressure is lower, then the media has undergone under-expansion and thus should be further expanded under constant volume at the lower pressure (Figure 2.14). When the condensation pressure is higher, then the medium has over-expanded and thus will reach the pressure of the condenser by isochoric compression (Figure 2.15).

Any of the above situations is considered a loss for the expander as it reduces its isotropic efficiency. Therefore, the maximum isotropic efficiency is achieved at this pressure ratio which for the inlet-outlet conditions corresponds to the "built-in" expansion ratio.

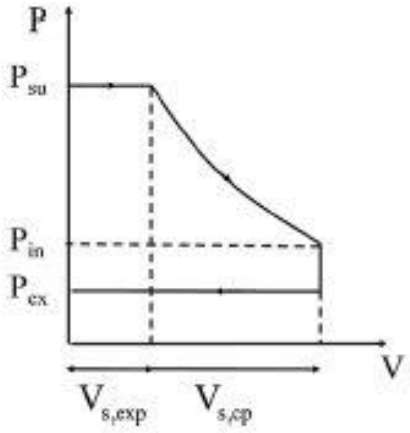

Figure 2.14: Under expansion process, in P-V diagram).[43]

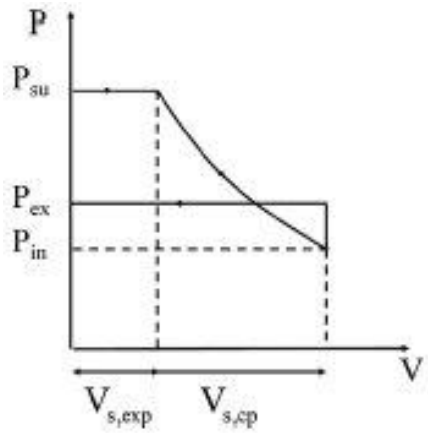

Figure 2.15: Over expansion process, in P-V diagram.[43]

On the other hand, the case of under-expansion can increase the work produced due to further isochoric expansion and is therefore usually desirable in heat recovery applications.

As a result to the above, two identical open-drive scroll expanders were installed in parallel arrangement in the experimental laboratory test rig, and each was coupled to an individual asynchronous motor (generator) through a belt drive. The design of the experimental test rig allowed the expanders to operate at 1500 rpm (at nominal operating conditions) allowing thus a 1:1 transmission ratio, since the generator was chosen to be a 4 pole motor. In order to avoid possible leaks in the open drive machines, suitable tip sealings were installed on the top of the fixed scroll. In addition, modifications included removing the oil pump, closing the air passage used for cooling when the machine was operating as a compressor, and additional sealing at the tips of the fixed and orbiting scroll.

The features of the scroll compressor modified in this installation are summarized in the following table:

Table 2.7: Characteristics of the helical compressor / expander.

	Scroll Compressor (Sanden TRSA12)
Swept volume (cm^3/rev)	121.1
Expansion ratio r_v	2.45
Maximum Pressure(bar)	35
Nominal Power output (expander mode in kW)	2.5

2.6 Selection of generators

In this specific application the power is generated by means of two 4 pole induction generators. The induction generator is practically an induction (asynchronous) motor, turning at a speed slightly higher than the synchronous. For a machine with P = 4 poles the synchronous speed in a network frequency of f = 50 Hz is:

$$N_s = \frac{120 \cdot f}{P} = 1500\ rpm \quad (2.7)$$

Table 2.8: Rotational speed of an electric motor depending on the number of its' poles and the network frequency of the helical compressor / expander.

Number of Poles P	Rotational speed in a network of 50Hz / 60 Hz
2	3000 RPM / 3600 RPM
4	1500 RPM / 1800 RPM
6	1000 RPM / 1200 RPM

As already mentioned, the generator-expansion coupling is realized with a belt and 1: 1 gear ratio.

Slipping on an induction machine is defined as:

$$s = \frac{|N - N_s|}{N_s} \cdot 100\% \quad (2.8)$$

Slipping in induction motors gets a maximum value, beyond which the torque exceeds the pullout torque limit, causing the generator to over speed sharply and usually is around 8 %. On the other hand, the nominal operating point of the machine is in the range of 33 % -50 % of the overturning torque and the slip values are in the range of 3 %. Between the synchronous rotational speed (where there is no electromechanical energy conversion) and the rated nominal operating point, the torque-speed curve is almost linear [44]. Since the speed does not vary much, the same can be said for the power output.

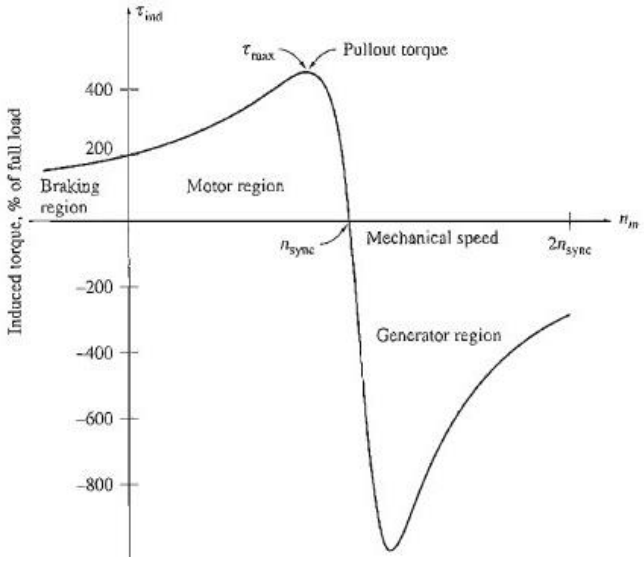

Figure 2.16: Characteristic curve of torque vs rotational speed of an inductive motor.[44]

The induction motors used in the experimental ORC test rig are from Valliadis company with rated power of 5.5 kW (model K123S-4). They belong to the same family of motors as the pump motor so their

behavior at points other than the rated is considered to be the same. Their characteristics at the nominal operating point are summarized in the following Table 2.9*:*

Table 2.9: Characteristics of inductive motors used in the experimental ORC test rig.

	Inductive generators(Valliadis K123S-4)
Number of poles / Synchronous rotational speed	4 / 1500RPM
Rated nominal power (kW)	5.5
Nominal electrical efficiency (%)	85.9
Slip at nominal operating point(%)	3.36

The two inductive generators are controlled using Siemens VFD (Variable Frequency Drive) (see section 2.11.1) for further details.

2.7 Selection of receiver

The installation of an adequate volume container tank (receiver) in a closed refrigerant circuit is necessary to ensure the required amount of medium needed to flow in any possible operating condition of the cycle. Through the receiver's port, the circuit can also be filled with refrigerant, if necessary.

In the experimental test rig, a 50 lt volume receiver was fitted with a maximum pressure of 46bar. Its placement was just after the condenser therefore the natural circulation of the working medium is facilitated. Also in order to minimize the cavitation phenomena at the feed pump inlet, it was decided that the receiver to be installed, with its longer dimension, in height, thus increasing the vertical distance from liquid surface inside the receiver to pump center line suction inlet.

Inside the receiver liquid and gaseous phase of the medium co-exist, while three level markers (balls) determine the height of the surface of the liquid phase. Therefore, the receiver, in equilibrium state, is always saturated.

2.8 Sub cooler heat exchanger

According to the preceding paragraph, the existence of the feed container (receiver) prior to the pump leads to the latter being fed to a near saturated organic medium (in fact there is a small hydraulic height available due to the level of the liquid inside the receiver but never exceeding 40 cm). To avoid cavitation in the pump (see section 3.1), therefore, it was necessary either to increase the height difference between the container and the pump - which for spatial reasons was not possible - or to cool the medium with a separate adequate heat exchanger.

The sub cooler heat exchanger, after various tests, was chosen to be an improvised counter flow shell and tube heat exchanger, where it practically consists of a barrel-shaped shell for the cold water stream exterior and a simple copper finned tube, located inside the former, within which the organic medium is passing through. The choice of this heat exchanger ensures satisfactory performance and low pressure drop for the working medium, elements sufficiently important to ensure a high available suction height.

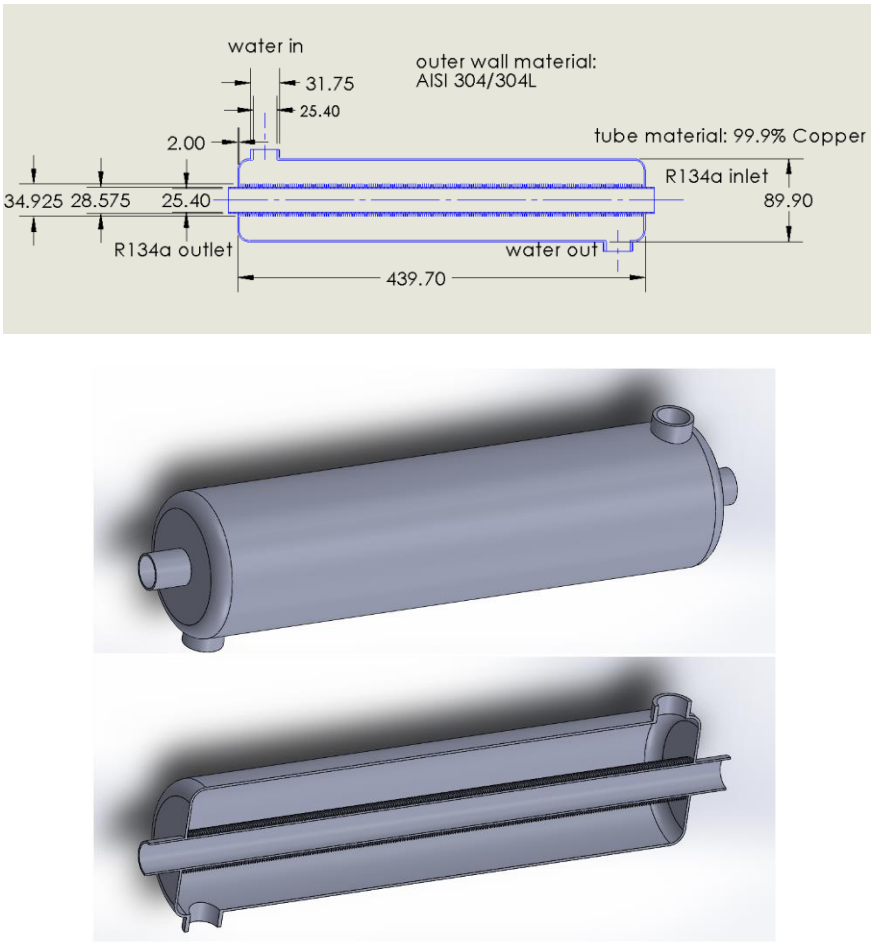

Figure 2.17: Construction drawing of the shell and tube sub cooler heat exchanger.[45]

2.9 High temperature water circuit

In order to simulate the HT water circuit of the ICE water jacket at the experimental laboratory test rig, an adequate high temperature water circuit was constructed. It, mainly, consists of a cast iron natural gas boiler manufactured by Thermis Greek Company and a natural gas burner by Johannes Company. The water circulates with a Wilo pump inverter, and the desired flow rate is regulated by a Belimo regulating valve that can be set using a 0-10 V analogue signal. In addition, the hot water circuit also has an automatic filling valve with manometer and an expansion tank. Of course, the boiler, automatic filling valve and expansion tank will not be installed in the actual engine room of the ship, since the heat source will be part of the HT cooling water of the engine itself. The following table summarizes all the hot water circuit equipment:

Table 2.10: Details of major components of HT water circuit test rig.

Thermis cast iron boiler details	
Company / Type of boiler	Thermis / Europa E7
Rated nominal power (kW_{th})	93
Maximum operating pressure (bar)	3
Wilo circulating pump	
Company / Type of pump	WILO / Stratos
Model	30/1-12
Nominal electrical power (W)	200
Belimo regulating valve	
Company / Type of valve	Belimo / R2..-LR/SR/NR-24-SR
Diameter inlet / outlet	1'' ¼ / 1'' ¼
Supply Voltage (Volt DC)	24
Analogue signal (Volt DC)	1-10

2.10 Cold temperature water circuit

The cold water circuit in the laboratory installation consists of two sub-circuits, the condenser's and the sub cooler's. The condenser is supplied with water from the NTUA – LSBTP soft water circuit with an average temperature of 18-20 °C, which is satisfactory for the rated operating point. The sub cooler heat exchanger is supplied with water cooled by a Daikin Heat pump (Chiller) of 12 kW rated power. The coolant thermostat was adjusted to keep the temperature of the sub cooled water to a desired value (normally at about 15 °C). An additional way to change the subcooling degree was through a regulating valve placed in the water circuit, just before it enters the heat exchanger. The action of the valve results in a regulation of the cold-water flow rate. The water flow rate to condenser heat exchanger was regulated by another CIM's manual regulating valve, as well.

2.11 Electrical and automation control system

Although the technical characteristics of the installed asynchronous motor generators were presented previously, in the present section all other electrical equipment and automation control will be presented briefly.

2.11.1 Speed regulator (VFD's)

On previous sections, where the pump and generator details were presented, have been reported that their speed is controlled by Siemens's Variable Frequency Drives (VFD's).

A typical speed regulator of this type consists of three individual electronic components, as illustrated in the following Figure 2.18. The mains current (network) is rectified through the diode assembly. An electrolytic capacitor (D.C. Link) ensures uninterrupted power flow to the circuit while converting to alternating current (A.C.) of varying frequency and voltage amplitude in the inverter assembly before being finally driven to the motor. The power flow in a generator connection is exactly inverted, that is, the diode arrangement is connected to the generator and the inverter to the mains network.

This VFD controls the speed of the electric motor by keeping the V / f ratio at a constant value, where V is the voltage at its ends and f the frequency. Therefore, when the electric motor is operating at speeds below synchronous, which means that the frequency at its ends is f <50 Hz, the voltage at its ends changes proportionally to a value of V <480 V.

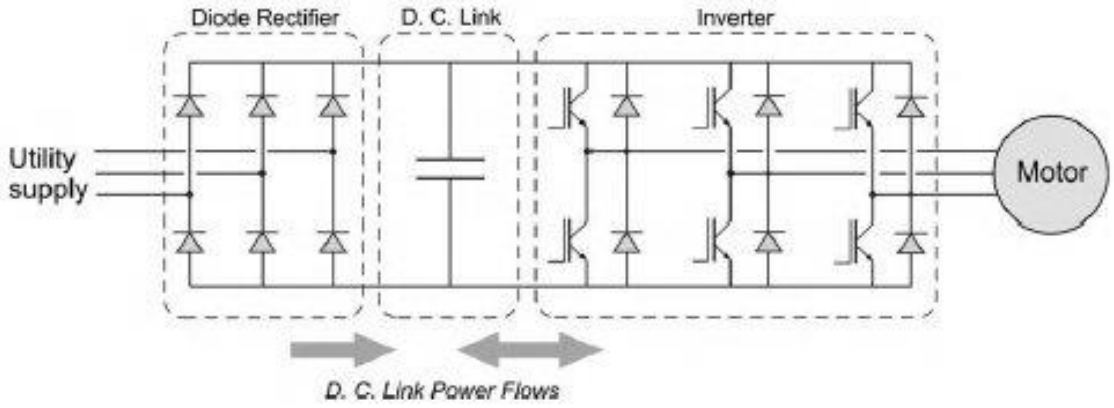

Figure 2.18: Schematic illustration of the electric circuit of a Variable Frequency Driver (VFD).

The above control is necessary in cases where the machine is driven at frequencies lower than that of the grid, as a reduction in speed requires a reduction in the frequency at the ends of the machine, which without decreasing voltage leads to an increase in magnetic flow. The latter can cause a dramatic increase in the magnetization current due to saturation of the magnetic core [44]. In addition, it results in less power output, since the voltage reduction must be followed by a reduction in current to avoid overloading of the windings. Typical characteristics curves of torque vs. speed for an induction motor are illustrated in the following Figure 2.19. For the induction generator the torque curve is mirrored in reverse to the motor ones, in respect to the horizontal axe, as illustrated in Figure 2.20.

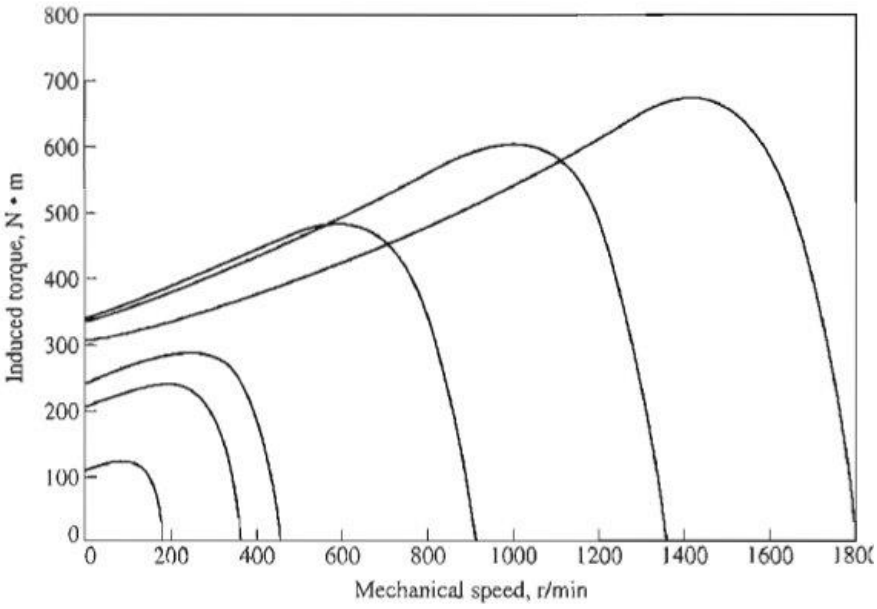

Figure 2.19: Variation of the characteristic curve of torque vs. speed of an induction motor with frequency for ratio V/f control.

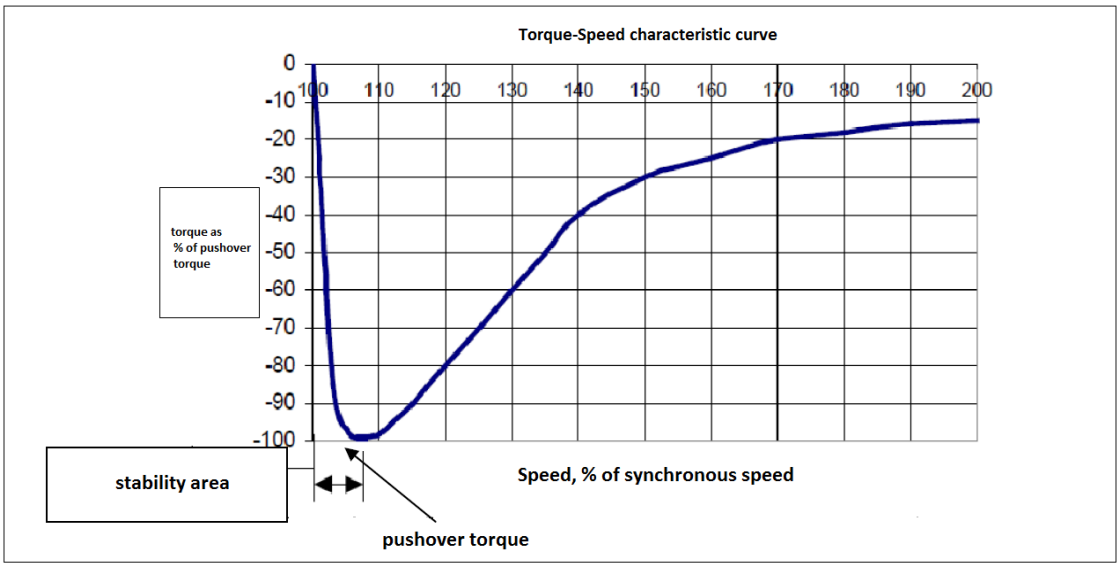

Figure 2.20: Torque - Speed characteristic curve of an induction generator.

To control the pump's speed, the Siemens **SinamicsV20** three-phase speed regulator was fitted. The inverter Sinamics V20 has little response time, maximum efficiency and the ability of controlling the frequency imposed to the motor either through the integrated basic operator panel (BOP) or through the PLC. The inverter comprises of 4 digital inputs, 2 digital outputs, 2 analog inputs, 1 analog output. When the AUTO mode of the ORC pump is enabled the frequency of the inverter is being controlled by the PLC through one of the analog outputs. Additionally, the inverter starts when the respective control relay sends signal to digital input 1 of the inverter. The digital output 1 of the inverter is connected to the PLC and states whether the inverter is on running mode, whereas the digital output 2 stops the ORC pump and protects the motor if a thermal overload is being detected. The analog output of the inverter returns the operating frequency to one of the analog inputs of the PLC. When the MANUAL mode is enabled the inverter is controlled only through BOP. The inverter has the capability of a PID control, though it is decided that the speed regulation will be performed by the PLC which will perform the PI control. The characteristics of Sinamics V20 are listed in the following table:

Table 2.11: Details of pump's speed regulator.

Siemens Sinamics V20	
Rated nominal power	1 kW
Range of rated frequency	47-63 Hz
I/O	Communication protocols: Modbus RTU, USS
	4 digital inputs
	2 digital outputs
	2 analog outputs
	1 analog output
	(All customizable)

Regarding the inductive generators, the Siemens **Sinamics G120** series regenerative inverters were necessarily selected. The difference between the regenerative speed regulators and the standard ones is that they allow the induction motor to operate as generator, by returning the electrical power generated by its braking to the grid. The Sinamics G120 frequency converter comprises of three basic components which are the Power Module, the Control Unit and the operating panel. The Power Module PM250 was selected with regeneration mode. The innovative circuit design (bidirectional input rectifier with "pared-down" DC link) allows the kinetic energy of a load to be fed back into the supply system when PM250 is used. This feedback capability provides potential for savings because generated energy no longer has to be converted into heat in a braking resistor. The Control Unit is CU 240E-2 and the operation panel is BOP-2. The Control Unit performs closed-loop control functions for the inverter. In addition to the closed-loop control, it has additional functions that can be adapted to the particular application through parameterization. The CU 240E-2 comprises of 6 digital inputs, 3 digital outputs, 2 analog inputs, 2 analog outputs. When the AUTO mode of the installation is enabled the frequency of the inverter is being controlled by the PLC through one of the analog outputs. Additionally, the inverters start when the control relay- d12/d13 send signal to digital input 0. The digital output 2 of the inverter is connected to the PLC and states whether the inverter is on running mode, whereas the digital output 0 stops the generators and protects the motor if a fault is being detected. The analog output of the inverter returns the operating frequency to one of the analog inputs of PLC.

Furthermore, the technical characteristics of the Siemens Sinamics G120 are summarized on the following Table:

Table 2.12: Details of generator's speed regulator.

Siemens SinamicsG120	
Rated nominal power	5.5 kW
Nominal electrical efficiency	95 %
Control Unit	CU240E-2
I/O	Communication protocols: Modbus RTU, Profibus, USS
	6 digital inputs
	3 digital outputs
	2 analog outputs
	2 analog output
	(All customizable)

During normal operation as already stated, the induction motors act as generators in the experimental ORC test rig. They are initially accelerated to the desired rotational speed by operating as zero-load motors. They then engage with the scroll expanders, whose torque slightly accelerates them to a speed higher than that of the synchronous. At this point, and based on the Figure 2.16, the engines enter generator mode. The inverter slows down the generators, keeping the speeds close to the current, which are determined by the desired frequency of the output current. So, essentially, the generated electrical power is returned to the grid as the braking power of the electric motor, which justifies the choice of this type of speed regulator.

The speed regulators are configured via the built-in screens. Especially generator speed regulators provide a variety of parameters, such as times for smooth acceleration and deceleration of engines as well as built-in PID controllers for speed control (not used as the control system was implemented via the PLC). Further information on the capabilities of the Sinamics G120 can also be found in the thesis of N. Antoniou [46].

2.11.2 Programmable Logic Controller (PLC)

A basic automatic control system of the experimental test rig was implemented using Programmable Logic Controller (PLC)of the Siemens Simatic S7-300 series. The central processing unit (CPU) model was the CPU 313C and was powered by the PSU 100S 24V / 5A power supply. Connecting the measuring instruments whose transducers gave analog signals outputs, required the installation of two additional cards of 8 analogue inputs of the SM331 series. The control of the three speed regulators and the hot water circuit regulator valve required the addition of built-in analogue outputs to the PLC central processing unit and the addition of a card of two 12-bit analogue outputs of the SM332 series. The integrated digital inputs and outputs in the central processing unit were enough to cover all the digital signals, so no extra cards needed to be inserted. Finally, to communicate the PLC with the computer as well as with meters providing Ethernet connectivity, a CP343-1 communication card was added, which has two RJ45 ports for connecting classic network cables.

The PLC characteristics of the installation are summarized in the following table:

Table 2.13: Details on the synthesis of Programmable Logic controller (PLC).

Type of PLC: Siemens Simatic S7-300 series			
Qty	**Model**	**Description**	**Input / Output signals**
1	**CPU-313C**	**Central Control unit**	**24 digital inputs** **16 digital outputs** **5 analog inputs** **2 analog output**
1	**PSU 100S 24V/5A**	**Power supply**	
2	**SM331**	**Analog input card**	**8 analog inputs** **(13bit resolution)**
1	**SM332**	**Analog output card**	**2 analog outputs** **(12bit resolution)**
1	**CP343-1**	**Communication card**	**2 RJ-45 ports**

During the tests, all signals from the test rig measuring instruments were driven to the PLC. At the same time, some basic security functions were programmed into the PLC, such as:

- Shutting down the experimental test rig in case of expanders being accelerated
- Shutting down in case of low or high pressure of the ORC low pressure circuit
- Shutting down in case of high pressure of the ORC high pressure circuit

- Shutting down the test rig in the event of a general emergency by pressing a button placed on the installation panel (Emergency Shutdown or ESD).

The PLC was connected to a computer via the Industrial Ethernet protocol using the National Instruments' OPC Server. At the same time, a graphical interface was built in the National Instruments Labview program, which handled the installation as well as recording the experimental data in xls (Microsoft Excel) file format.

The various control signals, before being driven to the PLC, pass through relays numbered in the electrical design of the installation. In addition, a 230 V AC / 24 V AC adapter and a 230 V AC / 12 V DC power adapter were required for the control signals of the analog hot water regulator and the expansion clutches respectively. The connection of the energy analyzers requires the installation of a CT (50A / 5A transformer per phase) for each analyzer.

In the low pressure circuit, two pressure control sensors were installed to protect the pump from too low and too high suction pressure, which were set at 5 bar and 16 bar respectively. The high-pressure circuit had an independent high-pressure pressure control sensor set at 28 bar. When one of these pressure control sensors was activated (i.e. pressure measured value below the minimum set value of the low pressure control sensor), the signal was read by the PLC and thus acting to stop the pump, expander and gas boiler. Rebooting the installation required manual reset of the pressure sensor that gave the error signal.

For the programming of Siemens PLC the software STEP 7 of the same company is being used. The user interface is named Simatic Manager and the version V5.5 + SP3 was used. The program was written with a combination of LADDER and STL (Statement list), both of them are languages of STEP 7 software.

2.11.3 Supervisory Control and Data Acquisition

The LabVIEW software from National Instruments has been chosen for acquiring, analyzing and storing all the measurements from PLC. NI Lab VIEW software can communicate with the PLC and specifically with the CPU through CP lean 343-1. OPC defines the standard for communicating real-time plant data between control devices and human machine interfaces (HMIs). The NI OPC Servers converts proprietary industrial protocols to the open OPC Classic and OPC Unified Architecture (UA) protocols. In our case the industrial protocol is industrial Ethernet. This conversion to OPC then enables NI LabVIEW software to communicate to our PLC through the OPC Client that is included with the LabVIEW Datalogging and Supervisory Control (DSC) Module. The combination of NI OPC Servers and LabVIEW provides the platform for delivering high-performance measurements and control of our system.

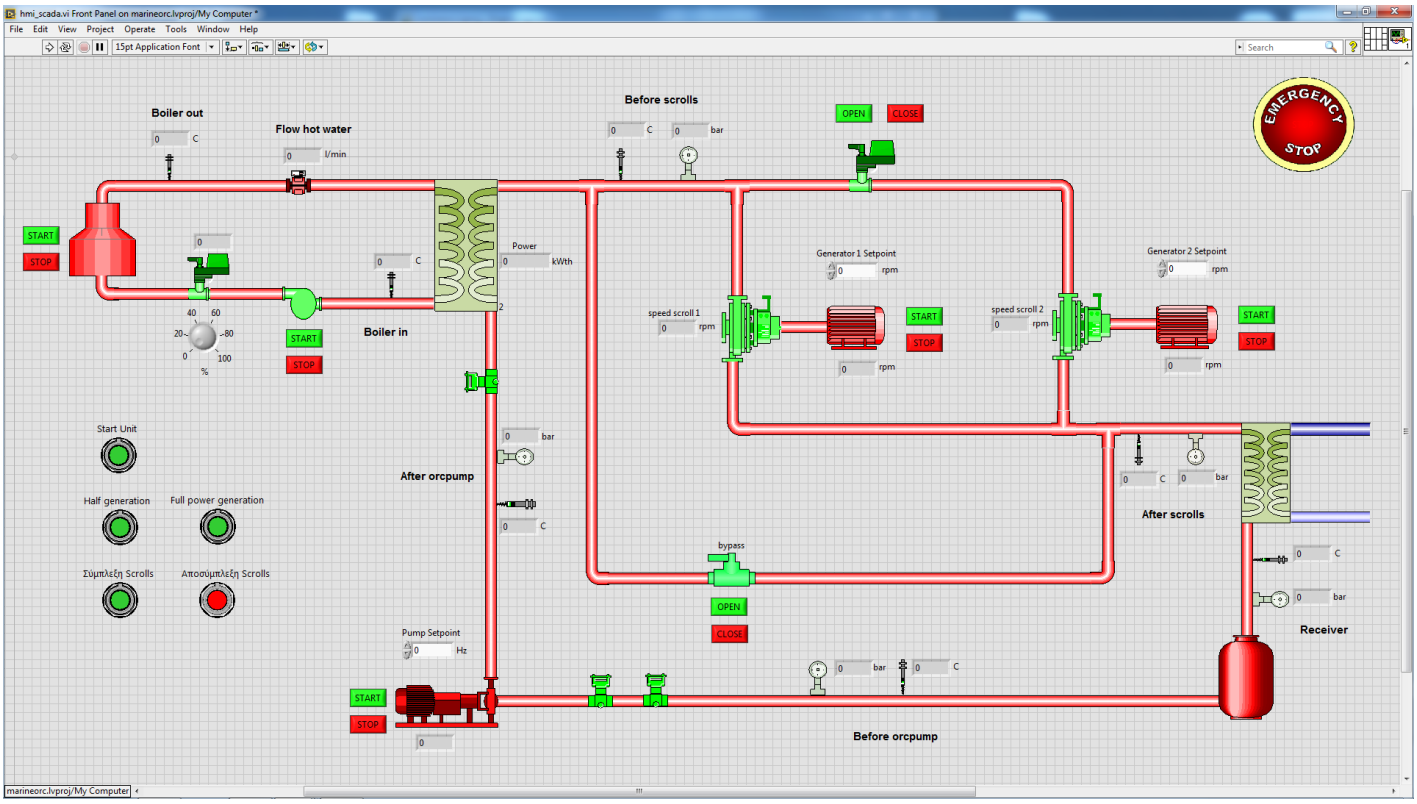

Figure 2.21: Main Virtual Instrument of experimental ORC test rig in LabVIEW.

In detail, NI OPC Servers is creating tags that are associated with the PLC program. For example, the tag with the name “pressure after ORC pump” has the address of the PLC program where the scaled value of pressure is stored, thus giving the ability to view this value. Similarly, we can create tags for all inputs, outputs, data blocks and internal memory of the PLC’s CPU. The connection between LabVIEW and OPC tags is being achieved by creating a LabVIEW interface called I/O server. The I/O server automatically updates LabVIEW with the current tag values at a specified rate. Subsequently, we create shared variables, which are bound to the OPC tags, thus giving native access in LabVIEW to PLC data. These shared variables are used for the development of the virtual instrument (VI) and the real-time data logging and control of our installation. All the signals send by the instrument transmitters and the machines are being stored in files and can be processed at moment or later.

Power analyzers were not connected to the PLC, but to the local network via a switch. In this way the computer was directly communicated to them by means of the MODBUS protocol. In the context of this work, a graphical interface was created with the LabVIEW program through which the two energy analyzers / meters from Ducati were presented and recorded. (see

Table *2.15* for further details)

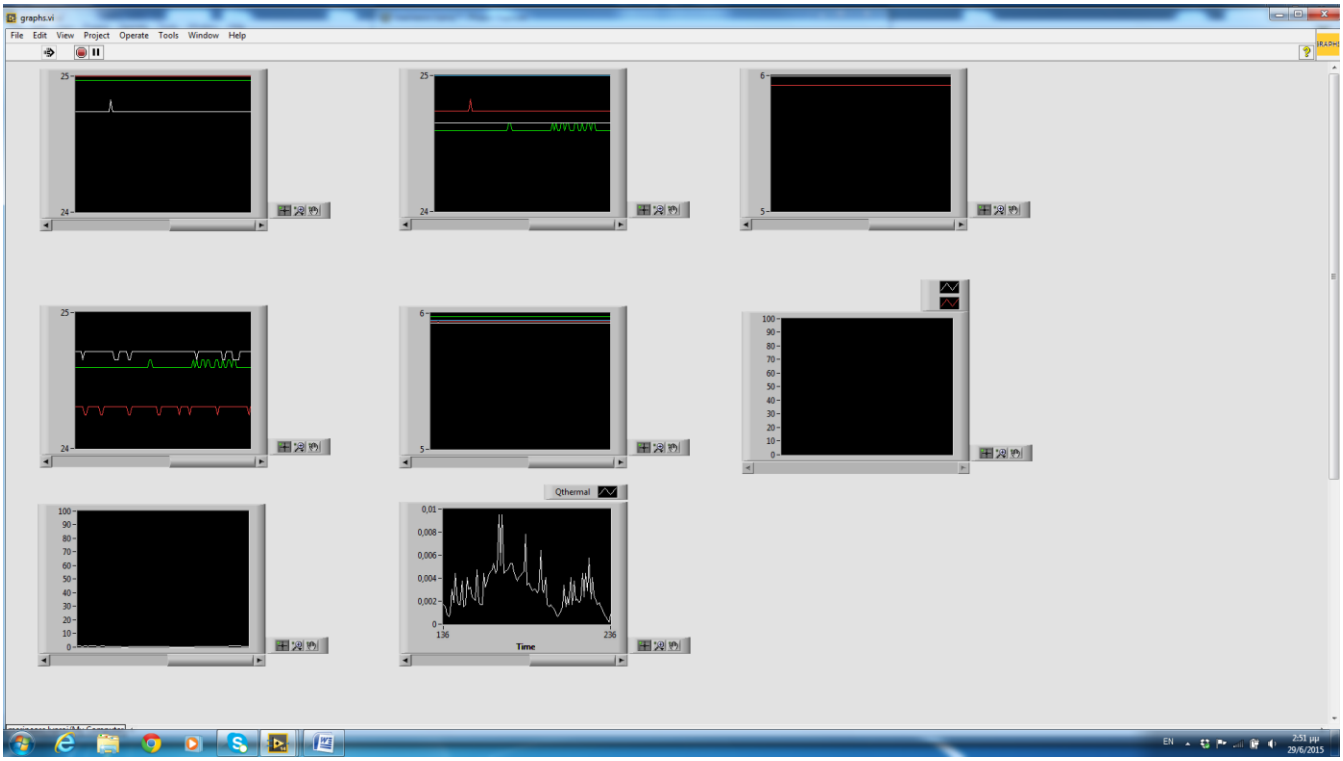

Figure 2.22: Real-time display of characteristics of Experimental ORC test rig (i.e. pressure, temperature) in LabVIEW.

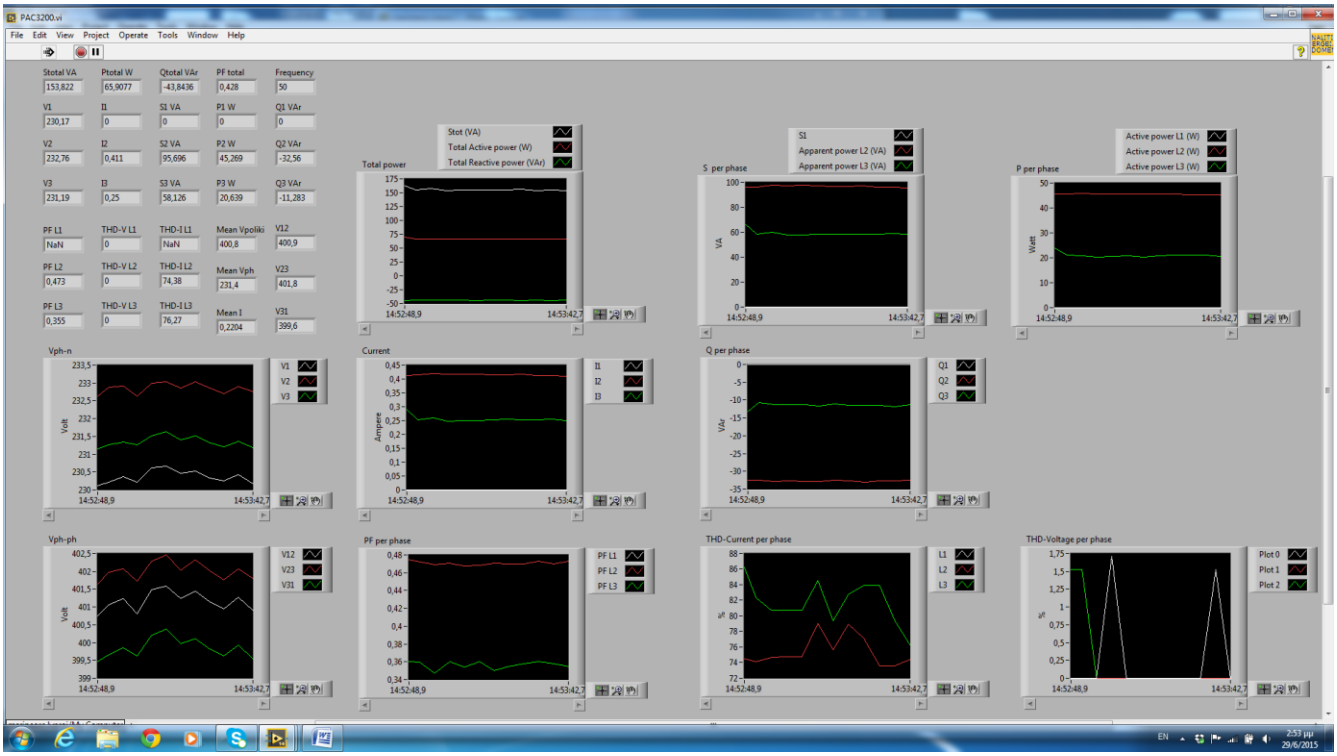

Figure 2.23: Real-time display of measured values from power analyzer in LabVIEW.

2.11.4 Electric panel of the experimental unit

The electrical subpanel of the installation is responsible for the automatic operation of the system and includes the necessary equipment for handling, protection, measurement and indication. It also includes the frequency inverter of the ORC pump, the two regenerative inverters and the PLC. The installed subpanel is metallic and waterproof, while it can be accessed only from the front side for inspection of the instrumentation and devices and sealed from the other sides.

The input line of the electrical subpanel includes:

1. One Tripolar circuit breaker, with rated capacity 25 A.
2. Three Indication lights 230 V.
3. One emergency stop for manual and automatic (from the PLC) stop of the system.

The output lines of the electrical subpanel include:

1. One 3-phase line for the feeding of the ORC pump, through frequency inverters, protected with magnetic and thermal circuit breaker with rated capacity 20 A.
2. Two 3-phase lines for the two generators, through frequency inverters, protected with magnetic and thermal circuit breaker with rated capacity 20 A.
3. Four 1-phase lines for the feeding of the electric valves, the natural gas boiler and the Wilo stratos circulator protected with magnetic and thermal circuit breakers with rated capacity 6 A.
4. One 1-phase line for the auxiliary circuit (indication lights and relays), protected with circuit breakers with rated capacity 10 A.
5. One 1-phase line for the automatic control system (PLC), protected with circuit breakers with rated capacity 10 A.
6. One 1-phase line for sockets, protected with circuit breakers with rated capacity 16 A.
7. One 1-phase line (for DC feeding), protected with circuit breakers with rated capacity 10 A and DC feeder 230/12 V for the scroll expanders' magnetic clutch.
8. One 1-phase line (for 24V AC feeding), protected with circuit breakers with rated capacity 10 A and AC feeder 230/24 V for the scroll expanders' magnetic clutch.
9. One 1-phase stand by line, protected with circuit breakers with rated capacity 16 A.

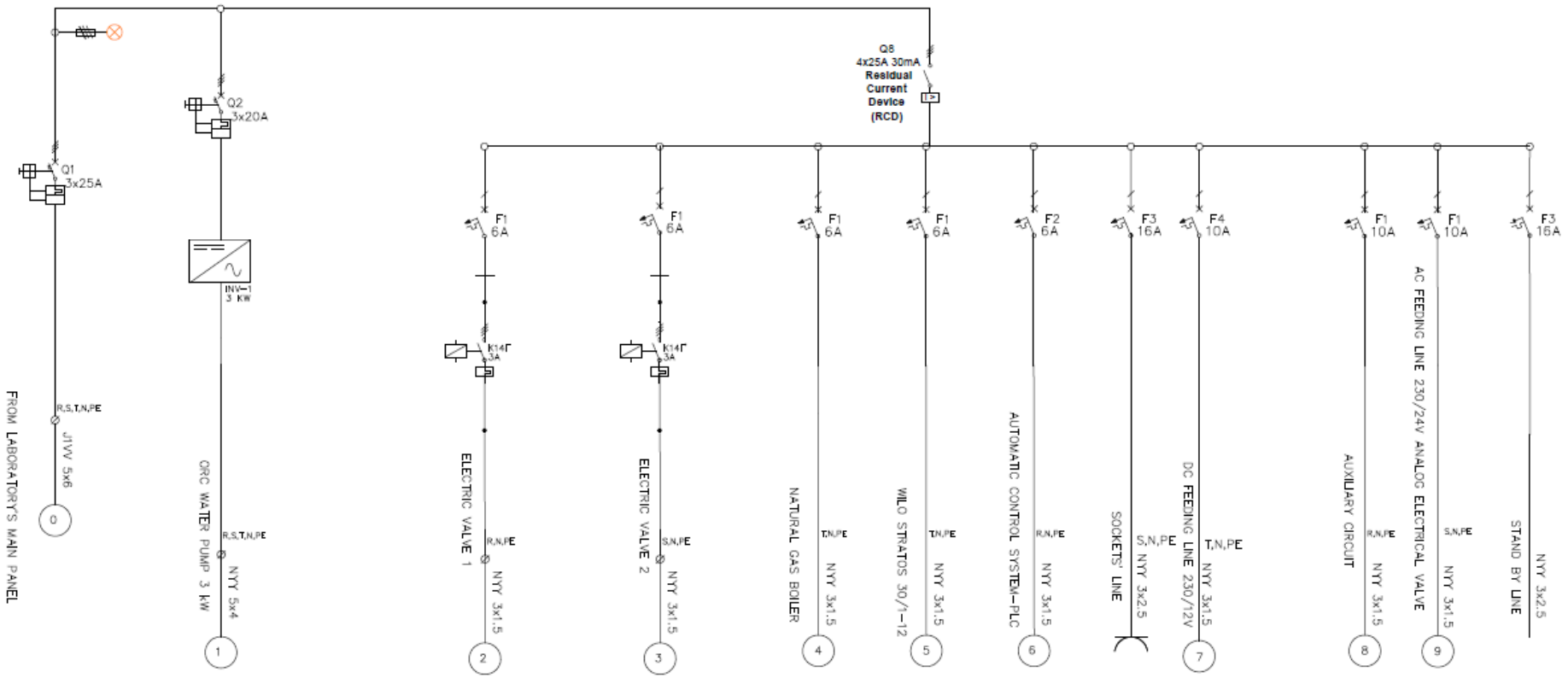

Figure 2.24: Wiring diagram of installation's feeding loads.

2.11.5 Measuring instruments

Many measuring and control instruments are mounted at specific locations, in order to evaluate in detail, the performance of the ORC unit. Pressure, temperature and rotational speed sensors have been installed, in order to record the low/high organic fluid pressure and temperature, as well as the rotational speed of the two expanders respectively. In addition to the aforementioned, other instrumentation such as mass flow and energy meters are installed in order to be able to monitor and log data of respective parameters required for the experimental campaign evaluation. For further details, the reader could use the following Table 2.14 &

Table *2.15* in conjunction to Figure 2.4.

As previously stated, monitoring and data logging of all measurands of the experimental ORC test rig requires the placement of a plurality of measuring instruments. These include:

- Seven (7) PT100 linear variable temperature resistance (RTD) sensors by WIKA. The signal is converted to 4-20 mA which is readily recognizable by the PLC of the installation through transducers (of the T19 family) of the same company mounted on a plastic box attached to the installation's frame. The measurement is done by contacting the sensor on the outer surface of the pipe and tightening it with insulating material.
- Five (5) submersible pressure sensors with S10 type transducers which also signal 4-20 mA by WIKA.
- Two (2) type 9210.001 tachometers used to measure the speed of generators using optical sensors and reflectors. The tachometers have an analog output of 4-20 mA.
- An electromagnetic flow meter to measure the hot water supply (ICE jacket HT water) and a variety of possible output signals (0-20 mA signal selected) by Signet.
- A Coriolis type flowmeter from KROHNE to measure the mass flow of organic media. The flowmeter enables two 4-20 mA analog outputs, so the second is used to measure the density of the medium. The Coriolis flow meter was installed at a later stage of the experimental campaign. For further details please refer to section 3.5.
- Three (3) energy analyzers, including:
  - One (1) of the Siemens Company, type PAC-3200, capable of communicating through the MODBUS protocol. It is used to measure all electrical quantities in the central supply of the subsystem of the plant and therefore to measure the net energy produced or consumed by the plant.
  - Two (2) of Ducati company, type DUCA-LCD96-IO. They are used to measure power and other electrical quantities in the pump motor and in one of the two generators. They provide two analog outputs of 4-20 mA or 0-20 mA but also communication via MODBUS.
- Two (2) display gauges mounted at two points in the ORC test rig to compare the measured values with those of the analog sensors connected to the PLC (Safety measure).
- Two (2) variable resistor type thermometers that have a display screen and are also mounted at two points in the ORC test rig to compare the measured values with those provided by the PLC sensors (Safety measure).

- A WIKA differential pressure gauge with indicator display to measure its pump head in the hot water circuit.
  In addition:
- A calorimeter of the General Electric Company. The flow rate is measured using an ultrasonic flow meter while the temperatures are measured with two variable resistance contact thermometers (Pt100). The use of this instrument allows the measurement of temperatures and supplies in the cold water circuit (Soft water / seawater circuit).
- A Ducati external power analyzer of the same type and characteristics as those installed on the installation board (DUCA-LCD96-IO).

In the following Tables, the technical characteristics (type, range, accuracy) and their measurement / installation location are mentioned.

Table 2.14: Technical characteristics (type, range, accuracy) of pressure and temperature sensors.

Description of instrument	Model / Type	Location	Range	Accuracy
Pressure sensor WIKA	S-10 16 bar	Before Expander	0-16 bar	0.25 % F.S.
Pressure sensor WIKA	S-10 16 bar	After condenser	0-16 bar	0.25 % F.S.
Pressure sensor WIKA	S-10 16 bar	Pump Inlet	0-16 bar	0.25 % F.S.
Pressure sensor WIKA	S-10 40 bar	Pump Outlet	0-40 bar	0.25 % F.S.
Pressure sensor WIKA	S-10 40 bar	After Evaporator	0-40 bar	0.25 % F.S.
Temperature Sensor WIKA	Pt100 0..+200 °C	Before Expander	-55 to 250 °C	0.3 °C
Temperature Sensor WIKA	Pt100 0..+200 °C	After condenser	-55 to 250 °C	0.3 °C
Temperature Sensor WIKA	Pt100 0..+200 °C	Pump Inlet	-55 to 250 °C	0.3°C
Temperature Sensor WIKA	Pt100 0..+200 °C	Pump Outlet	-55 to 250 °C	0.3 °C
Temperature Sensor WIKA	Pt100 40..+100 °C	After Evaporator	-55 to 250 °C	0.3 °C
Temperature Sensor WIKA	Pt100 0..+200 °C	Water in Evaporator	-55 to 250 °C	0.3 °C
Temperature Sensor WIKA	Pt100 0..+200°C	Water out Evaporator	-55 to 250 °C	0.3 °C

Table 2.15: Technical characteristics (type, range, accuracy) of various instruments.

Description of instrument	Model / Type	Location	Range	Accuracy
Electromagnetic flow meter - SIGNET	MAG. 3-2551-P0-42	Boiler Hot water Outlet	0.05-10 m/s	1.0 % F.S.
Coriolis flow meter KROHNE	OPTIMASS MFS 1000 S25/MFC 300C	Pump Outlet	0-6,500 kg/h	Mass: 0.15 % Temp: 1 °C
Digital Tachometer	9210.001	Generator 1	50-50,000 rpm	1 rpm (<10,000rpm)
Digital Tachometer	9210.001	Generator 2	50-50,000rpm	1 rpm (<10,000rpm)
Energy meter Ducati	DUCA96LCD-IO	Pump motor	I: 0.05–5 A V: 10-500 V	I: 0.5 % V: 0.5 % W: 1 %
Energy meter Ducati	DUCA96LCD-IO	Generator 1	I: 0.05–5 A V: 10-500 V	I: 0.5 % V: 0.5 % W: 1 %

The combination of temperature and pressure sensors allows thermodynamic states to be determined at each point in the cycle, provided, of course, that the organic medium at this position is not biphasic.

To conclude, the error propagation law was used to calculate the errors. So, for example, the error in the calculated enthalpy value is:

$$\sigma_h = \sqrt{\left(\frac{\partial h}{\partial p}\right)_T^2 \cdot {\sigma_p}^2 + \left(\frac{\partial h}{\partial T}\right)_p^2 \cdot {\sigma_T}^2} \quad (2.9)$$

When the instrument error is given in percentage form (such as for energy meter), then the absolute error is defined by the relative error as follows:

$$C_P = \frac{\sigma_p}{\bar{p}} \quad (2.10)$$

Where $\bar{p}$ the mean value of the respective measurand.

2.12 The completed experimental ORC prototype test bench

The experimental ORC prototype unit was designed and based on a conventional low-temperature subcritical Organic Rankine Cycle using R134a as working medium. This experimental unit has been designed as a waste heat recovery system for the jacket water of marine diesel auxiliary internal combustion engines (ICEs). In order to simulate the operating characteristics of such engines, the heat input is in the order of 90 kW_{th} at a low-temperature (90 ^{o}C), and is supplied by a natural gas boiler via an intermediate plate heat exchanger (evaporator).

The boiler thermal output is adjustable and thus part load operation and varying hot water supply temperature profile can be simulated as well. A schematic diagram of the unit is presented in Figure 2.4.

The cycle is fed by a receiver (feed tank) at a pressure between 7.5 to 9.5 bar and an average temperature of 30 – 35 ^{o}C. These parameters are controlled by the cold water flow in the condenser, which is adjusted by a regulatory valve.

The feed pump is a positive displacement multi-diaphragm pump that subsequently raises the pressure of the fluid at about 22-25 bar, depending on the operational conditions, and leads it to the evaporator. At a nominal speed of 960 rpm (6-pole motor at 50 Hz) a flow rate of 20 lt/min is achieved. The rotational speed of the pump is controlled by a frequency drive. As a result, the refrigerant mass flow rate can be adjusted according to the unit load and the desired superheating temperature of the vapor, given the fact that the delivered volume flow rate of diaphragm pumps is in most cases a linear function of their rotational speed.

The high pressure vapor is expanded in two parallel scroll expanders, while a by-pass section controlled by an electromagnetic valve can alternatively lead the flow directly to the condenser. This flow route is active during start and warm up procedure. Actually, these expanders are two open-drive scroll compressors in reverse operation as it is thoroughly explained in previous section 2.5.1. Each scroll expander drives an asynchronous motor/generator through a 1:1 belt drive, which can be coupled and uncoupled by an electromagnetic clutch. Both generators are connected to the 50 Hz/400 V electrical grid via a regenerative inverter module, which provides both grid stability and rotational speed control of the generators and hence of the expanders. For a given pump rotational speed (and thus mass flow rate), the inlet pressure of the scroll expanders is directly adjusted by their rotational speed, since the processed mass flow rate for volumetric machines is given by the product of the inlet density (ρ_{in}) multiplied by the swept volume (V_{swept}) and the rotational speed (N_{rot}) of the machine (Equation (2.11).

$$\dot{m} = \rho_{in} \times V_{swept} \times N_{rot} \qquad (2.11)$$

An increase (decrease) of the rotational speed allows for a decrease (increase) of the specific volume of the refrigerant at the expander inlet and thus causes a decrease (increase) of the respective inlet pressure. Finally, the expanded vapor is led to the condenser (plate heat exchanger) and the condensate returns to the feed tank and the cycle starts over. The ORC unit (Figure 2.25) produced 3.5-5 kW_{el} of net electrical power, at a maximum cycle pressure of 25 bar and a temperature of 82 ^{o}C, depending on the condensation achieved pressure.

The reason of using two scroll expanders in parallel is that they operate efficiently only in a relatively narrow range of pressure ratios. This means that at part load operation, lower pressure ratio would lead to low expander and system efficiency if a single expander was used. Instead, by using two expanders in parallel, the one can be by-passed when the available heat (and thus the refrigerant mass flow rate) is low or operate in lower rotational speed and thus reaching the desired pressure ratio.

As already explained, various instruments have been mounted at all key-points of the cycle (Figure 2.4), in order to evaluate the performance of the different components of the ORC unit. Thermocouples and pressure transducers record the thermodynamic procedure; an electromagnetic flow-meter supervises the hot water volume flow rate and two tachometers the scrolls' actual rotational speed. All important parameters regarding the electrical motors of both the pump and the generators, such as the consumed/produced active power are retrieved by the respective frequency drives.

It is noted that the automatic control of the system (including the frequency drives), the measurements and the data logging are materialised with the use of an industrial PLC (Programmable Logic Controller) and a SCADA (Supervisory Control and Data Acquisition) environment, which constitutes a first but an important step towards the fully automation of a WHR ORC unit and thus the standardization and commercialization of such micro-scale units or even larger scale units. (See sections 2.11.2 – 2.11.4).

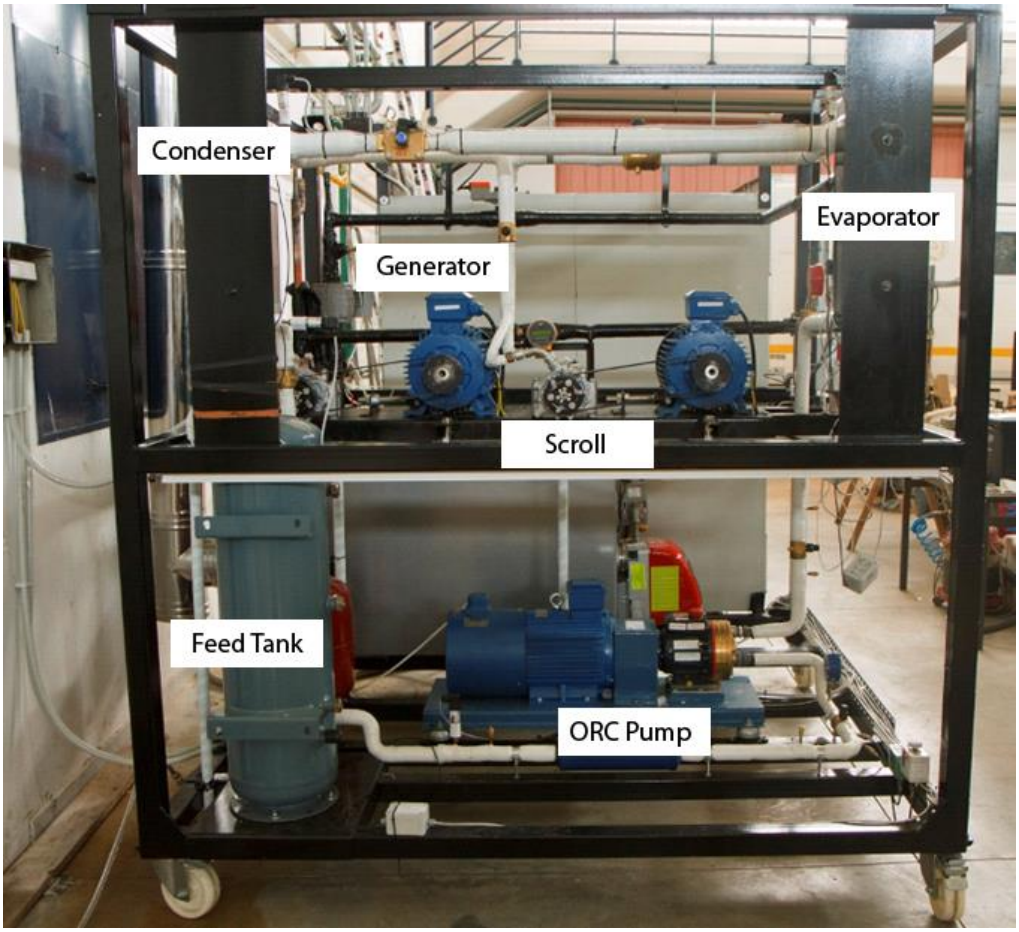

Figure 2.25: Side view of the Experimental ORC test rig.

Chapter 3. - Experimental operation & Results of laboratory ORC test rig

3.1 Cavitation effect on the ORC pump operation

A typical problem in micro scale ORC systems is the cavitation effect on the feed pump. Indeed, this problem was faced during the first steps of operation of the presented experimental unit, causing serious oscillations in its operation (mass flow rate, cycle pressure and temperature). In order to thoroughly understand this problem and finally solve it, an analysis of the pump operational conditions was conducted and is presented next.

First of all, in order to ensure stable operation of a pump, the **available** Net Positive Suction Head (**$NPSH_a$**) at the pump inlet should exceed the respective **required** Net Positive Suction Head (**$NPSH_r$**), given by the operation curves provided by the manufacturer (see Figure 3.1), by at least 100 mbar or an equivalent of 1 mH_2O. The $NPSH_a$ (mH_20) is calculated by the following equation:

$$\mathrm{NPSH_a} = \mathrm{P_{in}} + \mathrm{H_z} - \mathrm{H_f} - \mathrm{H_a} - \mathrm{P_{vp}} \qquad (3.1)$$

Where:

P_{in} = Pressure at the pump inlet

H_z=Vertical distance from liquid surface to pump center line

H_f = Friction losses in suction piping

H_a = Acceleration head at pump suction

P_{vp} = Absolute pressure of liquid at pumping temperature

Among the indications of how to calculate each term of the equation, the manufacturer suggests considering the friction losses as negligible if the pumped fluid is a water-like fluid. R134a can be accounted among water-like fluids because its viscosity values are very similar to the water ones. For example, at a temperature of 32 °C, the dynamic viscosity is:

$$\mathrm{Visc_{water}} = 0.7644 \text{ cP}$$

$$\mathrm{Visc_{R134a}} = 0.1791 \text{ cP}$$

where the value of R134a is even lower than the viscosity of water but of the same magnitude order.

As a result, H_f= 0 was assumed.

In positive displacement pumps, an another type of pressure loss must be considered when calculating the available Net Positive Suction Head (**$NPSH_a$**) at the pump inlet, which results from the successive deceleration and acceleration of fluid due to pump's operational principle (continuous intermittent operation). This type of pressure is the acceleration head factor (Ha) and it is calculated by equation (3.2).

$$H_a = \frac{C \cdot L \cdot Vel \cdot N}{K \cdot G} \qquad (3.2)$$

Where:

C = Constant determined by type of pump (in our case 0.066, Wanner Engineering, Hydra Cell D/G10) [36]

L = actual length of suction line

Vel = Velocity of liquid in suction line

N = RPM of crankshaft

G= Gravitational constant

K = Constant to compensate for compressibility of the fluid (2.5 for hydrocarbons with high compressibility)

As previous mentioned, the pump manufacturer [36] provides the required NPSH in order to ensure cavitation free operation of the pump. Thus, the condition of non-cavitation can be expressed as:

$$\mathbf{NPSH_a} > \mathbf{NPSH_r} \ (3.3)$$

Where $NPSH_r$ is the value of the required NPSH provided by the pump manufacturer (Figure 3.1). The value of $NPSH_r$ at 960 rpm (nominal speed for the electrical motor at f = 50 Hz) corresponds to 423 mbar (≈4,23 mH_2O). However, as the $NPSH_r$ vs. RPM curve indicates, the $NPSH_r$ is an increasing function with the speed. Since the operation of the ORC system, during the second experimental campaign, was at higher nominal mass flow rates, the frequency of the motor was set up to 60 Hz, corresponding to a motor/pump rotational speed of 1080 rpm (see section 3.5). Taking into account also this operational region, a safety $NPSH_r$ value of 5 mH_2O or an equivalent of 500 mbar is adopted and used for all calculations presented from this point and on.

Based on manufacturer's data (Figure 3.1), where the available Net Positive Suction Head (**$NPSH_a$**) at the pump inlet is given in relation to rotational speed for various types of pumps, a second degree polynomial equation was calculated, based on multiple pair values (NPSHr, RPM), derived from manufacturer's graph (Figure 3.1). This equation is as follows:

$$\boldsymbol{NPSH_r\left(m_{H_2O}\right) = 8.9 \cdot 10^{-7} N_p(RPM)^2 + 7.5 \cdot 10^{-5} N_p(RPM) + 3.508} \ (3.4)$$

A visual presentation, in form of graph, is depicted in Figure 3.2. This equation was mainly used during the next stage of experimental test rig evolution, where an automation and control strategy was designed and realized, based on the results of all experimental campaigns and the experience and knowledge accumulated during the almost five years of this research.

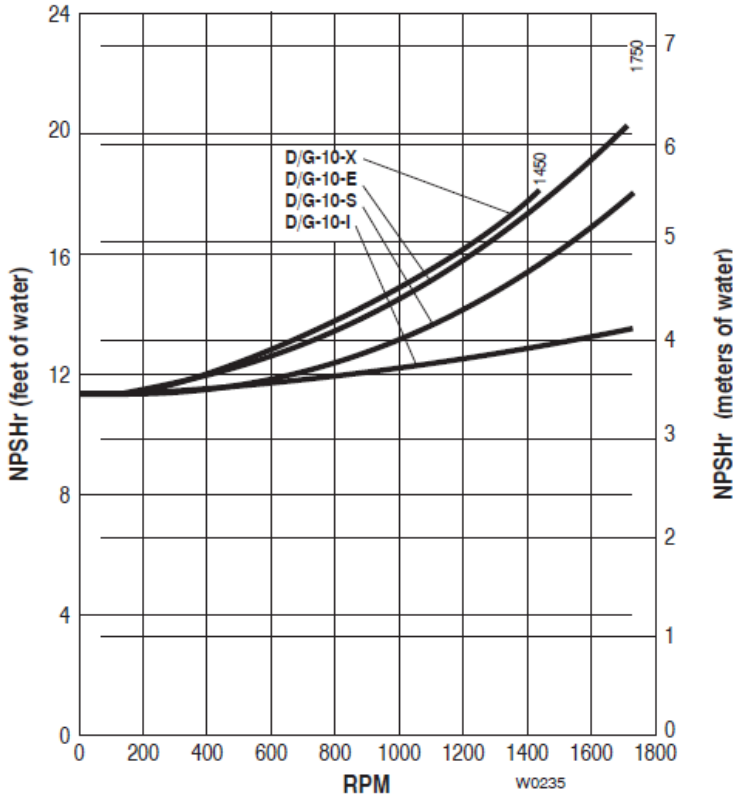

Figure 3.1: Required NPSH as a function of the rotational speed (rpm) according to the manufacturer.[36].

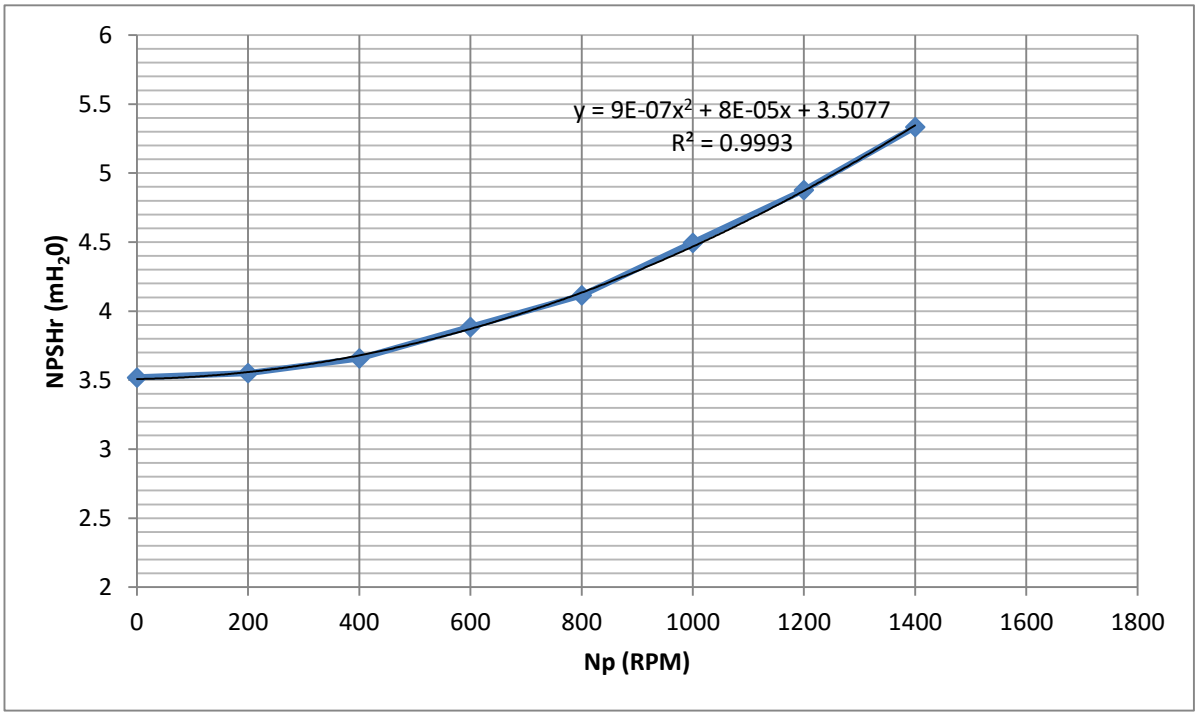

Figure 3.2: D10-X, required NPSH as a function of the rotational speed (rpm) according to the manufacturer. **[36].**

The main parameters of the ORC feed pump under operation with cavitation effect are depicted in Figure 3.3. In fact, the ORC pump was tested while just circulating the refrigerant around the ORC circuit via the scroll by-pass section and thus practically no pressure raise is implemented by the pump. Analyzing the pump operation at the first oscillation cycle (cold start), it is observed that initially the pressure at the pump inlet/outlet remains constant with time, indicating a constant mass flow rate, and that the $NPSH_a$ - $NPSH_r$ difference is maintained well above the threshold of 100 mbar (1 mH_2O). As the whole system is ramping up, the temperature at the condenser outlet raises due to the increase of the evaporator outlet temperature. Consequently, the temperature at the pump inlet raises but with a significant time lag caused by the thermal inertia of the feed tank, which stands between the condenser outlet and the pump inlet. With raising temperature at the pump inlet, the absolute pressure of the refrigerant (factor P_{vp} of equation (3.1) raises and as a result the $NSPH_a$ drops. When the difference $NPSH_a$ – $NPSH_r$ reaches a critical value of around 100 mbar (1 mH_2O), the cavitation effect is initiated and the circulating mass flow rate drops significantly. Simultaneously, the pressure of the circuit (controlled by the condensation temperature which drops due to the reducing refrigerant mass flow rate) also drops (factor P_{in} of equation (3.1)) and the unit's operation practically "collapses". To make things worse, even though at this point the refrigerant temperature at the condenser outlet drops dramatically, since there is practically a zero mass flow rate, the feed tank needs time to cool down and keeps feeding the pump at relatively high temperature (and thus high P_{vp}); at this point the $NPSH_a$ – $NPSH_r$ difference is strongly negative. Eventually the feed tank cools down, lowering the pumping temperature and thus raising the NPSH difference. Gradually the cavitation effect fades, the mass flow rate raises, and a new cycle starts over.

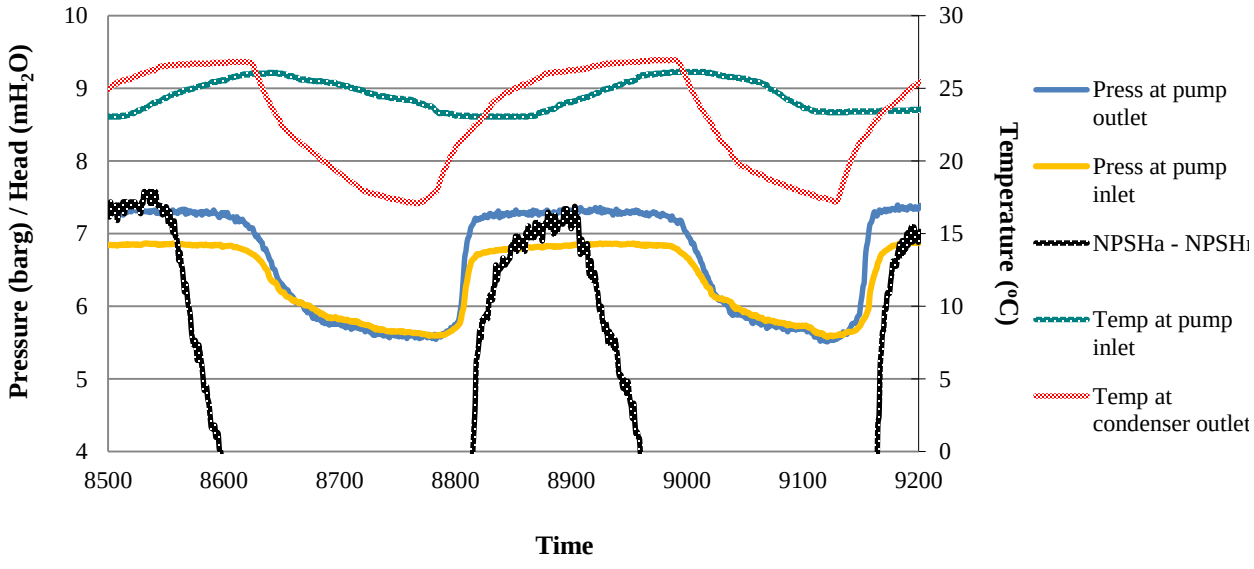

Figure 3.3: Cavitation effect on ORC pump operation.

According to Declayé [37]and to Quoilin et al.[53], several strategies can be set up in order to avoid cavitation. However, only three of them can be considered as the most suitable for micro-scale ORCs. In the following each of them is discussed, underlining the consequences on the system operation.

- **Addition of non-condensing gases:** when adding non-condensable gases (e.g. nitrogen), only a small part of them is dissolved in the working fluid; the main part remains in gaseous state and is

carried by the main flow to the condenser, where it accumulates because of the condensation of the working fluid. It is therefore in the condenser and in the liquid receiver that the concentration of non-condensable gases is highest. This allows for an increase of the receiver pressure and therefore of the pump inlet pressure, bringing a positive contribution to the NPSH available. In particular, the pressure at the pump inlet is the sum of two partial pressures:

-The partial pressure of non-condensing gases in the condenser and in the liquid receiver ($p_{part,ncg}$).

-The partial pressure of the working fluid in vapour phase, corresponding to the saturation pressure at the given temperature ($p_{part,wf}$).

$$\mathbf{p_{tot} = p_{part,ncg} + p_{part,wf}} \quad (3.5)$$

where p_{tot} is the total pressure at the pump inlet. When the working fluid leaves the gas–liquid interface toward the pump (i.e. it is no longer in contact with the non-condensing gases), its pressure is higher than the saturation pressure. It is therefore subcooled. The condition for no cavitation states that the amount of subcooling must be sufficient to provide the NPSH required by the pump, i.e. the partial pressure of the introduced non- condensing gases must be higher than NPSH:

$$\mathbf{\Delta p(subcooling\ degree) = p_{tot} - p_{part,wf} = p_{part,ncg} > NPSHr} \quad (3.6)$$

However, this solution probably affects the heat transfer coefficient in the condenser. Moreover, the increase of the pressure in the reservoir leads to reduce the power produced by the expander since the pressure ratio over the latter is reduced.

- **Gravity fed working fluid pump:** the elevation difference between the reservoir and the pump can be increased, gaining therefore static pressure that increases the Hz term. Unfortunately, this action alone is not usually sufficient in micro-scale ORCs in order to overcome cavitation problem. In order to explain better this issue, it is worth at this point to compare how a Hz = 1 m contributes in the $NPSH_a$ for different fluids. Water, R134a and R245fa are taken into account. For each one, the same temperature at the pump inlet is considered: T_{in} = 32 °C. Given this pump inlet temperature, the following table (Table 3.1) shows, for each fluid, the saturation pressure at this temperature and the static pressure contribution of H_z=1m.

Table 3.1: Hz factor contribution for three different fluids (Water, R134a, R245fa).

T_{in} = 32 °C; H_z = 1 m				
	P_{sat} (mH_2O)	Density (kg/m^3)	Static Pressure (mH_2O)	Contribution to $NPSH_a$
Water	**0.4854**	**994.985**	**0.99535**	**205 %**
R134a	**83.1527**	**1179.568**	**1.18000**	**1 %**
R245fa	**19.4574**	**1319.311**	**1.31980**	**7 %**

It is clear that, in the case of water, the contribution of 1-meter height is very important (205 %) because of the low saturation pressure. As far as refrigerants are concerned, the much higher saturation pressure makes the H_z term very small compared with the most important ones of (Equation (3.1), $NPSH_a$ and P_{vp}). Therefore, a very high elevation difference is needed in order to see an appreciable contribution and contribute to the $NPSH_a$. However, for kW scale ORC units, the necessity to obtain a high elevation difference is in contrast with the research for economical and compact solutions.

- **Thermal subcooling:** the required NPSH can be obtained by thermally subcooling the working fluid, with the aim to reduce the P_{vp} term. The most common way to perform it is with an additional heat exchanger at the suction line of the pump. This heat exchanger allows cooling down the fluid and therefore reducing its saturation pressure. Nevertheless, subcooling the liquid at the pump suction line has a negative effect on the cycle efficiency. Therefore, the increase of NPSH through the subcooling action is obtained at the expense of the cycle efficiency. Declayé [37] states that cycle efficiency decreases about 1.5 % if the subcooling raises from 0 K to 20 K.

In order to address the cavitation phenomena, the thermal subcooling strategy was adopted and a sub-cooling heat exchanger was installed in the suction line of the ORC pump downstream of the liquid receiver (Figure 3.5), so that the pumping temperature and thus the absolute pressure of the refrigerant (factor P_{vp} of equation (3.1) are maintained at lower values, ensuring stable pump operation. The cooling load of the heat exchanger (around 800 W) was first provided by a conventional air-conditioning external unit. At a later stage, a more permanent solution was decided by installing an air/ water Daikin Heat pump (Chiller) of 12 kW rated power. The existence of vapor bubbles and thus cavitation can also be visually controlled in-situ with the help of a newly installed sight-glass right before the pump inlet port (Figure 3.4).

The main parameters of the ORC pump under operation with the additional sub-cooling heat exchanger are depicted in Figure 3.6. The measurements have been obtained at similar operation conditions with Figure 3.1, allowing their direct comparison. The sub-cooling heat exchanger causes an average 2 K temperature drop at the suctioned refrigerant which has proved to be sufficient for the stable operation of the unit. As it can be seen in the diagram, the $NSPH_a$ is constantly kept above 17 mH_2O with a required $NPSH_r$ of 5 mH_20. Its main fluctuations are caused by the suction pressure, which in turn depends

on the cooling water mass flow at the condenser (or equivalently on the condenser outlet temperature) and naturally by the temperature at the pump inlet which affects the factor P_{vp} as already discussed. Accordingly, between t=300 and t=690 the $NPSH_a$ is slightly dropping even though the suction pressure is slightly raising, due to the greater influence of the raising temperature at the pump inlet (factor P_{vp}). The evident drops of $NPSH_a$ at t=700, t=840 and 1040 are caused by marginal steps of increasing cooling water mass flow rate at the condenser which directly influence the pressure at the pump inlet and thus the $NPSH_a$. At the respective intervals the observed $NPSH_a$ raise is caused by the slightly decreasing temperature at the pump inlet. It is finally noted that the stable operation of the feed pump can be confirmed by the observation of the almost constant delivered Head of the pump over time (P_{out}-P_{in}).

Figure 3.4: Installed sight-glass right before the pump suction port.

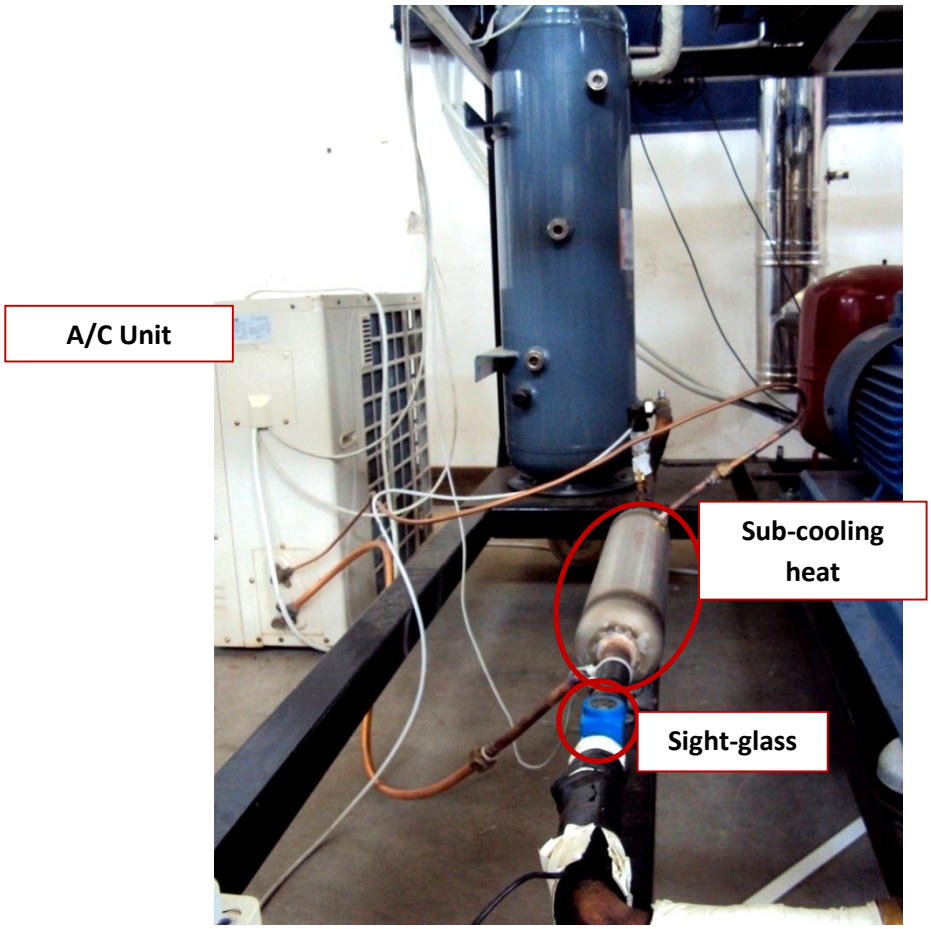

Figure 3.5: Installed sub-cooling heat exchanger & sight glass.

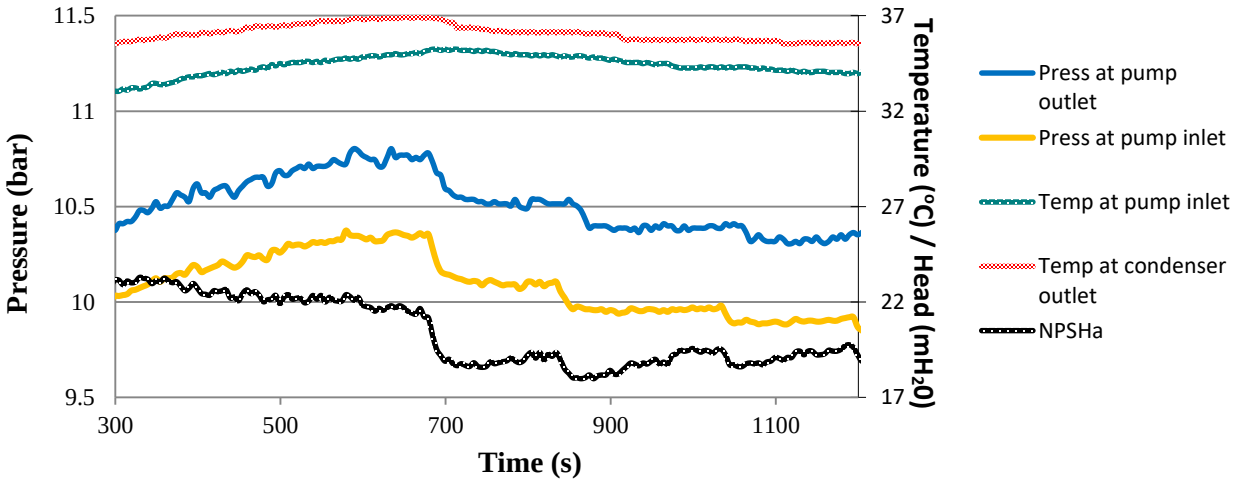

Figure 3.6: Cavitation free ORC pump operation with the addition of a sub- cooling heat exchanger.

3.2 Scroll expander's operation

In this section the scroll expander's operation is presented through diagrams of its main operational parameters. It is noted that at this point of studying, the presented data can be used for a qualitative analysis of the behavior of the used scroll expanders under various conditions and its comparison with the findings of other researchers. Figure 3.7 depicts the influence of the **scroll rotational speed** ($Nrot_{exp}$) and the **supply (inlet) temperature** (T_{su}) of the refrigerant on the **overall isentropic efficiency** (epsilons). The presented surface has been produced by the statistical fitting of the experimental data. $Epsilon_s$ is defined as:

$$\text{epsilon}_s = \eta_{is} = \frac{\text{Pel}_{gross}}{\dot{m}_{in} \cdot (h_{su} - h_{ex,is})} \qquad (3.7)$$

Where:

Pel_{gross} the gross electrical power output of the ORC unit (equal to the net electrical power output of the two scroll expanders)

$\dot{m}_{in}$ the total circulating mass flow rate

h_{su} the suppy enthalpy of the refrigerant at the expander inlet

$h_{ex,is}$ the enthalpy at the ideal isentropic expansion point at the measured exhaust pressure

Using this definition for the isentropic efficiency, all electromechanical losses, which can account for up to 40 % of the gross generated electrical power, are included and that is the reason why the efficiency appears to be quite low. The use of inverter frequency drives and induction motors/generators gives much room for improvements which could be part of the work planned ahead. This was confirmed by low measured values of the power factor which indicates the low electrical efficiency of the generators. In order to study the behavior of the expander itself separately a dyno-meter or torque meter should be installed directly on its shaft. At any case, the results are useful for the qualitative analysis of the system. Analyzing this diagram, the first obvious observation is that the isentropic efficiency is maximized near the nominal design conditions ($Nrot_{exp}$=1500 rpm / T_{su}=82 °C). From a thermodynamic point of view, this was expected since the optimization objective during the design of this system (as in most heat recovery systems) was the power output and not the cycle thermal efficiency [48], [49]. Moreover, the expander itself is expected to have a better efficiency near its design point (i.e. when the imposed volume/pressure ratio is near the built in volume ratio of the expander) where over-expansion and under-expansion losses are minimized.

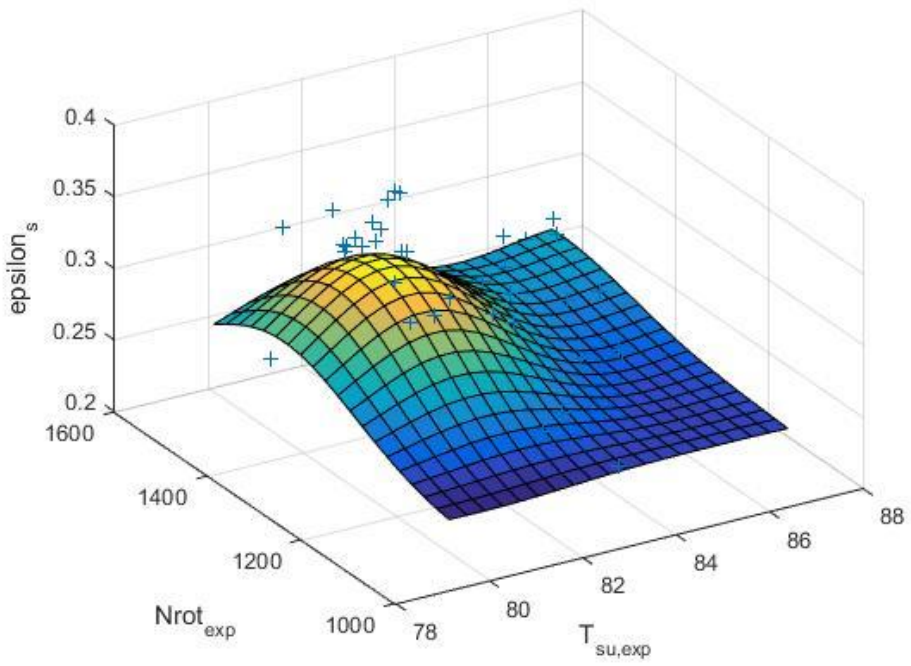

Figure 3.7: Scroll expander overall isentropic efficiency as a function of supply temperature ($T_{su,exp}$) and rotational speed (N_{rotexp}).

Focusing on the influence of the supply temperature, it is concluded that a 4 to 5K degree of superheating of the live vapor gives the optimum results (at 25 bar the saturated vapor has a temperature of 77.5 °C). As other researchers have pointed out [49], [50] & [51], the superheating at the evaporator exhaust should be at low levels when using high molecular weight organic fluids, such as R134a.

The impact of the rotational speed can be better understood by the explanation of Figure 3.8, which presents the overall isentropic efficiency of the expander as a function of the filling factor (ff) under various rotational speeds. The filling factor expresses a relative measure for the internal mass flow leakages and the respective power losses. The filling factor is defined as:

$$ff = \frac{\dot{m}_{in}}{V_{swept} \cdot N_{rot} \cdot \rho_{su}} > 1 \qquad (3.8)$$

Where:

$\dot{m}_{in}$ the total circulating mass flow rate

V_{swept} the bulit in swept volume of the scroll machine at expander mode

N_{rot} the expander rotational speed

ρ_{su} the suppy density of the refrigerant at the expander inlet

As expected, the rotational speed highly affects filling factor (ff), and as it can be observed in Figure 3.8, the lower the rotational speed is the higher the filling factor gets due to the larger relative impact of the internal leakages. This effect has also been noted by Lemort et al. [52]. in an experimental analysis of an open drive scroll expander. Other operational parameters such as the inlet pressure and the imposed pressure ratio also affect the filling factor and that is the reason why its value varies for constant rotational speeds. The correlation of the filling ratio with the imposed pressure ratio for various examined inlet pressure and rotational speed combinations was thoroughly investigated during the second experimental campaign and discussed in Section 3.11. Naturally, filling factor (ff) in turn affects the overall isentropic efficiency which gets reduced by increasing internal leakages.

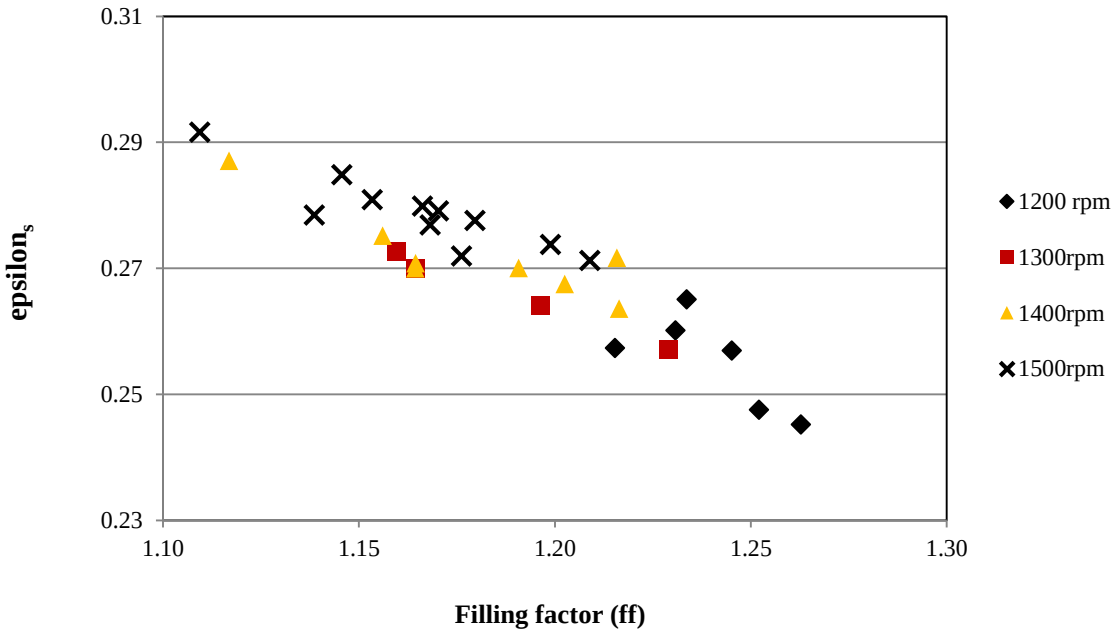

Figure 3.8: Scroll expander overall isentropic efficiency as a function of the filling factor (ff).

Another interesting issue is the actual mass flow rate that circulates through the ORC circuit. During the first experimental campaign, this value was calculated through the heat balance in the evaporator. The temperature and pressure of the heat source (water) as well as the volume flow rate are measured so the heat input rate ($\dot{Q}_{in}$) is known. At the same time the inlet and outlet conditions (pressure and temperature) of the refrigerant are also measured and thus assuming zero heat exchange losses the circulating mass flow rate ($\dot{m}_{in}$) can be calculated by the following equation:

$$\dot{m}_{in} = \frac{\dot{Q}_{in}}{(h_{out} - h_{in})_{refrigerant}} \qquad (3.9)$$

A cross-check of this value can be done through the heat balance at the system condenser. For this purpose, an ultrasonic mass flow meter and two thermocouples (condenser inlet-outlet) were installed at the cooling water circuit and the dissipated heat rate was this way indirectly measured. In the following

diagram (Figure 3.9), the values of the measured condenser dissipated heat rate (Q_{meas}) vs the respective calculated values (Q_{calc}) using the above-mentioned value (equation (3.9)) of the mass flow rate ($\dot{m}_{in}$) are presented. The relative deviation (ΔQ%) between these values is within 2-8 % which is satisfactory for the needs of the present level of studying. Moreover, the total system heat balance:

$$\mathbf{Q_{tot} = Q_{evap} + W_{pump} - W_{scrolls} - Q_{cond} - Q_{subcooler} - Q_{amb}} \quad (3.10)$$

gives a calculated Q_{amb} of about 600 W which is a realistic value for the non calculated ambient heat losses through the pipes of the system. However, in order to investigate in depth further certain operational issues such as the occurrence of partial cavitation in the ORC pump and the filling factor of the expander, accurate measurements of the mass flow meter with a Coriolis mass flow meter are necessary. All these are discussed in coming sections of this chapter where the results of the second experimental campaign are presented.

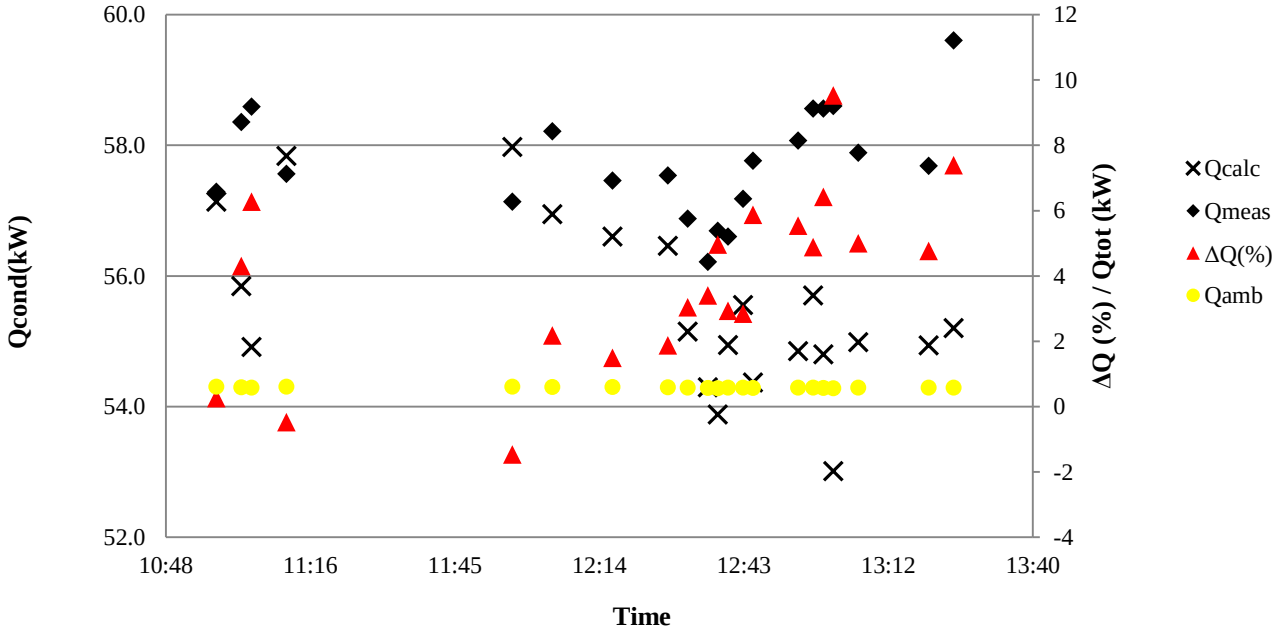

Figure 3.9: Condenser and overall heat balance.

3.3 Overall system performance

One of the main issues concerning the overall system performance was that with the current equipment and configuration it was not possible to reach the anticipated design point of the unit (5 kW_{el}, 90 kW_{th}). This is most probably caused by the occurrence of partial cavitation in the ORC pump while operating at high rotational speed and/or load. Partial cavitation means that a lower mass flow rate is achieved at the ORC circuit and thus less heat is recovered. Naturally the net power output of the unit is also lower in this case. Figure 3.10 shows the effect of the imposed motor drive frequency on the power output of the system. A maximum of almost 3.5 kW_{el} net power output was achieved at 50 Hz and with both scroll expanders working at 1500 rpm (Figure 3.11). The recovered heat at this point was about 70 kW_{th}.

There is a clear tendency of power output increase with raising mass flow rate. However, at high pump rotational speeds (above 45 Hz) this gain seems to be restricted, indicating the occurrence of partial cavitation, as already mentioned. In order to investigate this issue, the Coriolis mass flow meter is an indispensable part of measuring equipment. However, even if this issue is evidenced and should be solved, it would not be enough to reach the design point of the system. It is also necessary to be able to increase both the rotational speed of the pump and the expanders. Since the maximum drive frequency is limited to 60 Hz there is an option to substitute the existing motors/generators with other type of motors with less poles (i.e the 6-pole pump motor should be substituted by a 4-pole motor and the 4-pole generators with 2-pole generators).

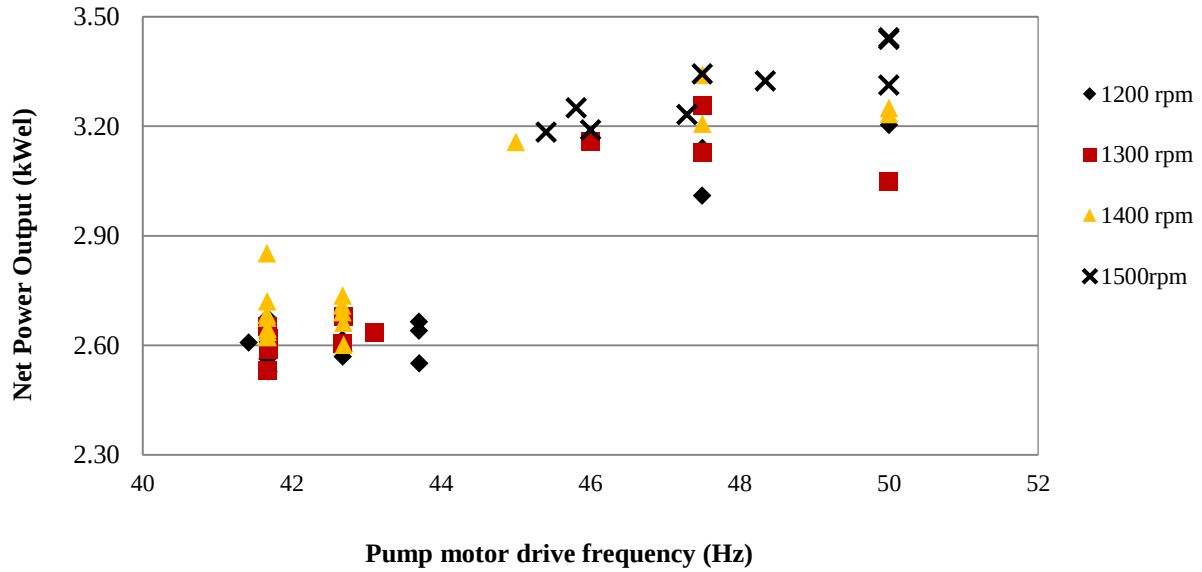

Figure 3.10: System power output vs pump motor drive frequency at different expander rpm.

Figure 3.11: Maximum electrical output achieved during first experimental campaign.

Even though the anticipated design point was not reached in terms of waste heat recovery capacity and net power output, the achieved thermal efficiency of the cycle is quite satisfactory. There is also potential of enhancing this efficiency by improving the electrical efficiency of the system as already explained. Figure 3.12 shows the cycle thermal efficiency as a function of the imposed pressure ratio at different expander rotational speeds. As expected, the efficiency is better near the built in volume ratio of the expanders (around 2.3). The main limitation for the imposed pressure ratio was the high cold soft water temperature used in the system condenser which was 24 ^{o}C during the test. However, a new test campaign was planned, when the available cooling water will be available at lower temperature and thus a much lower pressure can be imposed to the low pressure ORC circuit.

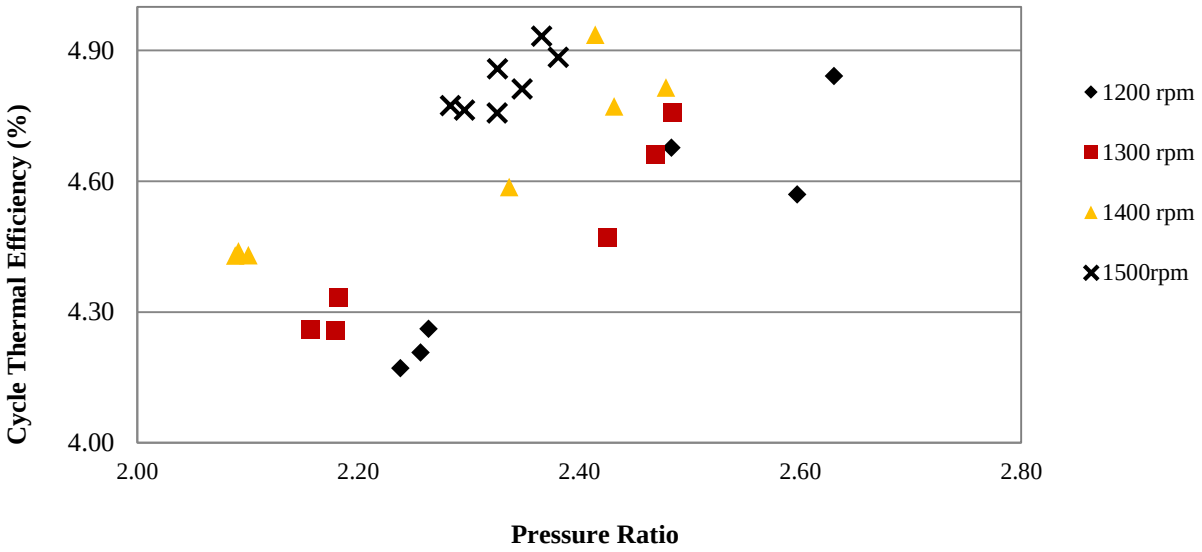

Figure 3.12: Cycle thermal efficiency vs imposed pressure ratio at different expander rpm.

Figure 3.13 shows the cycle thermal efficiency as a function of the pump motor drive efficiency at different expander rotational speeds. The main conclusion from this diagram is that for each expander rotational speed corresponds an optimum mass flow rate (or pump drive frequency). For 1500 rpm it is not clear where this is optimum, since the drive frequency is limited at 50Hz. If possible, it would be interesting to investigate the system's behavior for higher expander and pump rotational speeds. Another interesting observation derives from the comparison of Figure 3.12 with Figure 3.13 is that for the same mass flow rate, the lower the rotational speed of the expander is, the higher the imposed pressure ratio gets. This effect was expected according to the operation principles described in section 2.11.

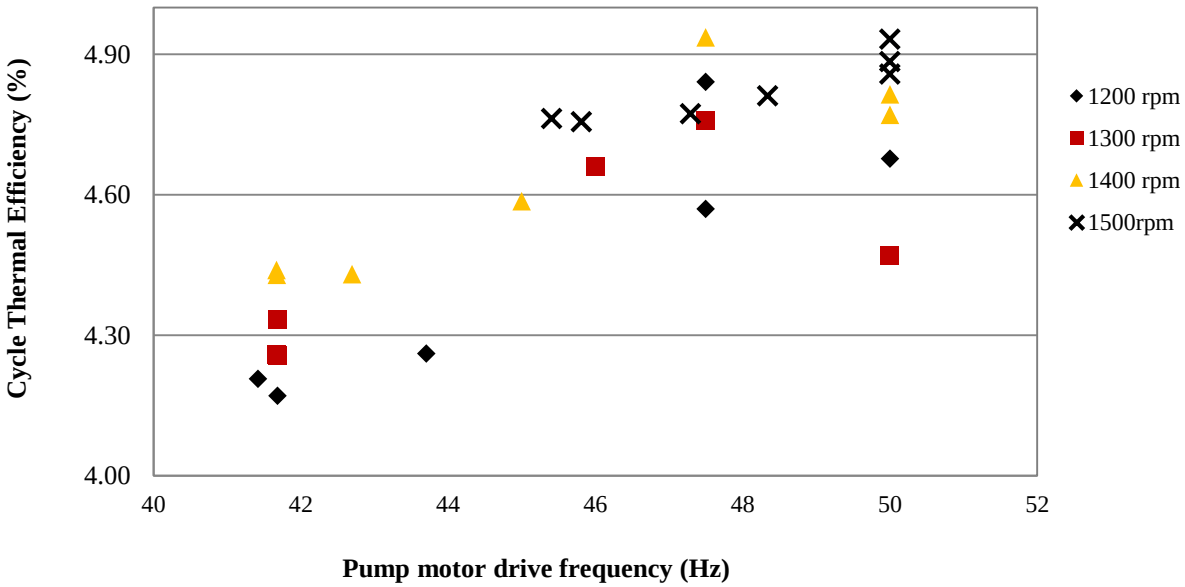

Figure 3.13: Cycle thermal efficiency vs pump motor drive frequency at different expander rpm.

Finally, in Figure 3.14 the Sankey diagram of a typical system operation point (T_{su}=83 °C, Pump motor frequency= 50 Hz, N_{exp}=1500 rpm) is depicted. The achieved cycle efficiency at this point was 4.93 %.

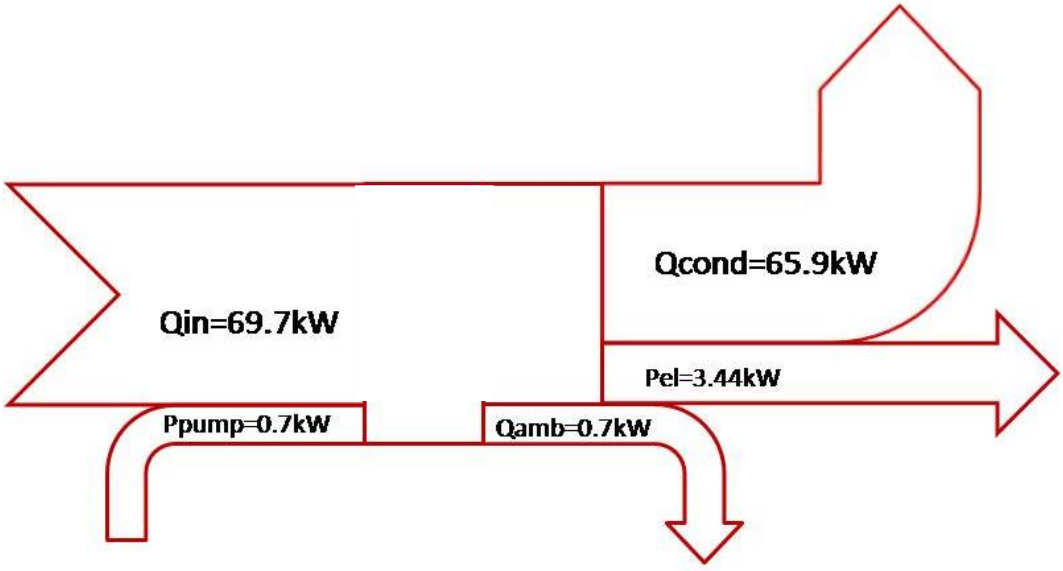

Figure 3.14: Sankey diagram of a typical operation point of the experimental unit.

3.4 Conclusions on the first experimental campaign results

The results and the conclusions arisen from the first experimental campaign of the ORC WHR unit are summarized below. Depending on the available resources, necessary corrective actions could be realized and their effect on the performance of the ORC WHR will be further investigated.

- A Coriolis mass flow meter is an indispensable part of the measuring equipment of such experimental benches.
- Cavitation effect in the ORC feed pump was dealt with the addition of a sub-cooling heat exchanger at the suction line of the pump. The effect of the sub-cooling degree on the cavitation effect as well as on the system performance needs further investigation.
- Partial cavitation at high pump loads and/or rotational speeds and its effect on the feed pump as well as on the overall system efficiency is another issue that requires further studying.
- The relatively low overall scroll expanders isentropic efficiency implies a low conversion of mechanical power into electrical. This was confirmed by low measured values of the power factor.
- A torque meter could be installed directly on the expander's shaft in order to evaluate its performance separately. This is will also assist on the performance optimization of the electrical power generation sub-system.
- The design point of the unit was not reached (5 kW_{el}, 90 kW_{th}) due to lower delivered mass flow rate by the pump. A suspected partial cavitation occurrence at the pump is probably the reason for this issue.

Regardless of the above statements, the overall goal was to build and operate an innovative experimental ORC WHR unit on laboratory conditions. This goal was achieved. The experimental unit was able to operate mainly on manual mode on various operating conditions. This achievement came of course with a lot of effort. More than 1000 hours were estimated as the time spend to trouble shoot and operate the unit in order to obtain the above depicted results. From author's point of view, significant knowledge on the behavior, influencing parameters and improvements that would increase the overall performance of the unit was obtained. This experience and knowledge was capitalized, through the evolution process of the experimental test rig. The ultimate final goal was the autonomous operation of the experimental unit after all, which was achieved at the very final end of the evolution process. The sequence of actions, research and planning will unfold on coming chapters.

3.5 Corrective actions prior to the second experimental campaign

As already presented, the experimental ORC test rig exhibits a number of innovative features regarding waste heat recovery from marine ICEs, such as micro scale range, advanced supervisory control and data acquisition system. Having in mind the results and the conclusions arisen from the first experimental campaign of the ORC WHR unit (see previous section 3.4) and that further research and development available resources were limited, the following corrective actions were realized and their effect / assistance on the ORC WHR further investigation procedure was extremely important.

The main **upgrades** to the experimental ORC test bench include:

- ✓ The installation of a Coriolis type mass flow meter. A Coriolis type flow meter (KROHNE: type OPTIMASS MFS 1000) was ordered and installed after the completion of the first experimental campaign. It was installed at the outlet line of the heat pump unit before the evaporator heat exchanger (Figure 2.4) for two reasons: a) the mass flow meter should handle the organic fluid in liquid phase b) the installation of the mass flow-meter at the suction line of the pump would cause an extra pressure drop which would have a negative impact on the available Net Positive Suction Head of the pump and thus on cavitation issues.
- ✓ The electrical adjustment of the 6-pole motor which originally operated at 960 rpm and 50 Hz, to 1080 rpm and 60 Hz. Thus the ORC-pump due to the increased maximum rotational speed, was able to deliver increased mass flow rate in the circuit. In this way the heat recover capacity of the unit and its power output was increased further.
- ✓ The replacement of the A/C operated sub-cooling heat exchanger with a water cooled plate heat exchanger. The cooling water would be provided by the cooling water circuit that feeds the condensing heat exchanger of the unit. In this way no additional power would be consumed for the sub-cooling of the refrigerant at the suction line of the ORC pump.

  The details of the water cooled plate heat exchanger by Alfa Laval, are presented in below Table 3.2.

Table 3.2: Characteristics of ORC test rig sub cooler (plate heat exchanger).

	Sub cooler (Alfa Laval AC30-EQ)
Number of plates	30
Heat transfer surface	0.644 m^2
Nominal heat transfer capacity	8.26 kW_{th}
Pressure drop at nominal flow (R134a) =0,5 kg/sec	0.34 bar

Surprisingly, the pressure drop was not as expected since the calculated /declared pressure drop by the provider/ retailer was almost one third than the measured one during the tests performed on the test rig. On the following Figure 3.15 and Figure 3.16, the measured mass flow rate, anticipated mass flow rate, the rotational speed of the pump and the measured pressure drop are presented.

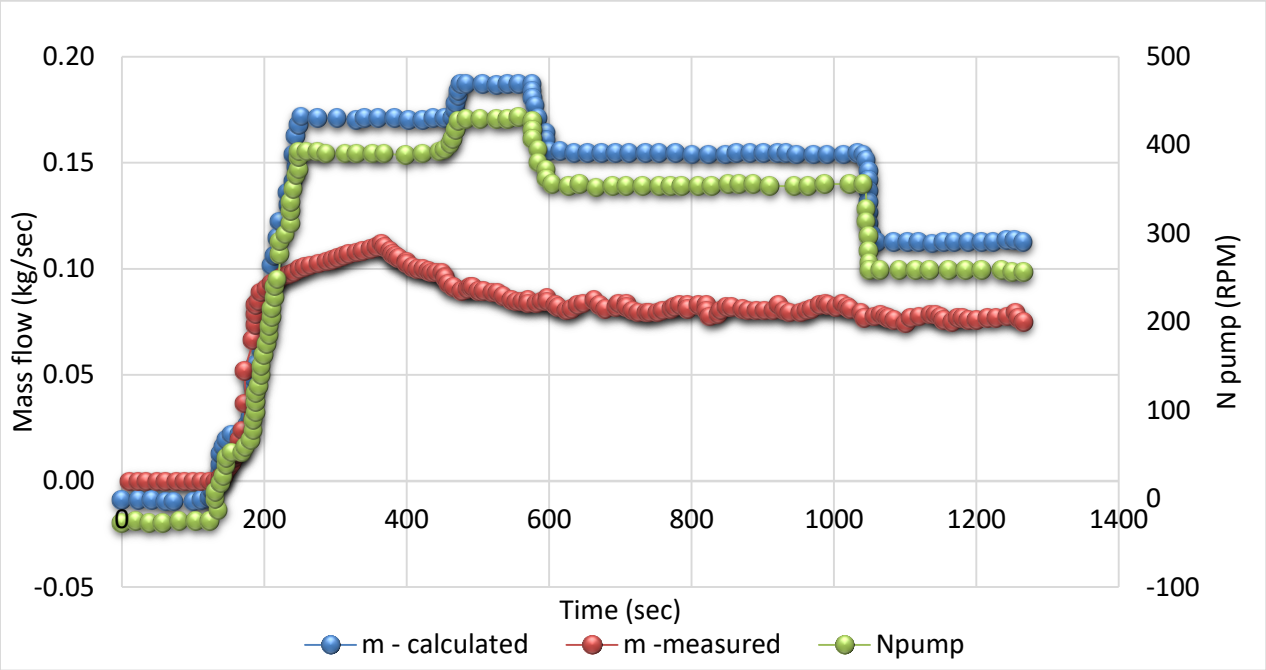

Figure 3.15: Measured mass flow rate, anticipated mass flow rate, the rotational speed of the pump, during assessment of subcooler heat exchanger pressure drop.

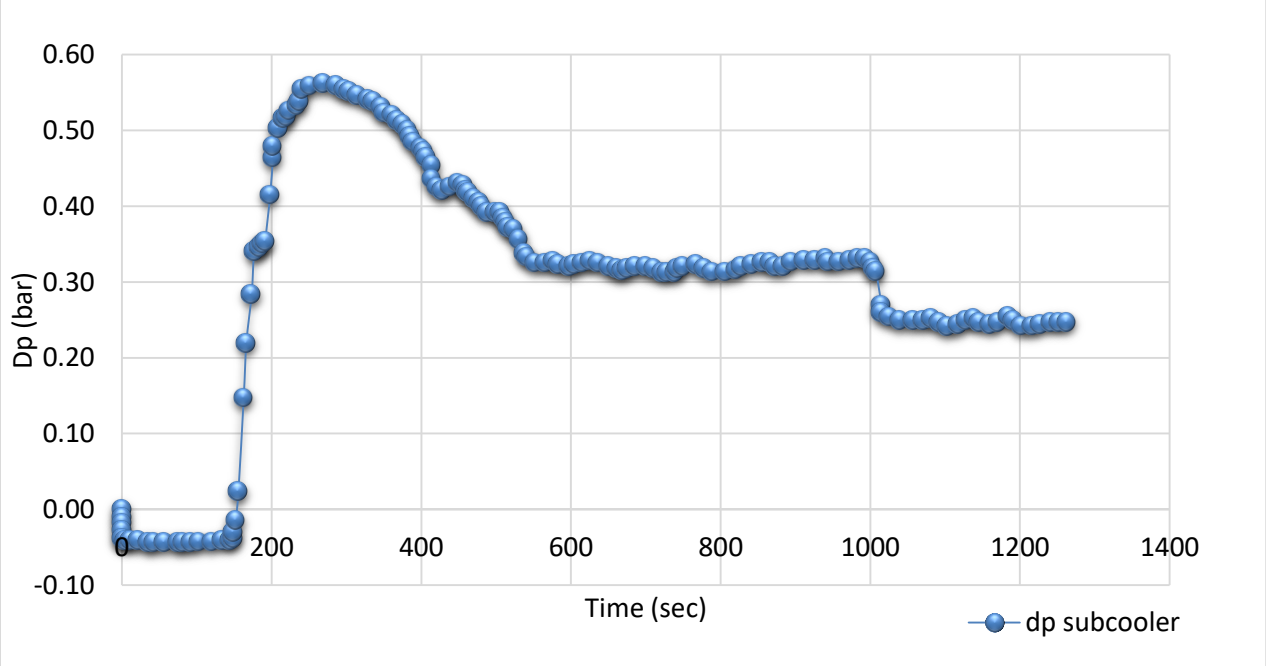

Figure 3.16: Measured pressure drop at subcooler heat exchanger.

The pressure drop in the subcooler is calculated as the difference of the measured pressure before the pump from that measured before the receiver. The inertia in the propagation of pressure through the receiver was found to be negligible, therefore, and the pressure before the feeder can be assumed to be equal to that of the receiver and thus with the inlet pressure at the sub cooler inlet. Of course this is not the case for the temperature due to significant thermal inertia of the receiver.

From the comparison of Figure 3.15 & Figure 3.16 it is evident that the declared pressure drop is reached at nearly 30 % of the nominal flow rate. This imposes significant levels of subcooling, in the magnitude of 3-5 ^{o}C, even for such low levels of mass flow rate. This significant pressure drop had a larger decreasing effect to parameter (P_t) at pump inlet than the positive effect of the desired sub cooling. It is also known that large levels of sub cooling also affect the cycle efficiency [56], which is something that usually should be avoided.

Eventually, the solution of the plate heat exchanger was abandoned, leading to the final decision to replace it back again with the counter flow shell and tube heat exchanger. The only improvement was that the sub cooler heat exchanger was supplied with water cooled by a Daikin Heat pump (Chiller) of 12 kW rated power. The coolant thermostat was adjusted to keep the temperature of the sub cooled water to a desired value (normally at about 15 °C). An additional way to change the subcooling degree was through a regulating valve placed in the water circuit, just before it enters the heat exchanger. The action of the valve results in a regulation of the cold-water flow rate. Thus, four cavitation tests have been performed by enforcing cavitation conditions on different operational conditions of the system.

The following additional upgrades originally pointed out, in previous section, were not realized. The primary reason was the substantial capital cost required. For the specific case of the torque meter installation, apart from the significant capital cost, additional hidden costs were expected, due to the extensive reconstruction of the scroll – motor shaft assembly.

- ✓ The installation of a torque meter at the shaft of one of the two generators.
- ✓ The replacement of the 6-pole motor (960 rpm at 50 Hz) of the ORC-pump with a 4-pole motor (1440 rpm at 50 Hz) in order to increase the maximum rotational speed of the pump and thus of the delivered mass flow rate in the circuit. A compromised solution was realized instead, where the frequency of the existing motor was increased.
- ✓ The replacement of the two 4-pole inductive motors/generators with two 2-pole motors/generators with a capacity of 3.5 kW each. This was proposed to be done for two reasons: a) the investigation of the expanders' operation at higher rotational speeds b) currently the generators are oversized (5.5 kW each) contributing to a very low electrical efficiency.

The above realized upgrades allowed for the further work that was planned and conducted during the second experimental campaign in order to investigate the optimum system configuration and operation.

On the following sections of this Chapter 3, the results of a secondary experimental campaign will be presented.

The main fields of **further work** include:

- ✓ Investigation of partial cavitation occurrence at high ORC-pump loads/rotational speeds.
- ✓ Investigation of the effect of the sub-cooling degree on the cavitation effect as well as on the system performance.
- ✓ Operation of the unit at higher pump rotational speed in order to get closer to the design point of the unit (5 kW_{el}, 90 kW_{th}). The Coriolis mass flow-meter as well as the partial cavitation study mentioned above will contribute crucially to the achievement of this target.
- ✓ Evolution of the control strategy in order to be able to operate as a standalone experimental ORC test unit.

3.6 Experimental investigation of the multi-diaphragm pump

During the specific, below described, experiment sessions, four main parameters have been controlled in order to achieve targeted working conditions:

- The natural gas supply flow rate to the boiler
- The mass flow rate of the cooling water through the condenser
- The speed of the pump and
- The speed of the expander

Each of these parameters has a strong effect on the balance of the system operation and its main influence can be clearly defined despite some secondary interactions / interferences between all parameters.

- Natural gas supply flow rate to the boiler: by adjusting the natural gas flow rate combusted in the burner, it is possible to achieve a fine regulation of the maximum pressure and temperature of the ORC system. An increase of the natural gas flow rate enables a higher heating rate of the hot water in the boiler that slowly increases its temperature. Due to a higher temperature of the evaporator inlet hot water, the temperature of the working fluid on the other side increases and this leads to a slow increase of its pressure as well. Exactly the opposite effect is obtained if the natural gas flow rate is decreased.

  With this procedure, a trade-off between the heat input to the cycle and the capacity of the system to exploit it can be achieved, leading to a general balance of the whole system and, as a result, to a steady-state condition. Moreover, in this way the superheating degree at the evaporator outlet can be adjusted.

- Condenser cooling water flow rate: its adjustment actively determines the parameters of the low-pressure part of the cycle. In particular, an increase of the cooling water flow rate through the condenser enables a higher cooling of the cycle (heat discharge). The cooling water temperature at the condenser outlet is lowered and the condensing pressure is therefore reduced. It is worth to underline that, on the side of the working organic medium, the pressure is the first parameter subject to change after increasing/decreasing the cooling water flow rate. Subsequently the temperature will also change but showing a slower variation.

- Pump rotational speed: as previously mentioned, the use of a variable speed drive for the motor of the pump allows for an optimal control of its speed. Furthermore, the mass flow rate delivered by positive displacement pumps, such as diaphragm pumps, is weakly related to the outlet pressure (see Figure 2.7). This means that, the higher the pump speed, the higher the mass flow rate is. By varying the speed, an accurate control of the superheating degree at the evaporator outlet can be achieved. A decrease/increase of the superheating is compensated by a decrease/increase of the pump speed for a given heat input. Related to this and given a fixed speed of the scroll expanders, an increase/decrease of the pump speed leads to an increase/decrease of the high pressure of the cycle.

- Scroll speed variation: as well explained by Declayé et al.[43], scroll expanders are volumetric machines, hence the volumetric flow rate can be theoretically expressed as the product of the rotational speed and the swept volume. In steady-state conditions, this flow rate is equal to the volumetric flow rate of fluid at the expander inlet:

$$\mathbf{V_{S,exp} \cdot N_{rot,exp} = \dot{M} v_{su,exp}} \quad (3.11)$$

Since the pump imposes the mass flow rate and the swept volume is constant, a modification of the rotational speed of the expanders therefore induces a change in the specific volume (or equally at the density) at the expander inlet, which depends on both pressure and temperature. Moreover, the superheating (i.e. the temperature) is controlled by the pump and the natural gas flow rate in the boiler, thus a modification of the expander rotational speed leads only to a modification of the expander inlet pressure which is the high pressure of the cycle. Particularly, an increase (resp. decrease) of the expander rotational speed causes a decrease (resp. increase) of the inlet pressure.

3.6.1 Efficiency definitions of the multi-diaphragm pump arrangement

In this section the performance parameters used to define frequency driver, electric motor and pump are defined. All these definitions are used during the evaluation of all experiments performed on the multi –diaphragm pump arrangement. Hence, starting from the frequency drive and going towards the pump:

a) **Efficiency of the frequency driver:**

$$\boldsymbol{\eta_{fd}} = \frac{\dot{\mathbf{W}}_{\mathbf{el,mot}}}{\dot{\mathbf{W}}_{\mathbf{el}}} \quad (3.12)$$

Where W_{el} is the power absorbed by the frequency drive and $W_{el,mot}$ is the power output at the desired frequency.

b) Efficiency of the motor:

$$\boldsymbol{\eta_{mot}} = \frac{\dot{\mathbf{W}}_{\mathbf{mech}}}{\dot{\mathbf{W}}_{\mathbf{el,mot}}} \quad (3.13)$$

defined as the ratio of shaft power output over electrical power input.

c) **Efficiency of the pump** (or pump shaft efficiency):

$$\boldsymbol{\eta_{pp}} = \frac{\dot{\mathbf{W}}_{\mathbf{hyd}}}{\dot{\mathbf{W}}_{\mathbf{mech}}} \quad (3.14)$$

which, according to the power chain, represents the ratio between the hydraulic power delivered to the working fluid and the mechanical power absorbed by the motor output.

The two most important efficiencies that were deeply investigated in the second experimental campaign are the global efficiency and the volumetric efficiency of the pump.

d) **Global efficiency of the pump:**

The global efficiency of a pumping system composed of a pump, an induction motor and a frequency drive can be defined as:

$$\eta_{glob} = \frac{\dot{W}_{hyd}}{\dot{W}_{fd}} = \frac{\dot{V}\Delta p}{\dot{W}_{fd}} \quad (3.15)$$

where $\dot{V}$ is the volumetric flow rate [m³/s] and Δp the pressure difference [Pa] under which the pump works. The definition takes account of all the losses described here over. Hence, **the global efficiency** can also be expressed as:

$$\eta_{glob} = \eta_{fd} \cdot \eta_{mot} \cdot \eta_{pp} \quad (3.16)$$

where it can easily be noticed that the global efficiency includes the efficiency of every device in the power chain.

In similar studies, as well as in the present, the electrical power absorbed by the motor is used instead of the power absorbed by the inverter that is the one directly derived from the grid. This choice is here justified by the fact that the energy meter dedicated to the pump system is installed between the frequency drive and the electrical motor. Thus, in order not to base the global efficiency evaluation on some general assumptions about the VSD efficiency, the power input of the motor $\dot{W}_{el}$ replaces the power input of the inverter $\dot{W}_{fd}$. In this way, the approach is merely experimental, without any theoretical hypothesis to pass from one power input to another.

e) Volumetric efficiency of the pump:

The proper definition of the volumetric efficiency is:

$$\eta_{vol} = \frac{\dot{V}}{\dot{V}_{th}} = \frac{\dot{V}}{N_{rot} V_{swept}} \quad (3.17)$$

where $\dot{V}$ = volumetric flow rate [m³/s]

$\dot{V}_{th}$ = theoretical volumetric flow rate [m³/s]

N_{rot} = rotational speed [Hz]

V_{swept} = swept volume [m³/rev]

The calculation of the theoretical volumetric flow rate requires the value of the swept volume of the pump. Unfortunately, this geometrical information cannot be easily found because it is not specified in the technical data sheet of the pump, and manufacturers do not provide accurate data about it. For this reason, as it is suggested in [37], volumetric efficiency will be assessed replacing the theoretical volumetric flow rate with the volumetric flow rate delivered by the pump at the specified rotational speed, as declared by the manufacturer. Thus, the definition becomes a relative volumetric efficiency:

$$\eta_{vol,rel} = \frac{\eta_{vol}}{\eta_{vol,manu}} = \frac{\dot{V}}{\dot{V}_{th}} \cdot \frac{\dot{V}_{th}}{\dot{V}_{manu}} = \frac{\dot{V}}{\dot{V}_{manu}} \qquad (3.18)$$

where $\dot{V}_{manu}$is the volume flow rate that the pump should deliver according to the characteristic curves provided by the manufacturer (see Section 2.2). Hereafter in this work, the expression "volumetric efficiency" is always used for simplicity but its meaning is that of "relative volumetric efficiency", as just defined in above Equation (3.18).

3.6.2 Closer look of the multi-diaphragm pump arrangement

The pump system integrated in the ORC experimental unit (described in section 2.12 and depicted in Figure 2.4) consists of a multi-diaphragm pump, an induction motor and a variable speed drive. A closer look (enlargement) of this arrangement of the test rig is shown in Figure 3.17. The Figure also shows the main measuring equipment for the assessment and analysis of the pump performance.

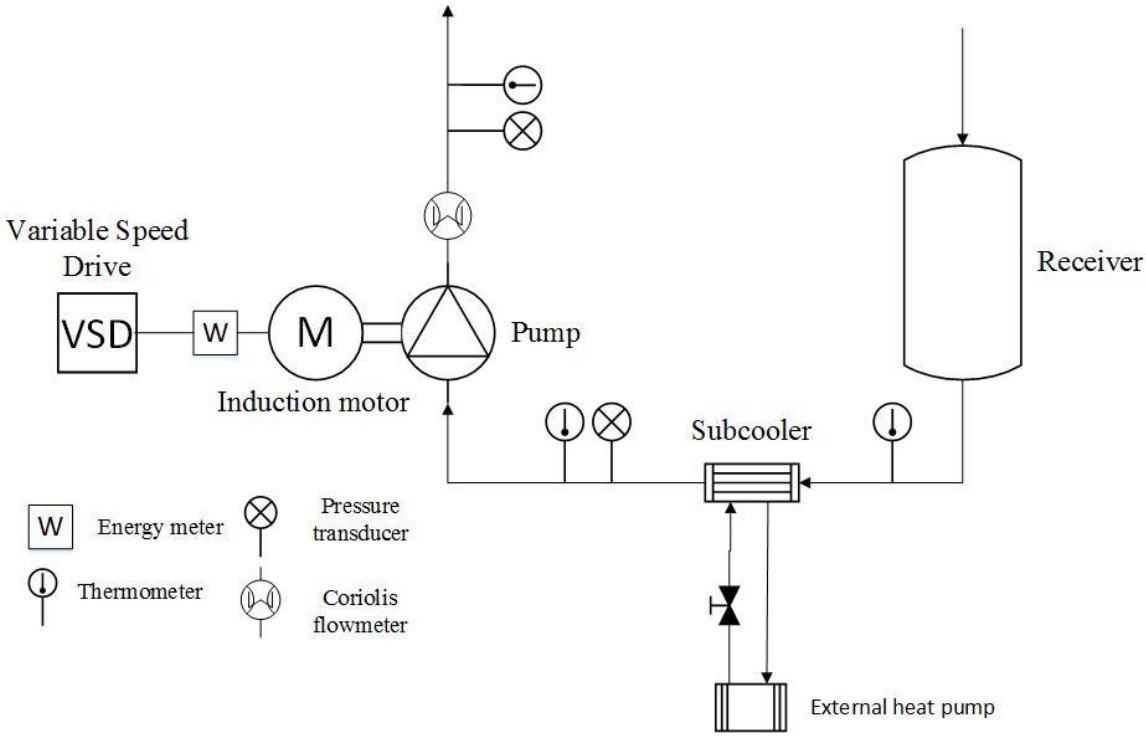

Figure 3.17: Scheme of the test rig section used to measure the performance of the multi-diaphragm pump.

The main components of this part of the test bench are:

- A feed tank that receives the working fluid after the condenser

- A heat exchanger (subcooler) which allows controlling the subcooling of the liquid. The heat exchanger is fed by soft water cooled by a Daikin Heat pump (Chiller) of 12 kW rated power. The coolant thermostat was adjusted to keep the temperature of the sub cooled water to a desired value (normally at about 15 °C). An additional way to change the subcooling degree was through a regulating valve placed in the water circuit, just before it enters the heat exchanger. The action of the valve results in a regulation of the cold-water flow rate.
- The pump to be tested is driven by an induction motor through a shaft. The speed of the motor/pump is controlled by a variable speed drive (VSD).
- Thermometers to measure the working fluid temperatures.
- Pressure transducers to measure the inlet and outlet pressure
- A Coriolis mass flow meter.
- An energy meter to measure the pump electrical consumption. This device is placed after the frequency drive and measures the input power to the electric motor.

The range and accuracy of each sensor are mentioned in Section 2.11.5. The piping is covered with 9mm thermal insulation in order to reduce heat exchange with the environment.

3.7 Pump mass flow rate: manufacturer vs experimental data

As already stated, during the second experimental tests campaign, the mass flow rate of the working organic medium (R134a) has been constantly monitored by a Coriolis mass flow meter that can continuously display the mass flow rate [kg/s], the density of the working fluid[kg/m^3] and the volume flow rate [l/h] at the pump discharge conditions. Moreover, as seen in section 2.2 dedicated to the pump's technical data sheet provided by the manufacturer, the volume flow rate processed by the pump for a given rotational speed can be easily determined (Equation (2.3)).

As already underlined, there is a direct proportionality between the delivered volume flow rate and the speed of the pump with a weakly dependence on the outlet maximum pressure. The manufacturer shows this weakly dependence by presenting three lines, each referred to a different outlet pressure (14, 35, 70 bar) (Figure 2.7). It can be easily noticed that, as the outlet pressure increases, the slope of the line slightly decreases, showing a perceptible divergence from one to the other only at operations for high values of rpm.

Given the characteristic curves provided by the manufacturer that attest the linear dependence between volume flow rate and speed (Figure 2.7), a comparison between these values and the actual ones (from the experimental data set) has been carried out. The following diagram (Figure 3.18) shows the two curves from the manufacturer for the outlet pressures of 14 and 35 bar and the line derived from experimental points. These points have been taken at different rpm and at the same outlet pressure of 23bar.

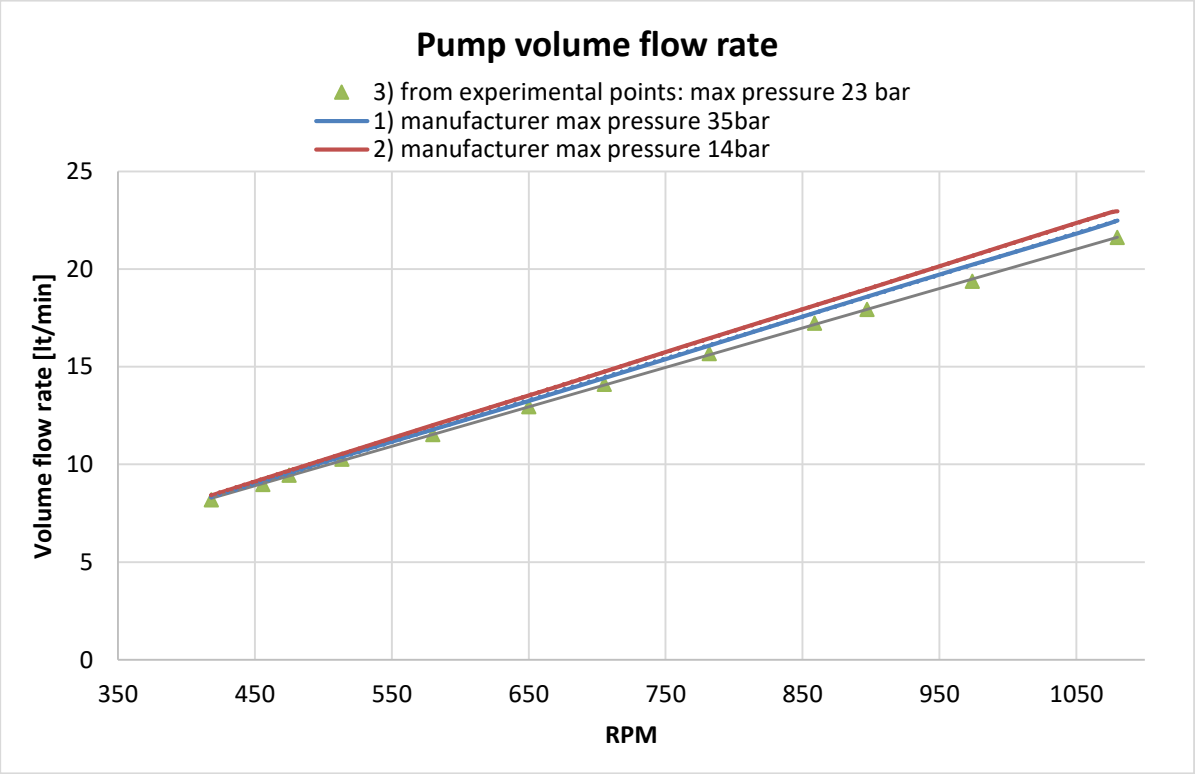

Figure 3.18: Declared by manufacturer and experimental volume flow rate curves.

A small divergence from the manufacturer curves can be noticed, especially for higher rpm where it becomes larger. Referring to the 1080-rpm operation where the deviation is larger, the measured volume flow rate is lower than the manufacturer value at 14 bar by about 5.824 %. Although the pump manufacturer provides lines with a range of rpm that goes from 0 to 1450, the pump speed of 1080 is the highest reached during the tests (full load operation at 60 Hz).

Thus, the investigation of the volume flow rate curves refers only to the tested range of speeds. The equation found for the experimental line is:

$$\dot{V} = 0.020179*RPM - 0.166632 \quad (3.19)$$

Considering that, a theoretical9 line for 23bar as maximum pressure should have a slightly lower slope than the one of 14 bar and that the maximum deviation from this is 5.824 %, the experimental line has been assumed as the reference one for cavitation detection. With the comparison between the volume flow rate value from the experimental line and the measured one during the cavitation tests, it is possible therefore to assess if the pump is delivering the anticipated mass flow rate at that speed or if it is working in partial cavitation conditions. As a threshold between the normal operating conditions and the inception of cavitation conditions, a 5 % decrease of the measured volumetric flow rate from the theoretical one has been assumed in a similar approach to the work of Declaye [37].

3.8 Results and discussion of the multi-diaphragm pump test campaign

Several experimental points have been collected by testing the pump in several operational conditions. The results can contribute to a deeper investigation of the pump-motor system, the global efficiency of which achieves the maximum values of about 47-48 %. The derived efficiency values enrich therefore the literature background. Moreover, cavitation tests provide useful information for the integration of this type of pump in micro-scale ORC systems.

3.8.1 Global and volumetric efficiency

Three main parameters are usually investigated to assess the performance of a pump integrated in an ORC system: the pump shaft efficiency, the volumetric efficiency and the global efficiency. While the first two refer merely to the pump, the latter refers to the performance of the wider pump system, taking into account the electrical motor and, in some studies, also the variable speed drive (VSD). For the definitions of these parameters, see section 2.2 & 2.11.1.

As the experimental ORC test bench is not equipped with a torque meter for the pump shaft (to be installed between the electrical motor and the pump), it is not possible to evaluate the mechanical work transferred to the pump by the motor. Thus, the pump shaft efficiency cannot be measured and investigated experimentally. Evaluations of this efficiency can however be accomplished on the basis of the power required by the pump that the manufacturer provides by means of the equation in the pump data sheet (Equation (2.4)).

As far as the global efficiency is concerned, it is necessary to specify which devices of the pump system (pump, motor, VSD) are included in its experimental evaluation. For example, Declayé [37] takes into account all the losses of the pump system, and defines the global efficiency on the basis of the electrical power adsorbed by the inverter from the grid ($\dot{W}_{fd}$). Bala et al. [54] define the overall efficiency as the product between the efficiency of the pump and the efficiency of the motor. As already discussed when the global efficiency has been defined, the same definition of Bala et al. [54] is also used in this work, due to the position of the energy meter and due to the desire of using a pure experimental approach in the evaluation of this efficiency.

The aim of this section is mainly to show two important patterns of the global and volumetric efficiencies:

- Under variable pressure difference imposed between the inlet and outlet of the pump for the same pump rotational speed (rpm).
- Under variable pump speed (rpm) for the same pressure difference imposed.

Measurement uncertainties are calculated at each measuring point starting from the uncertainties of the instruments declared by the manufacturers and reported in Section 2.11.5. This calculation is carried out using EES error propagation algorithm. In this way, the inaccuracies of the instruments and systematic errors are taken into account, but random and repeatability errors are not considered. The experimental

sessions are indeed very time-consuming and did not allow repeating the same procedure many times in order to include also this type of errors.

3.8.1.1 Constant pump speed and variable pressure difference

Within the experimental procedure under variable pressure difference and constant rotational speed, two different approaches have been applied:

a) The outlet pressure of the pump (cycle maximum pressure) is kept constant and the inlet pressure (cycle low pressure) is adjusted by regulating the cooling water mass flow rate at the condenser inlet as explained in Section 3.6.

b) The inlet pressure of the pump is kept constant and the outlet pressure (cycle maximum pressure) is varied by changing the rpm of the scroll expanders.

1st approach: constant p_{max} and variable p_{inlet}

This first approach was originally applied with the purpose of estimating an efficiency curve for the scroll expanders. The established methodology was designed to acquire a data set for three different inlet pressures (cycle maximum pressure) and each data set should include several points with pressure ratios in the range of 1.8 – 2.9. Being focused on the behaviour of a single scroll expander, the system has been run in half-power-generation mode, meaning partial load conditions and with the operation of only one of the two scrolls. For this reason, the data related to the pump, which have been used for the evaluation of the two efficiencies, consist of low-speed operation of the pump (between 21 and 28 Hz).

In Figure 3.19, the trend of the global efficiency with the imposed pressure difference for four different pump frequencies (21.6 Hz; 24.6 Hz; 26.5 Hz; 27.5 Hz) is presented. These speeds have been chosen to obtain the desired conditions for the scroll tests. The expander has been tested in order to assess its isentropic efficiency for different combinations of three inlet pressures (22, 23 and 25 bar) with three rotational speeds (1150, 1300, 1450 rpm) (please refer to section 3.11). The derived data for the pump show that the global efficiency is an increasing function of the pressure difference. What is interesting to notice is that the changing value of the maximum pressure does not affect the trend of the global efficiency. For example, at the frequency of 21.6 Hz, a variation of the scroll rpm from 1150 to 1300 and consequently of the maximum pressure from 23 to 22 bar, does not entail any changes in the global efficiency pattern: the range of increase remains between 0.145 and 0.185.

Each diagram shows almost the same range of pressure difference and an evident change in the global efficiency values can be noticed when varying the pump speed. Particularly, by increasing the frequency, the variation range of the global efficiency shifts to higher values. For a pressure difference between 10 and 18 bar, it results to be:

- 21.6 Hz: $\eta_{glob} = 0.145 \div 0.185$
- 24.6 Hz: $\eta_{glob} = 0.16 \div 0.2$

- 26.5 Hz: $\eta_{glob} = 0.18 \div 0.24$
- 27.5 Hz: $\eta_{glob} = 0.21 \div 0.265$

Values of the global efficiency for higher pumps frequencies is presented in the second approach of the tests.

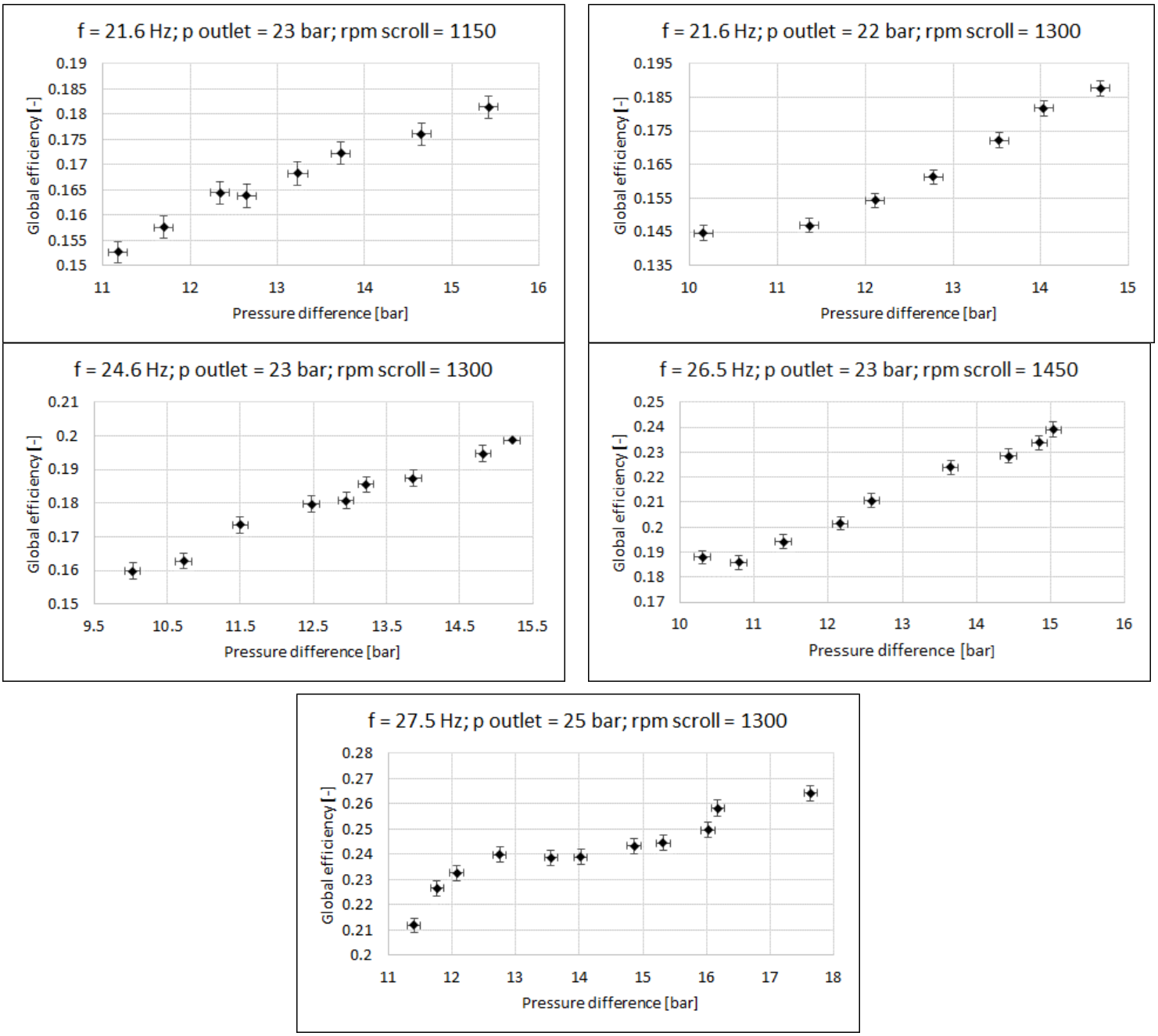

Figure 3.19: Global efficiency of the pump with varying pressure difference for different pump rotational speeds.

As regards the volumetric efficiency, operation under variable inlet pressure and constant outlet pressure does not allow for a useful evaluation of this efficiency. The expected trend, in which the volumetric efficiency decreases with the increase of the pressure difference, cannot be identified and random values are obtained, as shown in Figure 3.20. The diagrams show the values of volumetric efficiency vs. pressure difference for the same rotational speeds analysed in the study of the global efficiency. The impossibility of identifying the expected trend is related to the strong impact of the inlet pressure variation on the pump operation itself. A change in the effectiveness of the cooling circuit involves new thermodynamic conditions of the working fluid at the inlet of the pump. An increase of the cold water flow rate in the condenser leads to a decrease of temperature and pressure of the working fluid that, as a result, enters the pump with a higher density and consequently a higher mass flow rate considering the same volume flow rate at the pump suction.

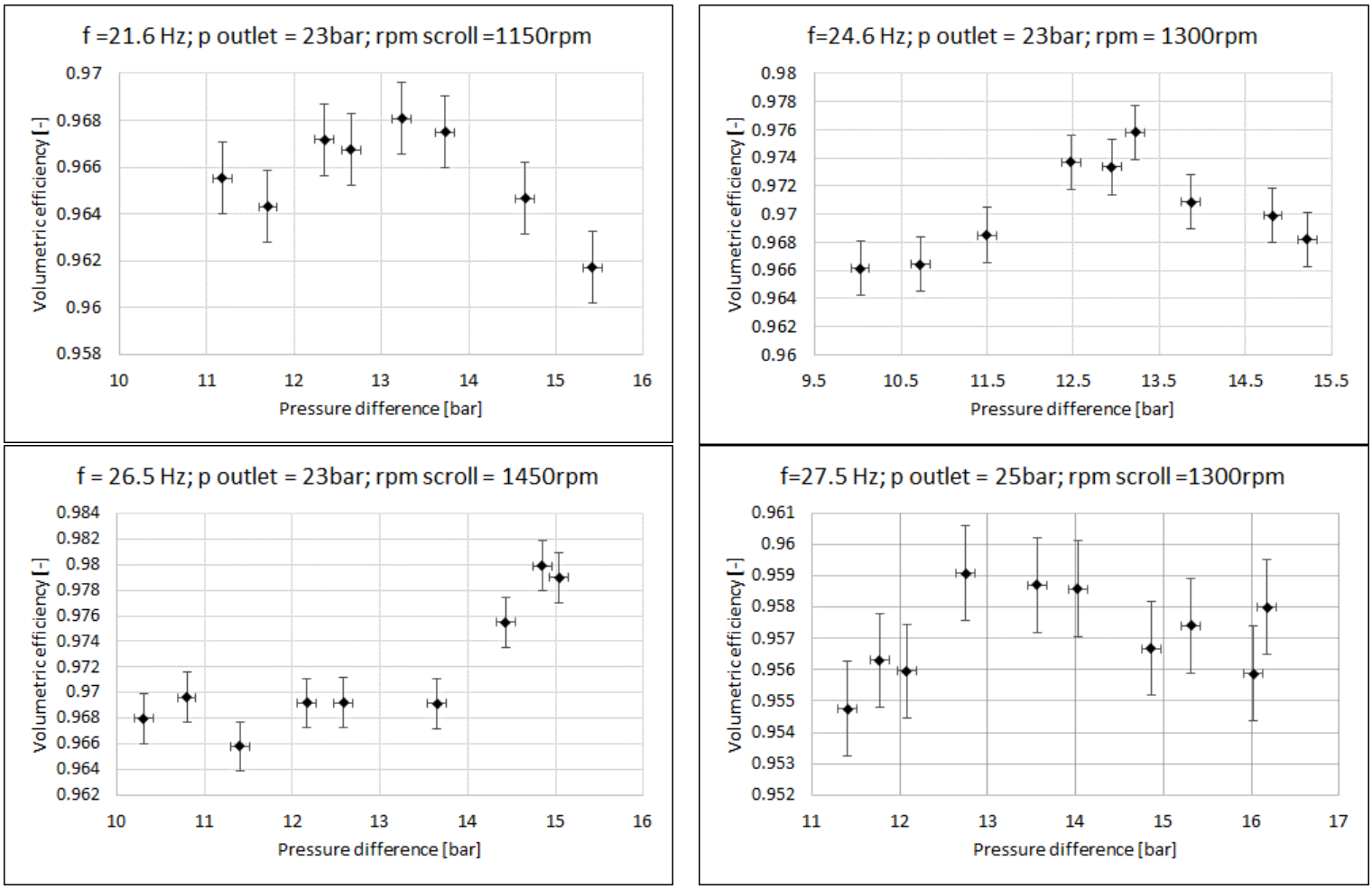

Figure 3.20: Volumetric efficiency of the pump with varying pressure difference for different pump rotational speeds.

A much more stable procedure for the operation of the pump is obtained by keeping constant the inlet conditions and by varying only the outlet pressure (by changing the speed of the scrolls). Moreover, it is faster, since it avoids instability problems due to the inertia of the condenser. Usually, the experimental evaluation of the volumetric efficiency is conducted according to this second procedure [37] which is also

applied in the second approach of this experimental investigation (constant inlet pressure and variable outlet pressure) presented next.

2nd approach: variable p_{max} and constant p_{inlet}

The second procedure derives from tests completely dedicated to the investigation of the pump. The system works at full load and therefore both the scroll expanders are running in parallel. The inlet pressure is set as low as possible by fully opening the regulator valve in the cooling water circuit. The reached value is 8 bar and is kept constant during the tests by adjusting the same valve. The choice of reaching a minimum value for the pressure allows the pump to be tested in a range of pressure differences that is as wide as possible for this system arrangement, since the maximum value of the high pressure (outlet of the pump) is limited to 25 bar for structural/safety reasons.

On the other hand, the maximum pressure is varied, as already specified, by varying the speed of the scroll. More specifically, under constant low pressure of the cycle, if the scroll speed is decreased (resp. increased), the maximum pressure is increased (resp. decreased). This approach, which requires the variation of only one parameter (scroll rpm), allows the system to be moved quickly throughout the different steady-state points, ensuring stable operation.

Three different data sets have been collected and each of them refers to a different pump speed:

a) Frequency = 26.5 Hz ⟶ rpm = 513

b) Frequency = 36.5 Hz ⟶ rpm = 705

c) Frequency = 46.5 Hz ⟶ rpm = 897

The expected trends should be an increasing global efficiency and a decreasing volumetric efficiency with the increase of the pressure difference.

A. Frequency = 26.5 Hz

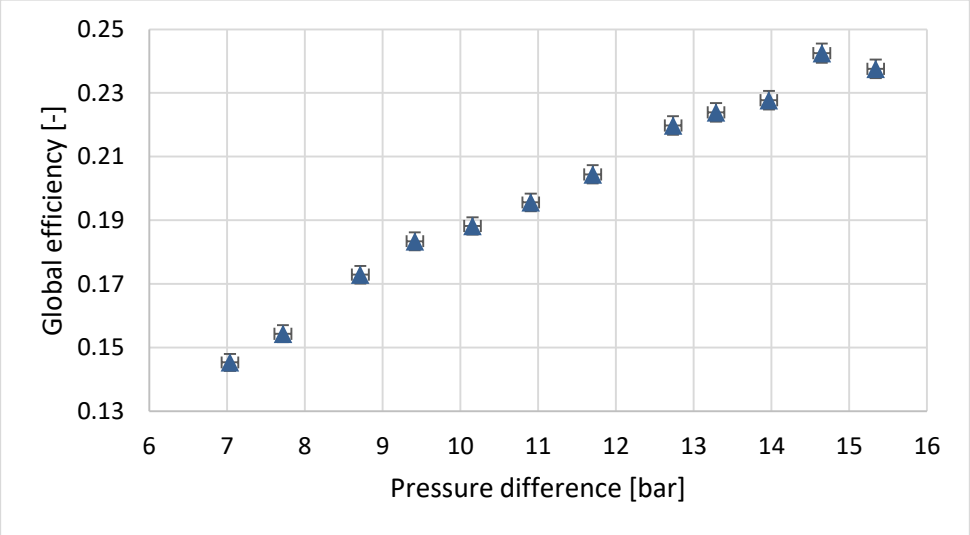

Figure 3.21: Global efficiency vs. pressure difference for a pump frequency of 26.5Hz.

The trend shown in Figure 3.21 has the same shape of the one illustrated in the 1st approach for the same frequency (Figure 3.19). The range of the pressure difference is wider in comparison with that of Figure 3.19, since it varies from 7.03 bar to 15.34 bar instead of 10.3 to 15. This is a consequence of being at a low frequency operation and of a great variation of the scrolls speed: from 550 to 1500 rpm. Due to the low frequency operation of the pump (26.5 Hz), indeed, the pressure difference is low (7.03 bar) for the maximum scroll speed (1500 rpm), while the maximum pressure of the cycle (25 bar) can be reached for low values of the scroll speed (550 rpm).

Furthermore, the comparison with the diagram at 26.5 Hz of Figure 3.19 shows similar values for the global efficiency that, for example, reaches the same maximum value of 0.24. Given these observations, the conclusion is that the different approach does not affect the experimental evaluation of the global efficiency.

On the other hand, using the 2ndapproach, the volumetric efficiency shows a clear decreasing trend with the increase of the pressure difference. In Figure 3.22, a very different curve shape compared with that of Figure 3.20 at the same frequency is evidenced.

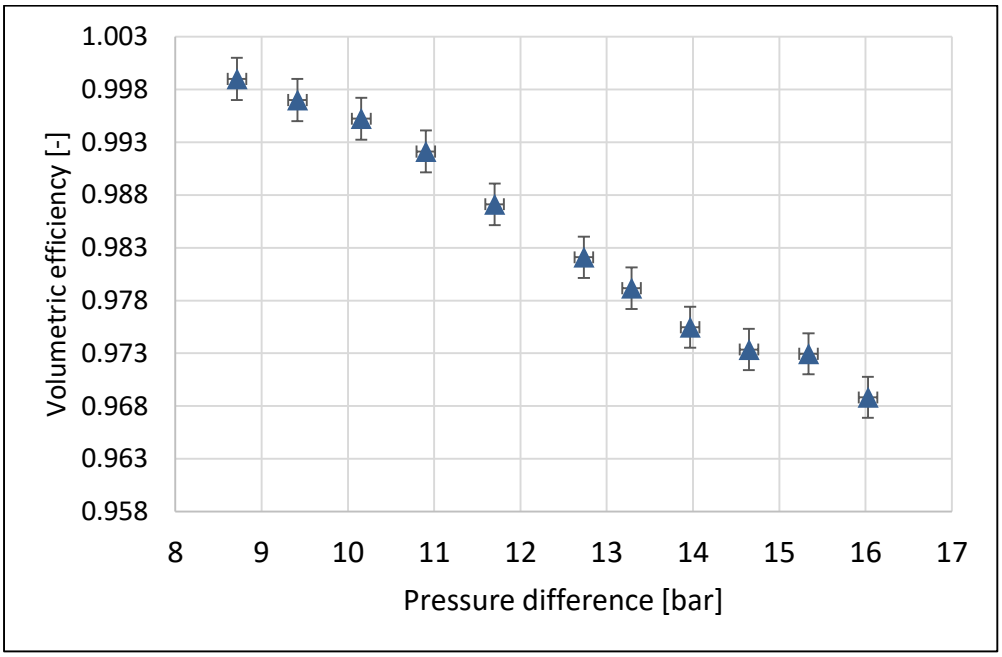

Figure 3.22: Volumetric efficiency vs. pressure difference for a pump frequency of 26.5 Hz.

The efficiency decreases by about 3 % within a pressure difference increase of 9bar. This means that the multi-diaphragm pump is poorly affected by the pressure difference. This slight decrease depends on the pump structure and operation system that allows keeping the leakages low even though the pressure increases considerably. For example, if it was a piston or a gear pump, the value of the efficiency would be much lower: 0.8 and 0.9 respectively for a pressure difference of 10 bar [37].

A similar approach has also been followed by Declayé in his work [37]. Global and volumetric efficiencies are experimentally assessed for five different technologies of volumetric pumps (mono-

diaphragm, multi-diaphragm, gear, piston and plunger). Moreover, the efficiencies have been investigated for two different operational conditions:

- At nominal operation (50 Hz) and
- At 66 % of the nominal speed (26.5Hz).

Since the results related to the multi-diaphragm pump are shown only for the nominal operation, only the two diagrams at the nominal speed are reported here (Figure 3.23 and Figure 3.24).

The two diagrams in Figure 3.21 and Figure 3.22 are in accordance with the patterns of the multi-diaphragm pump reported by Declaye in Figure 3.23 and Figure 3.24. Similar values for the global efficiency are found, even though the results refer to the two different operation points at 50 Hz (Declayé) and 26.5 Hz respectively. As it will be shown in the following for higher frequencies, the global efficiency will reach higher values than those obtained by Declayé, while the volumetric efficiency remains in the same region. This discrepancy about the global efficiency can find justification in the fact that Declayé's data came from a smaller multi-diaphragm pump (Wanner Hydra cell G13: flow rate = 4.86 l/min at 685 rpm). An electrical motor of 0.37 kW has been coupled with this pump. In the pump system of the experimental ORC under investigation, the multi-diaphragm pump has a higher capacity (volume flow rate = 14.177 l/min at 685 rpm) and the electrical motor is oversized, with a nominal power of 3.0 kW. The two systems include therefore a scale factor and, what is more important, a different motor sizing for the shaft power required by the pump.

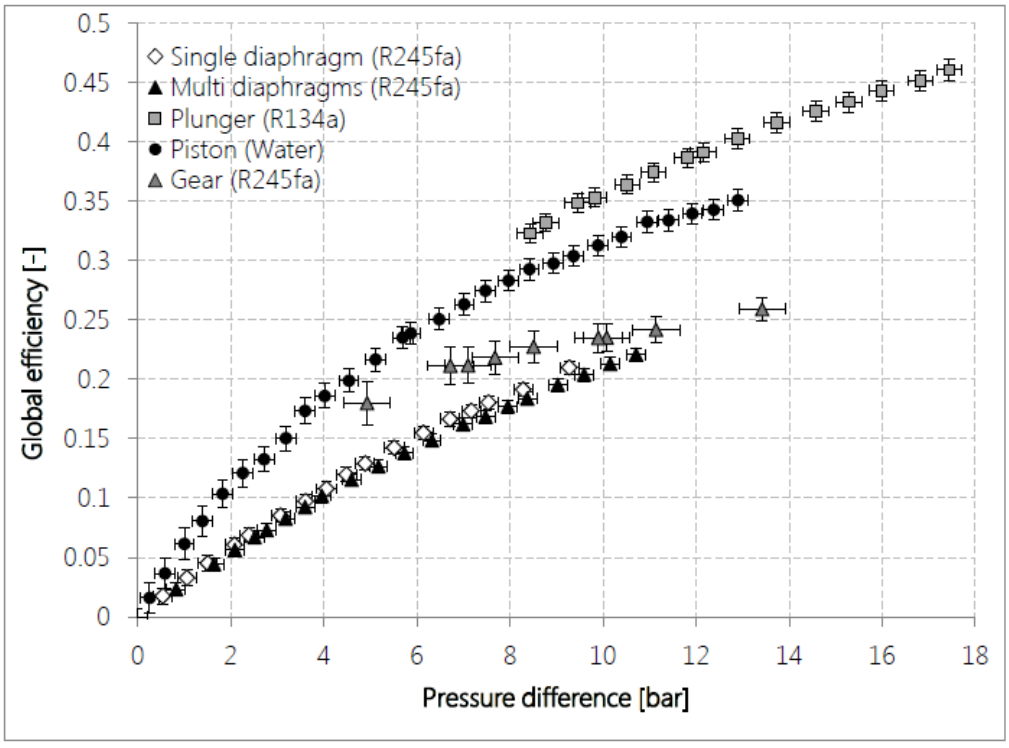

Figure 3.23: Global efficiency vs. pressure difference for five different pump technologies. [37]

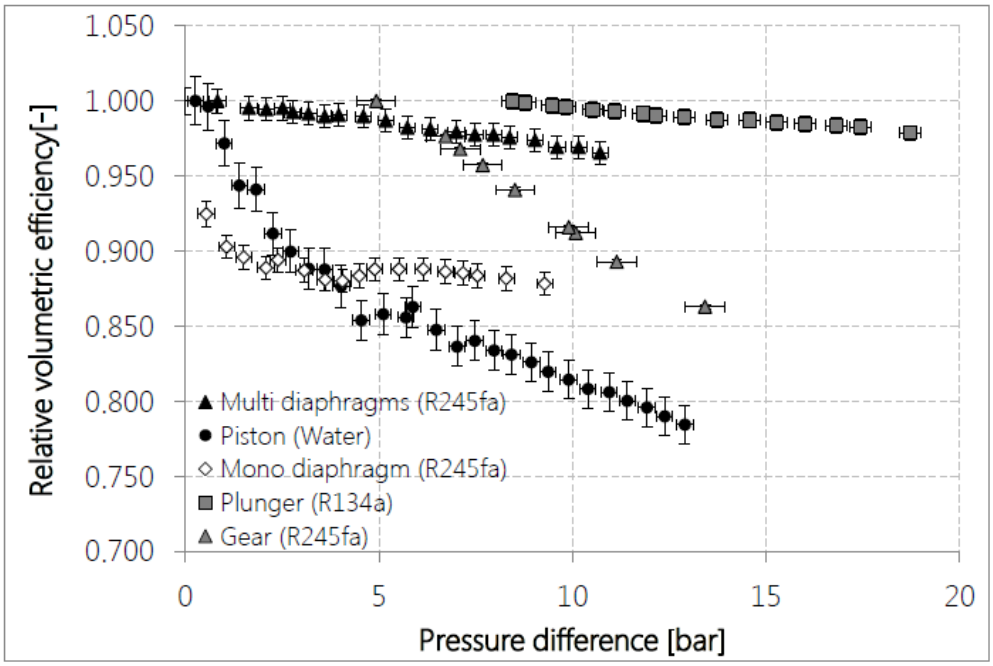

Figure 3.24: Volumetric efficiency vs. pressure difference for five different pump technologies. [37]

B. Frequency = 36.5 Hz

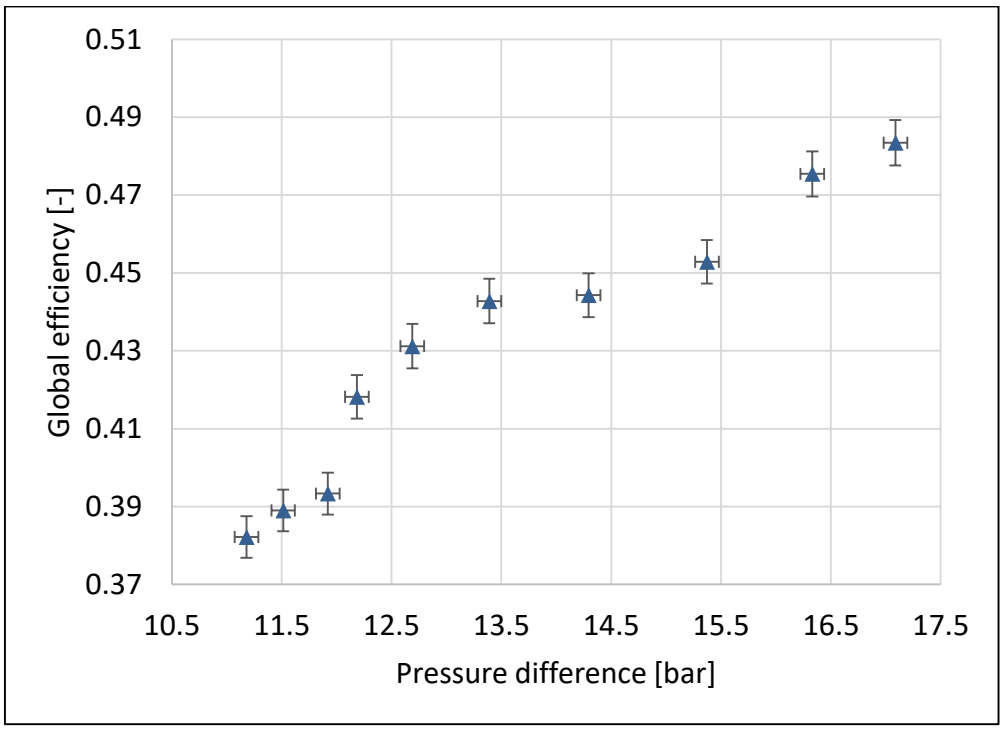

Figure 3.25: Global efficiency vs. pressure difference at a pump frequency of 36.5 Hz.

Figure 3.25 shows that the same trend of the global efficiency is maintained for the higher frequency of 36.5 Hz. However, its values are higher than those shown for the frequency of 26.5 Hz; particularly the variation range is between 0.392 and 0.483 for pressure differences ranging from 11.17 bar to 17.03 bar.

The volumetric efficiency diagram (Figure 3.26) presents the same trend as well. Furthermore, it is characterized by values similar to those of the previous test.

The operation at a higher frequency reduces the range width of the pressure differences that can be investigated. In particular, the lowest outlet pressure that can be reached (at the scroll speed of 1500 rpm) was 19.16bar and the highest admissible pressure of 25 bar is achieved with a scroll speed of 830 rpm.

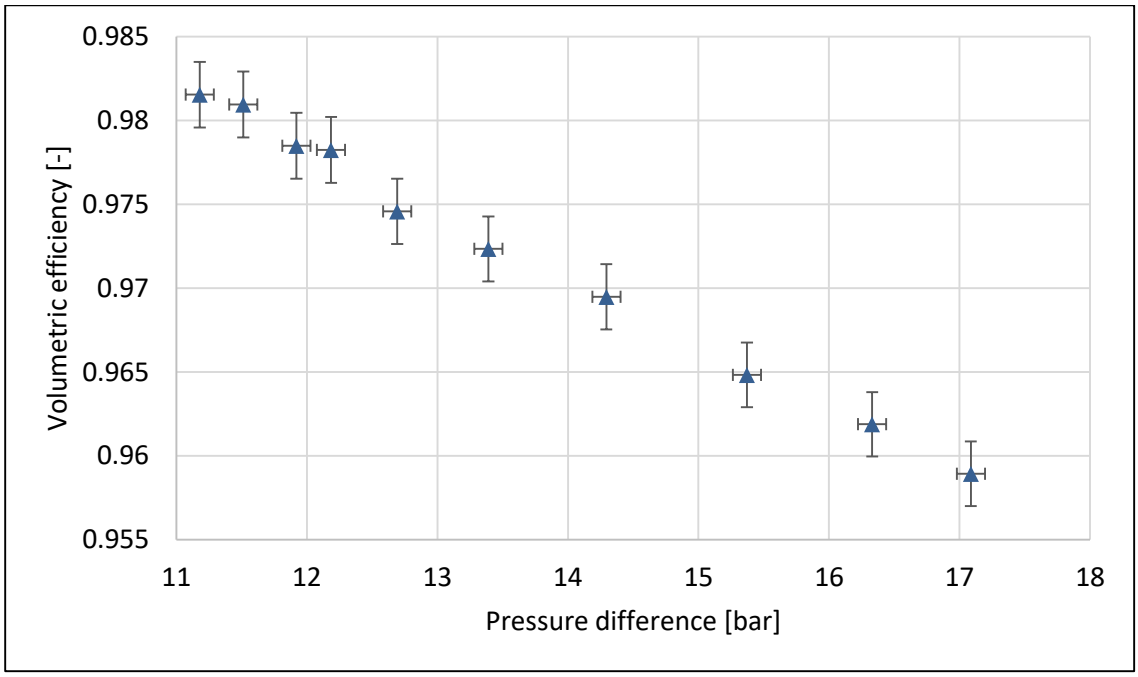

Figure 3.26: Volumetric efficiency vs. pressure difference at a pump frequency of 36.5 Hz.

C. Frequency = 46.5 Hz

The frequency of 46.5 Hz has been chosen as the highest one that, according to the procedure of this approach, can still give profitable results. This is, in fact, the highest pump speed that allows obtaining from the system a pressure difference variation of at least 2.5 bar. Even though the range of pressure difference is small, the increasing trend of the global efficiency is still confirmed. Nevertheless, its values vary in a range which is very close to that one at 36.5 Hz, without noticing an increase, as it was found for the passage from 26.5 Hz to 36.5 Hz.

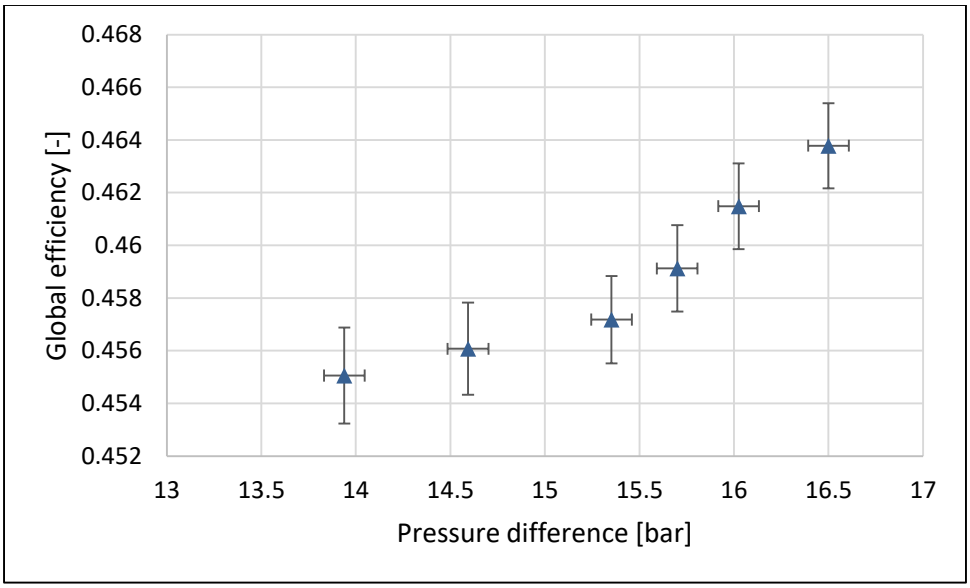

Figure 3.27: Global efficiency vs. pressure difference at a pump frequency of 46.5 Hz.

Passing from one rotational speed to another, the behaviour of the oversized motor plays a major role in determining the magnitude of the global efficiency variation. In each of the experimental tests, the load of the motor has always been below 35 %, meaning a very bad and unpredictable operation in terms of both efficiency and power input stability. In particular, the combination between such a low load and low speed (26.5 Hz) leads to a very low efficiency (29-30 %) that makes the motor use the same amount of energy as if it worked at nominal speed with higher load. Once the speed is increased (at around 34 Hz), the electrical motor starts working better, hence the consumed power for the same load decreases and consequently a higher global efficiency is revealed.

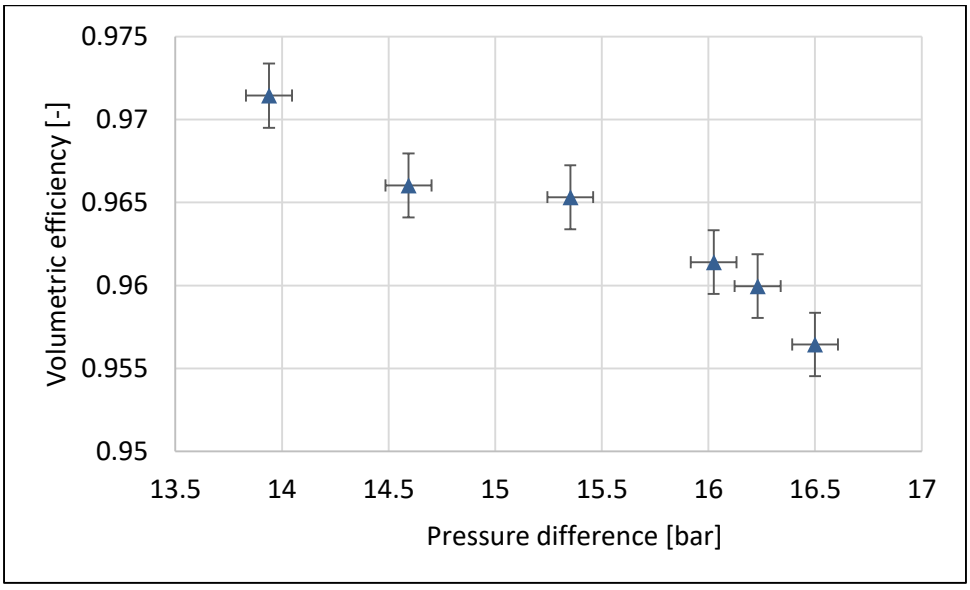

Figure 3.28: Volumetric efficiency vs. pressure difference at a pump frequency of 46.5 Hz.

According to Figure 3.28, the volumetric efficiency shows the same decreasing trend with the increase of the pressure difference. Starting from a value of 97.14 % at 13.94 bar, it goes down until 95.64 % at 16.5 bar. The variation is still very small and among high values, typical for a multi-diaphragm pump.

In conclusion, a good match between the results of this section and the ones reported by [37] may be affirmed. It is worth to underscore that both global and volumetric efficiency are strongly affected by the pressure difference. More in detail, the global efficiency shows an increasing trend with the increase of the pressure difference, while the volumetric efficiency presents a decreasing pattern. Furthermore, the global efficiency shows a strong dependence on the pump-motor speed, while the volumetric efficiency varies within the same values at each speed.

3.8.1.2 Constant pressure difference and variable rotational speed

Among the data collected for the experiments carried out and described in Constant pump speed and variable pressure difference, some points are selected in order to investigate the trend of the global efficiency at variable pump rotational speed and constant pressure difference. In present section only the global efficiency is taken into account, since, from the previous experimental sessions, no notable changes of the volumetric efficiency with the pump speed have been assessed.

Hence, as already underlined in Constant pump speed and variable pressure difference, the ranges of global efficiency variation show an increasing trend switching from lower to higher rpm. However, some particularities have been noticed in the passage from 36.6 to 46.5 Hz. Up to 36.5 Hz, a constant increase of the global efficiency range has been found, but, increasing the frequency to 46.5, no increase is registered; on the contrary, a small decrease is observed. The goal of this section is to illustrate this increasing trend and point out the deviations from the expected values.

Three different pressure differences are analysed:

- Eleven (11) bar
- Twelve (12) bar and
- Fifteen (15) bar.

Given each of these differences, points for different rpm are presented in Figure 3.29. A common increasing trend can be noticed for each pressure difference. Nevertheless, this trend reaches a peak at around 750 rpm, showing a value of about 0.47 – 0.48; then it smooths and decreases, stabilizing at around 0.45 for rpm ≥780 (for f ≥ 40 Hz). In order to explain better this behaviour, it is necessary to go deeper in how the power consumption of the electrical motor affects the measured values. A deep discussion of the measured power absorbed by the motor is presented in following section 3.9. As a first explanation, given a pressure difference, the adsorbed power by the motor is very high at low frequencies and comparable with that absorbed at f ≥ 46 Hz (≈ 1 kW). In the middle range of speeds (35 Hz≤ f ≤ 42 Hz), instead, the measured power is lower (≈600 W). This abnormal consumption at low frequencies makes the power scuttle in the middle-frequency range and is responsible for the pattern of the global efficiency described above. The peaks of the global efficiency that appear in the mid-speed range (Figure 3.29), are in perfect

correspondence with the hollow of the power consumption shown in Figure 3.32 and discussed in the next subchapter.

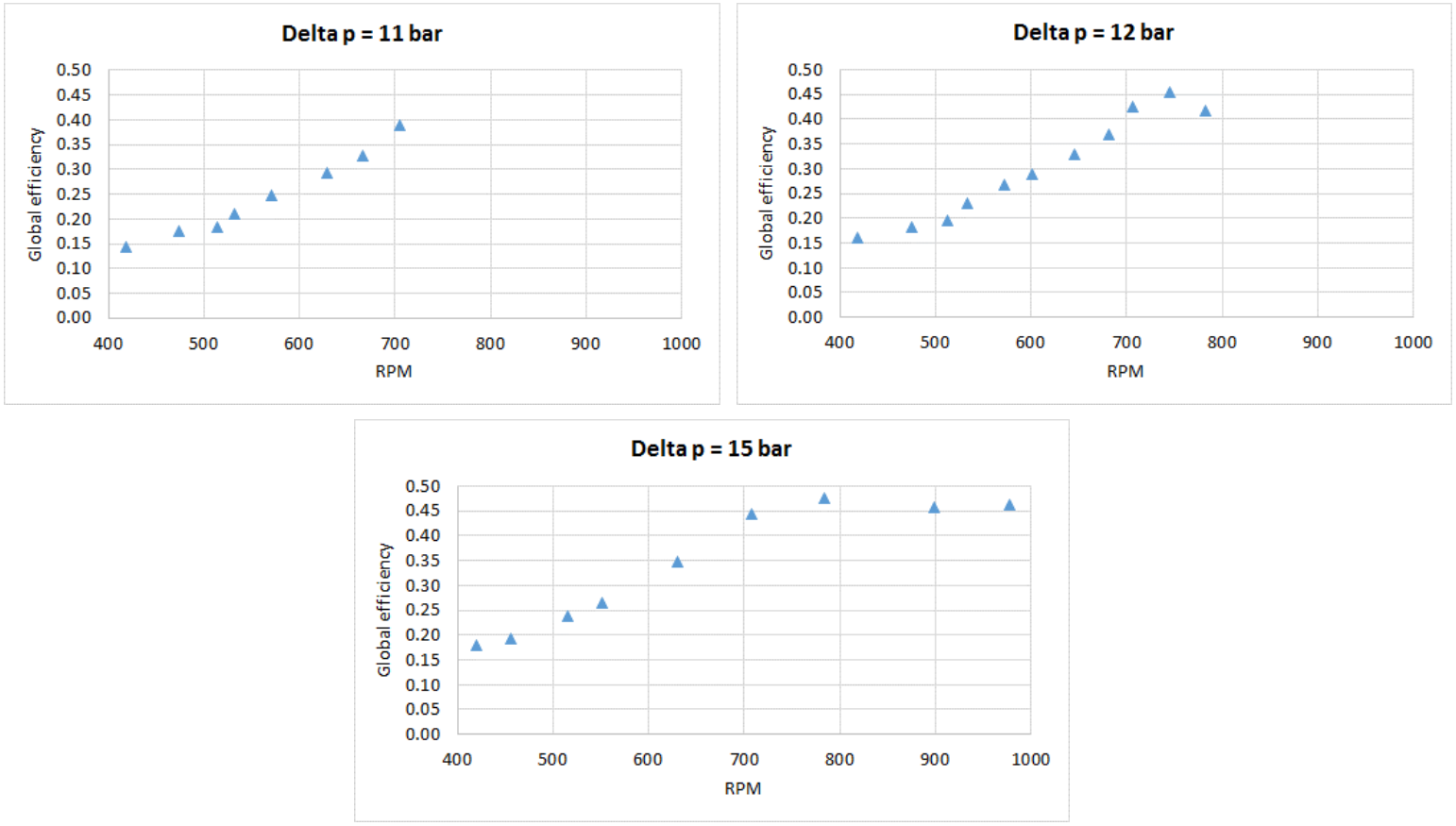

Figure 3.29: Global efficiency vs. pump speed [rpm] for three pressure differences [11, 12, 15 bar].

3.9 Analysis of motor power consumption

From the test report of the manufacturer [36], some efficiency values can be derived. In particular, the manufacturer provides some points where the motor efficiency is expressed as a function of the motor load. The latter is defined as

$$\phi = \frac{\dot{W}_{sh,calc}}{\dot{W}_{m,nom}} \quad (3.20)$$

Where:

φ = motor load

$\dot{W}_{sh,calc}$ = calculated shaft power required by the pump

$\dot{W}_{m,nom}$ = nominal power of the motor (3000 W)

Figure 3.30 shows the provided points. As it can be seen, they mainly cover the range above the 50 % load, where the motor is usually supposed to work. However, in the performed experiments, the motor is permanently working at a load ≤ 33 %. Thus, a problem arises in calculating the motor efficiency in these conditions, since no clear pattern of the efficiency vs. load can be surely determined for such low loads. At this point, it is worth mentioning that it is a usual practice in industrial applications to use oversized motors in order to ensure longer life span of the equipment and less maintenance work, compromising somewhat the efficiency of system.

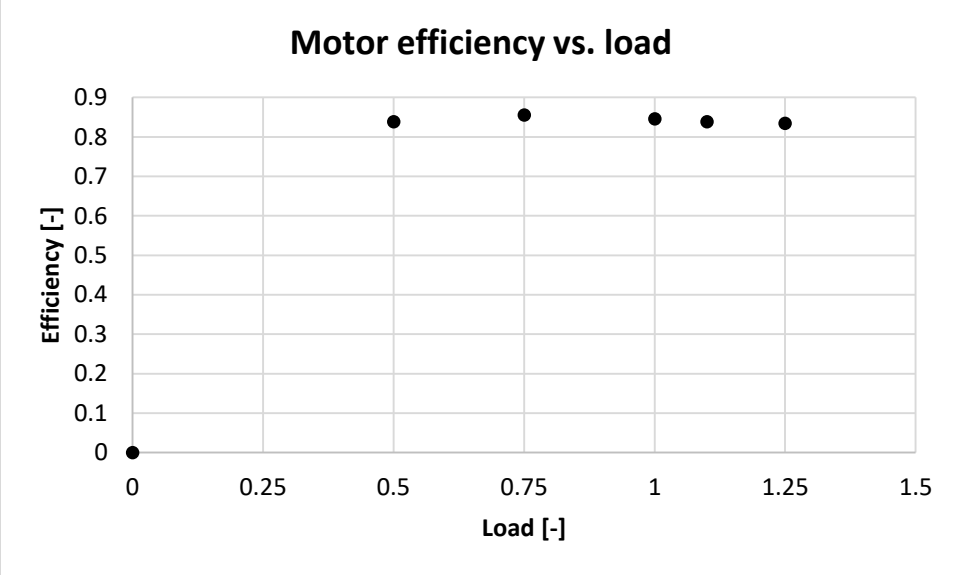

Figure 3.30: Motor efficiency points vs. load provided by the manufacturer.[36]

Furthermore, the motor efficiency is not only dependent on the load, but also on the rotational speed (rpm). Finally, the VSD control also affects the performance of the motor, since the points provided by the manufacturer are based on an inverter free operation. All the previous aspects contribute in a very complicated determination / estimation of the motor efficiency.

The dependence of the motor power consumption on pressure difference and rotational speed are here investigated. The load of the motor is calculated as the ratio between the pump shaft power ($\dot{W}_{sh,calc}$ – Equation (2.4)) and the nominal electric power of the motor ($\dot{W}_{m,nom} = 3000\,W$). The shaft power derives in turn from the hydraulic power after the addition of the pump losses. The hydraulic power delivered to the fluid by the pump is:

$$\dot{W}_{hyd} = \dot{V}\Delta p \qquad (3.21)$$

where $\dot{V}$ is the volume flow rate and Δp the pressure difference.

Therefore, the motor load is directly connected to the pressure difference and it is worth analysing its influence on the measured power consumption. In Figure 3.31 the trend of the electrical power with the pressure difference is illustrated for four different pump speeds: 418 rpm (21 Hz), 513 rpm (26 Hz), 705 rpm (36 Hz) and 897 rpm (46 Hz).

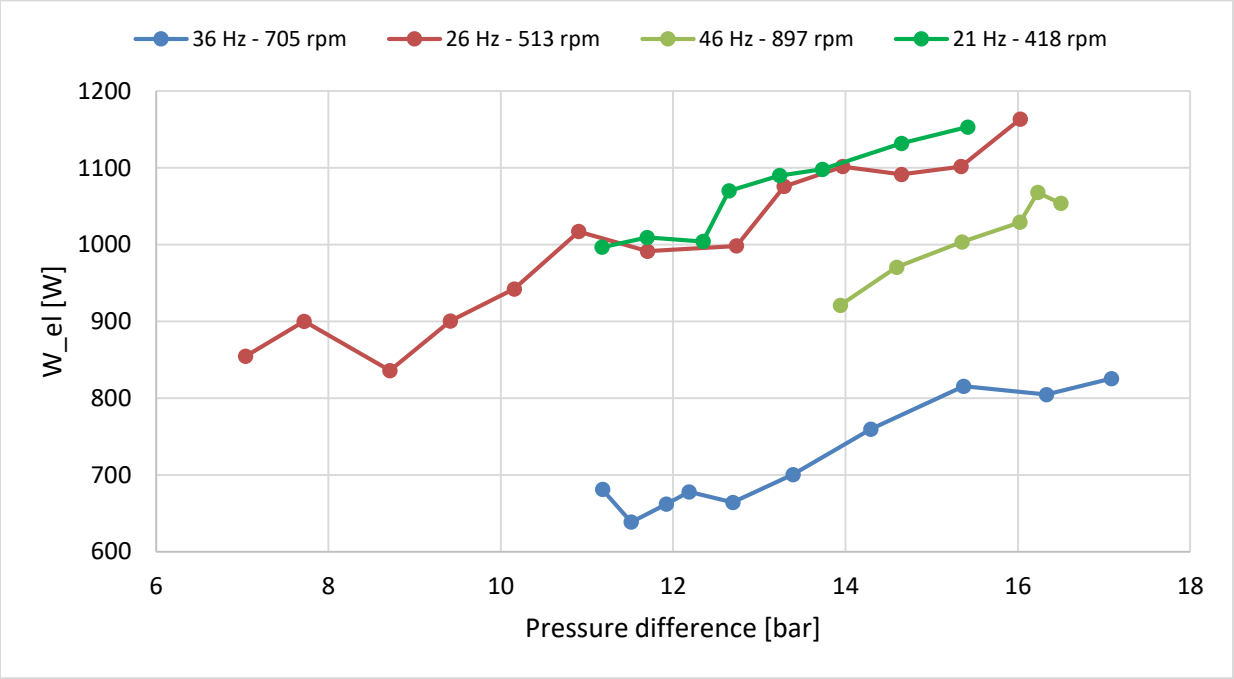

Figure 3.31: Motor consumption [W] vs. pressure difference [bar] for four different pump speeds: 418, 513, 705, 897 rpm.

For each rotational speed, a clear increase of the power with the pressure difference is shown. This is an expected result since, for higher pressure differences, the hydraulic power is higher; consequently, the shaft power increases and, going up the chain of the pump system, the power input of the motor increases as well. Nevertheless, a strange behaviour is noticed when switching from a speed to another.

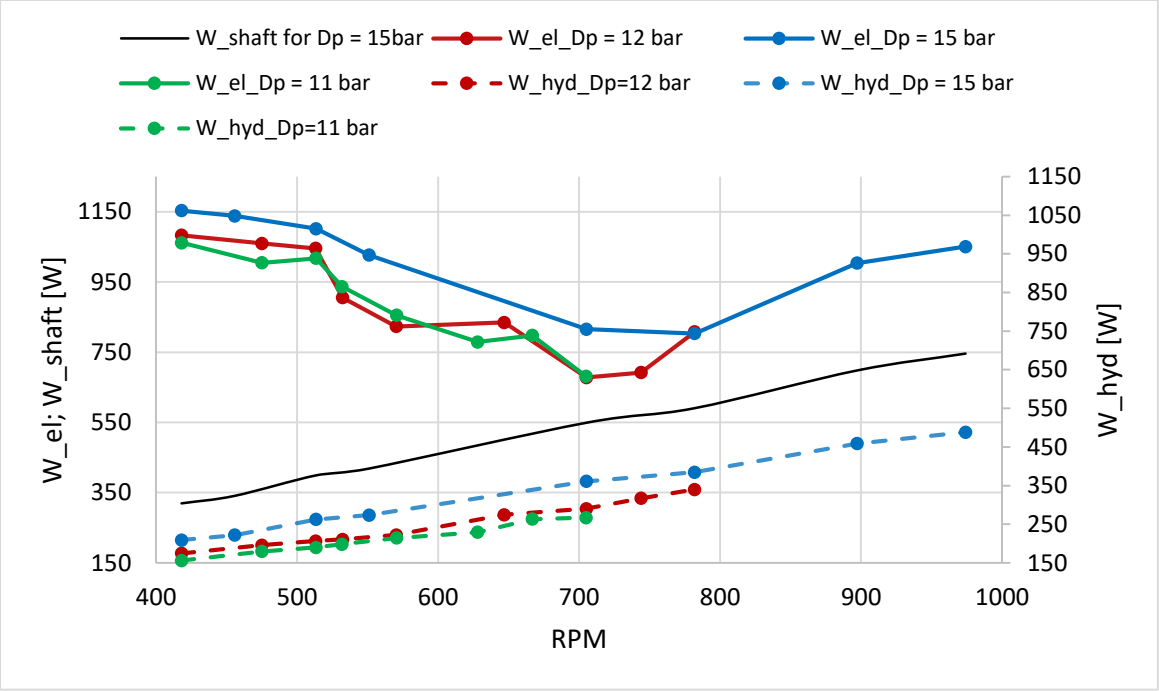

Figure 3.32: Experimental power consumption W_{el} [W] and hydraulic power [W] vs. rotational speed [rpm] for three different pressure differences: 11, 12 and 15 bar.

Instead of showing an increasing trend when switching from a lower to a higher frequency, the highest consumption is found for the lowest speeds: 418 and 513 rpm. With the experimental points at 36 Hz a sharp decrease of the consumption is shown, since they are placed in the lowest part of the diagram. Going up towards the nominal speed of the motor (50 Hz), the power increases and is placed around the reasonable value of 1000 W. In order to investigate better this anomaly, the influence of the speed on the power consumption is illustrated in Figure 3.32.

The hydraulic power shows an increasing trend with the rpm. Figure 3.32 shows a direct proportionality between rpm and volume flow rate, hence, if the speed increases, the volume flow rate increases with a linear trend and, from equation (3.21), the hydraulic power increases with the same linear trend as well. Switching from a lower (12 bar) to a higher pressure difference (15 bar), the correspondent power line goes over the previous one, showing a higher hydraulic power, as expected from equation (3.21). However, the increasing trend of the hydraulic power is not kept for the motor power consumption. An abnormal hollow is registered indeed in the range 650 ÷ 800 rpm. Note that only the points with a pressure difference of 15 bar cover all the speed range. Due to a lack of experimental points, the other two pressure differences miss some higher rotational speeds; nonetheless, the same trend is easily recognizable. In Figure 3.29, a peak for the global efficiency was observed around the rotational speed of 750 rpm, as already explained in the previous subchapter. This trend agrees with the electric power consumption of the motor versus the rotational speed shown in Figure 3.32, where a hollow in the mid-range of 700-800 rpm can be seen. The hydraulic power delivered to the fluid by the pump increases linearly with the rotational speed and the pressure difference, being defined as the product between volume flow rate ($\dot{V}$) and pressure difference (Δp). Indeed, the volume flow rate is a linear function of the rotational

speed (rpm), as appears from the curves provided by the manufacturer (Figure 2.7). The shaft power required by the pump is not directly measured but is evaluated by equation (2.4) provided by the pump manufacturer [36]. This power shows a similar trend (linear) to the hydraulic power, as expected (see the black line in Figure 3.32 (above), where the only curve at Δp=15 bar is shown for clarity). The electric power consumption of the pump system (W_{el}) shows instead a minimum around 700 rpm for every value of the pressure difference, due the decreasing efficiency of the motor at lower load. It is worth reminding that the motor works at loads lower than 33 % in each test, with the consequent efficiency penalty. Moreover, the effect of higher order harmonics on the motor generated by the VSD is not considered. On the other hand, the manufacturer of the energy meter ensures accuracy for AC currents above 35 Hz.

As it can be understood from Figure 3.32, the motor consumption is strongly affected by the rotational speed. As a result, the motor efficiency, (Figure 3.30) changes with the rotational speed.

3.10 Cavitation test campaign of the multi-diaphragm pump

As already mentioned, in order to address the cavitation phenomena, the thermal subcooling strategy was adopted and a sub-cooling heat exchanger was installed in the suction line of the ORC pump downstream of the liquid receiver (Figure 3.33) and before the suction inlet of pump. Since, partial or full cavitation phenomena affect dramatically the system performance, a comprehensive cavitation test campaign was designed and carried out. The outcomes of the aforementioned test campaign were used also, as important design, diagnostic & control parameter during the last evolution stage of the experimental test unit, where the unit is able to operate in full automated mode.

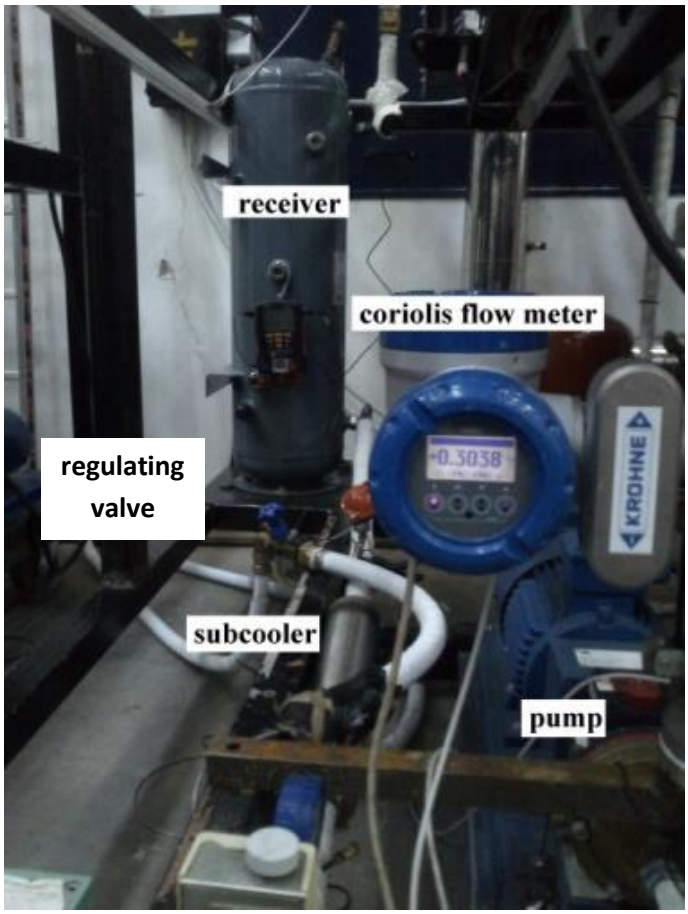

Figure 3.33: Overview of the pump-subcooler setup in experimental ORC unit (cold water supply from external HP arrangement).

Therefore, four cavitation tests have been performed by enforcing cavitation conditions on different operational conditions of the system.

For each test, the operational conditions of the system and the procedure to achieve cavitation are here briefly described:

A. Full load operation at nominal conditions (2 scroll expanders running): f = 50 Hz, scroll rpm = 1450, p_{max}=23.8 bar, T_{max}=83.7 °C; Cavitation induced by increasing the cold water temperature.

B. Full load operation at nominal conditions (2 scroll expanders running): f = 50Hz, scroll rpm = 1500, p_{max}=23 bar, T_{max}=82 °C; Cavitation induced by reducing the cold water flow.

C. Partial load operation at nominal conditions (2 scroll expanders running): f = 41.5 Hz, scroll rpm = 1300, p_{max}=22 bar, T_{max}=82 °C; Cavitation induced with both the increase of the water temperature and the regulation of the valve in the subcooling line.

D. Partial load operation at nominal conditions (1 scroll running): f = 28.5 Hz, scroll rpm = 1450, p_{max}=25 bar, T_{max}=82 °C; Cavitation induced with both the increase of the water temperature and the regulation of the valve in the subcooling line.

In the next three sections (3.10.1-3.10.1.3), the main results for each test are presented and analysed in detail.

In the present work, the criteria used for cavitation detection is a 5 % volumetric flow drop. The drop is considered with reference to the volumetric flow rate derived by the experimental characteristic curve of the pump (Volume flow vs. rpm) presented in Section 3.7and shown in Figure 3.18.

3.10.1 Cavitation tests at the pump frequency of 50 Hz

The first two performed tests refer to a nominal operation of the experimental ORC test rig: both scroll expanders are working at the speeds of 1450 and 1500 rpm and the pump is running at the motor nominal frequency of 50Hz. In the first test, cavitation is enforced by varying the temperature of the cold water supplied by the external heat pump. In the second test, instead, the water temperature is kept constant and cavitation conditions are achieved and controlled by means of the regulating valve in the subcooling line. Carrying out the tests at nominal conditions allows deriving important guidelines about the $NPSH_a$ that needs to be fulfilled in order to ensure stable operation. The right magnitude of $NPSH_a$ enables the system setup to work for a long time in the same nominal conditions, as it is expected from a micro-scale ORC system.

3.10.1.1 Nominal operation: f = 50 Hz – scroll rpm = 1450 – variable cold water temperature (test A)

During test A, the regulating valve of the subcooling line is kept fully opened, while the only parameter that varies is the temperature of the cold water. The temperature set point of the external heat pump is changed and this variation imposes a different degree of subcooling. At the beginning of the test, the temperature is set at 5 °C in order to reach the maximum subcooling degree. In this way, the term P_{vp} of the $NPSH_a$ equation (Equation (3.1)) is minimized and, considering constant values for the other three terms, the $NPSH_a$ is maximized. Starting from this point, the temperature is gradually increased, in order to

reduce the $NPSH_a$ until cavitation occurs. For this purpose, the temperature of the cold water is changed from 5 °C to 16 °C. At the highest temperature (16 °C), the flow rate starts dropping at a $NPSH_a$ threshold equal to 9.03 mH_2O. Thus, if the temperature drop in the subcooler does not provide a $NPSH_a$ that exceeds this threshold, cavitation may occur affecting the operation of the whole system. Figure 3.34 shows the results of this test.

While increasing the water temperature, that is reducing gradually the $NPSH_a$, the volume flow rate decreases slowly until it reaches the threshold of a 5 % flow rate drop. From this point on the pump is no more able to keep up the system and inevitably, prominent cavitation develops. The flow rate is now subjected to a sharper drop, as the point ($NPSH_a$ = 8.09 mH_2O; relative vol. flow = 0.758) witnesses. For the examined procedure of decreasing the subcooling degree and for this operational speed of the pump (50Hz), the pump shows a $NPSH_a$ threshold of about 9 mH_2O. As it will be shown next, this threshold value depends on the rotational speed and the operating conditions of the pump.

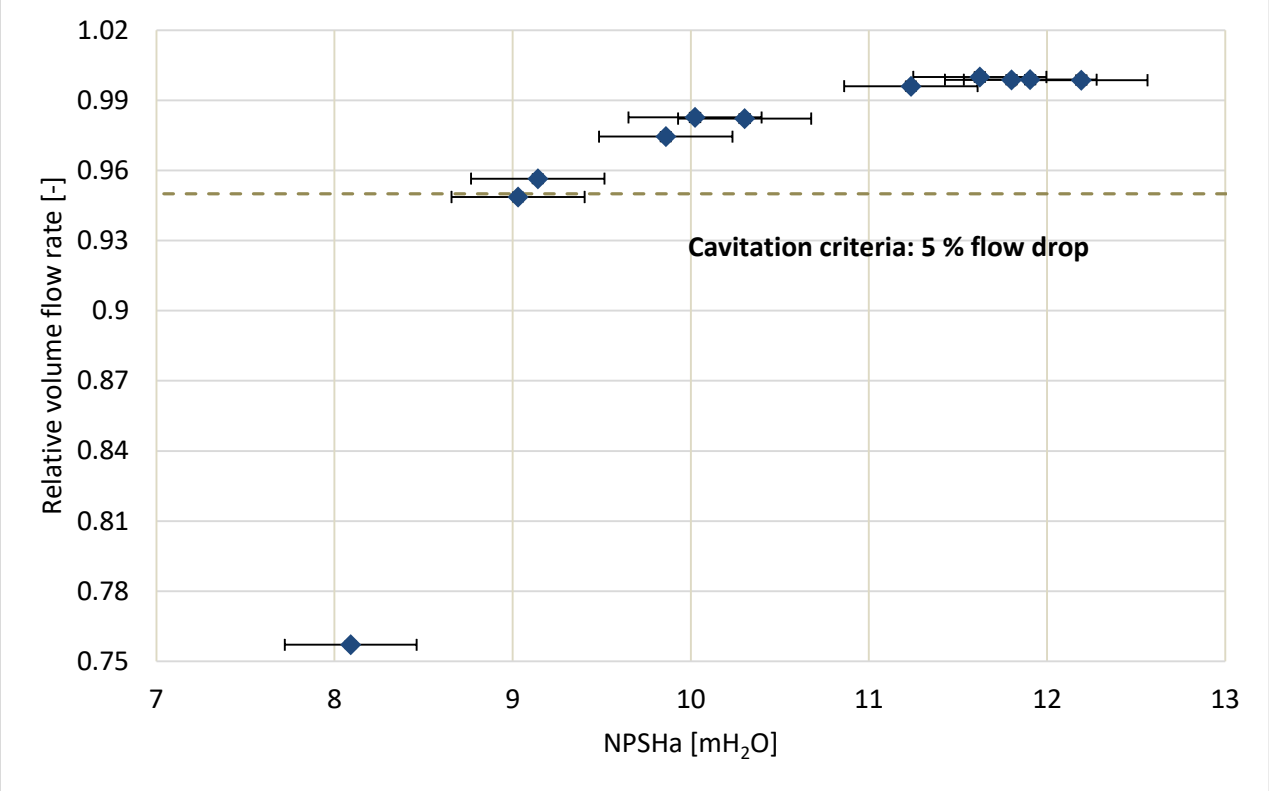

Figure 3.34: Relative volume flow rate vs. $NPSH_a$ at f=50 Hz. Results for nominal conditions of the system and variation of the subcooler water temperature.

3.10.1.2 Nominal operation: f = 50 Hz – scroll rpm = 1500 – variable subcooling water flow (test B)

From test B and on, the procedure of varying the water supply flow rate to the subcooler has been applied. This is achieved by opening/closing the regulating valve placed in the subcooling line that goes from the heat pump to the heat exchanger. The cold-water temperature is set to 9 °C and at the beginning, the valve is fully open allowing the maximum water supply flow to the subcooler. Afterwards the valve is closed step by step and the water temperature is kept at the initial set value. Between two consecutive closing actions, the system is let reaching an intermediate steady state point. Figure 3.35 shows the points collected during this second test.

Figure 3.35 highlights a $NPSH_a$ threshold of about 7.85 ÷ 8.1 mH_2O before cavitation occurs sharply, implicating strong effects on the delivered volume flow rate of the pump. Unlike Figure 3.34, all points before cavitation occurrence appear in a much narrower range of $NPSH_a$: from 8.3 to 8.7 mH_2O. In Figure 3.34 instead, these correspondent points are spread in a wider range: from 9 to 12.2 mH_2O. The reason for this difference could be acknowledged to the different procedure adopted for decreasing the subcooling degree which in the first case starts from a more favourable point (cooling water at 5 °C - full flow) compared to the second case (cooling water at 9 °C - full flow). In this context, as a remark it can be stated that, since P_{vp} is the most influencing parameter in the calculation of $NPSH_a$, a change in the pump inlet temperature through the variation of the subcooling degree affects strongly the $NPSH_a$.

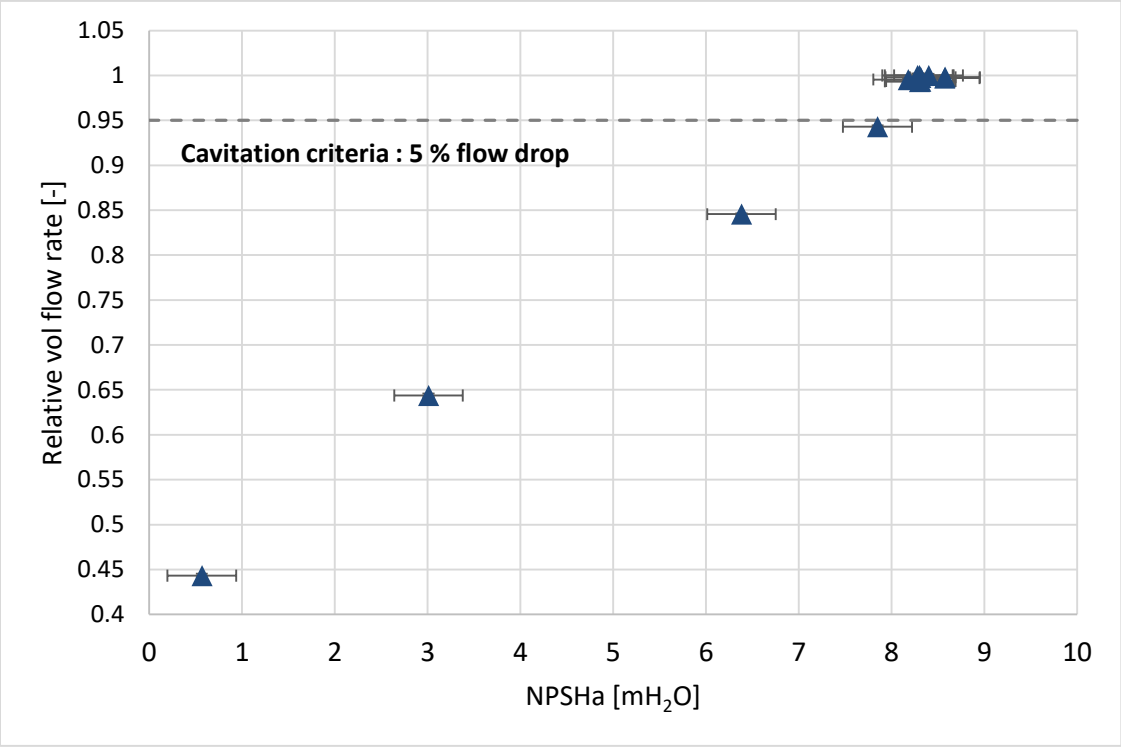

Figure 3.35: Relative volume flow rate vs. $NPSH_a$ at f=50 Hz. Results for nominal conditions of the system and subcooling degree variation by means of a regulating valve.

As already mentioned, in the first test (section 3.10.1.1), the initial set temperature for the cold water is 5 °C instead of 9 °C and this contributes to broaden the range of NPSH, achieving higher values. Moreover, in the second test, the adjustments on the regulating valve do not produce steady state conditions that, in terms of $NPSH_a$, can be clearly distinguished from each other. It should be noted that this is the case only for the cavitation-free area of the diagram. Therefore, this means that closing the valve does not produce relevant temperature increases and does not allow for an appreciable separation between the points. On the other hand, a gradual variation of the water temperature (Test A) is a more effective way to obtain clearly separated points (Figure 3.34).

Looking closer at Figure 3.35, the decrease of the volume flow rate below the cavitation threshold follows a linear path. From the experimental points, it is indeed clear how they lay on a straight line while the flow rate is constantly decreasing from the threshold value. This would mean that, when cavitation occurs for this multi-diaphragm pump, the flow rate is not abruptly brought to a minimum value but it has a stepped decrease. Even though the phenomenon is very fast, it is quite gradual allowing for corrective adjustments from the side of the control system to prevent the full development of cavitation and restore the stable operation of the system before it reaches the critical point of cavitation where the whole system collapses. This remark is further analysed in the next section 3.10.1.3.

A similar experimental procedure has been carried out in the study of Declayé [37]. The comparison is allowed by the same operating conditions in which the Declayé's test and the tests A. and B. are performed. Cavitation is indeed enforced during nominal operation of the system, with a frequency of the pump set to 50 Hz. However, the multi-diaphragm pump tested in [37] delivers a smaller volume flow rate (up to 11.3 lt/min) and handles a different fluid (R245fa). Moreover, its $NPSH_r$ is 3.5 mH_2O, which is lower than that one of the pump analysed in this work (5 mH_2O). The experimental results obtained in [37] are illustrated in Figure 3.36.

As it can be easily noticed, the criteria used in [37] to detect the occurrence of cavitation is a 3 % volumetric flow drop. A similar trend of tests A. and B. is found in Figure 3.36. Looking at the pattern of the multi-membrane pump, the threshold for NPSH available is placed between 4.95 and 5.2 m. Indeed, a sharp decrease of the flow is noticed in this zone. The necessary $NPSH_a$ is therefore lower in [37] than in tests A. and B., where the values for the $NPSH_a$ threshold are 9 and 7.9 mH_2O, respectively. This difference could be attributed to the different fluid and pump model used in [37], as well as to the different ORC setup in which the pump is tested. Furthermore, unlike Figure 3.35, inFigure 3.36 only two points below the cavitation threshold are presented. Thus, the fast but gradual decrease of mass flow rate below the threshold (found in Figure 3.35) does not find support in Declayé's analysis. This behaviour is further analysed in following sections (3.10.2.1-3.10.2.2) where during the two tests (tests C. and D.), many more points under the threshold have been collected.

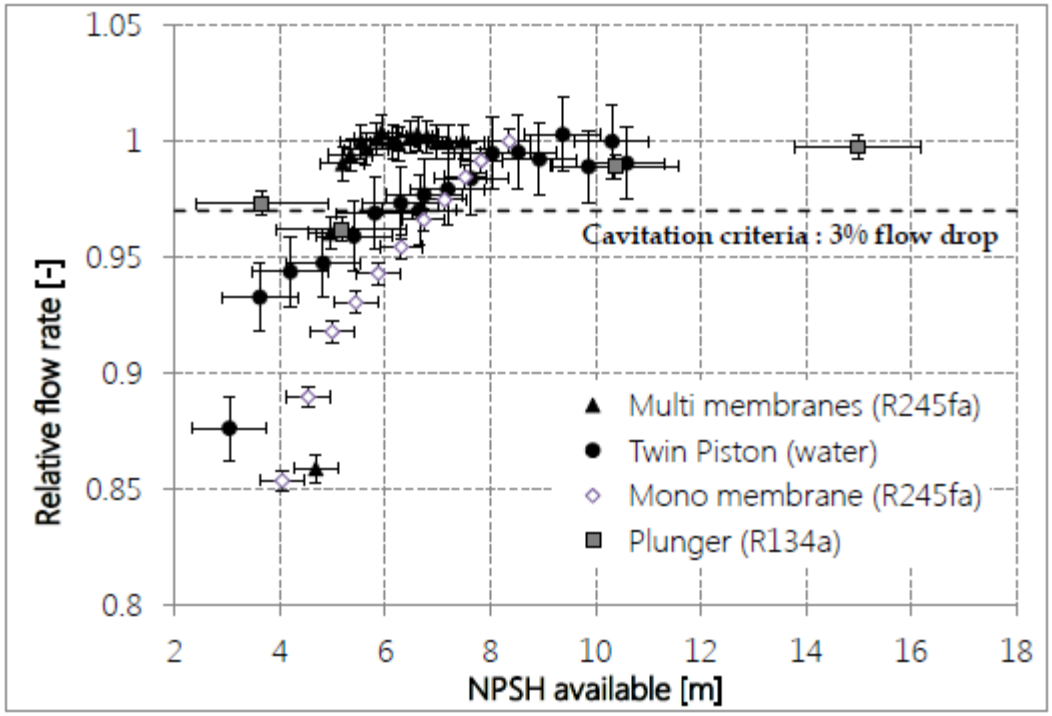

Figure 3.36: NPSH of different types of pump at nominal speed.[37]

3.10.1.3 Restoring stable operation after cavitation occurrence

In this section, a further analysis of the second experiment is carried out on the following basis: After deep cavitation conditions have been achieved, stable operation is restored before a new cavitation condition is imposed.

Figure 3.37, Figure 3.38, Figure 3.39 and Figure 3.40, illustrate the trends of the main parameters during stable operation, occurrence of cavitation, transition recovery phase and the re-established stable operation after the recovery of the system, respectively.

The recovery of the system from the first cavitation conditions is accomplished by fully re-opening the subcooling valve in a single step. After the latter action, the system goes through a transient phase where oscillating behaviour of the main parameters is recorded. In the next moments, the system reinstates its stable operational.

The previous figures present a time frame that ends up in the same moment, when new actions are taken to cause a new cavitation event. As it will be observed, this period is not sufficient for the system to fully reach steady state conditions.

In the first points, when the adjustment of the valve (closing) is applied, an evident increase of the temperatures is registered (Figure 3.37). By reducing the subcooling degree, the pump inlet temperature is the first parameter subjected to an increase and consequently it is conveyed to the following temperatures at the pump outlet and after the condenser. The increase of the inlet temperature entails an increase of

the saturation pressure at this temperature (P_{vp} in Figure 3.38) and hence a decrease of the $NPSH_a$. A 5 % drop of the volume flow rate means a decrease of the mass flow rate from 0.3987 kg/s at stable conditions to 0.379 kg/s at the cavitation threshold.

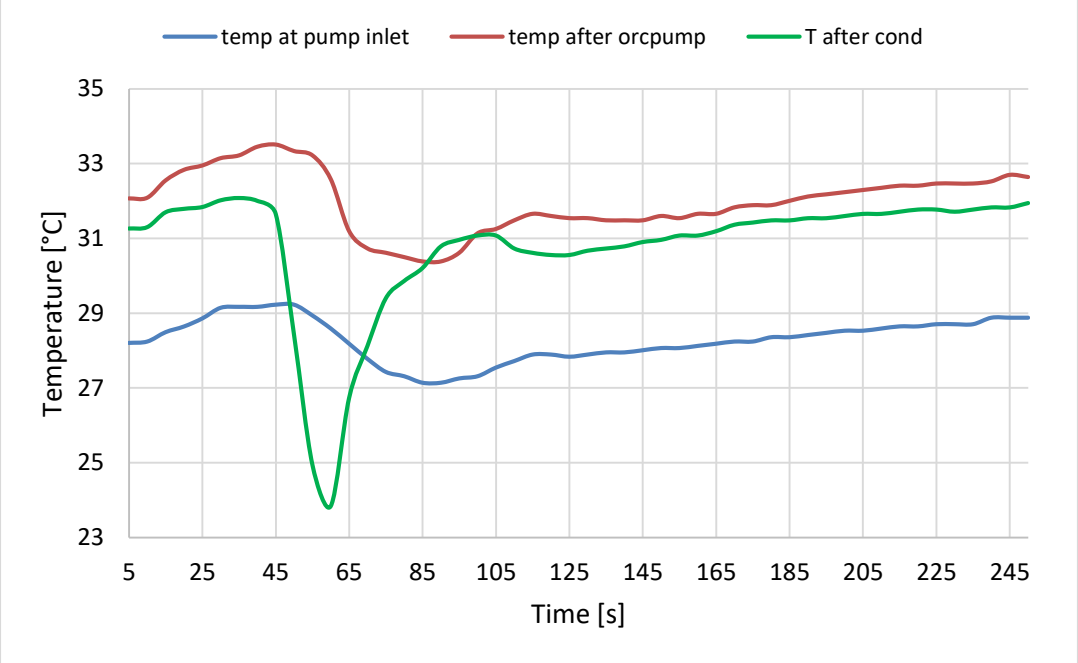

Figure 3.37: Temperatures after the condenser, at the pump inlet and outlet during the cavitation process.

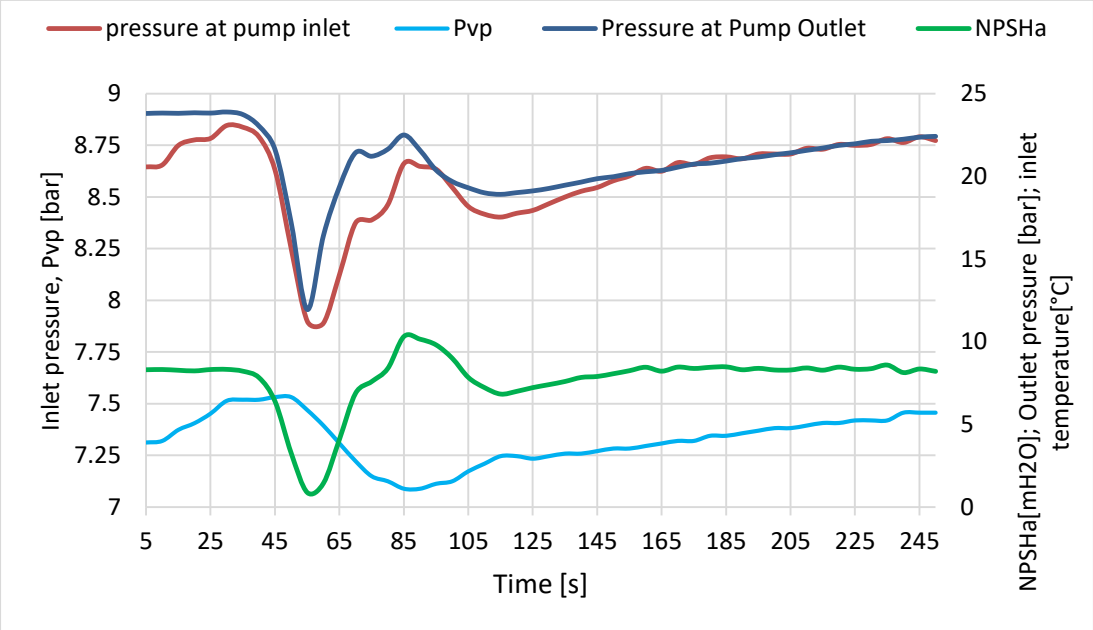

Figure 3.38: Pressures during the cavitation process.

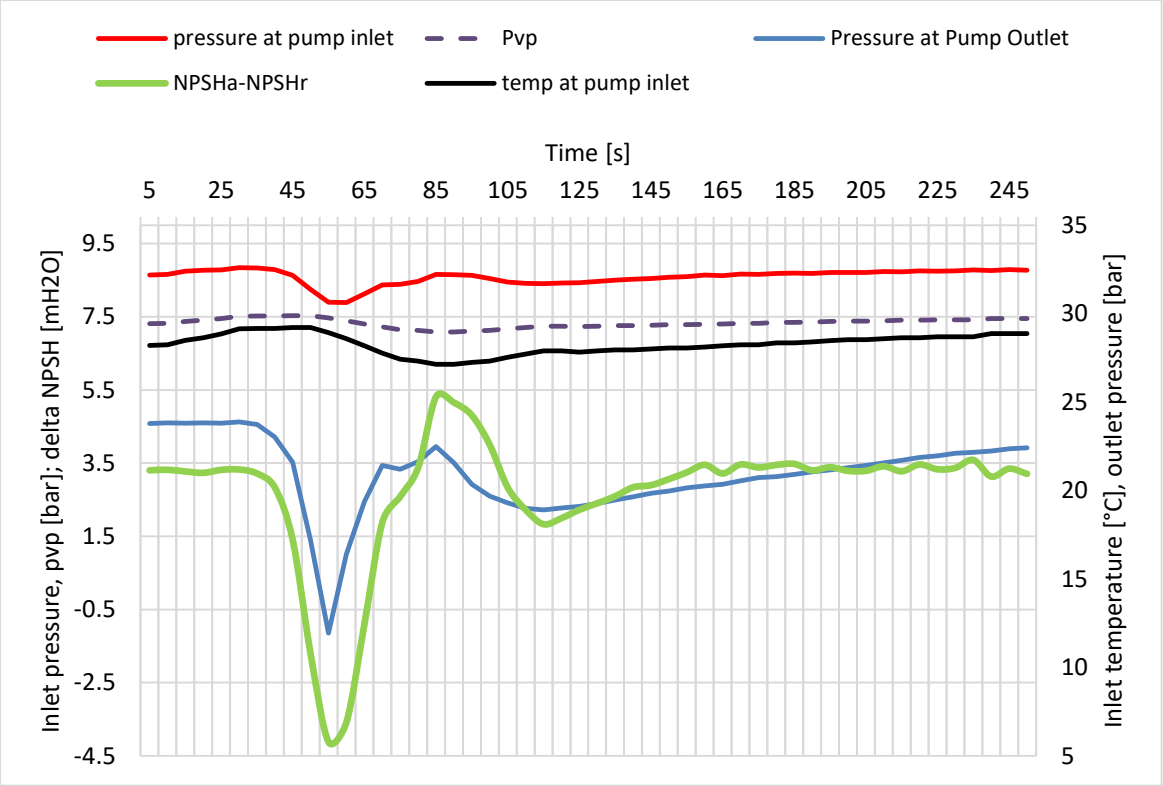

Figure 3.39: Comparison between pressures and temperatures during the cavitation process.

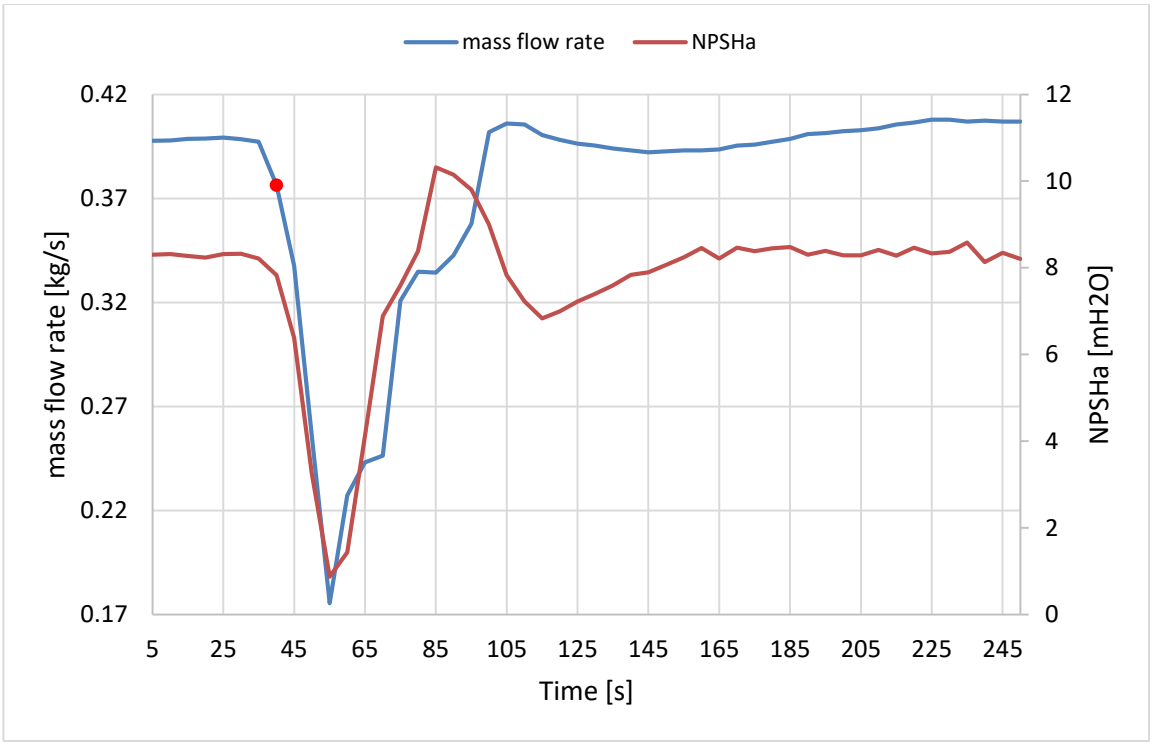

Figure 3.40: Mass flow rate [kg/s] and $NPSH_a$ [mH_2O].

In Figure 3.40, a point (red dot) from the data set immediately below the threshold (0.376 kg/s), has been pointed out. Up to this instant (t=40 sec), the $NPSH_a$ slowly decreases, while the mass flow rate starts dropping from the previous sampled value (t=35 sec, $\dot{m}$=0.3972 kg/s) with a steeper slope. From this point on, both the $NPSH_a$ and the mass flow rate drop strongly with the same slope and cavitation conditions are fully developed. The fall of the $NPSH_a$ (and that of the mass flow) are well synchronized with the decreases of both inlet and outlet pressure (Figure 3.38). Precisely, the inlet pressure reaches the minimum value 5 sec later (t=60 sec) than the outlet pressure and $NPSH_a$ (t=55 sec). This delay is reset during the next transitional and oscillating phase of the system recovery. The receiver is the major responsible for this small time lag due to its damping action. Although, mass flow rate and outlet pressure have already reached their minimum value, the receiver feeds the pump with a pressure value that is higher than its minimum value. In other words, it needs some time to adapt its pressure (and hence the pump inlet pressure) to the big falls of the mass flow rate and maximum pressure of the whole system. Furthermore, it is interesting to notice how a fall of the inlet pressure of about 1 bar (from 8.79 to 7.88 bar) propagates through the pump and results in a much bigger fall of the outlet pressure (from 23.73 to 16.4 bar = 7-bar fall). This effect appears as a consequence of the drop of the mass flow rate: due to cavitation occurrence, the pump is no more able to raise the pressure of such an amount of fluid that can keep up the system. Thus, along with the drop of the mass flow rate, the outlet pressure drops sharply up to t=55 sec, when the mass flow starts increasing again. The strong decrease of the mass flow rate is transmitted to every component of the system and reaches in a while also the condenser. Figure 3.37 shows clearly how, with a slight delay (5 sec), the temperature after the condenser starts dropping. The mass flow rate is indeed so small that, given the same supply of cooling water to the condenser, its temperature is greatly reduced.

When, at t=55 sec, the mass flow rate reaches the minimum value, the subcooling valve is immediately fully opened. This action results in a sudden increase of the $NPSH_a$ that continues to be perfectly synchronized to the inlet and outlet pressure, following a similar trend in the same time intervals (Figure 3.38). Figure 3.40 shows the time lag between the upturn of the mass flow rate in comparison to that of the $NPSH_a$. Moreover, $NPSH_a$, inlet and outlet pressure reach suddenly the highest peak, while the increase of the mass flow rate is more gradual.

At this point, it is worth underlining the considerable time lag of the inlet and outlet temperature compared to the occurrence of the cavitation phenomenon. Indeed, looking at Figure 3.38 and Figure 3.39, the minimum value for the inlet and outlet temperature is reached in correspondence to the highest peak reached by $NPSH_a$ and the pressures when the restoring phase of the system has already started. In particular, the pressures and the $NPSH_a$ reached their minimum at t=55 sec while the temperatures at t=85 sec, revealing a time delay of about 30 sec. The same behaviour is registered for the trend of the saturation pressure (P_{vp} –Figure 3.38), since it is dependent on the inlet temperature variation and follows faithfully its pattern. This 30-second delay is caused once again by the presence of the receiver. The inlet temperature starts to decrease after that the receiver is cooled down. This process is slow due to the low mass flow rate circulating in the system as cavitation fully develops, even though the refrigerant temperature at the condenser outlet drops dramatically. When eventually the receiver starts feeding the pump at a lower temperature, $NPSH_a$ rises strongly and reaches a maximum in correspondence with the minimum value

reached by the inlet temperature. This steep increase allows the system to recover, bringing mass flow and pressures back to higher values that, although instable, oscillate around the nominal conditions.

After the sudden increase of the $NPSH_a$, the system goes through a transient phase towards a new stable condition. In this phase, abrupt oscillations of the pressures and $NPSH_a$ are noticed, while smoother ones are observed for the mass flow rate. At t=160 sec, $NPSH_a$ settles at around 8 mH_2O that was the same value of the stable operation before the cavitation occurrence. Pressures and temperatures start a slow and continuous increase that does not stabilize yet in the presented time frame. On the other hand, the mass flow rate shows wide and smooth oscillations, reaching, at t=225 sec, a slightly higher value than the one before cavitation. Since a stable operation is not reached at the end of the time span, this higher value of mass flow rate is probably still part of a further oscillation. During the cavitation phenomenon, the maximum temperature and pressure of the ORC system have reached values far away from the stable ones. In particular, the maximum pressure (pump outlet pressure) has dropped as described previously, while the maximum temperature has increased because the natural gas boiler continues to deliver the same amount of heat to a much lower mass flow rate of the working fluid. Thus, until these two parameters do not reach again the first stable values and bring back the system to a new steady state condition, the mass flow rate will not reach the nominal value and will be always within a low amplitude slow oscillation. Referring to the period after t=225 sec, the mass flow rate tends progressively to reduce its value from the highest reached values ($\dot{m}$=0.4078 kg/s) to the first nominal values of 0.398 kg/s.

3.10.2 Cavitation tests at lower pump rotational speeds

For the last two remaining tests, a combination of the control strategy developed in the previous two tests (A and B) has been adopted in order to adjust the subcooling degree. First, the temperature of the subcooling water is increased and second, adjustments on the regulating valve and hence to the cooling water flow are applied. The purposes of combining the two actions are mainly the following ones:

- Enlarge the range of the $NPSH_a$ above the cavitation threshold. This means approaching to the first test conditions in order to imitate the slow decrease of $NPSH_a$ from higher values towards the threshold one.
- Achieve a finer regulation under the cavitation threshold by adjustment of the subcooling valve. This means trying to collect more points during the cavitation phenomenon that is usually characterized by a very sudden drop of the delivered flow rate.

3.10.2.1 2-scroll generating mode – f = 41.5 Hz - scroll rpm = 1300 – variable flow rate and temperature of the subcooling water (test C)

During test C, the system is still in full-power-generation mode (both scrolls are running), but at lower load, since the pump frequency is set to 41.5 Hz and the speed of the scrolls to 1300 rpm. The points acquired for the cavitation phenomenon in this system configuration are presented in Figure 3.41.

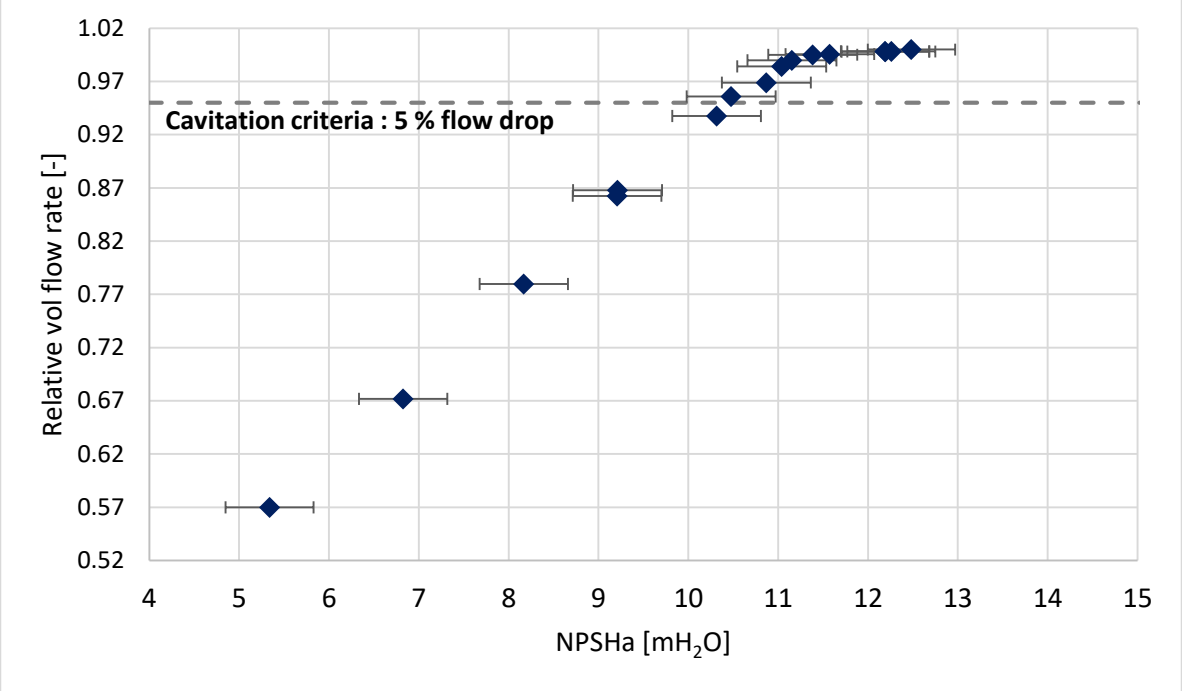

Figure 3.41: Relative volume flow rate vs. $NPSH_a$ at f = 41.5 Hz - Subcooling degree variation by means of regulating valve and change of water temperature.

In comparison with Figure 3.34 and Figure 3.35, Figure 3.41 shows that cavitation starts at $NPSH_a$ = 10.4 mH_2O, which is higher than 9 and 7.9 mH_2O in tests A. and B., respectively. Moreover, the combination of the two actions for the reduction of subcooling shows the desired results: the $NPSH_a$ range above the threshold is higher than that of Figure 3.35 and many more points are collected below the threshold, when the cavitation phenomenon is fully developed.

Once more, an almost linear decrease of the flow rate can be identified starting from the threshold and going deeper in the cavitation region.

3.10.2.2 1-scroll generating mode – f = 28.5 Hz - scroll rpm = 1450 – variable flow rate and temperature of the subcooling water (test D)

A partial load operation of the system was examined in this last test. Since only one scroll is running, the frequency of the pump needs to be lower than in the previous ones; hence, it is set to 28.5 Hz. However, the working conditions of the scroll resemble the nominal conditions, because its inlet pressure and temperature are set to 25 bar and 82 °C respectively and its rotational speed is set at 1450 rpm. Similarly to previous test C (section 3.10.1.2), a combined strategy to control the subcooling degree is also applied in this test. The interesting points collected while testing this system configuration are presented in Figure 3.42.

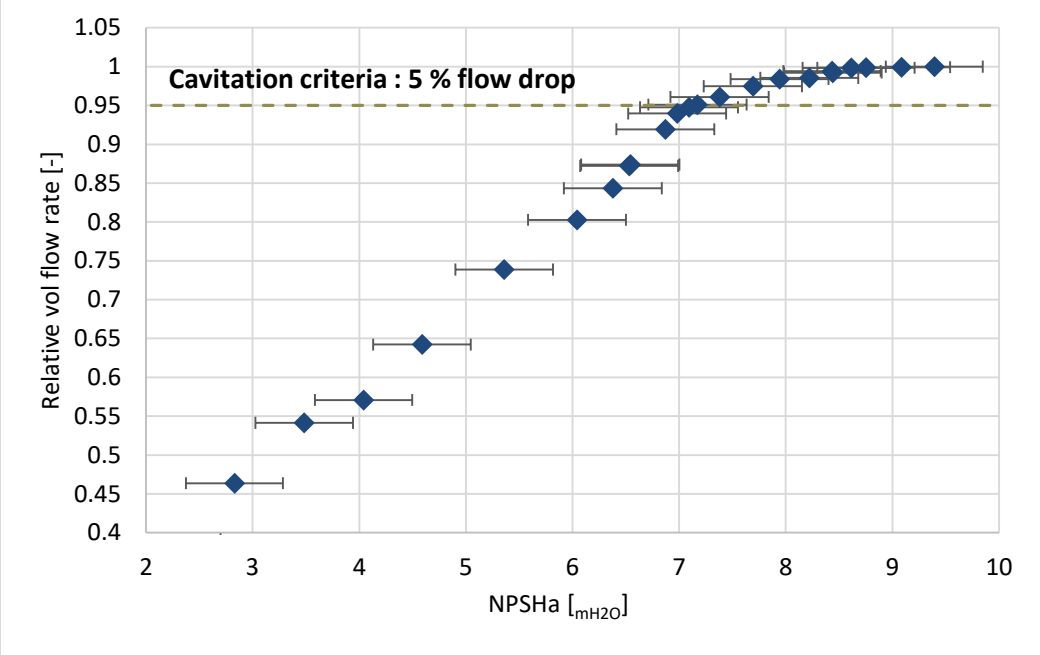

Figure 3.42: Relative volume flow rate vs. $NPSH_a$ at f = 28.5 Hz - Subcooling degree variation by means of regulating valve and change of water temperature.

As previously hinted, the most interesting results are obtained in this test by using the combined strategy to control the subcooling. In above Figure 3.42, a good range of $NPSH_a$ has been achieved and thus, investigated above the cavitation threshold and a good amount of points can be noticed also below the cavitation threshold. These points maintain an almost linear pattern, hence, as already underlined in the previous tests, the decrease of the flow rate is fast but not sudden and abrupt. Before reaching the minimum sustainable value that prevents the system from collapsing, many intermediate points are registered. Unlike the results reported by Declaye [37] in Figure 3.36, more points are also reported between the threshold and the 85 % of volume flow rate, showing a more stepped and predictable direction of decrease.

Cavitation starts at an $NPSH_a$ value between 6.87 and 7.38 mH_2O, which is lower than the respective values obtained in the previous tests. This observation supports what has been pointed out by D'Amico,

Pallis, et al.in [47] and among the conclusions of Leontaritis, Pallis, et al. reported in [55]: higher rotational speeds encourage cavitation occurrence. The latter conclusions were thoroughly defined at section 3.1 as a result of the first experimental campaign of the ORC test unit.

According also to the respective curves provided by the manufacturer (Figure 3.1), the required NPSH increases for higher rotational speeds, and therefore the available NPSH should also be higher in order to avoid the occurrence of cavitation. Nevertheless, a distortion is found while comparing the tests at f = 41.5 Hz and at f = 50 Hz. As a matter of fact, $NPSH_a$ should be higher at f = 50 Hz than at f = 41.5 Hz but, comparing Figure 3.41 with Figure 3.35, an opposite behaviour is noticed. The NPSH threshold for f = 50 Hz is 8 mH_2O, while the one for f = 41.5Hz is 10.48 mH_2O, which is higher instead of lower. In general, some inaccuracies could influence the computation of $NPSH_a$: errors in the temperature measurements in the range of 0.5 to 1 $^{\circ}C$ have been traced comparing the values of the thermocouples installed on the ORC circuit with external thermocouples.

3.11 Experimental test campaign of expanders

The next round of experiments during the second experimental campaign focused on the study of the two helical expanders. This study came as an extension and update of first experimental campaign results. In the literature there are very few models for helical expanders, of which the most widely used have a multitude of parameters that need to be determined experimentally, hence these experimental results will provide a useful data base in case of building a model on helical expanders.

Therefore, the scope of the experimental campaign was to correlate the isentropic efficiency ($n_{is,exp}$) and the expander filling factor (ff) with the pressure ratio for different values of the inlet pressure and the rotor speed. Thus the experiments were organized according to the following procedure:

- The installation operated with only one expander, maintaining the solenoid valve of the second expander closed (half power generation mode). The startup was in accordance with the operating protocol of the ORC installation and the pump speed was set to about half of the rated.
- The expander rotational speed was set to a specified value, depending on the set of measurements.
- The boiler natural gas supply (heat input) and pump speed were carefully adjusted to achieve the required inlet pressure to the expander, determined by the set of measurements. The expander's inlet temperature was such that the superheating temperature was in the range of 2-10 °C.
- Coolant water supply to the condenser was reduced as much as possible by closing the regulating valve in the cold water circuit. At the same time the speed of the feed water pump supplying the condenser was reduced as much as possible.
- Based on the above procedure, the high temperature of the refrigerant in the condenser dictates a relatively high pressure on the condenser, leading to the lowest value for the pressure ratio r_p. This pressure was in most cases about 12 bar, a value that was difficult to overcome, mainly due to the inability of the cold water feed pump to operate at lower loads/ flow rates.
- Once the system was balanced, values were recorded from all measuring devices/ sensors for at least 5 minutes. The electricity produced was measured with one of the Ducati energy analyzers described in Chapter 2 – Section 2.11.5. The average value was calculated for each measured variable in order to approximate the steady state of the cycle as closely as possible.
- Once the values for a "measuring point" were recorded, the flow of coolant to the condenser gradually increased by opening the regulating valve. This reduced gradually the pressure on the condenser, increasing the pressure ratio r_p with the expander's inlet pressure constant. Thus following this sequence of actions, the correlation of the isentropic efficiency with the pressure ratio for a desired expander's inlet pressure and pump rotational speed was formed. During this process the boiler's natural gas supply may need to be adjusted to maintain the pressure at the inlet of the expander close to the value decided.

- The same procedure was repeated in subsequent sets of measurements for different pump rotational speeds and / or pressure at the inlet of the expander.

Completing the experimental campaign on the expander a total of fifty-two (52) operating points for the following conditions were obtained:

Table 3.3: Operating points obtained during expander's second experimental campaign.

P_{in} (bar)	N_{exp} (RPM)	rp
23	1450	1.81 – 2.84
25	1450	1.84 – 3.00
23	1300	1.77 – 2.93
25	1300	1.84 – 3.35
22	1300	1.86 – 3.00
23	1150	1.95 – 3.01

The maximum isentropic efficiency was measured at 25 bar and 1450 RPM that is at rated operating conditions and was:

$$\eta_{is,max} = 62.8\ \%$$

while the minimum isentropic efficiency was measured at 23 bar and 1150 RPM and found equal to:

$$\eta_{is,min} = 46.5\ \%$$

The value of the maximum isentropic efficiency is in good agreement with the values obtained by corresponding investigations in open-type scroll expanders [57], although generally a bit lower. At this point, it should be once more stated that the calculated isentropic efficiency includes, all electromechanical losses, which could account for up to 40 % of the gross generated electrical power. In addition, a significant difference between the calculated isentropic efficiency in first experimental campaign is notable. The main argument could be that the isentropic efficiency results of the first experimental campaign had significant uncertainties. The most important sources of uncertainties were the estimated rather than measured mass flow of the organic medium, the electric consumption of pump and the gross power output per expander. All introduced significant errors. That is why the results of the first experimental campaign were used only for qualitative analysis of the behavior of the used scroll expanders, as already denoted in Section 3.2.

Thus, the equation used for the calculation of the isentropic efficiency during the second experimental campaign is still the same equation (3.7), as described in Section 3.2.

The following Figure 3.43 –Figure 3.46 illustrate the correlation of the isentropic efficiency with the imposed pressure ratio for various examined inlet pressure and rotational speed combinations. In each of the first two, Figure 3.43 & Figure 3.44, the rotational speed was kept constant and the expander's inlet

pressure was altered, while in the following two, Figure 3.45 & Figure 3.46, vice versa. The presented error bars were calculated on the basis of the used measuring instruments accuracy and the error propagation law (Section 2.11.5).

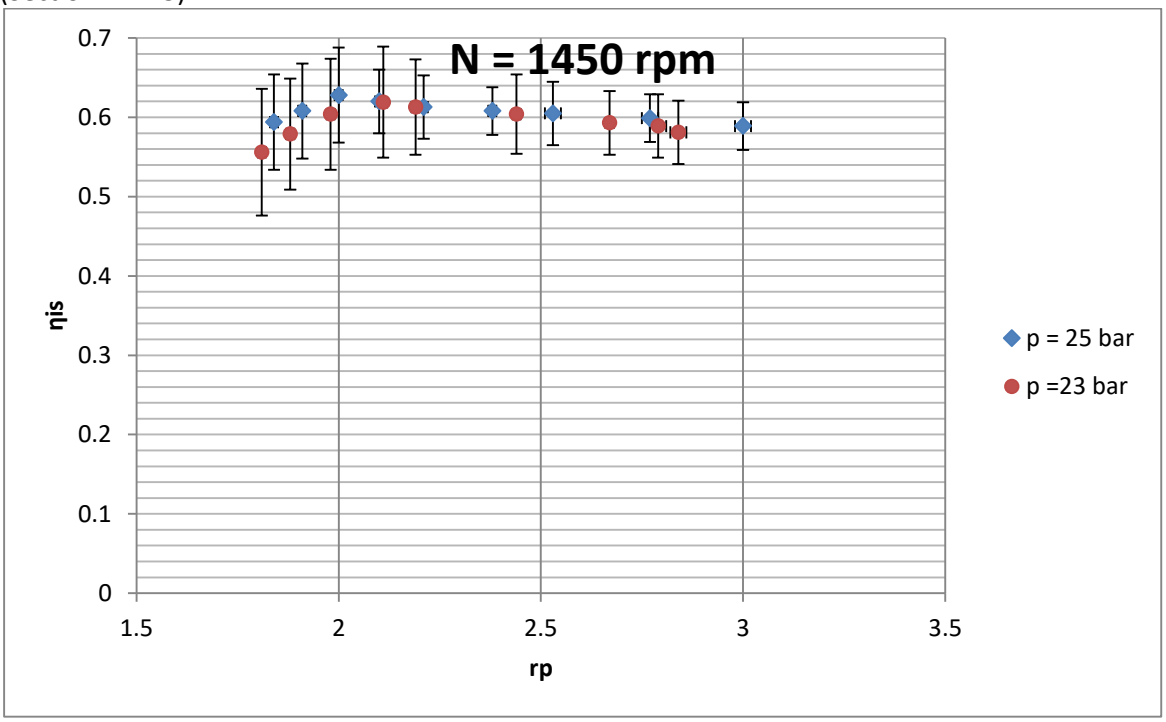

Figure 3.43: Measured isentropic efficiency as a function of expander's pressure ratio (rp), for 23 bar & 25 bar pressure inlet and Nexp=1450RPM.

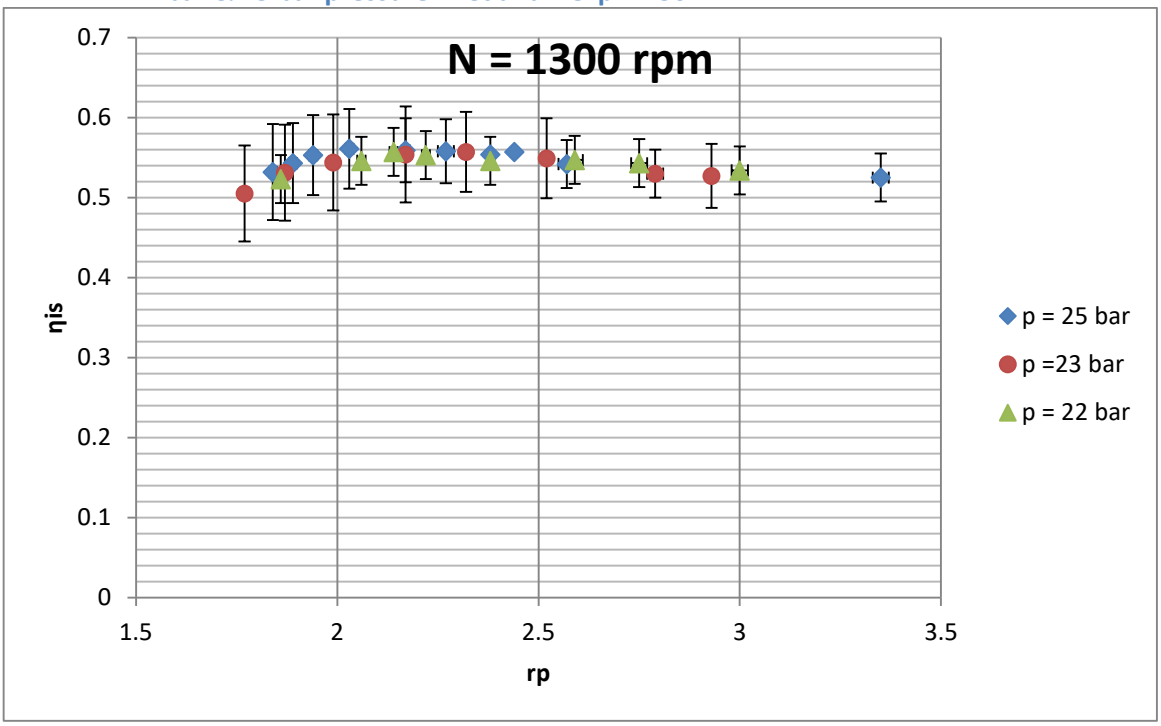

Figure 3.44: Measured isentropic efficiency as a function of expander's pressure ratio (r_p), for 22 bar, 23 bar & 25 bar pressure inlet and N_{exp}=1300 RPM.

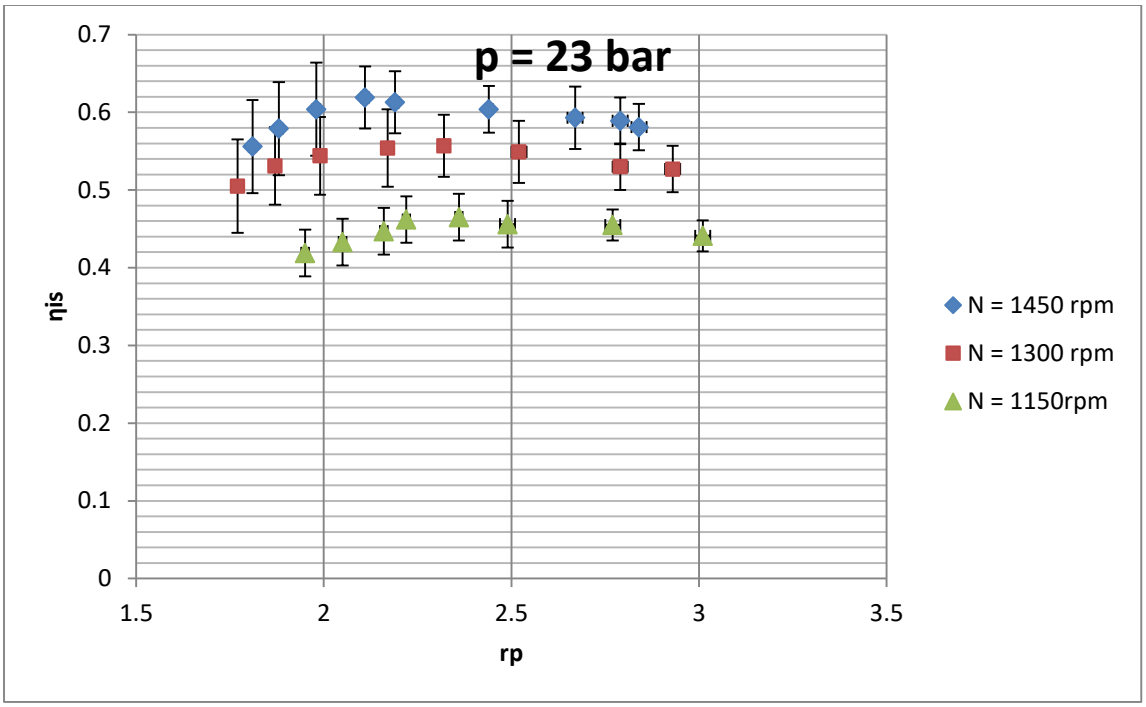

Figure 3.45: Measured isentropic efficiency as a function of expander's pressure ratio (r_p), for 23 bar pressure inlet and N_{exp}=1150, 1300 & 1450 RPM.

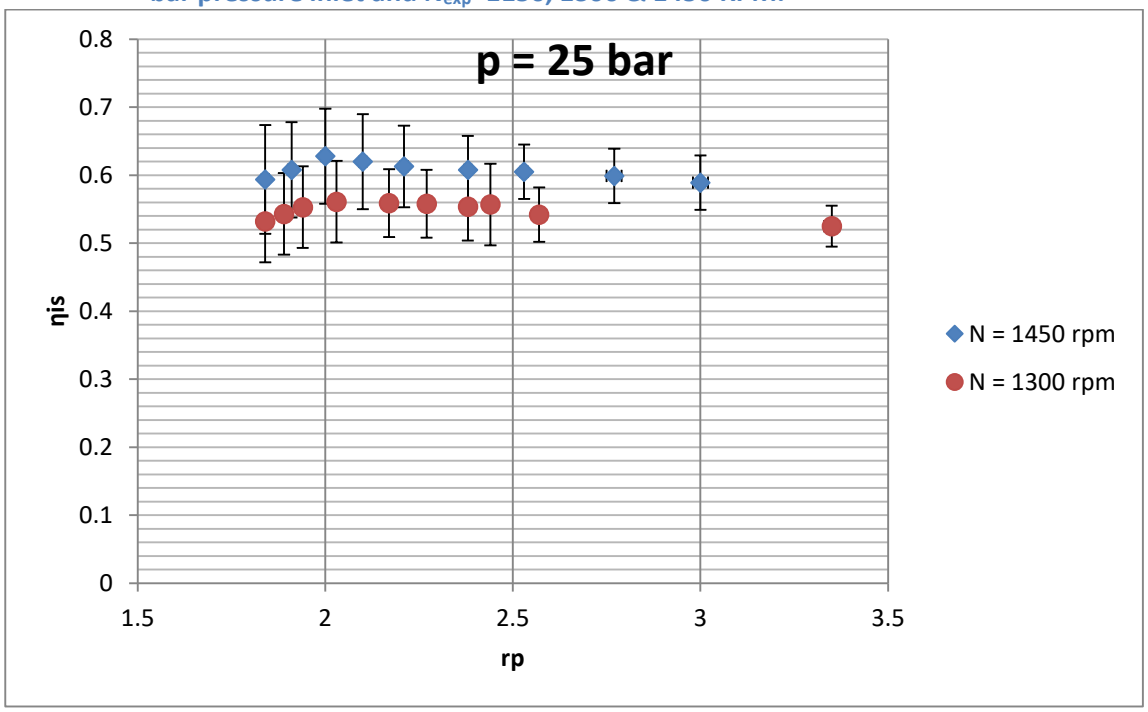

Figure 3.46: Measured isentropic efficiency as a function of expander's pressure ratio (r_p), for 25 bar pressure inlet and N_{exp}=1300 & 1450 RPM.

The shape of isentropic efficiency curves is in good agreement with literature [41],[43], which resembles that of Pacejka's equation for specific values of its parameters, as shown in below Figure 3.47. For relatively low pressure ratios the isentropic efficiency decreases sharply due to over expansion losses

and for large pressure ratios it exhibits a smooth decrease due to under expansion losses, as already presented in Section 2.5.2. In all tests the pressure ratio could not obtain values lower than $r_{p,min}$ = 1.8 due to the limitations described at the beginning of this section 3.11 to reduce the condenser cooling water supply.

Based on previous Figure 3.43-Figure 3.46, the immediate observation that can be made is that the isentropic efficiency is significantly influenced by the expander's rotational speed and indeed has an increasing tendency as the speed increases. This observation contradicts the observations of some researchers [43], who again point out a significant change in the isentropic efficiency with expander's rotational speed but with exactly the opposite trend, namely decreasing the isentropic efficiency as the rotational speed increases. The explanation for this contradiction is based on the fact that the specific research study focused on relatively low rotational speed (lower 1500 rpm).

In general, the efficiency of such an expansion machine is drastically reduced at high values of rotational speed due to mechanical losses, which are usually proportional to the square of speed. However, at lower speeds their mechanical losses are more or less constant, as shown in the following Figure 3.48 & Figure 3.49 (source [58]). These expanders are designed to operate as compressors at speeds of about 7000 rpm and so it makes sense to exhibit an uptrend of their isentropic efficiency at speeds below 1500 rpm, which relate to the range of presented experiments due to the prevalence of the increase of power generated against mechanical losses.

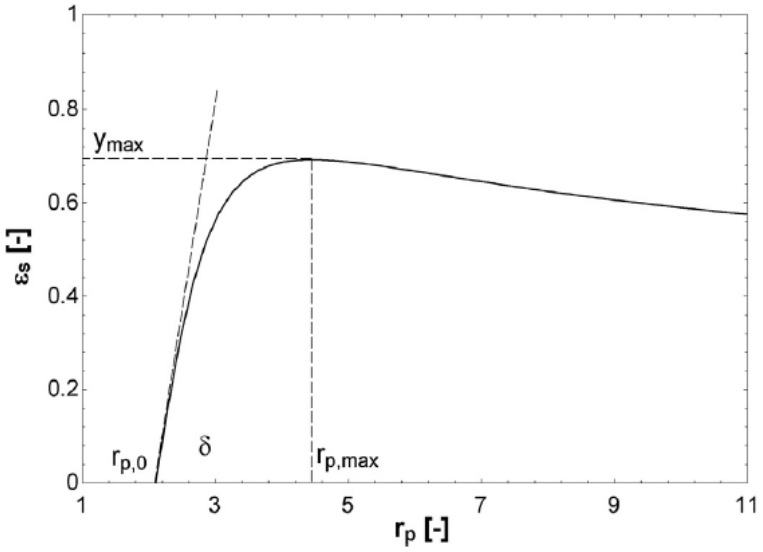

Figure 3.47: Mathematical significance of the empirical Pacejka equation parameters.[43]

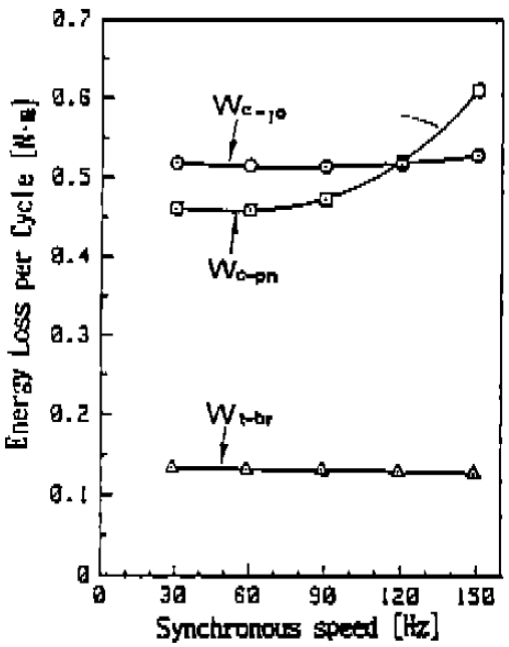

Figure 3.48: Mechanical losses of a scroll compressor in relation to rotational speed.[58]

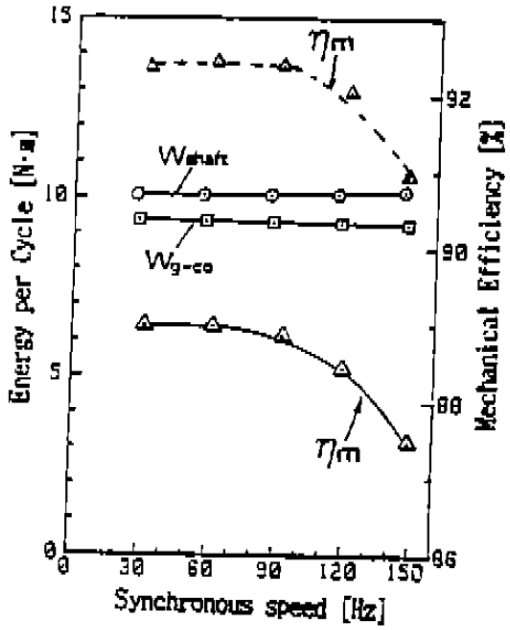

Figure 3.49: Mechanical efficiency of a scroll compressor in relation to rotational speed.[58]

As will be presented later on, the prevailing type of loss in this area of rotational speed is due to mass leaks, which tend to decrease with increasing rotational speed.

On the contrary, the value of the isentropic efficiency does not appear to be significantly influenced by the expander's inlet pressure. Nevertheless, an increase on the expander's inlet pressure increasingly causes a slight increase in the isentropic efficiency, as has been observed by other researchers. [59]

Another worth noticing observation from the above Figures is the transition of the specific pressure ratio showing the maximum isentropic efficiency $r_{p,\,max}$, at higher values by decreasing primarily the rotational speed and the expander's inlet pressure. This behavior has already been explained by Lemort et al. [41] and is due to the effect of different types of losses that are influenced by rotational speed and inlet pressure (suction pressure drop, leakage and friction losses), although the built in volume ratio of the expander is constant and constitutes a structural parameter.

Finally, the introduced errors in calculating the isentropic efficiency, it seems, are quite significant. The main source of inaccuracy and uncertainty is the calculation of enthalpy from pressure and temperature measurements, and therefore special measures should be taken to improve the accuracy of experiments in future experimental test rigs, in particular by improving mainly the accuracy of the temperature sensors as much as possible. Apart of the built in accuracy of each measuring instrument, significant role plays the correct installation of each. Immersed sensors should be selected and not clamp on.

Contrary to the isentropic efficiency, the electrical power output produced is constantly increasing with the pressure ratio.

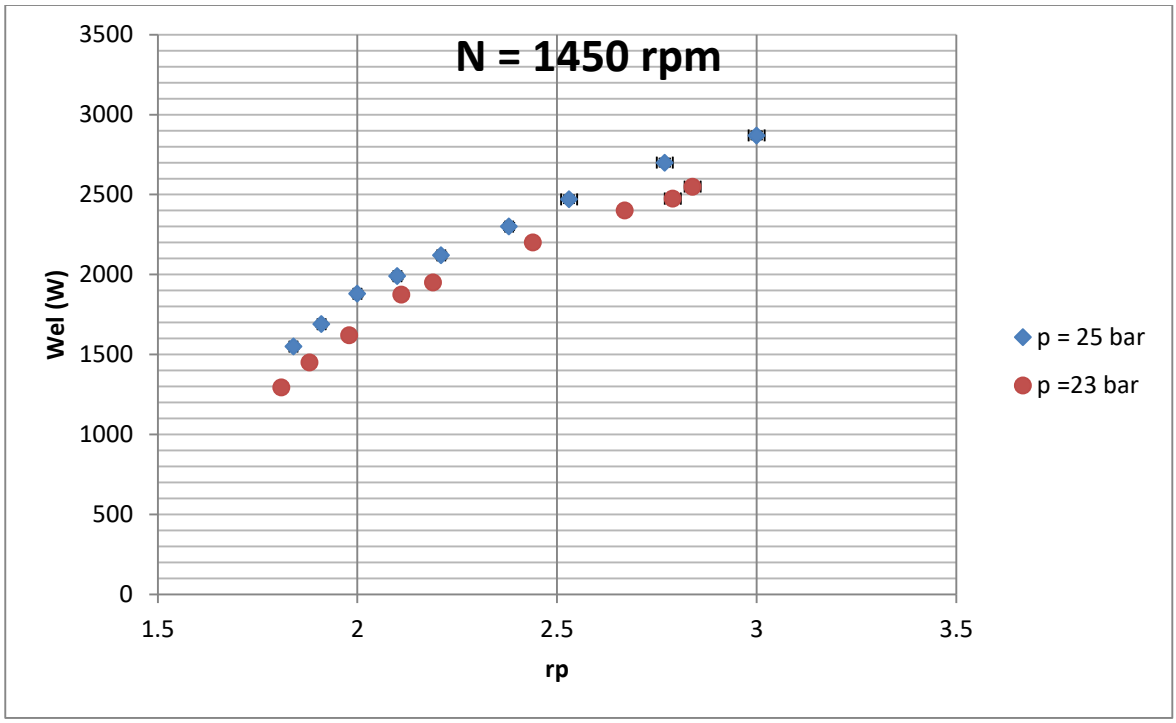

Figure 3.50: Measured electrical power output as a function of expander's pressure ratio (r_p), for 23 & 25 bar pressure inlet and N_{exp}=1450 RPM.

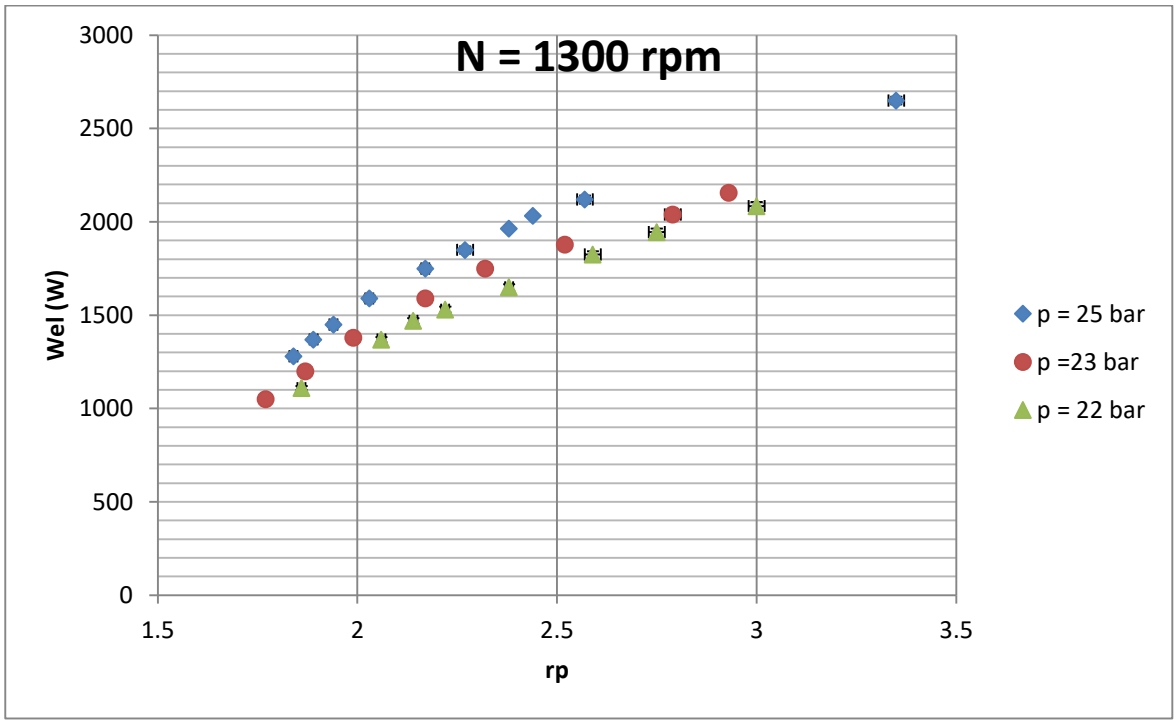

Figure 3.51: Measured electrical power output as a function of expander's pressure ratio (r_p), for 22, 23 & 25 bar pressure inlet and N_{exp}=1300 RPM.

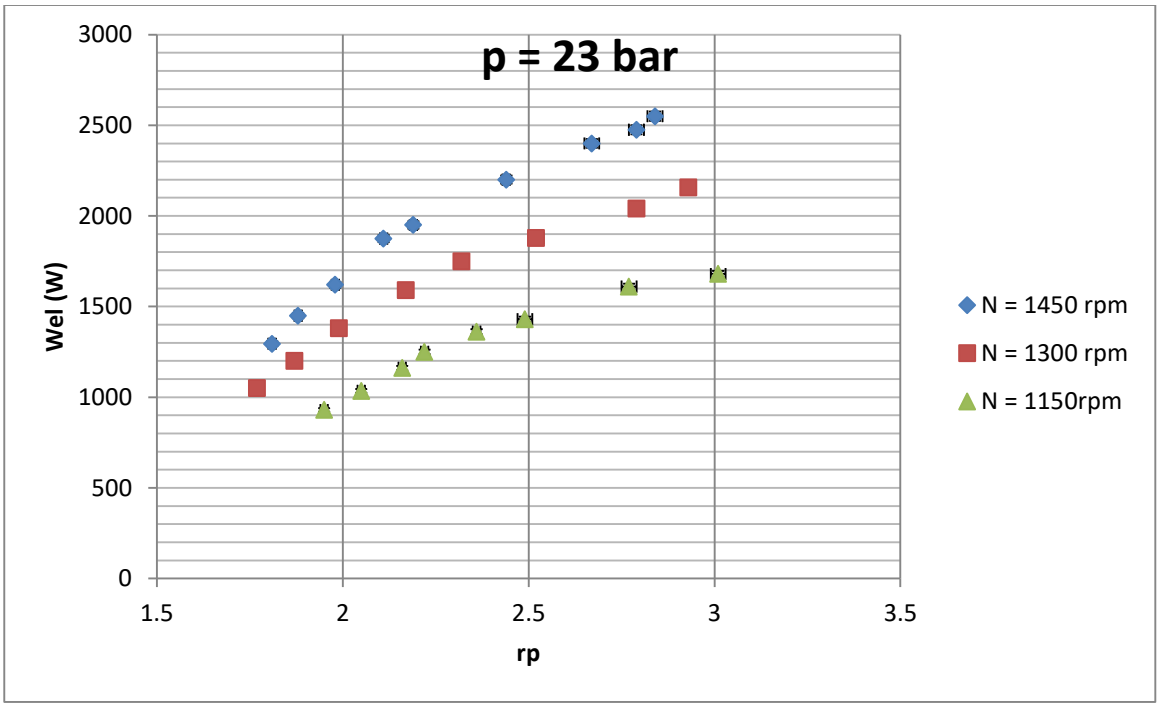

Figure 3.52: Measured electrical power output as a function of expander's pressure ratio (r_p), for 23 bar pressure inlet and N_{exp}=1150, 1300 & 1450 RPM.

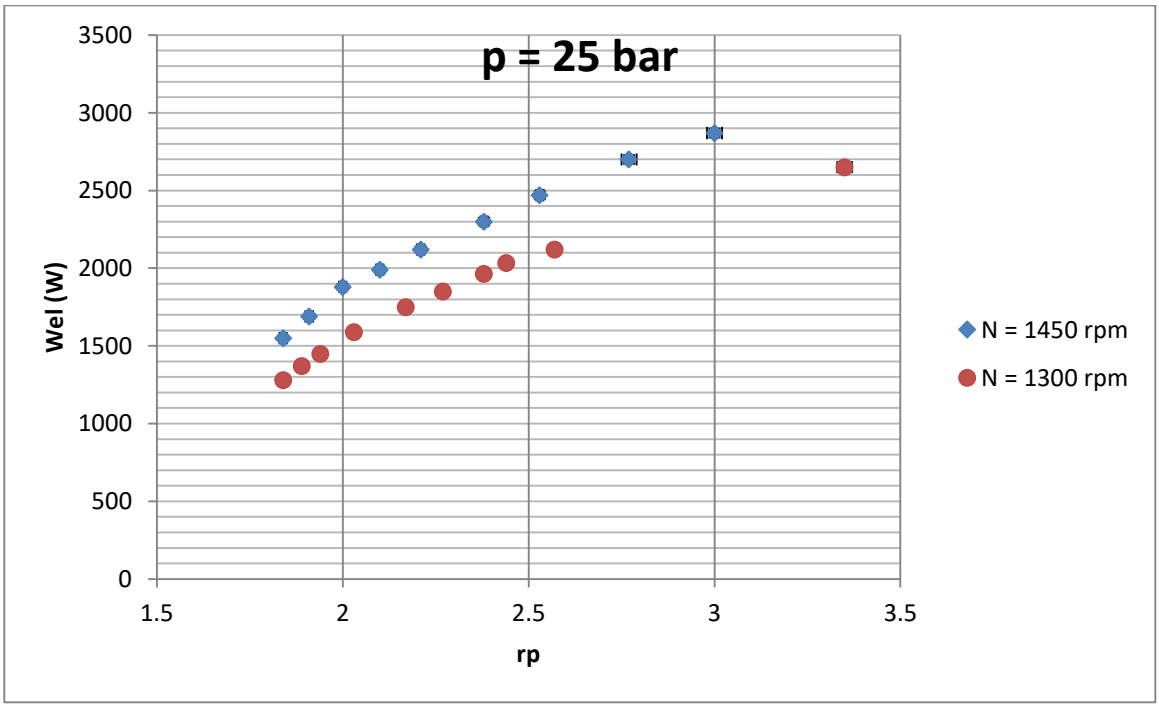

Figure 3.53: Measured electrical power output as a function of expander's pressure ratio (r_p), for 25 bar pressure inlet and N_{exp}=1300 & 1450 RPM.

An explanation of this phenomenon has already been given in section 2.5.2, where it is stated that although the under expansion losses cause a decrease in the isentropic efficiency, they also result in an

increase in the produced output power by it, due to the isochoric expansion at the expander's outlet. Of course, this increase in the produced output power declines as the pressure ratio increases. So although the operation of the expander at pressures ratios higher than $r_{p,\,max}$ is desirable, it is generally avoided at very high pressures ratios.

In addition, it is noted that the expander's output power increases with increasing rotational speed, as has been observed in all experimental investigations of the helical expander. At the same time, a smaller increase in the electrical power output is also noticed when increasing its inlet pressure. The fact that the power of the expander does not increase significantly -although higher inlet pressure means higher enthalpy at the inlet - is due to the simultaneous increase in pressure losses in the inlet section of the expander with increasing inlet pressure.[43], [52].

In evaluating the above observations, it should always be reminded that the measurements relate to the net electrical power produced and therefore the behavior described relates to the expander-generator pair and not to expander itself. This was also the case for first experimental campaign results (Section 3.2).

The second critical parameter considered, once more, during this experimental campaign, was the expander's filling factor (ff) defined originally in equation (3.8) and now presented in a different form in equation (3.22):

$$ff = \frac{60 \cdot \mathrm{m} \cdot \mathrm{v_{in}}}{\dot{\mathrm{V}}_{\mathrm{swept,exp}} \cdot \mathrm{N(RPM)}} \qquad (3.22)$$

Where:

m the total circulating mass flow rate

$V_{swept,exp}$ the bulit in swept volume of the scroll machine at expander mode

N the expander rotational speed

v_{in} inlet specific volume of the refrigerant at the expander inlet

The specific volume (v_{in}) at the expander's inlet was calculated from the measured pressure and temperature values at the corresponding positions.

In following Figure 3.54, Figure 3.55, Figure 3.56 & Figure 3.57, the correlation of the filling ratio with the imposed pressure ratio for various examined inlet pressure and rotational speed combinations is illustrated. Furthermore, in respective Figure 3.54 & Figure 3.55 corresponding to constant expander's rotational speed and altering the inlet pressure parameter, two parallel doted lines have been added. These lines correspond to the ± 2 % limit based on the average value of filling factor obtained in all test runs with the same rotational speed.

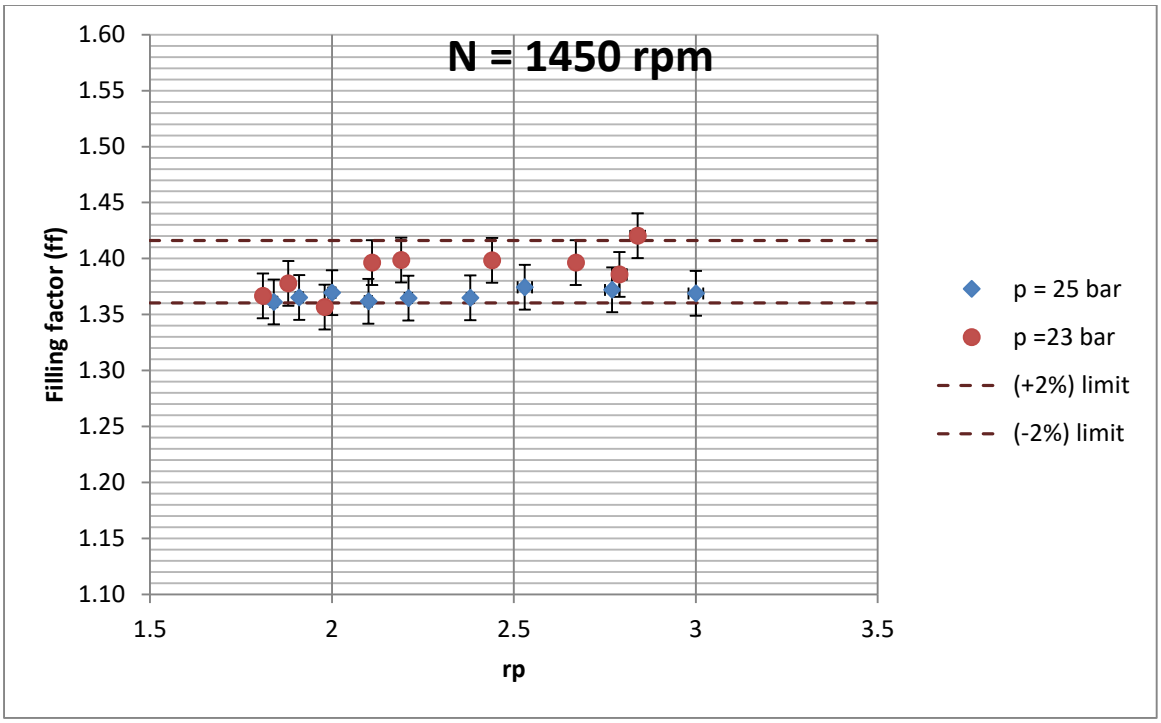

Figure 3.54: Measured filling factor as a function of expander's pressure ratio (r_p), for 23 & 25 bar pressure inlet and N_{exp}=1450 RPM.

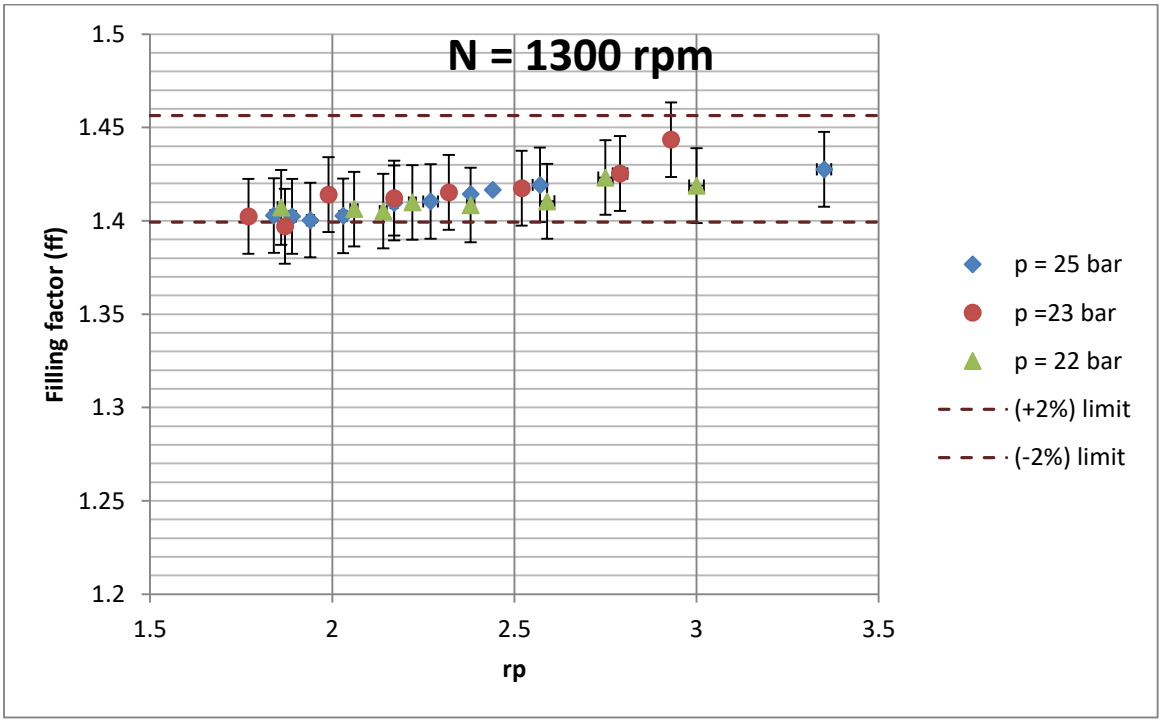

Figure 3.55: Measured filling factor as a function of expander's pressure ratio (r_p), for 22, 23 & 25 bar pressure inlet and N_{exp}=1300 RPM.

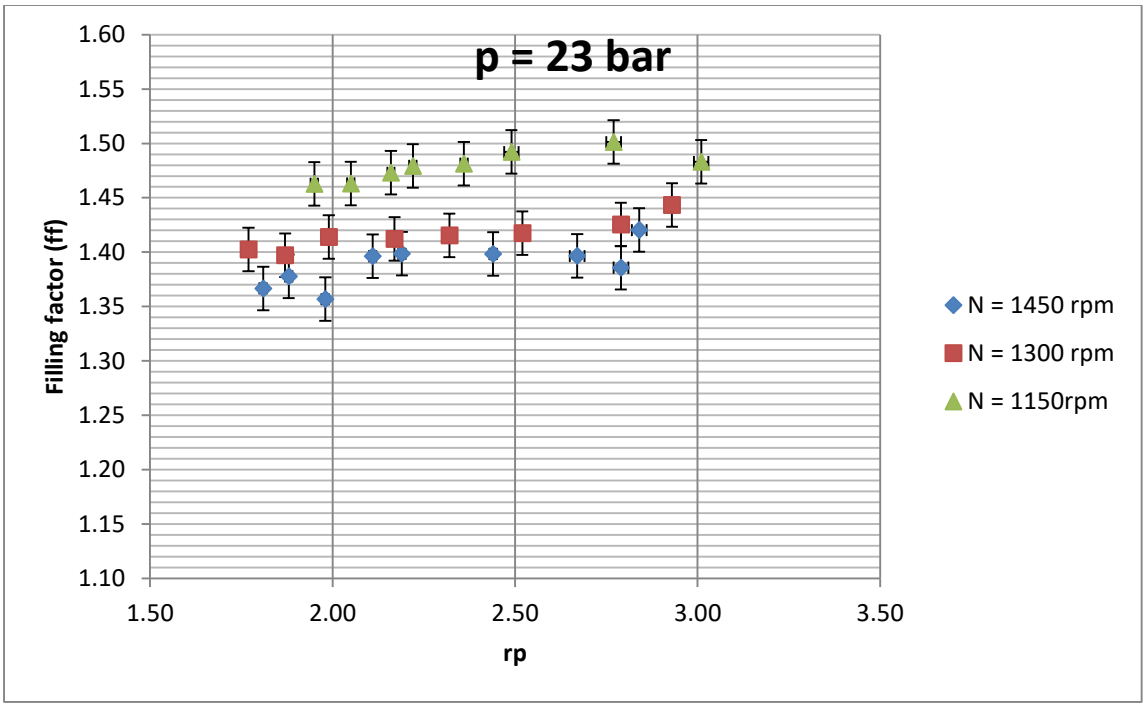

Figure 3.56: Measured filling factor as a function of expander's pressure ratio (r_p), for 23 bar pressure inlet and N_{exp}=1150, 1300 & 1450 RPM.

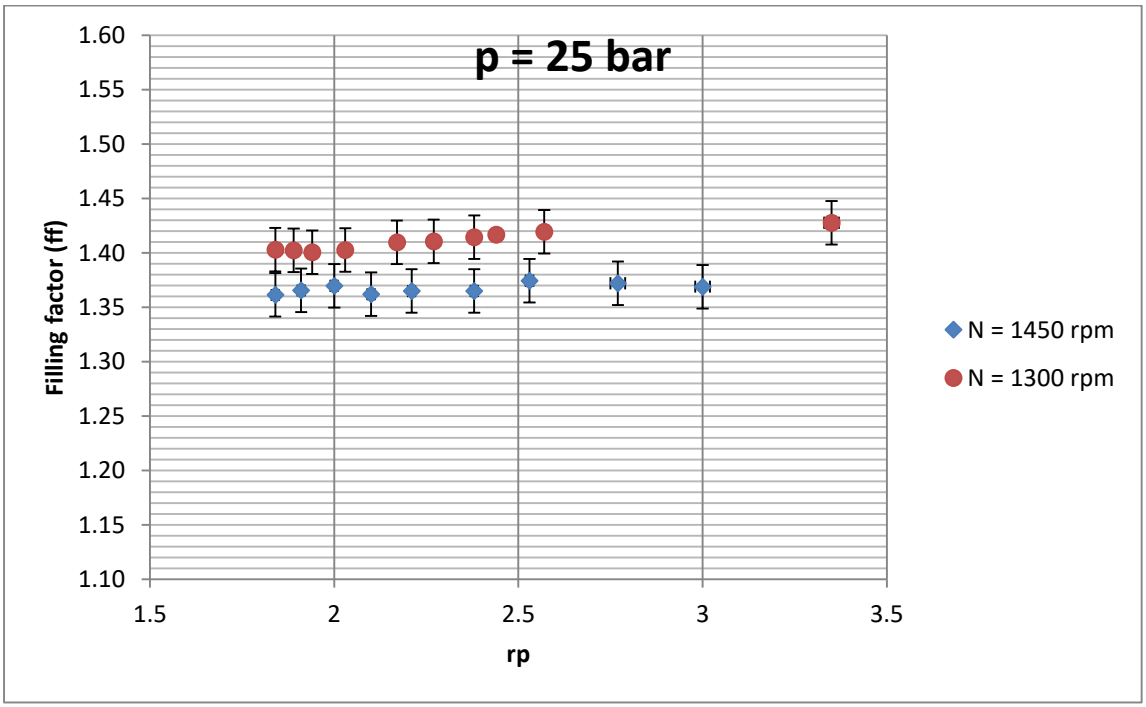

Figure 3.57: Measured filling factor as a function of expander's pressure ratio (r_p), for 25 bar pressure inlet and N_{exp}=1300 & 1450 RPM.

A first remark on the above diagrams is the relatively large values of the filling factors compared to those found in the literature, especially for hermetic scroll expanders. The above fact can, of course, be

justified by the general conclusion drawn from the literature that the open-type scroll expanders exhibit quite a large mass losses during their operation compared to the hermetic ones. [57]

In addition, the filling factor appears to be significantly influenced by the expander's rotational speed, with its values increasing as the speed decreases. This pattern has also been observed by Zanelli and Favrat and is related to the relative decrease of the internal clearance losses and the increase of the inlet throttling losses as the rotational speed increases [60]. At the same time, in accordance with the observations of the aforementioned researchers, the filling factor exhibits a fairly constant behavior at a given rotational speed over the range of pressure ratios tested.

The next remark is that the effect of the inlet pressure on the filling factor can be considered negligible, as the Figure 3.54 & Figure 3.55 show that the inlet pressure deviations do not exceed the 2 % threshold based limit based on the average value of filling factor obtained in all test runs for a given rotational speed. According to Lemort et al [52], this very low dependence of the filling factor on the inlet pressure is due to the fact that the increase in pressure causes two contradictory effects on the mass loss in the expander: On the one hand, as expected, it has the tendency to increase internal leakages, on the other hand, also results in an increase in pressure losses at the inlet, thus leading to a relatively unaffected behavior of the filling factor.

In following Figure 3.58 & Figure 3.59, a three-dimensional representation of the scroll expander's overall isentropic efficiency as a function of expander's pressure ratio (r_p) and rotational speed (N_{rotexp}), for two different inlet pressures, p_{in} = 23 bar and p_{in} = 25 bar respectively. These Figures illustrate the behavior of the isentropic efficiency with respect to the aforementioned variables as described above.

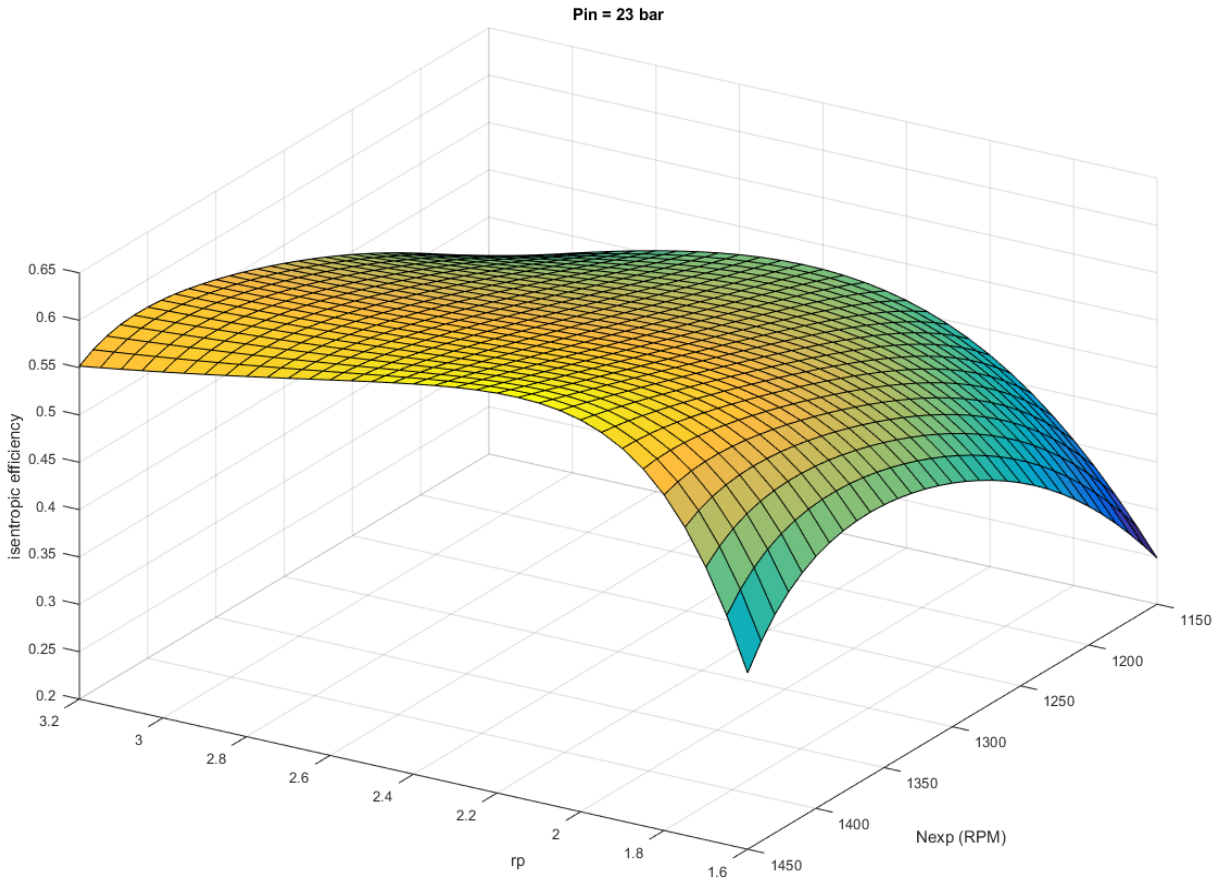

Figure 3.58: Scroll expander overall isentropic efficiency as a function of expander's pressure ratio (r_p) and rotational speed (N_{rotexp}), for 23 bar pressure inlet.

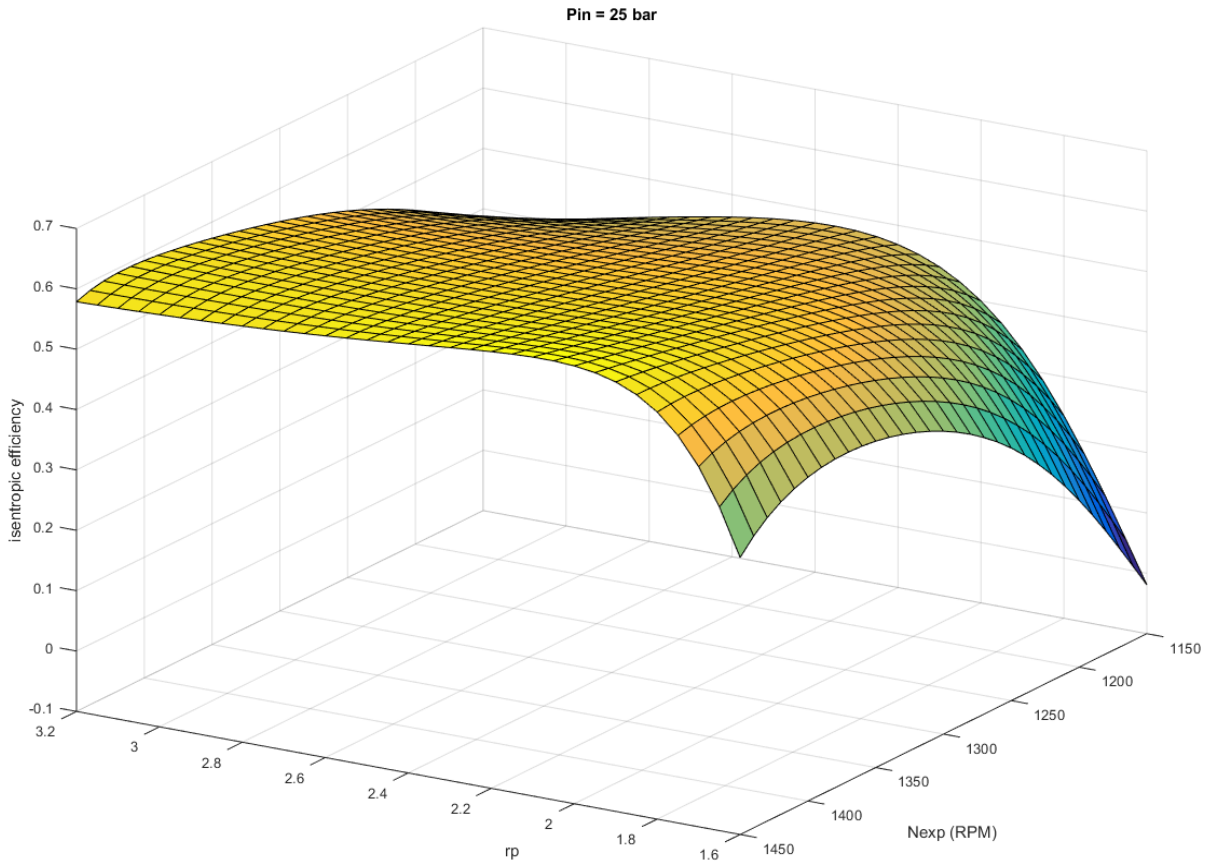

Figure 3.59: Scroll expander overall isentropic efficiency as a function of expander's pressure ratio (r_p) and rotational speed (N_{rotexp}), for 25bar pressure inlet.

The following conclusions are drawn from the above two three dimensional figures:

- To maximize expander's isentropic efficiency, the expander is required to operate at the highest possible rotational speeds. Of course, the rate of increase in isotropic efficiency decreases as expander's rotational speed approaches the maximum value examined, that is, 1450 RPM.
- Expander's isentropic efficiency is kept relatively high for the range of pressure ratios (r_p) of 2.2 to 3 and for high rotational speeds. As the rotational speed decreases, the decline becomes steeper. At the same time, as already reported, the electrical power output increases with increasing pressure ratio for given operating conditions. The above range of efficient operation extends to lower pressure ratios for higher inlet pressure.
- Increasing the inlet pressure has a positive effect on expander's isentropic efficiency but to a lesser degree than its imposed rotational speed.

3.12 Conclusions from the second experimental campaign results

The second experimental campaign concluded after the in depth evaluation of two critical components such as the ORC feed pump and scroll expander. The results and conclusions arisen from the second experimental campaign of the ORC WHR unit are summarized briefly below.

- The installed Coriolis mass flow meter was proven very useful, since it provided the means to better understand the operation of critical components such as the ORC feed pump and scroll expander.
- It also provided accurate measurements of mass, and along with pressure and temperature measurements in many measurement points, a valuable database was formed, describing the behavior of the experimental test rig under various operating conditions.
- As above mentioned, the operation of the multi-diaphragm pump integrated into the experimental micro-scale ORC has been deeply investigated. An extensive experimental characterization has been carried out. An experimental campaign was properly planned to create an ORC system setup, which makes a sufficient number of pump operating points available in the whole range of operation. Particular attention was also given to the search for the operating condition leading to cavitation and to the system reaction to this phenomenon.
- The pump performance has been evaluated under variable pressure difference imposed between inlet and outlet of the pump for constant pump rotational speed (rpm) and using two different approaches:
    - 1st approach - constant outlet pressure of the pump (cycle maximum pressure) and variable inlet pressure,
    - 2nd approach - constant inlet pressure and variable outlet pressure.

  An increasing trend of the global efficiency with the pressure difference was proven, as can be observed in all cases in respective Figures, as already shown in [37], and does not depend on the approach being followed. For operating conditions at f >36 Hz, global efficiencies of about 45 ÷ 48 % were achieved. These values are much higher than those reported in other studies for the same type of positive displacement pump [37], [53]. As regards the relative volumetric efficiency, a decreasing trend with the pressure difference is found only with the second approach. The first one, instead, does not provide the same expected trend, due to the big instabilities that this experimental procedure entailed. Values of the relative volumetric efficiency always above 96 % were found for the multi-diaphragm pump, as confirmed also in [37].
- Cavitation tests revealed that a $NPSH_a$ > 7 mH_2O at partial load and a $NPSH_a$ > 9 mH_2O at full load are necessary to guarantee operation stability. These values of $NPSH_a$ can be effectively achieved using a subcooler at pump inlet. With the development of cavitation conditions, a fast but quite gradual decrease of mass flow rate was observed, which allows for an effective action of the control system towards a stable operation of the system.
- As far the results and conclusions regarding the expander, in order to maximize expander's isentropic efficiency, the expander is required to operate at the highest possible rotational speeds. Of course, the rate of increase in isentropic efficiency decreases as expander's rotational speed approaches the maximum value examined, that is, 1450 RPM.
- The expander's output power increases with increasing rotational speed, at the same time, a smaller increase in the electrical power output is also noticed when increasing its inlet pressure.

All experimental data derived from the second test campaign were used in parallel research activities [45], [47], [61] & [62]. The main goal was to establish models of critical components. These models were calibrated against the experimental data of the second experimental campaign.

The experimental unit operated mainly with the use of the LabVIEW software interface but it required a manual control in order to achieve various operating conditions.

In the below Figure 3.60 and Figure 3.61, the overview of the experimental unit as it was until late 2017 is presented.

1. Natural gas boiler
2. Hot water circulation pump
3. Evaporator
4. Coriolis mass flow meter

Figure 3.60: Side view of the experimental ORC test rig (until November 2017).

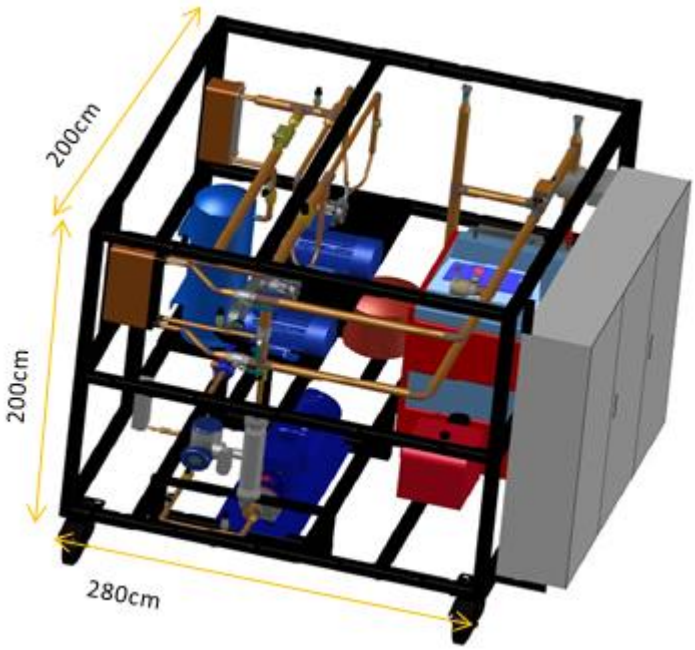

Figure 3.61: 3D AutoCAD drawing of the experimental ORC test rig (until November 2017).

On December 2017, a new ambitious goal was set. With the support of DNV GL, it was decided to proceed with the design and software development of a complete autonomous experimental test rig. In addition, a reconstruction process of the test rig would cope with the on ship requirements set by DNV GL in order to perform long term evaluation of the experimental test rig on board. This development phase would use all experimental data and knowledge acquired during the recent years in order to address all requirements and challenges of such a project. In the following Chapter, all actions, challenges and milestones within this last evolution process will be presented.

Chapter 4. - Final development of WHR ORC prototype

4.1 General scope & challenges

It must be acknowledged that, the evolution and development of the experimental ORC test rig, as described in previous sections, was co funded by DNV GL, Strategic Research & Innovation East Med., Black & Caspian Seas/ Piraeus Hub in the frames of the "Marine-ORC project".

As a consequence, after the successful completion of the second experimental campaign and the demonstration of a continuous trouble free operation of the ORC prototype, a new ambitious goal was set. The opportunity of operating the ORC test rig under real life conditions was proposed through the business channels of DNV GL. This goal could be entitled as

"Building and operating a complete autonomous Waste Heat Recovery ORC prototype at real life conditions"

for a long period of time.

The case, briefly, was to operate the experimental ORC prototype in a real engine room as a standalone facility without any physical supervision. The ORC prototype would be connected to the HT circuit of the cooling jacket of a main ICE (evaporator) and at the sea water cooling system (condenser and sub cooler), as originally designed and until then operated at laboratory conditions. The ship was a new built cruise ship that would be ready for ship trials in 10 -12 weeks' time. Despite of the introduced extreme time constraint, the decision was easy. In following Figure 4.1 and Figure 4.2, the engine room P&ID of the high temperature and sea water cooling temperature are presented, respectively. In addition some side, over views and access ports of the ship are given in Figure 4.3 and the final site installation of the ORC prototype in ship's engine room (Figure 4.4) in order to have an idea of how difficult the access and installation phase would be.

In Figure 4.5, the connection of the ORC prototype supply and return ports / flanges on the ICE's cooling circuit and on sea water circuit are depicted. The ship's ICE is cooled with soft water of the high temperature circuit (HT Cooling Circuit), which passes through the cylinders of the engine, extracting heat from their jackets. This water is then cooled in the central cooler of the vessel with seawater, at a temperature dependent to that of the sea at the given time. To avoid heat stress, a three-way valve maintains the water inlet temperature of the ICE's jacket by mixing it with part of the exiting soft hot water.

It is worth mentioning that ORC prototype will use a small portion of the total discharged heat by the cooling jacket of a main ICE. Consequently, the ORC high temperature refrigerant circuit (evaporator) will be supplied with hot water just after the jacket's circuit exit. Since the hydraulic losses are much larger, through the evaporator and the much smaller cross-section piping leading to it, than those of the rest of the ship's cooling circuit, it was necessary to install a hot water pump controlled by ORC PLC. The water coming out of the evaporator is re entering and mixed with the rest jacket's hot cooling water before the bypass pipe leading to the three-way control of the coolant water inlet temperature to engine's jacket.

As can be seen, when the ship's engine is running at a partial load, the heat flux from the cooling circuit is reduced. Consequently, and based on the Figure 4.5, since the water flow through the engine and the coolant water inlet temperature are kept constant, the water outlet temperature of the ship engine should be lowered. Of course, due to the controlled inlet temperature, this decrease is relatively small.

As already mentioned, this temperature is also the water inlet temperature of the ORC prototype evaporator. On the other hand, the supply of hot water to the evaporator will not change as long as the hydraulic balance of the ship's high temperature cooling circuit is not disturbed. Consequently, in addition of evaluating the nominal operating point of the ORC prototype, its behavior at different water inlet temperatures at the evaporator should be provided useful information, in case of evaluating its performance on a yearly / seasonal basis.

Last, cooling of the condenser and the sub cooler is carried out by sea water directly from the ship's central cooler.

Of course, this ambitious goal imposed several new challenges and requirements that were never taken into consideration during the previous stages of the ORC test rig development. A master plan was formulated in order to be able to address all challenges and requirements. Hence, the following procedure was applied. First, extensive hazard identification was performed in order to identify all risks, causes and consequences associated to each hazard. All derived outputs of the hazard identification procedure were used, if necessary, as inputs in the re construction phase of the ORC test unit and in the automation and control strategy architecture. At the same time, several dimensional constraints imposed by the ship's access ports and engine room site had to be taken in to account. In addition, the ORC prototype should be designed in a modular format, insuring that the transport and assembly on board would require only few hours. As well as, additional requirements set by the ship owner and mainly had to do with the electrical connection / supply of the experimental ORC unit with the ship's electrical grid, required several adaptive / corrective actions. These actions had an effect on the supplementary equipment and the general design of the automation and control, as it will be described in a following section. Last but not least, all DNV GL rules for classification had to be met in order to be able to have the appropriate certificate of compliance and thus DNV GL approval to proceed with on board installation and operation.

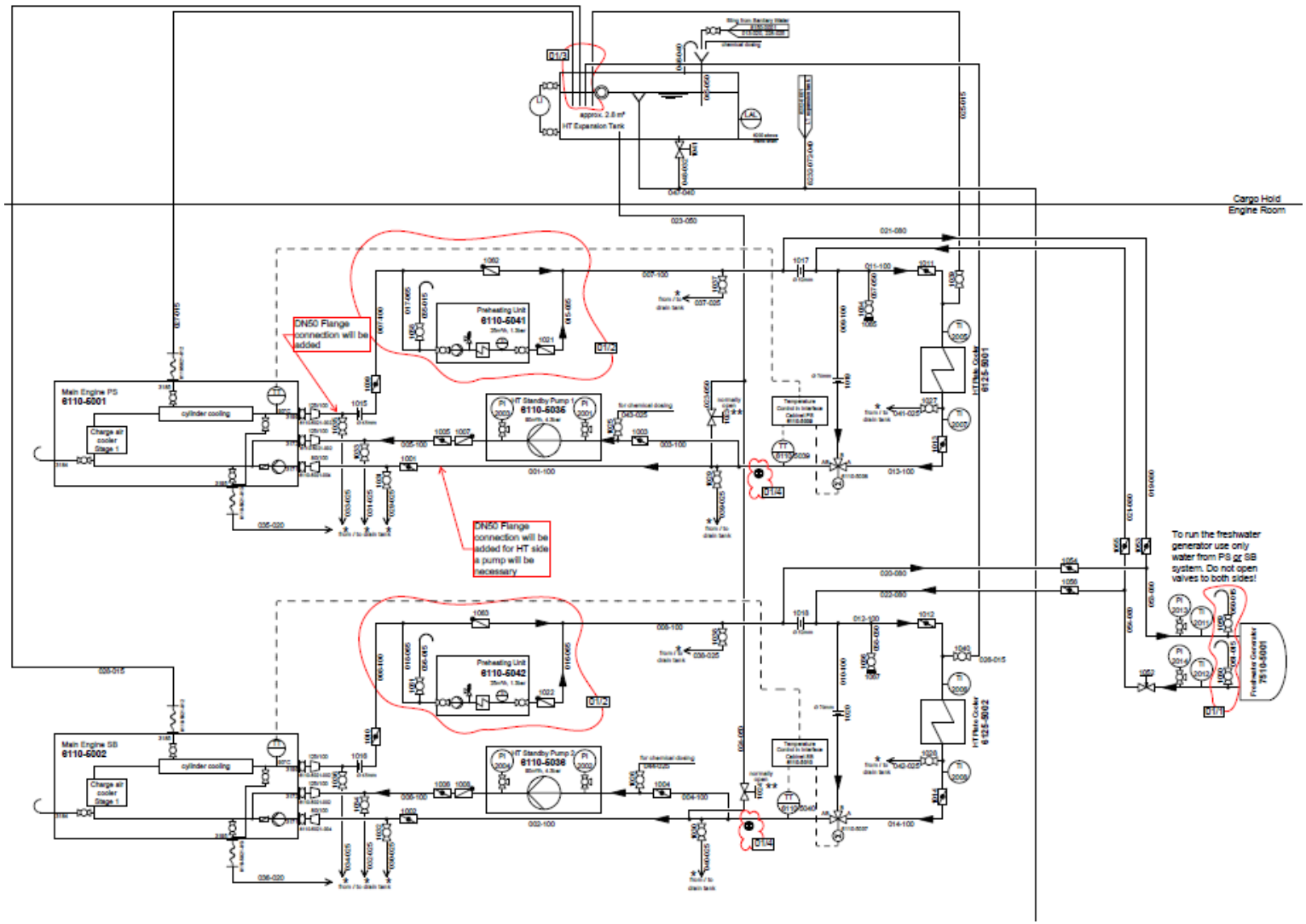

Figure 4.1: P& ID of the HT jacket cooling circuit of main ICE.

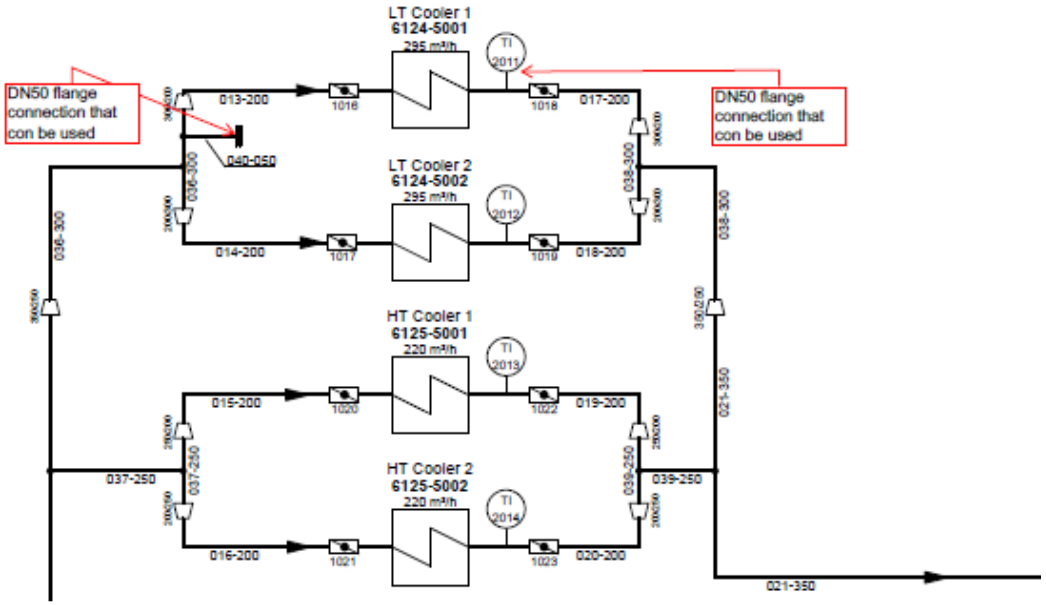

Figure 4.2: P& ID of the sea water cooling circuit of main ICE.

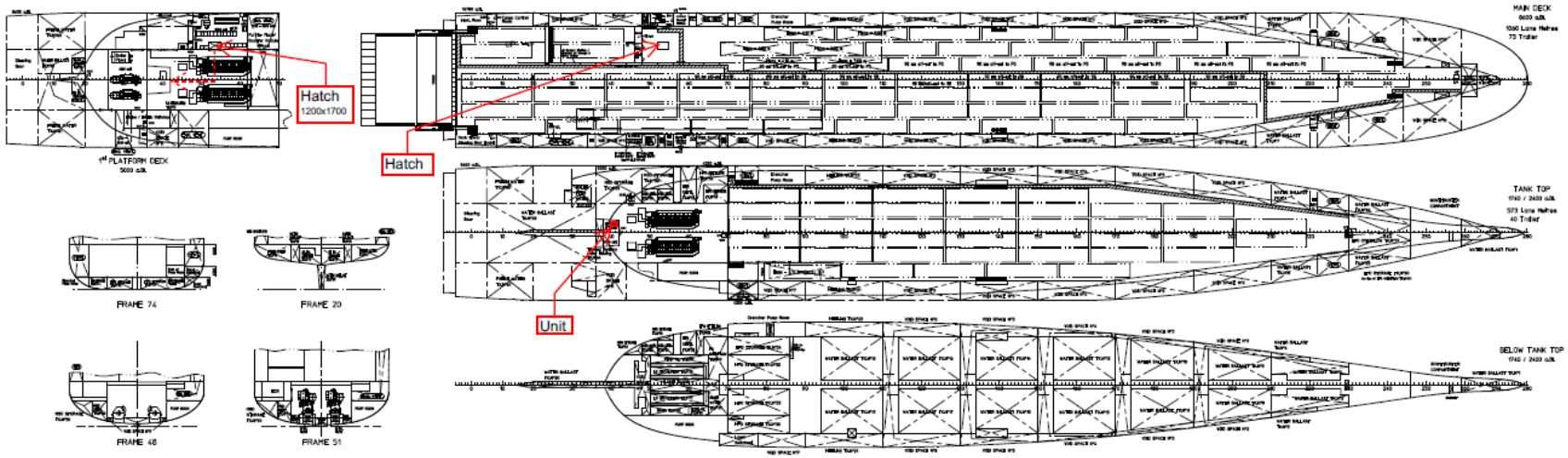

Figure 4.3: Side, over views and access ports of the cruise ship.

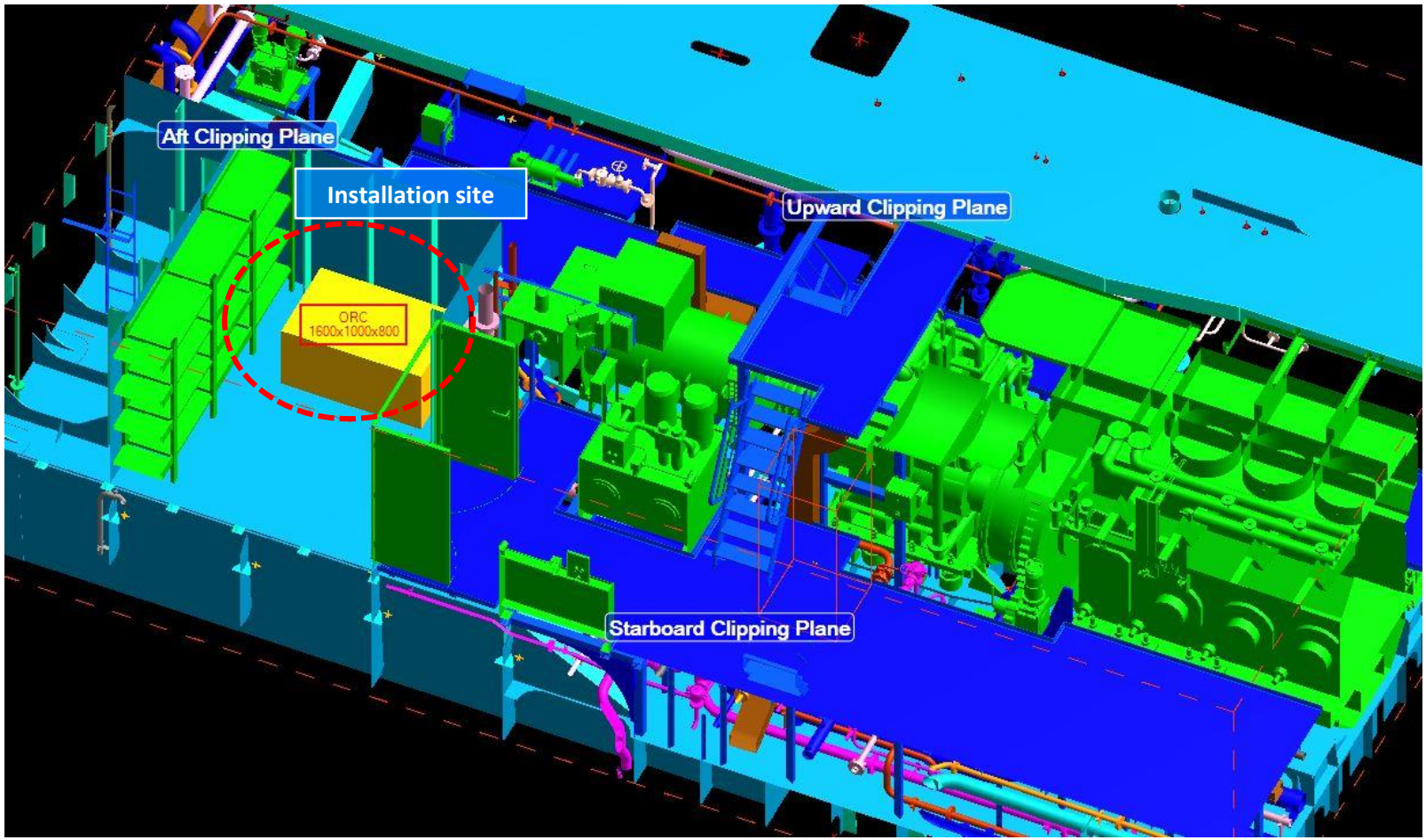

Figure 4.4: Site installation of the ORC prototype in ship's engine room.

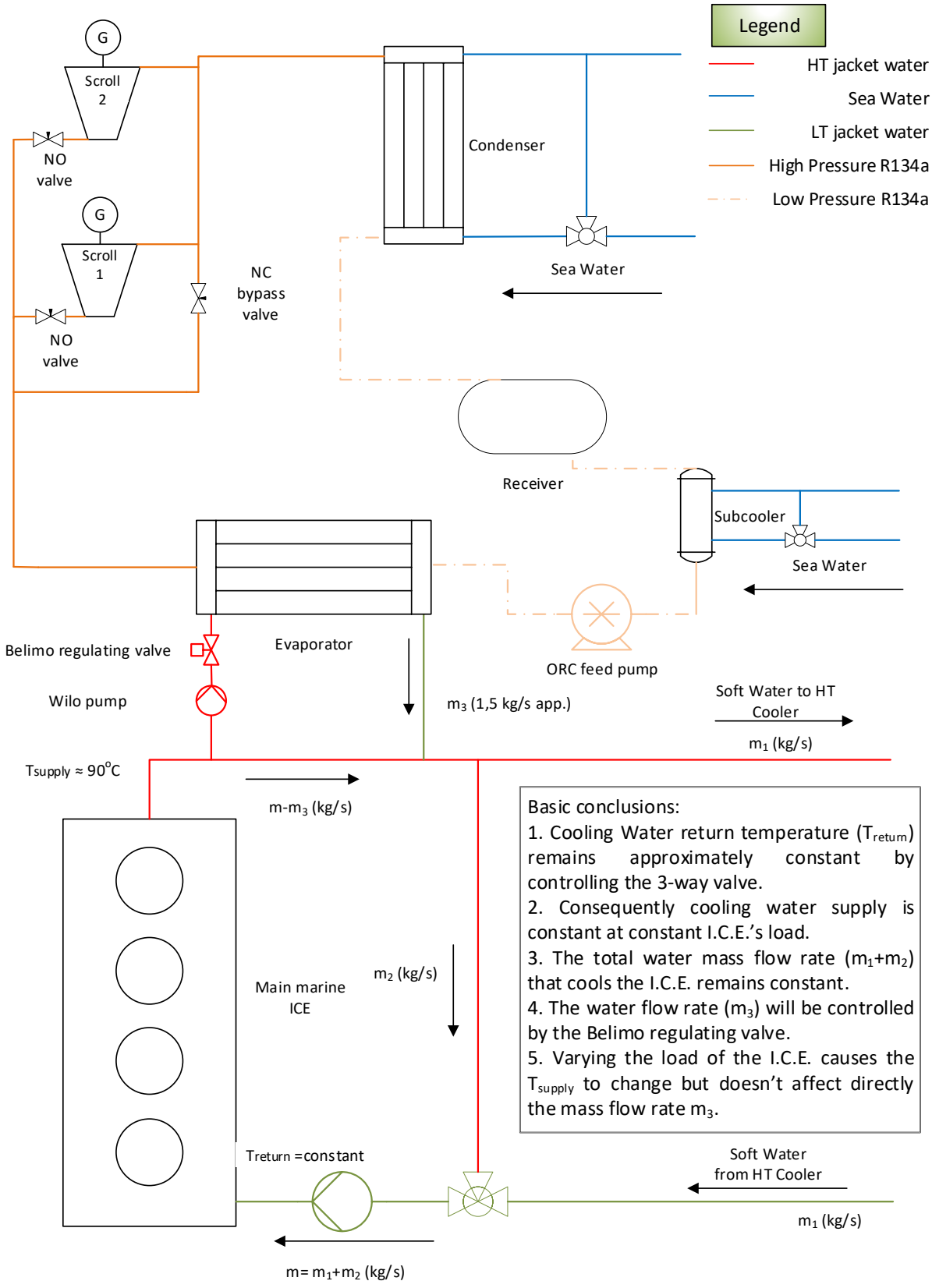

Figure 4.5: Schematic of the installation of ORC prototype loop into ship's engine HT cooling system.

The final master plan can be visualized in the following Figure 4.6. As can be observed, the re construction of the ORC test rig needed several inputs in order to be correctly designed and realized. Simultaneously, the automation & control of the ORC prototype would be revised and updated, following the basic requirement that the ORC prototype should be able to operate completely autonomous and thus entering or exiting specific defined and programmed states (modes) of operation. In addition, a complete data log, alarm log and "trip" log should be accessible from a Human Machine Interface (HMI). The latter would serve and provide a real time monitoring of the main components status and operating conditions (i.e. temperature, pressure, rotational speed, etc). In Figure 4.24, the ORC- NTUA Human Machine Interface (H.M.I.) layout chart is presented.

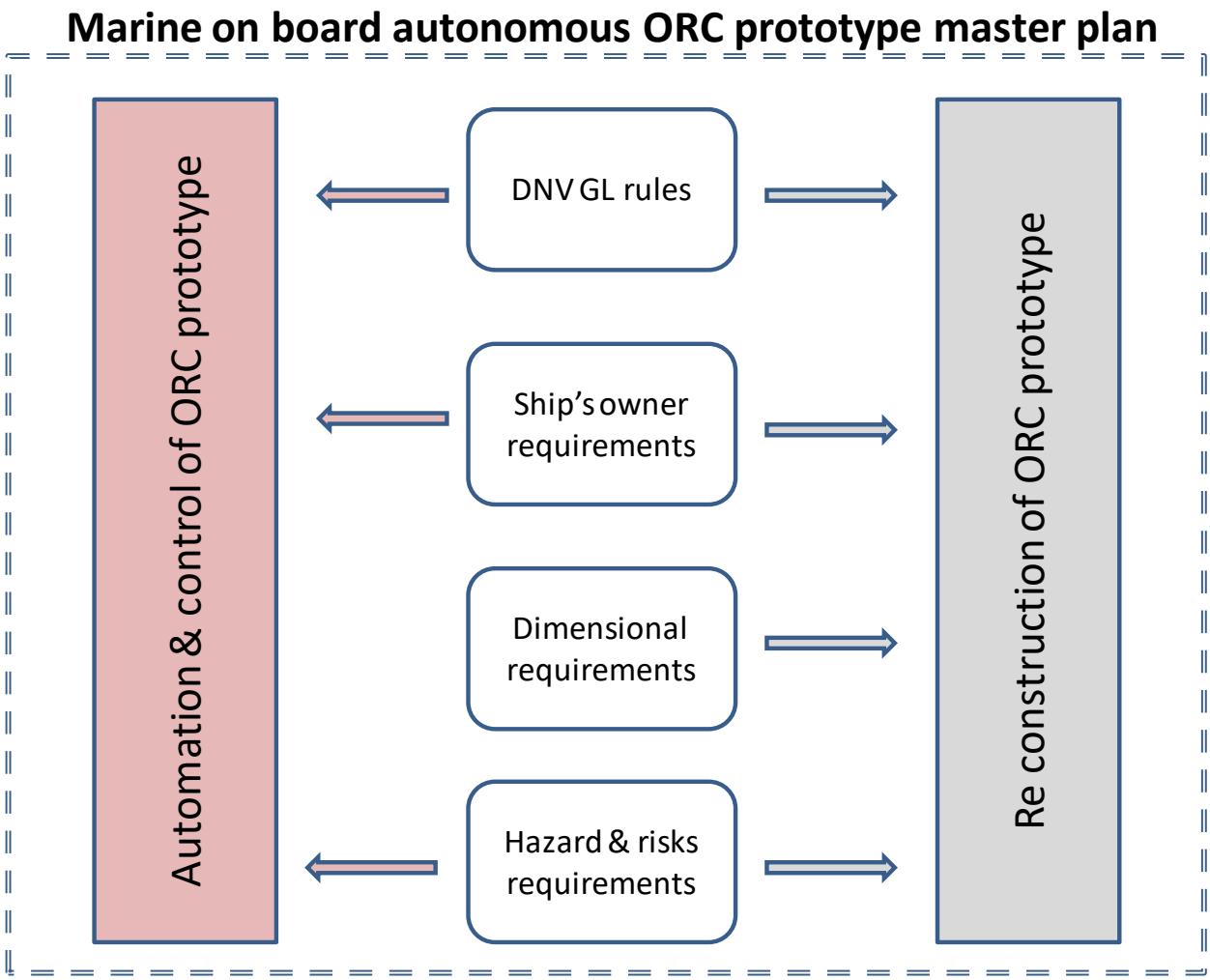

Figure 4.6: Master plan flow chart of marine on board autonomous ORC prototype.

4.2 Hazard identification procedure

As already mentioned, extensive hazard identification was performed in order to identify all risks, causes and consequences associated to each hazard. A systematic examination of all aspects of the ORC arrangement and operation which was conducted according to the following principles:

- What could cause injury or damage or failure
- Whether the existing risks can be eliminated, and
- What preventive or protective measures need to be taken to control possible risks.

The hazard and risks were evaluated on the operational security of the ORC test rig and any potential to cause harm to either the ship's personnel or the machinery of the engine room. The hazard identification and evaluation was performed in parallel, for three different ORC sub systems. These sub systems were:

- ✓ The piping and pressure equipment sub system,
- ✓ The electrical sub system and
- ✓ The automation and control sub system.

In addition, corrective actions were designed in order to cope with every identified hazard. All derived outputs of the hazard identification procedure were used, if necessary, as inputs in the re construction phase of the ORC test unit.

In following tables the outcomes of the performed hazard identification and risk analysis are presented. In every case the five basic consecutive steps of risk assessment were followed, as visualized in Figure 4.7.

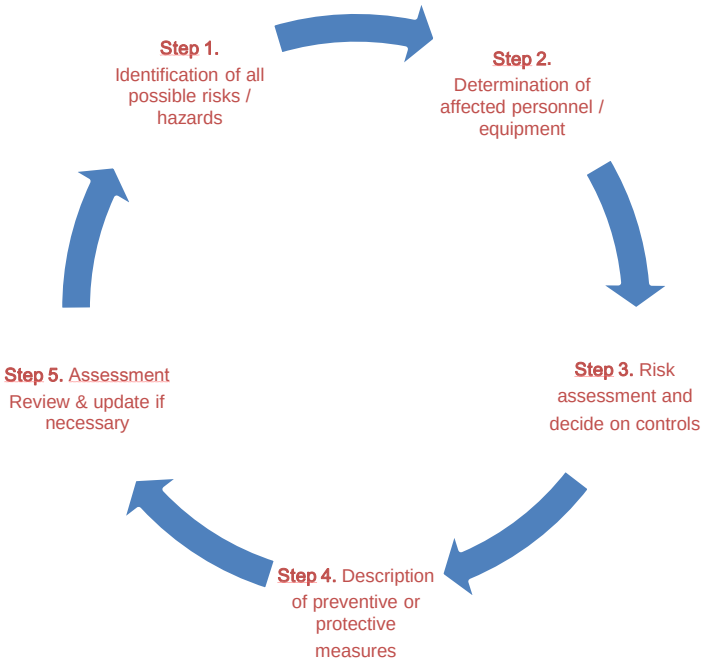

Figure 4.7: Flow chart of five basic consecutive steps of risk assessment.

Table 4.1: Risk assessment on the piping and pressure equipment sub system.

Risk / Hazard	Affected personnel / equipment	Risk assessment	Description of preventive or protective measures	Assessment review / remarks
Hot water circuit: ME HT circuit not able to cover minimum evaporator's DP	No personnel affected			
	ORC system fails to operate	Low risk	An independent pump is installed at ORC Hot water inlet	In case of ORC HT pump failure, the system again fails to operate
Sea water circuit: ME cooling water circuit not able to cover minimum condenser's & sub cooler's DP	No personnel affected			
	ORC system fails to operate.	Medium risk	The high pressure switch of the low pressure circuit will be activated. The system will shutdown	The PLC must shut off the Belimo regulating valve at High temperature water supply.
Pressure vessels Requirement: Volume (L) x pressure (bar) =>1500 for each pressure vessel (for approval)	Evaporator	Low risk	Over pressure switch at high pressure circuit	Requirement index = 9.17 lt x 30 bar= 275 No need for further approval
	Condenser	Low risk	Over pressure switch at low pressure circuit	Requirement index = 29.4 lt x 30 bar= 882 No need for further approval
	Sub cooler	Low risk	Over pressure switch at low pressure circuit	Requirement index = 5.1 lt x 30 bar= 153 No need for further approval
	Receiver	Medium risk	Over pressure switch at low pressure circuit + independent pressure relief valve (Double measure)	Requirement index = 50.0 lt x 30 bar= 1500 Double measure minimizes any associated risk
	Personnel	Low risk	All vessels have certification at least 1.3 x 25 bar (Max. operating pressure) = 30bar	In case of high pressure, the system shuts down.

Table 4.1(continue): Risk assessment on the piping and pressure equipment sub system.

Risk / Hazard	Affected personnel / equipment	Risk assessment	Description of preventive or protective measures	Assessment review / remarks
Safety valve failure	ORC refrigeration circuit	Safety valves installed at high and low circuit. Low risk	Equipment is not isolated therefore one Relief Valve is enough. Scroll expanders also have Relief Valves.	No need for further action
	Personnel	Safety valves installed at high and low circuit. Low risk	Equipment is not isolated therefore one Relief Valve is enough. Scroll expanders also have RVs.	Galvanized protection panel will be installed on site, preventing direct contact. Low flammability / toxicity of refrigerant (ASHRAE A1)
Flammable gases	ORC test rig	No pressurized flammable gases existing, only minor amounts of flammable liquids (lube oil / grease) Low risk	No specific actions designed	Low flammability / toxicity of refrigerant (ASHRAE A1)
	Personnel	No pressurized flammable gases existing, only minor amounts of flammable liquids (lube oil / grease) Low risk	No specific actions designed	Low flammability / toxicity of refrigerant (ASHRAE A1)
	Engine room	No pressurized flammable gases existing, only minor amounts of flammable liquids (lube oil / grease) Low risk	No specific actions designed	Low flammability / toxicity of refrigerant (ASHRAE A1)

Table 4.1(continue): Risk assessment on the piping and pressure equipment sub system.

Risk / Hazard	Affected personnel / equipment	Risk assessment	Description of preventive or protective measures	Assessment review / remarks
Leakages	ORC refrigeration circuit	Small quantity. Low risk	Because of the small quantity (<70 lt in total) no specific measures are required. The engine room ventilation circuit will handle. Eventually the under pressure switch at low pressure circuit will be activated and shuts off the system.	Low flammability / toxicity of refrigerant (ASHRAE A1) / Before startup the circuit will be subjected to a leak test. All leakages will be tracked and fixed.
	ORC High Temperature circuit	Medium risk	Manual ball valves are installed at inlet and outlet of HT circuit of the ORC.	In case of leakage, appointed engine room personnel must shut off the valves. The system will enter sleep mode. An emergency shutdown button will also be available. Before startup the circuit will be subjected to a leak test. All leakages will be tracked and fixed.
	ORC sea water circuit	Medium risk	Manual ball valves are installed at inlet and outlet of SW circuit of the ORC.	In case of leakage, appointed engine room personnel must shut off the valves. The emergency shutdown button must be activated. Before startup the circuit will be subjected to a leak test. All leakages will be tracked and fixed.

Table 4.1(continue): Risk assessment on the piping and pressure equipment sub system.

Risk / Hazard	Affected personnel / equipment	Risk assessment	Description of preventive or protective measures	Assessment review / remarks
General Personnel safety issues	Personnel	No hot surfaces (above 200 °C). Piping and electrical system, including resistor. Low risk No warm surfaces (above 100 °C) reachable by attending personnel. Low risk	Galvanized protection panel will be installed on site, preventing direct contact. Additional metal mesh frame will cover the resistor bank, a hot surface sign will be placed on the resistor's bank metal frame.	No further actions planned
Scroll expander failure	ORC test rig overall operation	Low risk	Two proximity sensors (speedometer) are installed in each pair of scroll expander / asynchronous motor. Any difference detected in the each pair of measurements is evaluated by the PLC with a 5 % permissible limit of differentiation and a ≤1500RPM upper limit.	No further actions planned

Table 4.1(continue): Risk assessment on the piping and pressure equipment sub system.

Risk / Hazard	Affected personnel / equipment	Risk assessment	Description of preventive or protective measures	Assessment review / remarks
Belt failure (scroll expander)	ORC test rig	Medium risk	Covering panel to the belts. System alarm and shutdown	Second pair of speedometers installed at scroll expander shaft.
	Personnel	Low risk	Galvanized protection panel will be installed on site, preventing direct contact	Low flammability / toxicity of refrigerant (ASHRAE A1)
Equipment endurance / reliability issues under long term operation	ORC piping and pressure equipment	Low risk	An at least 48 hour test of continuous operation will be performed at Laboratory facilities. Most of equipment has operated for more than 1000 hours.	All piping will comply with requirements set by DNV GL rules for classification (Part 4 Chapter 6)

Table 4.2: Risk assessment on the ORC electrical sub system.

Risk / Hazard	Affected personnel / equipment	Risk assessment	Description of preventive or protective measures	Assessment review / remarks
Supply generated power back to ship's grid	Stability of ship's grid	Harmonic distortion Low risk	A measure of harmonic distortion was conducted during operation of the ORC test rig at Laboratory facilities. Not a significant distortion was noticed and documented.	Complying with ship owner's requirements an electrically isolated subsystem with a motor-generator solution was realized. As a consequence, a resistor bank will cope with the produced electricity. The motor generator and the resistor bank will be controlled by the PLC of ORC.
Frequency drive failure	ORC pump	Failure to control the refrigerant cycle. Low risk	System unable to operate. No mass flow by the Coriolis, hence system shutdown.	The PLC must shut off the Belimo regulating valve at High temperature supply.
	ORC asynchronous motors	Low risk	Speed motor increase. Over speed detected by speedometers. System "Trip" shutdown	The PLC must shut off the Belimo regulating valve at High temperature supply.
Faulty connection to grid	ORC electrical system	Low risk	Qualified personnel will perform the electrical connection. A check will be performed by a second authorized person.	No further actions planned
	Ship's grid	Produced electric power consumed by local consumer (resistor). No connection to ship's. Low risk	No further actions are required	No further actions planned

Table 4.2(continue): Risk assessment on the ORC electrical sub system.

Risk / Hazard	Affected personnel / equipment	Risk assessment	Description of preventive or protective measures	Assessment review / remarks
Motor generator failure	ORC electrical system grid	Low risk	System unable to operate. Expect if it is already at normal operation condition. Then the system, since it produces a surplus of electrical power output it will continue to operate.	No further actions planned
Resistor bank module failure	ORC electrical system grid	Fails to transform electrical power to heat. Low risk	Resistor bank is equipped with 10 additional modules, 1kW each. In case of module burnout, the PLC will automatically switch to the next available.	No further actions planned
General Personnel safety issues	Personnel	No un-sheltered electrical connections reachable by attending personnel. A locked electrical panel will host most of electrical equipment. Low risk	Galvanized protection panel will be installed on site, preventing direct contact.	No further actions planned

Table 4.2(continue): Risk assessment on the ORC electrical sub system.

Risk / Hazard	Affected personnel / equipment	Risk assessment	Description of preventive or protective measures	Assessment review / remarks
Motor / generator overheating	ORC electrical system grid	Low risk	Digital signal to inverters, thus activation of power relays for unit shutdown	The PLC must shut off the Belimo regulating valve at High temperature supply.
Equipment endurance / reliability issues under long term operation	ORC electrical system grid	Low risk	An at least 48 hour test of continuous operation will be performed at Laboratory facilities. Most of equipment has operated for more than 1000 hours.	No further actions planned
No authorized access to high or low electrical voltage circuit	ORC electrical system grid	No un-sheltered electrical connections reachable by attending personnel. A locked electrical panel will host most of electrical equipment Low risk	A copy key will be given to chief electrical engineer.	No further actions planned

Table 4.3: Risk assessment on the ORC control and automation sub system.

Risk / Hazard	Affected personnel / equipment	Risk assessment	Description of preventive or protective measures	Assessment review / remarks
Master PLC failure	ORC overall test rig	Fail to operate Medium risk	Two independent PLCs: one for control and a second for shut-down (ESD) / trip functionality.	No further actions planned
ESD PLC failure	ORC overall test rig	Failure to shutdown Low risk	The master PLC will override the malfunction and shuts down the ORC test rig	No further actions planned
Sensors out of limits / sensor error	ORC overall test rig / specific sensor / available data Ship's grid	Medium risk	The system will continue to operate if possible, unless one of the below critical sensors. - Low Pressure Trip - ORC low pressure section - High Pressure Trip - ORC low pressure section - High Pressure Trip - ORC high pressure section - Generator Scroll 1 overspeed trip - Generator Scroll 2 overspeed trip - Generator 1 Drive failure trip - Generator 2 Drive failure trip	In case of critical sensor failure, system shutdown. The PLC must shut off the Belimo regulating valve at High temperature supply.

Table 4.3(continue): Risk assessment on the ORC control and automation sub system.

Risk / Hazard	Affected personnel / equipment	Risk assessment	Description of preventive or protective measures	Assessment review / remarks
Sensors failure to operate at harsh engine room conditions	ORC overall test rig	Fail to operate Low risk	Electronics are suitable for marine use. Sensors are able to withstand the anticipated temperature and vibrations.	No further actions planned
Refrigerant control solenoid valves	By pass Normally Open solenoid valve	Failure to close. Low risk	The system will fail to operate, since most of the flow will by pas the scroll expanders.	No further actions planned
	Normally Close solenoid valve	Failure to open. Medium risk	The system will fail to operate. High pressure switch activated. System shutdown. By pass valve open	No further actions planned
Asynchronous generator failure	ORC electrical system grid	Low risk	Speed motor increase. Over speed detected by speedometers. System "Trip" shutdown Speed motor decrease. Scroll rotational speed decreases, thus pressure increases, high pressure switch activated	No further actions planned

Table 4.3(continue): Risk assessment on the ORC control and automation sub system.

Risk / Hazard	Affected personnel / equipment	Risk assessment	Description of preventive or protective measures	Assessment review / remarks
ORC alarm system & ESD / trip functions operation	ORC automation & control sub system	Low risk	All alarm & trip testing and functional test will be checked at Laboratory facilities. Most of sensors & equipment have operated for more than 1000 hours. System to be witnessed by a DNV surveyor on board or at Laboratory facilities: All alarm & trip testing and functional test.	No further actions planned
ORC alarm system & ESD / trip functions notification status	Ship's control room	Low risk	Ship's control room needs to be aware in case of alarm activation. A wired signal will be send to control room.	Appropriate output signal from PLC, further information will be provided through the HMI screen. A specific optical signal (Alarm led or trip led) will flash & noise signal (siren) is activated. Each can be de activated only manually by engine room personnel.
Equipment endurance / reliability issues under long term operation	ORC automation & control sub system	Low risk	An at least 48 hour test of continuous operation will be performed at Laboratory facilities. Most of sensors & equipment have operated for more than 1000 hours.	No further actions planned

Table 4.3(continue): Risk assessment on the ORC control and automation sub system.

Risk / Hazard	Affected personnel / equipment	Risk assessment	Description of preventive or protective measures	Assessment review / remarks
No authorized access to automation & control sub system key parameters	ORC automation & control sub system	A locked electrical panel will host most of automation & control equipment. Low risk	A copy key will be given to chief electrical engineer. Access will be provided through HMI interface, placed in front side of the aforementioned panel. Access will be limited only for operational monitoring and acknowledgement of alarm / trip history log file.	No further actions planned

All major conclusions and key results from the hazard – risk assessment are summarized as follows. In general, all corresponding preventive and protective actions must be taken in to account during the automation and control strategy's design and realization.

As far the results from the piping and pressure equipment sub system assessment, almost all pressure vessels are well below the 1500 (bar *lt) threshold, with the exception of the receiver. For the latter, an independent relief valve is installed, minimizing any associated risk from over pressure. In case of an on board leakage, everything can be handle by the existing safety equipment, the designed control strategy, ER ventilation system and ER personnel. The presence of no pressurized flammable gases and only minor amounts of flammable liquids relate to no additional specific risk. Last but not least, all piping will comply with requirements set by DNV GL rules for classification (Part 4 Chapter 6). Each circuit will be subject to a leak test which will be documented if required. All leakages will be tracked and fixed before startup.

In the electrical sub system assessment, the isolation of the ORC electrical grid minimizes all related risks to the ship's electrical grid. In addition, since all electrical systems and components involved are below the "class limit" of 100kW, no special risk related to the electrical system needs to be considered further.

Furthermore, in the control and automation sub system assessment, an independent ESD PLC module will be designed and realized, thus minimizing related risks. In case of alarm, trip or emergency shutdown appropriate output signal from PLC to control room is foreseen and specific information will be displayed on the HMI screen. A specific optical signal (Alarm led or trip led) will flash & noise signal (siren) will be activated. Each can be de activated only manually by engine room personnel, thus assuring the acknowledgment of the alarm or trip origin by authorized personnel. All alarm, trip & operating function of the ORC automation and control will be checked by Laboratory personnel and witnessed by a DNV surveyor on board or at Laboratory facilities.

In general, a trouble free continuous operation after the completion of all related works will be demonstrated at laboratory facilities.

As far the personnel safety aspect, in general, neither hot surfaces (above 200 ^{o}C) nor warm surfaces (above 100^{o}C) reachable by attending personnel are expected. Appropriate actions against loosening of moving parts (i.e. belts) are taken. Un- sheltered electrical connections are not expected. As an extra safety measure, galvanized protection panels will be installed in each side of ORC modular unit on site, preventing direct contact. Additional metal mesh frame will cover the resistor bank and a hot surface sign will be placed on the resistor's bank metal frame.

4.3 Dimensional requirements

As previously mentioned, the ORC laboratory experimental test rig had to be extensively re constructed, given the dimensional restriction imposed by ship's access ports and hatches. Another important requirement was that transportation process and all work carried out on board, in terms of assembly, wiring, filling, testing, tuning and finally setting in operation should be kept as short in time as possible and do not exceed the 36-hour limit. This time constraint reflects the particularities of the marine market and industry where proper planning and multi tasking are considered as a must and could be summed as "a ship never waits". Therefore, several actions needed to be performed simultaneously. Considering the fact that only refrigerant circuit's filling and leakage testing would require 8 -10 hours, assembly and wiring should be kept as short as possible.

As, presented in Figure 4.3 & Figure 4.4, the transportation of the ORC prototype from entry level to engine room level would be feasible only if a certain dimensional rule was followed. Every item should not exceed the following dimensions (L x W x H) ≤ (1.6 m x 1.0 m x 0.8 m) constraint.

In following Table 4.4, the dimensions and weight of each module that formulates the marine on board ORC prototype are presented. In addition, Figure 4.8 illustrates the new dimensions of the marine on board ORC prototype in relation to the existing, until that moment, experimental ORC unit. It is obvious that reducing the external dimensions of the ORC unit by more than 30 %, maximizing the compactness and modularity of the redesign ORC prototype were obligatory.

Table 4.4: Dimensions and weight of marine on board ORC prototype modules.

Description	Dimensions (L x W x H) [m]	Weight [kg]
Bottom ORC sub frame	**1.600 x 1.000 x 0.550**	**250**
Medium ORC sub frame	**1.600 x 1.000 x 0.600**	**380**
Upper ORC sub frame	**1.600 x 1.000 x 0.800**	**380**
Electrical Panel 1st frame	**1.000 x 0.400 x 1.600**	**250**
Electrical Panel 2nd frame (including sensors wiring)	**0.800 x 0.400 x 1.600**	**220**
Motor Power Generator Module	**0.850 x 0.790 x 0.635**	**260**
Resistor Banks Module	**0.880 x 0.560 x 0.860**	**80**
Total weight		**1,820**

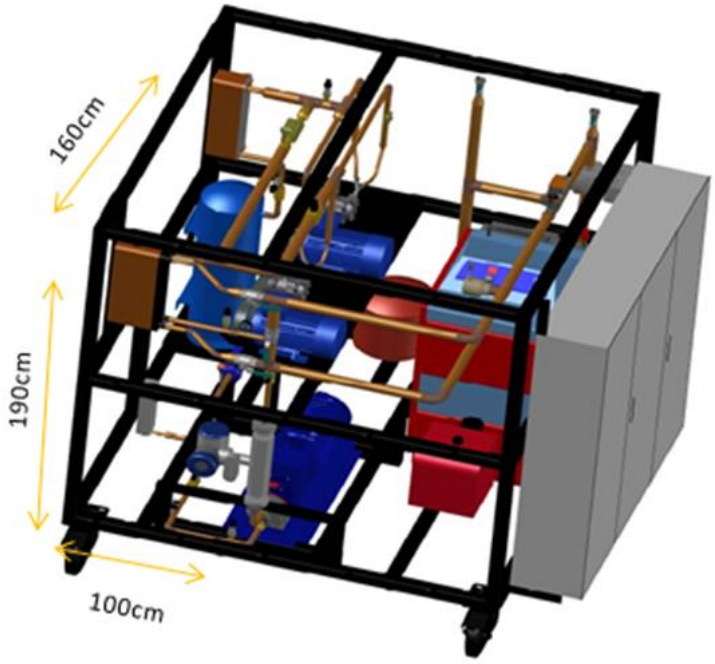

Figure 4.8: 3D AutoCAD drawing of the experimental ORC test rig (until November 2017) with the denoted required dimensions of the marine on board ORC prototype.

Specific details on the necessity of the motor power generator module and the resistor bank module are provided in the following section 4.4.

The ORC sub frames architecture was realized according to below principles:

- Minimizing the assembly time and effort,
- Maximizing the available suction head $NPSH_a$
- Ease of access to equipment and sensors.

Thus the piping interconnection for all three independent circuits (organic, hot water and sea water) between modules was achieved with the use of appropriate flanges. In order to be able to construct each piping a new detailed 3D module for each circuit independently was designed. Further details are provided in section 4.5, where the re construction of the on board marine ORC prototype is presented in detail.

4.4 Ship owner's requirements

Harmonic distortions are common voltage and current variations due to changes in frequencies within the electrical distribution systems. In particular, there are deviations from the typical sinusoidal variations in voltages or currents. Harmonics are mainly caused by nonlinear loads such as those associated with power electronic converters including variable frequency drives (VFDs) installed for fans and pumps, drawing in current in abrupt short pulses. The short pulses cause distorted current waveforms, which in turn cause harmonic currents to flow back into other parts of the power system.

Because equipment and machinery can malfunction or fail in the presence of high harmonic voltage and/or current levels, harmonic distortion has become a growing concern for facility managers, users of automation equipment, and engineers. While the presence of harmonics won't make it impossible for a facility or ship's grid to operate, the degree of impact depends on how much the power system can withstand and how susceptible the equipment is to harmonic distortion.

As a consequence to the above, the ship owner has required that the ORC internal electrical circuit design and ORC electrical supply and demand realization should address this possibility.

Hence, although the harmonics were measured with an external sophisticated energy analyzer (Ducati UPM6100) (Figure 4.9) and was found that harmonics distortion was, as expected, negligible to ship's grid capacity, the ship owner decided to impose the electrical isolation of the ORC prototype. This requirement was designed and realized as follows.

The basic idea, which was simple, was based on the installation of a motor generator module (Figure 4.11). The motor will be connected to ship's grid and through a belt pulley will rotate the generator. The motor generator module operation will be controlled via a VACON inverter model CXL4A710. The inverter will also operate a soft staring up device and its settings are presented in Table 4.6.

Hence, the generator will provide energy to the ORC for its starting-up while a set of passive load (5 air cooled 2 kW resistors) is connected to the common bus. As soon as the reverse power starts to flow, the regenerated power is to be dissipated on the passive loads. Via this interface the following are achieved:

- The ship electric energy system (450 V, 60 Hz) will be isolated during operation of the ORC unit. The only minor effect is anticipated to take place at the starting – up of the rotary frequency converter (high inrush motor current accompanied by significant voltage dip). In order to alleviate this phenomenon a soft-starting up device is to be used.
- The ORC unit will operate at 400 V/ 50 Hz i.e. no amendments are required compared with the operating conditions at NTUA / LSBTP premises.
- Following the main pre-requisite, no recovered energy will be injected to the ship electric grid.
- No current harmonics will be injected to the ship electric grid.

A similar version of this solution is used in military applications (warships) where a sensitive electronic equipment needs to be supplied by electric energy of high power quality without being subject to any harmonic distortion, and/or transients.

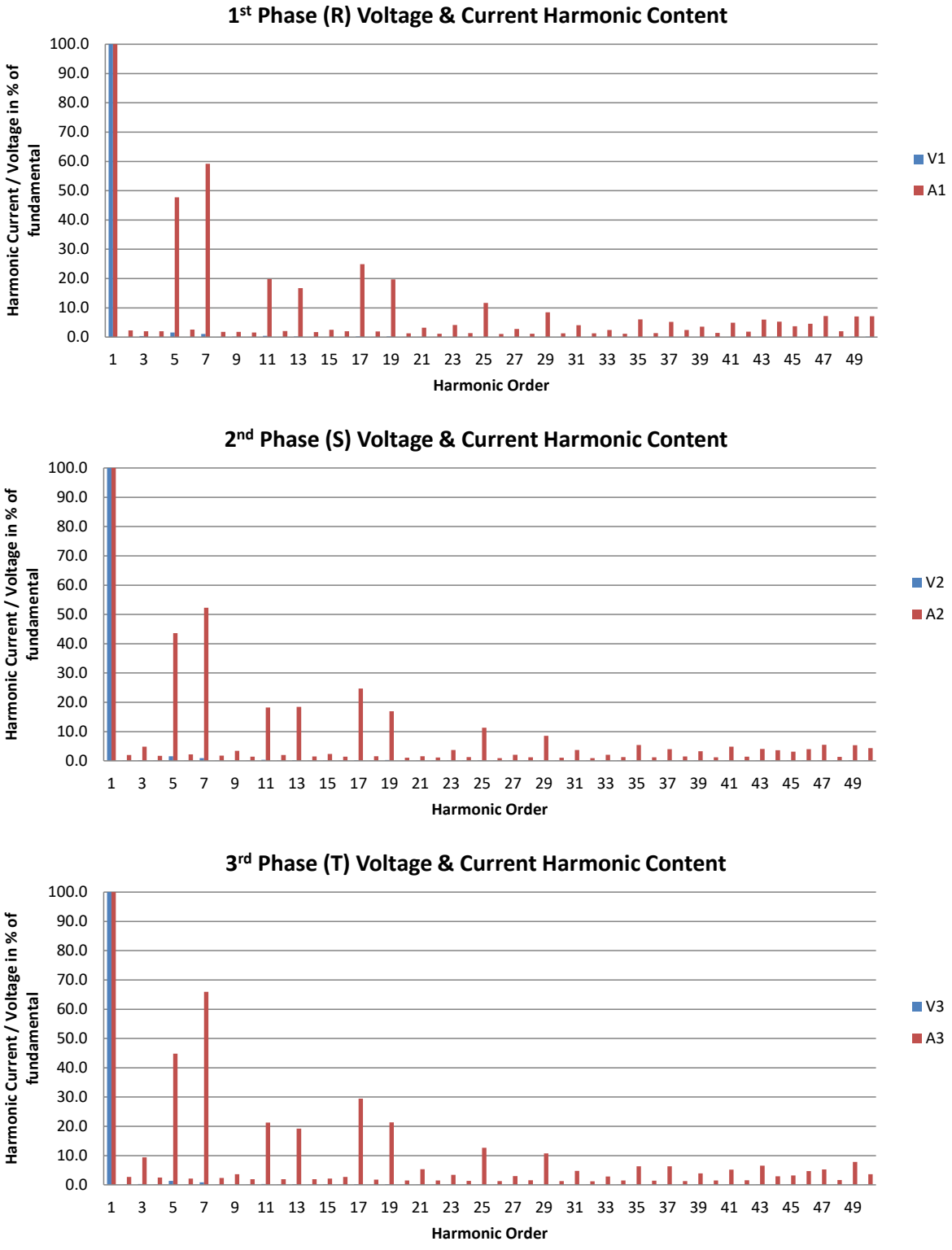

Figure 4.9: 3 - Phase Voltage & Current Harmonic Content during ORC prototype unit operation.

In following Figure 4.10, the basic electrical connection layout to ship's power grid is presented. As it will be described in section 4.6.3.4, the user can select the electrical grid to which the ORC unit will be connected (land grid or ship grid).

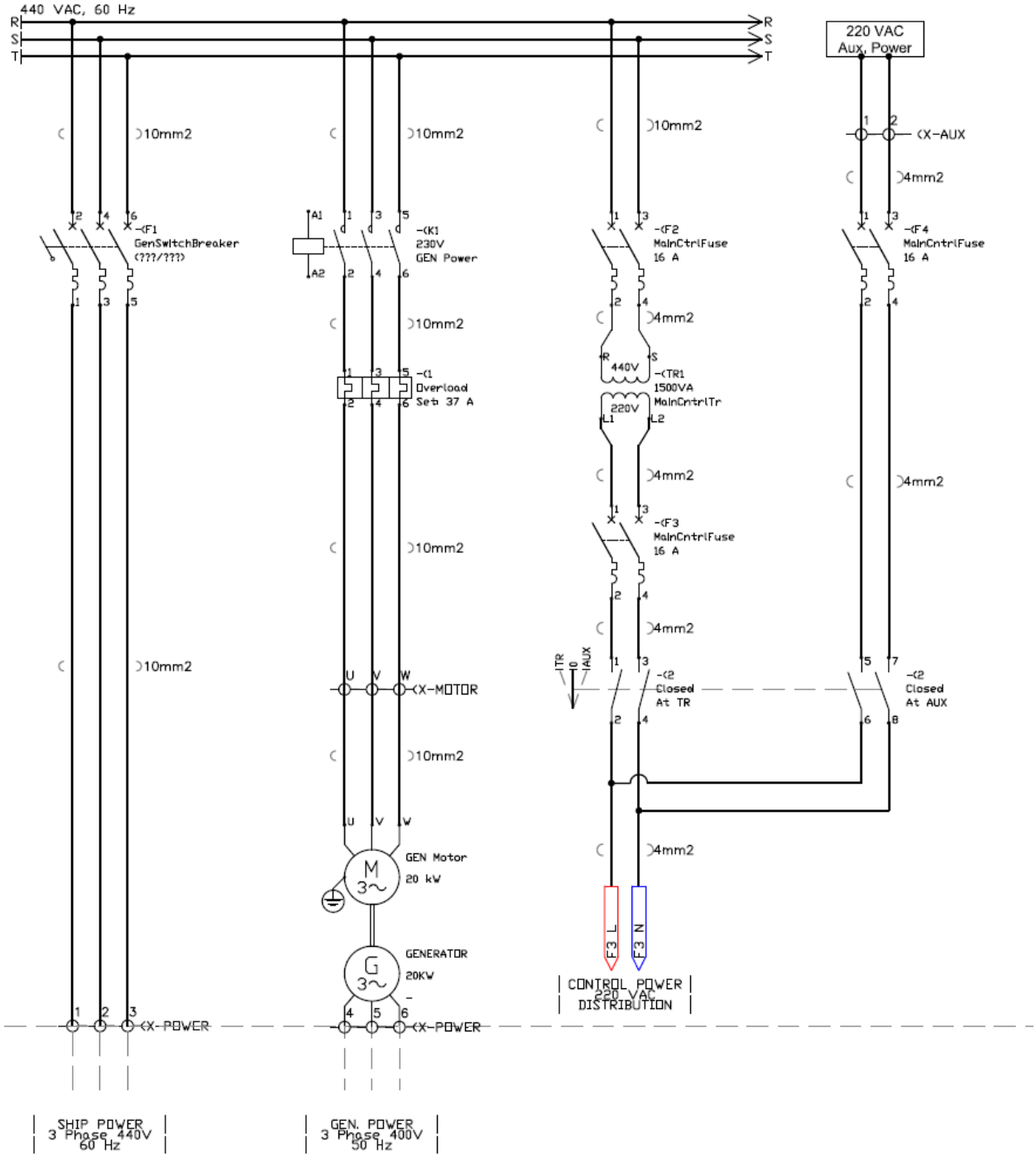

Figure 4.10: Basic electrical connection layout to ship's power grid or Auxiliary power (land grid).

In Table 4.5, the model, manufacturer details and technical characteristics of the motor generator module are presented. The motor generator arrangement is equipped with tension adjusters and a pulley/

belt for rotational speed transformation from 1750 / 1500 RPM. In addition, in Figure 4.11, the basic dimensions of the motor generator module are depicted on its overview and side view layout.

Table 4.5: Technical characteristics of motor generator module.

Motor Manufacturer	UMEB	Generator Manufacturer	MARELLI Motori
Family / Frame	ASNA 180M-4pole	Family / Frame	MJB 160 XA4
Rated Power	18.50 kW	Rated Power	14.0 kVA
Rotational speed	1500 / 1800 RPM	Rotational speed	1500 RPM
Efficiency FL	89 %	Efficiency FL	85 %
Power Factor	0.87	Power Factor	0.80
Frequency	50 / 60 Hz	Frequency	50 Hz
Voltage / Connection	400-Δ / 690 - Y	Voltage / Connection	400 V
Full load current	35 A / 20 A	Full load current	20.2 A
Insulation class	F	Insulation class	H
Enclose	55IP	Enclose	23IP
Feature	Cast iron - motor	Feature	Cast iron - motor
Code	E1097/2013	Code	MJB16X2G000M0M
Weight	136.0 kg	Weight	110.0 kg

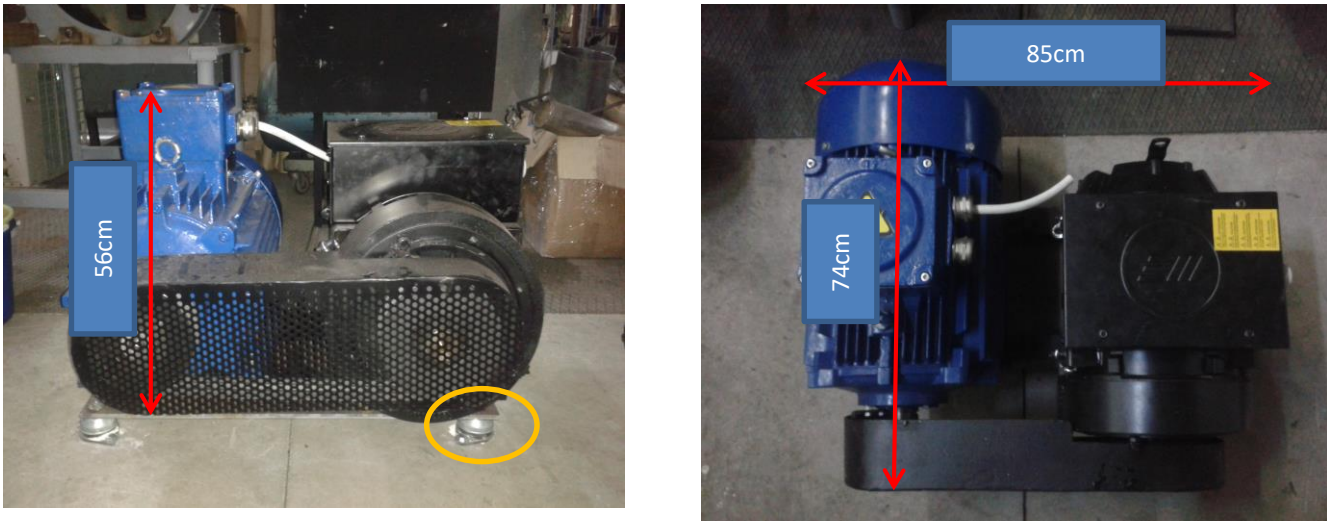

Figure 4.11: Basic dimensions of the motor generator module on its overview and side view layout.

Table 4.6: Technical characteristics & settings of motor generator module's VACON inverter.

VACON inverter - Model: CXL4A710 - Basic Settings						
Number	Parameter	Range	Selection	Step	Default	Description
0.1	Application Selection	1-7	1	-	-	1=Basic Application
0.3	Language Selection	0-2	0	1	0	0=English
1.1	Minimum Frequency	0-f_{max} (Hz)	60	1	0	
1.2	Maximum Frequency	f_{min}-120 / 500 Hz	60	1	50	
1.3	Acceleration Time 1	0.1-3000 sec	30	0.1	3.0	
1.4	Deceleration Time 1	0.1-3000 sec	30	0.1	3.0	
1.5	Reference Selection	0-15	13	-	0	
1.9	U/F Ratio Selection	0-1	0	1	0	0=Linear
1.10	Nominal Voltage of Motor	180-690 V	400	1	230	Voltage supplied to the Motor
1.11	Nominal Frequency of Motor	30 -500 Hz	50	1	50	From motor's rating plate
1.12	Nominal Speed of Motor	30 – 20000 RPM	1450	1	1420	From motor's rating plate
1.13	Nominal Current of Motor	2.5 x I_{nCT} (A)	35	0,1	I_{nCT}	From motor's rating plate
1.14	Supply Voltage	380-440 (V)	380 / 400	-	400	
1.15	Parameter Conceal	0-1	0	1	-	0=All parameter groups visible

During power generation operation, the net produced electrical power will be dissipated on the passive loads. The resistor bank is of 15 kW nominal capacity and includes fifteen (15) resistor modules, one (1) kW each. For the purpose of the ORC marine project, only 10 of those will be used in five pairs. According to previous experimental results, depending on the thermodynamic characteristics of the cycle, the ORC prototype produces from 3 to 5 kW net power. Thus, the simultaneous use of only three out of five resistor module pairs will be sufficient. The remaining 2 pairs will serve as backup and will be deployed

automatically by the automation and control system in case of other resistor failure. The model, manufacturer details and technical characteristics of the resistor bank are presented in Table 4.7. In addition, Figure 4.12 illustrates the side dimensions and the internal assembly of the resistor modules.

Table 4.7: Technical characteristics of resistor bank.

Motor Manufacturer	**GINO ESE**	**Voltage / Connection**	**3 phase 400 V**
Family / Frame	**DEG27430**	**Full load current**	**15 x 2.0A**
Total Rated Power	**15.0 kW**	**Enclose**	**23IP**
Resistor Number	**15**	**Feature**	**Stainless steel**
Efficiency FL	**100 %**	**Serial Number**	**726381**
Frequency	**50 Hz**	**Weight**	**App. 65.0 kg**

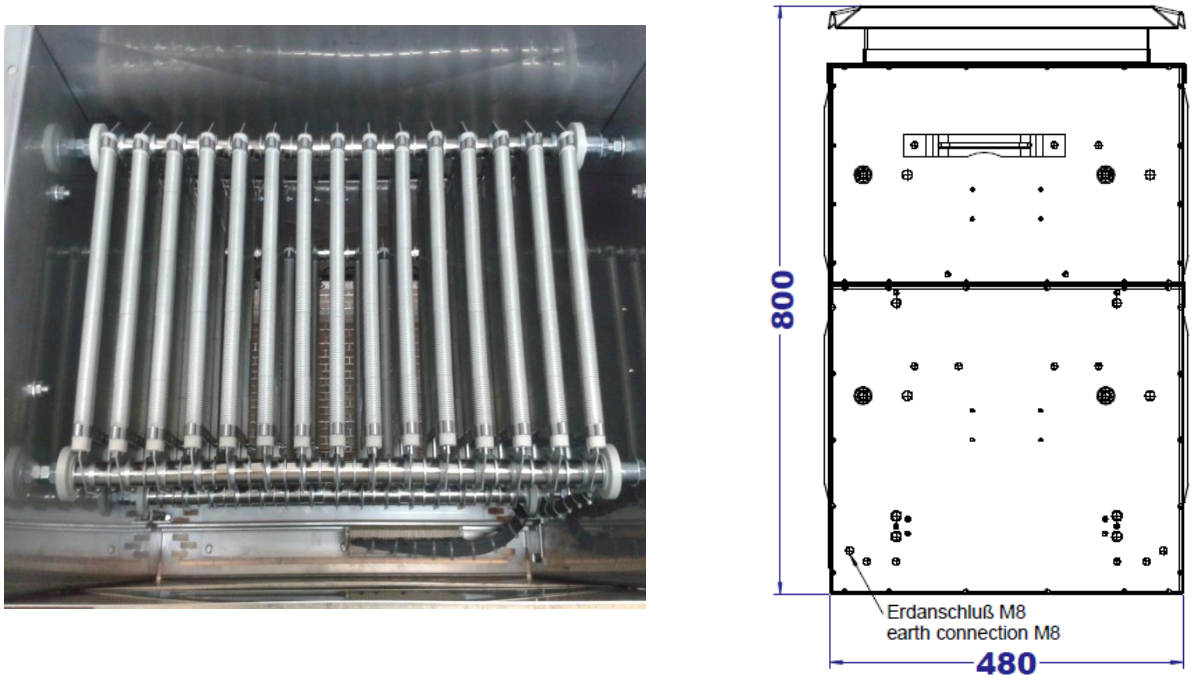

Figure 4.12: Side dimensions and the internal assembly of the resistor modules.

4.5 Re construction of the Lab scale ORC prototype

In the evolution towards the marine on board ORC prototype, an extensive re construction phase was designed and realized. As depicted in Figure 4.6 and described in corresponding sections of this chapter, several inputs by

- Hazard identification procedure,
- Dimensional constraints imposed by the ship's access ports and engine room site,
- Additional requirements set by the ship owner and
- DNV GL rules for classification

were taken into account during the design and realization of re construction phase of the ORC test unit.

These imposed inputs/ requirements had led to the following major alterations and improvements of the ORC prototype.

The ORC prototype was designed in a modular format. Apart from the dimensional constraints imposed by the ship's access ports and engine room site had to be taken in to account. In addition, the ORC prototype should be designed in a modular format, insuring that the transport and assembly on board would require only few hours. (See section 4.3)

An extensive reconstruction of the sea water circuit. The implementation procedure of DNV GL rules revealed several mistakes that originally were made during the design and construction of the first experimental ORC. These mainly had to do with the poor selection of appropriate equipment's material that consist the sea water circuit. Surprisingly, DNV GL Part 4 Systems and components Chapter 6 Piping systems Section 2 Clause 1.1.1 dictates that "traditional stainless steels, including 316 or 316L, should not be considered suitable for use in seawater systems". This requirement resulted in a complete reconstruction of the sea water circuit, since the condenser, sub cooler and piping was constructed by 316 stainless steel material. Hence two new copper-nickel-alloy heat exchangers by Bitzer Company were installed with an appropriate certificate of conformity for sea water systems (Bitzer K573HB and K123HB for condenser and subcooler respectively). At the same time the sea water piping was made from galvanized seamless carbon steel pipes according to International Standard ISO1461:2009. Furthermore, two 3-way valves are added along with the new condenser and subcooler. Each valve is controlled by a PID controller, which allows for regulation of both condensing and subcooling degree. In Table 4.8 and Table 4.9 below, are presented the basic characteristics of the condenser and sub cooler.

Sensors, PLC and other miscellaneous equipment. An independent emergency shutdown PLC, a new master PLC, two additional speedometers (Model 9210.001), two additional power meters (Model DUCA96LCD-IO) and other minor equipment were installed as a consequence, mainly, to hazard identification procedure and ship owner requirements. (See section 4.6)

A power supply motor generator module and a resistor bank were installed. This arrangement isolates the ship power grid from that of ORC prototype without compromising the necessary external power supply to ORC unit during startup and shutdown procedure. (See section 4.4)

Furthermore, detailed **electrical, P&ID and ORC prototype drawings (as built)** (i.e Figure 4.10, Figure 4.14 and Figure 4.15) were designed. In comparison to Figure 2.4, the updated P&ID of the WHR ORC prototype, as presented in Figure 4.15, includes all the necessary replacements of equipment, as a consequence of the requirements imposed by as described in present Chapter 4 (i.e. piping material, heat exchanger replacement, automation and control necessary equipment, etc).

Finally, after almost 15 weeks, the onboard marine ORC unit was ready for testing in the laboratory facilities (Figure 4.13). A tremendous effort by LSBTP personnel and external associates was the driven force of such an accomplishment. Nevertheless, a lot of work was needed to be done, namely debugging the automation & control strategy, testing all operational modes, alarm and trip functions and demonstrate a trouble free operation for at least 24hour and 48hour demo operation on laboratory test rig. Further details are provided in section 4.8.

Table 4.8: Characteristics of ORC prototype's sea water type condenser.

	Condenser (Bitzer K573HB) 4 pass connection
Length / Diameter (in mm)	1218 / 236
Heat transfer surface	1.330 m^2
Nominal heat transfer capacity (ΔT 15K)	86.2 kW_{th}
Maximum pressure	33 bar
Nominal flow rate (m^3/h)	8.33
Nominal Pressure drop, (bar)	0.59
Volume (lt)	29.4

Table 4.9: Characteristics of ORC prototype's sea water type subcooler.

	Condenser (Bitzer K123HB) 4 pass connection
Length / Diameter (in mm)	881 / 125
Heat transfer surface	0.300 m^2
Nominal heat transfer capacity (ΔT 15K)	15.0 kW_{th}
Maximum pressure	33 bar
Nominal flow rate (m^3/h)	1.37
Nominal Pressure drop, (bar)	0.28
Volume (lt)	5.1

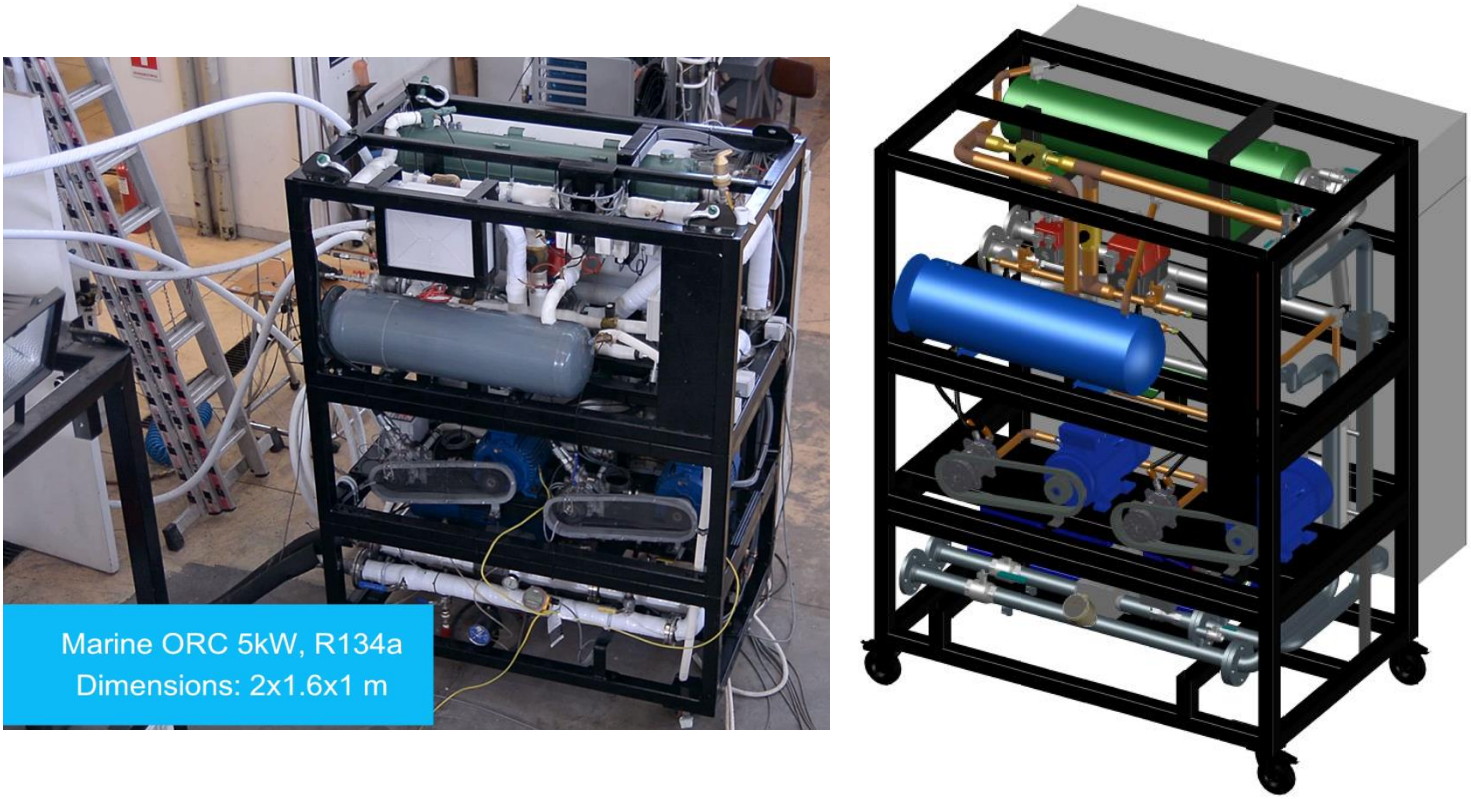

Figure 4.13: Final arrangement of on board marine ORC prototype & 3D AutoCAD drawing.

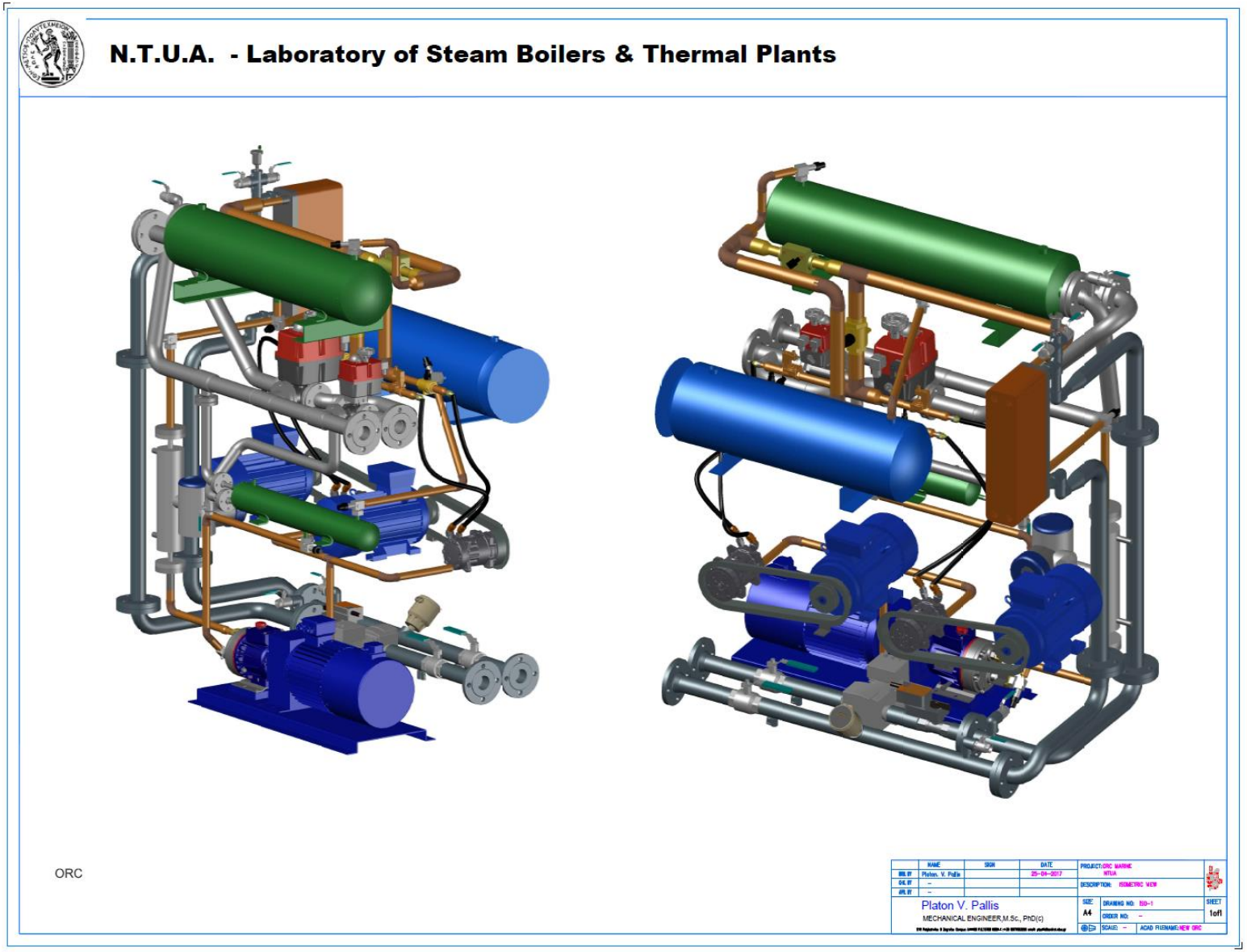

Figure 4.14: Final arrangement of all three independent circuits of the ORC prototype (Refrigerant, Hot water and Sea water circuit).

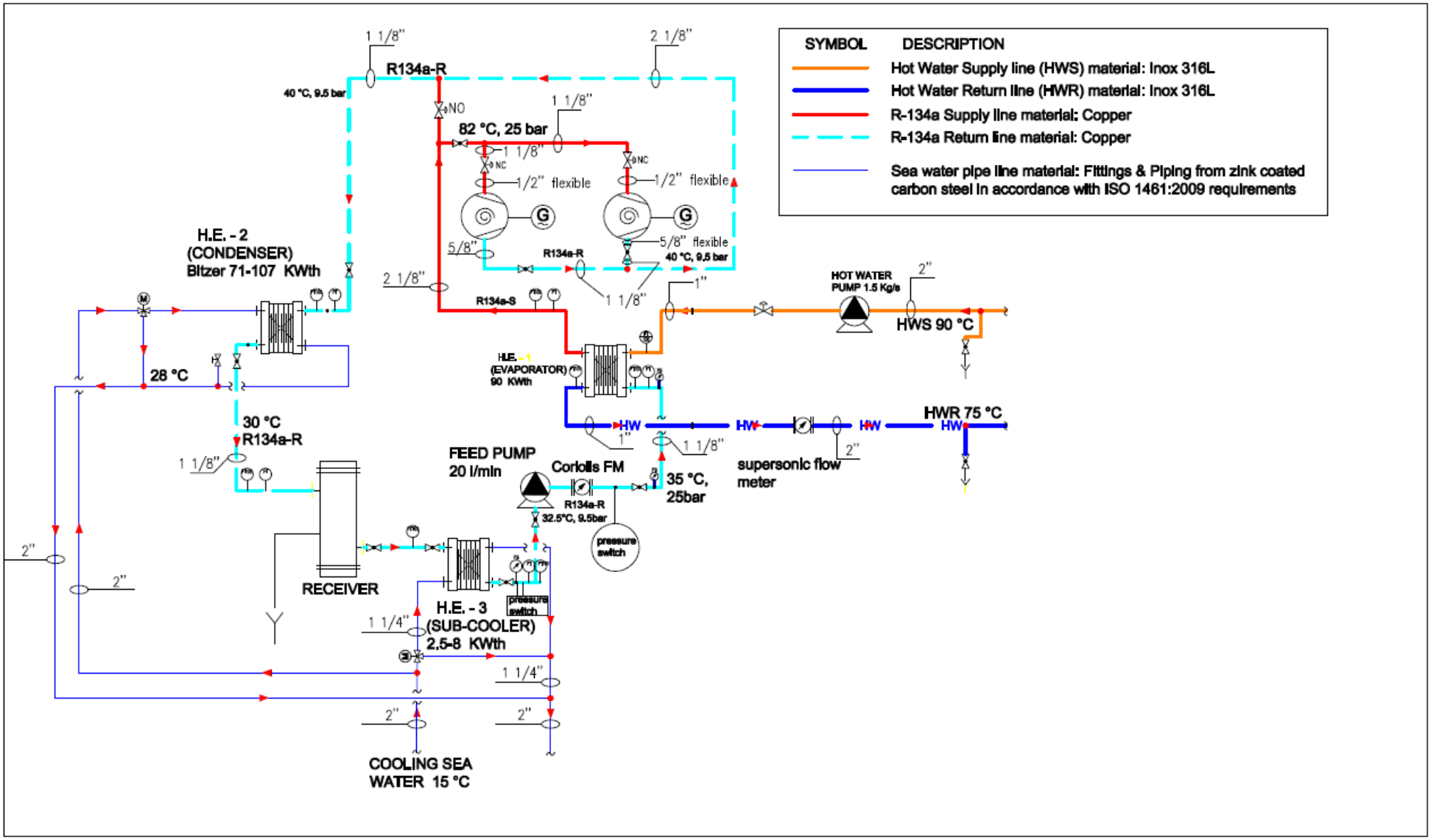

Figure 4.15: P&ID schematic of marine WHR ORC prototype (as built) & approved by DNV GL.

4.6 Automation & control of on board ORC prototype

4.6.1 Design and description of the automation system

Based on the conclusions arisen from the experimental investigation of the operation of the ORC prototype under different laboratory conditions, the ship owner's requirements and all corresponding remarks from the hazard / risk assessment, a strategy and structure were developed for the automation and control of the ORC prototype, necessary for its safe and uninterrupted operation on board.

The main issues that the automation and control system has to address are related to:

- Safe startup and shutdown of installation.
- Protecting the pump from cavitation phenomena.
- Controlling the vapor pressure to prevent the ORC from being shutdown (trip function) by the over-pressure switch.
- Achieving the most efficient operation of the installation, depending on the operating condition.
- Data logging and remote installation monitoring and control.
- Ensure emergency shutdown, in pre define occasions / incidents.

Following the safety requirements set by the risk assessment, it was considered necessary to install two different PLCs, one of which would function as a safety PLC. The latter PLC would control the installation for critical faults and cause its immediate shutdown at any of those, through the realized emergency shutdown (ESD) procedure. At the same time, the main PLC will monitor and control the ORC prototype under normal operating conditions and also record data from all existing sensors and metrics (Section 2.11.5) and those added during the last stage of development (Section 4.5).

In order to upgrade the ORC prototype control during normal operating conditions, it was decided to place two three-way valves at condenser and sub cooler inlet, respectively. These three-way valves will be used to control the low cycle pressure and the subcooling level respectively, by adjusting the cold water supply to the two heat exchangers. The hot water supply will be controlled with the already existing Bellimo control valve (see Section 2.9). As described previously, the hot water circuit will also use the circulating pump (Wilo Stratos) to ensure the desired water supply to the evaporator. The aforementioned equipment in combination with the pump speed and the scroll expanders / generator regulators are the automation system actuators. All of the above are illustrated in Figure 4.5.

Finally, it is reported that a normally open (NO) solenoid valve (bypass valve) and two normally close (NC) solenoid valves were used to bypass or supply the expanders during different operational states. Further information is given at respective section 4.6.3. The above valves are also illustrated in Figure 4.5.

4.6.2 Design and description of the emergency shutdown (ESD) autonomous system

The independent emergency shutdown PLC is Schneider's TM221-M16R model from the Modicon M221 series. It has eight digital inputs and eight digital outputs, and also has two analog inputs for 0-10 V type signals. It also has the capability of communicating either serially or online with the Modbus RTU or Modbus Ethernet protocol respectively. This way the security PLC can communicate with the PLC that controls the normal operation of the installation and can share data or give commands.

The key controls (trip functions) made by the emergency shutdown PLC are:

- ✓ Check for faults in the regulators/ controllers of the expanders and the pump. Each controller gives a digital signal if an error/ fault is detected (eg due to DC Link overload), so fault checking on all controllers uses 3 digital inputs of the emergency shutdown PLC, in total.
- ✓ Detection of possible overpressure or under pressure in the low pressure circuit and overpressure in the high pressure circuit. In more details, at the low pressure circuit, two pressure control sensors were installed to protect from too low and too high pressure, which were set at 5 bar and 16 bar respectively. The high-pressure circuit had an independent high-pressure pressure control sensor set at 28 bar. These pressure sensors were already part of the "old automation system" and occupied three other digital inputs of the emergency shutdown PLC, in total.
- ✓ Check for expander's over speed, which is realized by installing two new speedometers (similar to those installed in generators) on the shafts of the two scroll expanders. Hence, at the last development phase, two proximity sensors (speedometer) are installed in each pair of scroll expander / asynchronous motor. Thus, installation is monitored and secured, at the same time, from possible over- speed of the generators due to pullout torque (section 2.6) and expander over speed due to belt failure. The latter is realized according to the following conditions, any difference detected in each pair of measurements is evaluated by the PLC with a 5 % permissible limit of differentiation and a set ≤1500 RPM upper limit (double condition). According to previous, the two new speedometers utilize the two analog inputs of the emergency shutdown PLC.
- ✓ Activating the emergency shutdown sequence when pressing the emergency shutdown button on the front side of ORC electrical panel (one additional digital input).
- ✓ Signal from the main PLC of the ORC prototype when one of the pressure or temperature sensors is malfunctioning (alarm) or if the main PLC itself is not functioning properly (eg due to damage), which is realized by communicating the two PLCs via Modbus.

If any of the above controls fails with the exemption of non critical sensors, the system enters ESD. The procedure for immediate shutdown provides for the following actions:

- Stop refrigerant pump operation
- Close the isolation valves (NC solenoid valves) of the two expanders and open the bypass solenoid valve (NO solenoid valve).
- Stop of induction generator speed regulators
- Stop the hot water pump in the high temperature circuit (evaporator)
- After a short time, fully open the three way valves that regulate the condenser and subcooler cooling water flow in order to reduce the average refrigerant temperature.

As can be seen from the above description, the integrated inlets and outlets of the emergency shutdown PLC processing unit are sufficient for the checks and controls to be carried out, so no additional cards are required.

4.6.3 Design and description of the control strategy

Different strategies for controlling an ORC plant are mentioned in the literature, but few focus on plant control with positive displacement pumps and scroll expanders and none to the specific requirements imposed by the ship engine room's particularities and constraints. [63] & [64]

The realized control strategy in the marine on board ORC prototype is based on controlling the pressure and temperature of the cycle's superheating by controlling expander/generator and feed pump rotational speeds with the deployment of standard PID controllers. This straightforward control concept is designed to maintain the superheating temperature and related pressure at their nominal rated values, or be adapted to the optimal settings, depending on real system conditions and may have resulted from a steady-state modeling of the cycle. Its philosophy is similar to that described by S. Quoilin et. al. [65]. In this way, the controller set points can be variable and calculated as a function of the operating conditions of the cycle.

During the control strategy design, the basic conclusions arisen from experimental campaigns and risk assessment were set as corner stones of the architecture. Some of those are summarized as follows:

- Optimizing the operation of the ORC prototype in terms of output power requires maintaining the expander's rotational speeds at 1450 RPM (see Section 3.11& Section 3.12).
- A constant value of subcooling temperature between T_{sc} = 4.5 to 5 °C ensures efficient and free cavitation pump operation of the ORC prototype. Thus, the control of a dedicated three-way valve was decided and realized.
- The low pressure at all operating points does not change significantly unless the temperature of the cooling water of the condenser is changed significantly. On the other hand, in the event of a change in the cooling water temperature, the low pressure can be maintained at a constant value by adjusting its flow rate with the use of a dedicated three-way valve.

- In order to avoid a two phase state at the outlet of the evaporator when the hot water inlet temperature is lowered, it is necessary to reduce the pump rotational speed (and therefore the flow rate). This reduction could be based on maintaining the high pressure at a value that ensures the maximum net electrical power output, which is a function of the hot water temperature and implemented with a variable set point controller. [61]
- For simplicity reasons, for the operation of the installation on board, maintaining the superheating temperature at a constant value by controlling the pump rotational speed proved to be able to ensure that the working medium would always exit the evaporator in superheated state, without reducing significantly the power output.
- Controlling the vapor pressure below 25 bar, at all times, also requires the operation of a second controller that will act on the regulating valve of the hot water circuit (section 2.9).

At the same time, the observations made during the experimental trials served as good operational practices and taken in to consideration during the design process. Those observations could be summarized as:

- A sharp decrease in the temperature of the cold water in the condenser, or an increase in its supply, can cause cavitation in the pump due to the thermal inertia of the feed container. As a consequence, a sharp reduction in the pressure of the container which may lead to a reduction in the suction height available before the pump should be avoided.
- The receiver temperature must be maintained above a certain value both during start-up and during operation of the ORC prototype, due to a reduction in the suction height available at the pump suction inlet and the efficiency of the subcooling exchanger. Otherwise, subcooling should be increased to avoid cavitation effects on the pump.

Based on the above, it was decided to control the marine on board ORC prototype by using five PID controllers.

1st PID controller. A controller will control the receiver's pressure by regulating the cold water flow to the condenser through the corresponding three-way valve. When the temperature of the cooling water drops, the three-way gradually closes, keeping the receiver pressure to the desired value, preventing it from cooling down further, which may make it difficult to protect the pump from cavitation effects. When the water temperature rises again, the three-way valve will open by increasing its supply to the condenser in order not to further reduce the installation pressure ratio and consequently the output power. Based on experimental investigation results, the controller was set to the realistic value of:

$$p_{receiver\ set\ point} = 8.5 \text{ bar}$$

2nd PID controller. A controller will control the desired subcooling temperature T_{sc} by adjusting the supply of cold water to the subcooler through the corresponding three-way valve. When the cooling water temperature drops, its supply will also be reduced to avoid raising the subcooling temperature which

adversely affects the efficiency of the plant. If the temperature of the cooling water increases, its supply will be increased to keep the cooling temperature at the desired levels to avoid cavitation in the pump. Based on experimental investigation results, the controller was set to the realistic value of:

$$T_{subcooling\ set\ point} = 5\ ^oC$$

The following two controllers were realized specifically for the ORC prototype operation in the ship's engine room:

3rd PID controller. This third controller will control the high pressure of the refrigerant cycle so that it does not exceed the limit of 25bar by adjusting the supply of hot water to the evaporator with the Bellimo regulator valve. The operation of this controller serves as an automated way to limit the vapor pressure of the cycle below a certain value without interrupting its operation by the high pressure switch. The set point of this controller will be at:

$$p_{high\ pressure\ set\ point} = 25\ bar$$

4th PID controller. The next controller will control the superheating temperature of the cycle, and thus assuring that it always be set accordingly in order to avoid the supply of two-phase organic medium into the expander. The control will be realized by adjusting the rotational speed of pump's motor and thus the organic medium supply flow rate. This value should be as minimum as possible in order to increase the power of the system and was therefore chosen as:

$$T_{superheating\ set\ point} = 2.8\ ^oC$$

The superheating temperature is calculated as below

$$\mathbf{T_{sh}=T_{evap,ex}-T_{sat}} \quad (4.1)$$

where T_{sat} is the saturation temperature for the measured evaporating pressure, which can be correlated with the following polynomial function:

$$\mathbf{T_{sat}\ (°C)= -0.02574 \cdot p_{evap}\ (bar_a)^2+3.1810 \cdot p_{evap}\ (bar_a)+14.0488} \quad (4.2)$$

5th PID controller. The last controller will cope with the pump's cavitation phenomena if present. As long as the system is in normal operation, a continuous check for cavitation on the pump is carried out. If cavitation phenomena are present, the 5th PID controller overrides - deactivates the 2nd & 4th PID controller. When, the cavitation is resolved, then the 5th PID controller allows the 2nd & 4th PID controller to resume their control sequence. Further details are presented on following sections 4.6.3.1 & 4.6.3.2.

The above controllers' architecture allows the safe operation of the installation at the ship's engine room, while based on Chapter 3 results, also ensures that the net power output is kept to the maximum possible in the event of a hot water temperature drop. In addition, the decision to be fixed-point

controllers, greatly simplifies the implementation of the automation & control system strategy, given the extreme time constraints imposed by the project.

The gains of these controllers were regulated during the testing phase performed in laboratory facilities.

4.6.3.1 Startup and shutdown mode of the installation

The startup process and the normal shutdown process were the two fundamentals modes of the control system implemented.

The startup process is initialized with the click of a button on installation's HMI. The consecutive steps that are followed are as follows:

1. Checking for either a sensor or the main PLC failure or for a signal from the ESD PLC due to the failure of any of the controls it performs. The process will only continue if the above checks are successful.
2. 50 % opening of the regulator valve in the evaporator.
3. The hot water pump is activated.
4. Check whether the temperature of the hot water inlet in the evaporator is above 70 °C. Otherwise, the system will be in a sleep mode (see section 4.6.3.4) until the above condition is met (ie $T_{hw} \geq 70$ °C).
5. The NO Bypass solenoid valve remain open (see Figure 4.5 or Figure 4.15) while the NC solenoid valves at expanders' inlet remain closed.
6. The T_{sc} subcooling temperature controller is activated.
7. The pump starts ramping smoothly from 0-20 Hz (approx. 400 RPM).
8. After a short time, the condensing pressure controller $p_{receiver}$ is activated.
9. The two asynchronous machines start as motors, with their speeds being set at 800 RPM.
10. The system is operated under these conditions until the organic medium temperature at evaporator's outlet exceeds the 74 °C. Once this condition is satisfied, the system resumes the startup process (step 11).
11. The high pressure controller $p_{high\ pressure}$ is activated. Under normal conditions this should open the hot water regulator valve completely at the evaporator inlet, since the pressure should be well below 25 bar.
12. The two scroll expanders are engaged with the induction motors and their NC solenoid valves are opened at the same time. The passing fluid accelerates the induction motors beyond synchronous rotational speed and thus they now act as generators.

13. The pump is accelerated smoothly up to 50 Hz (approx. 960 RPM) which is the speed at the rated operating point of the installation.
14. The expanders' rotational speed is adjusted following pump's rotational speed increase. The pair values of pump and expanders' rotational speed are summarized in the below Table 4.10.
15. The system reaches the rated rotational speeds for the pump and the scroll expanders.
16. The superheating temperature controller is activated, controlling the pump rotational speed so as to always achieve the desired superheating temperature of the medium.

Table 4.10: Paired set of values of pump rotational speed and expander's rotational speed during startup or shutdown process.

Pump rotational speed N_{pump} (Hz)	Expanders' rotational speed N_{exp} (RPM)
20	**800**
30	**1100**
40	**1300**
50	**1450**

Reaching step 16, the system is in its normal operating state, with the first four PID controllers described in the previous section, controlling and adjusting the cycle variables.

At the same time, as long as the system is in normal operation, a continuous check for cavitation on the pump is carried out (5th PID controller). This control is based on the following condition:

$$\Delta m < 5\ \% \qquad (4.3)$$

where:

$$\Delta m = \frac{m_{th} - m_{meas}}{m_{th}} \qquad (4.4)$$

the relative difference of theoretically calculated mass flow from the real time measured with the Coriolis flow meter.

Theoretical mass flow can be calculated from the following equation:

$$\boldsymbol{m_{th} = \rho \cdot \dot{V}} \quad (4.5)$$

where $\dot{V}$ the volume flow rate pumped by the pump (see equation (**3.19)**) and (ρ) the mean density at the pump inlet conditions. As just mentioned, the volume flow rate calculation is based on the equation **(3.19)** derived from the experimental investigation and not from the theoretical equation (2.3) as derived by given manufacturer Figure 2.7 (for further details see section 3.7).

The above relationship requires the calculation of the density of R134a as a function of pressure and temperature real time measurements at pump inlet. Of course, since the pressure has very little influence on the density of the medium, which is in the subcooled state, it can alternatively be assumed that p = p (T) and finally the density can be approximated by an equation resulting from the correlation of pair values which gives a library of thermo physical properties (i.e. CoolProp) only in relation to the temperature of the medium.

In practice, since the receiver temperature will vary in a narrow range, and in order to simplify the control strategy algorithm, an average value of the density (ρ) was used, corresponding well with the ORC operating conditions. This value is set to:

$$\boldsymbol{\overline{\rho} = 1236.98 \ \frac{kg}{m^3}} \quad (4.6)$$

Finally, the above average value of density in conjunction with equation**(3.19)** finally gives the following expression (equation **(4.7)**) for the theoretically expected mass flow rate.

$$\boldsymbol{m_{th}\ (kg/sec) = 0.00416\ N_p\ (RPM) - 0.00344} \quad (4.7)$$

where N_p is the feed pump rotational speed.

If the condition of equation **(4.3)** is not satisfied, the installation is considered to operate in cavitation mode. Further information on the specific operational mode / state is provided in coming section 4.6.3.2.

Also, if the organic medium temperature at evaporator's outlet corresponds to a temperature of less than or equal to 74°C, the system enters standby mode (see section 4.6.3.3).

Reverse to startup procedure, **the shutdown sequence** is initialized with the click of a corresponding button on installation's HMI. The consecutive steps that are followed are as follows:

1. The pump's rotational speed controller is switched off.
2. Pump rotational speed is reduced smoothly down to 20 Hz (approx. 400 RPM).
3. The expanders' rotational speed is adjusted following pump's rotational speed decrease. The pair values of pump and expanders' rotational speed are summarized in previous Table 4.10.
4. As soon as the pump reaches 20 Hz, the bypass solenoid valve opens.
5. The NC solenoid valves at expanders' inlet are closed and at the same time expanders are disconnected (clutch deactivated) from the induction generators.

6. The two induction motors (which now operate in no load) cease to operate.

7. The evaporator pressure controller is shutdown.

8. The hot water control valve is adjusted to 50 %.

9. The ORC feed pump is stopped.

10. The hot water pump stops & after a while hot water control valve is fully closed.

In Figure 4.17, the general flowchart of automation & control strategy and procedure is illustrated. The conditions and sequence between all modes of operation are presented.

4.6.3.2 Cavitation mode

As mentioned above, during operation of the ORC prototype, a continuous check is carried out for possible cavitation at pump's suction inlet, independently from the operation of the sub cooling and low pressure (receiver) PID controllers.

If the condition of equation **(4.3)** is not satisfied, the installation is considered to operate in cavitation mode. This means that

$$\mathbf{\Delta m > 5\ \%} \quad (4.8)$$

So when the control system calculates that the relative difference of real time measured with the Coriolis flow meter from the theoretically expected mass flow exceeds the 5 % threshold, the following procedure is performed:

- From the all four PID controllers operating in the normal operation of the ORC prototype, the super heating temperature T_{sh} and the sub cooling temperature T_{sc} PID controllers are deactivated, while the remaining two PID controllers are still activated.
- The three-way valve of the sub cooler is now controlled by a new PID controller which has the following set point:

$$(\Delta m)_{setpoint} = 3\ \%$$

- In addition, the pump rotational speed is controlled by a new controller, as well, with the same set point as above:

$$(\Delta m)_{setpoint} = 3\ \%$$

These two controllers will tend to increase the water supply to the sub cooler and at the same time reduce the pump rotational speed, as the difference Δm deviates from the value of 3 % due to its constant increase. The reason the first PID controller was added is obvious. For the latter it is remind that the critical suction height $NPSH_r$ is an increasing function of the pump rotational speed and the magnitude of the acceleration head factor H_α (equation (3.2)). Therefore, reducing the pump speed can drastically help increase the difference

$$\mathbf{\Delta NPSH = NPSH_a - NPSH_r - H_a} \quad (4.9)$$ (see also section 3.1).

- At the same time as the pump speed decreases, the speed of the expanders decreases according to Table 4.10.
- The activation of the above controllers remains until the difference Δm is:

$$\Delta m < 4\ \%$$

- When the above criterion is met, the two controllers no longer affect the pump speed and the three-way water of the subcooling exchanger. The system remains in this state for about 30 seconds to balance and then accelerates according to Table 4.10 to normal operating speeds. The two controllers for the subcooling temperature and superheating temperature are reactivated and the system is functioning normally.
- If in this mode the pump rotational speed is lower than or equal to 20 Hz (400 RPM), the system exits the cavitation mode and is driven to Standby-Bypass mode (section 4.6.3.3)

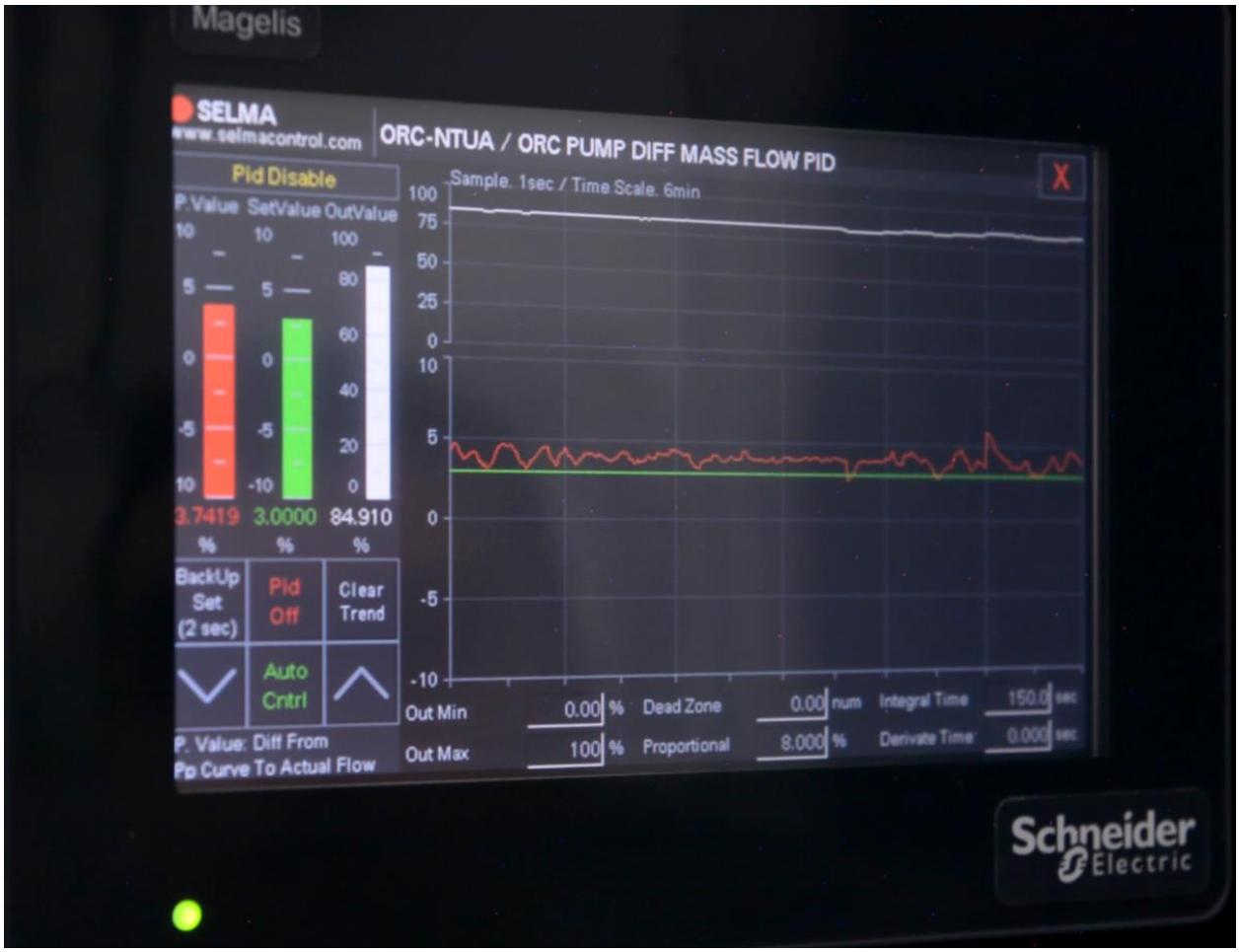

Figure 4.16: ORC- NTUA 5th PID controller (based on pump's mass flow difference).

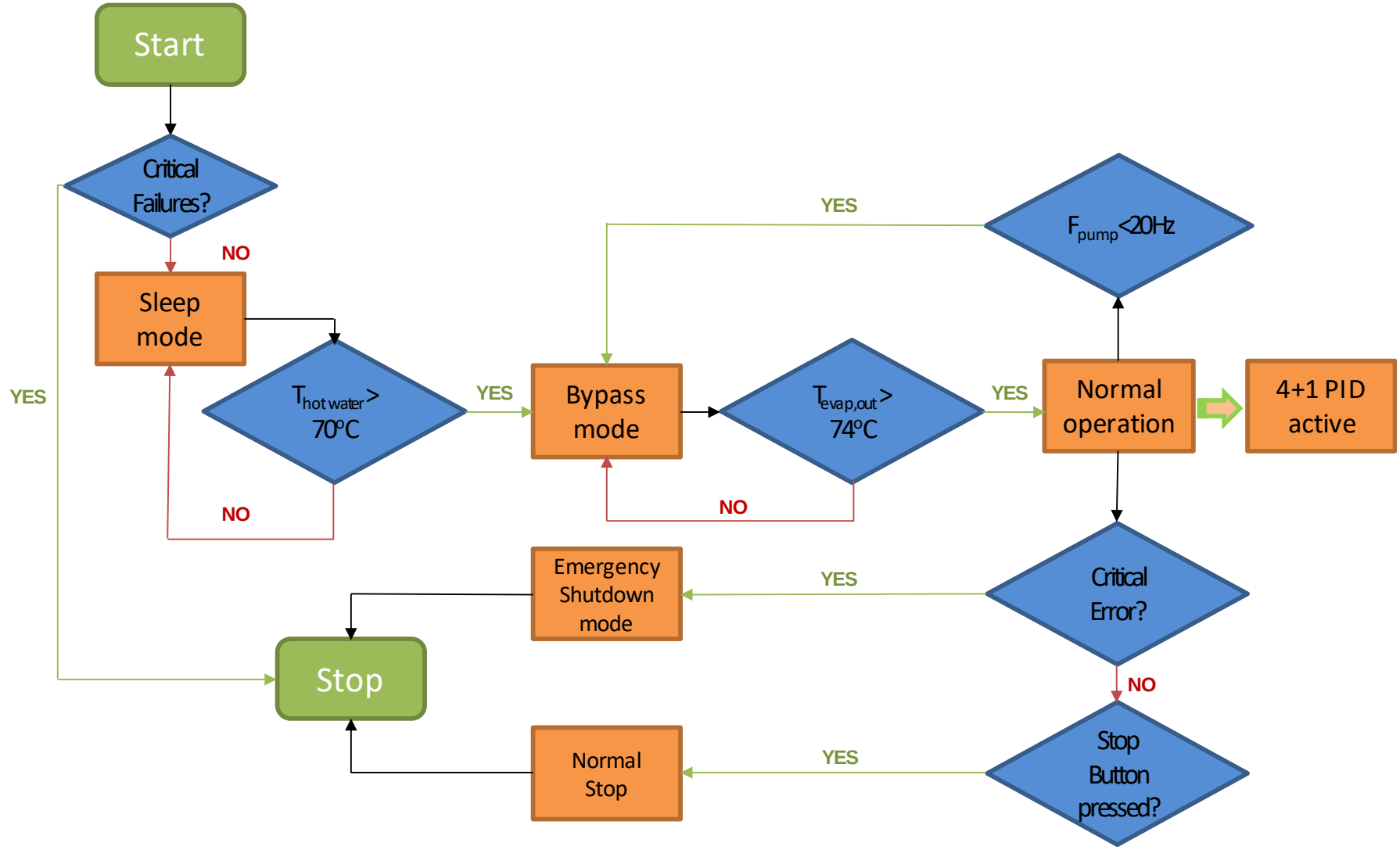

Figure 4.17: General flowchart of automation & control strategy and procedure.

4.6.3.3 Standby – Bypass mode

This mode is activated in any of the following two occasions:

During the cavitation mode: If the cavitation phenomena is so rapid and intense that the pump rotational speed reaches values less than or equal to 20 Hz. In this case, the ORC prototype should not interrupt its operation but wait until the origin/ cause for the cavitation is eliminated (i.e. abrupt decrease of the condenser cooling water temperature or inability to sub cool the organic medium due to high cooling water temperature).

During the normal operation of the ORC prototype: If the organic medium temperature at the evaporator outlet falls / is below 74 °C during normal operation of the ORC plant, then the produced net power output will decrease so drastically, that will be useless. The plant remains in this state until the high cooling water of the ship's main engine can raise the temperature of the organic medium in the evaporator outlet above the 74 °C threshold.

According to control strategy architecture, for one of the above reasons, in this mode, the following actions are realized:

- The superheating temperature controller T_{sh} is deactivated.
- Pump rotational speed is reduced smoothly down to 20 Hz (approx. 400 RPM).
- The expanders' rotational speed is adjusted following pump's rotational speed decrease. The pair values of pump and expanders' rotational speed are summarized in previous Table 4.10.
- The Bypass solenoid valve opens.
- The NC solenoid valves at expanders' inlet are closed and at the same time expanders are disconnected (clutch deactivated) from the induction generators.
- The other three PID controllers of normal operation remain activated.

In order for the system to exit standby mode both following conditions must be satisfied:

$$\Delta m < 4\ \%$$

$$T_{evap,\,out} > 74\ °C$$

Hence, if above conditions are met, the system returns to normal operation following steps 12-16 of the startup process (section 4.6.3.1).

During standby, the systems pump remains in operation, while the working medium passes through the bypass circuit that leads to the condenser. It is obvious that during standby mode, the installation absorbs, indirectly, power from the ship's electricity grid, waiting until appropriate conditions are met to return to normal operation. On the other hand, if the hot water temperature gets even lower, there is no reason for the system to remain in this state at all.

Consequently, in the event that the hot water temperature inlet at the evaporator gets lower than

$$T_{hotwater} < 70\ °C$$

the system enters its last possible mode, which is called “sleep mode”.

4.6.3.4 Sleep mode

As already mentioned, sleep mode is only activated when the hot water temperature at the evaporator’s inlet is lower than 70 °C. In this case, the operation of the system is considered unnecessary from an energy point of view, since the organic temperature at the evaporator’s outlet will be insufficient.

Consequently, during this mode, the installation follows the normal shutdown procedure but bypasses step 10, that is, turning off the hot water pump and shutting off the hot water control valve.

The hot water circulator remains active to constantly monitor the high temperature of the jacket’s cooling water circuit. When this temperature reaches temperatures above 70 °C, the installation exits the sleep mode and follows the normal start-up steps to return to its normal or standby mode operation.

4.6.4 Description of the master PLC

A new master PLC is used to control the installation based on the philosophy described in the previous sections. This is a Schneider PLC and belongs to the Modicon M340 series and the exact model of the central processing unit is the BMXP-342020. This unit has communication capabilities via Modbus RTU and Modbus Ethernet, just like the installation PLC security.

In order to provide the necessary inputs and outputs to the PLC, two 16-digit Input Cards (BMX-DDI-1605), two 16-Input Digital Cards (BMX-DDO-1602), three 8-Input Cards (BMX-AMI-0810) and two 4-way output cards (BMX-AMO-0410) were used. Finally, the PLC is powered by the same power supply (BMX-CPS-3020).

In addition to the PLC, a 7 ''Schneider HMI-G3U series touch screen was installed to handle the installation and display the sensor values. This display has a built-in HMI-DT351 processor which, among other things, can communicate either serially or with a local area network through the Modbus protocol.

The touch screen and the two PLCs (master and ESD PLC) of the plant are located on a common local area network via a switch. This computer can be connected to any computer in order to retrieve data from the PLC of the installation or modify any of the parameters of the control system (eg controller set points). The ability to modify parameters and record data on an SD card is also provided via the touch screen.

Existing and extra power analyzers are connected directly to the plant's master PLC through the Modbus RTU serial communication protocol. Speed regulators communicate with the PLC through their analog inputs and outputs. The same applies to all pressure and temperature gauges of the cycle and both flow meters. Finally, the three-way valves and the regulating valve in the water circuits are controlled through the analog outputs of the master PLC.

4.6.5 Description of the Human Machine Interface layout

As already mentioned, the marine ORC prototype is equipped with a Human Machine Interface (H.M.I.) which allows the parameterization and operation of the marine ORC prototype, according to the conditions and scope of operation.

As presented in Figure 4.24, the H.M.I. operation and parameterization is based on a four sub planes concept and architecture.

In the first plane (Main Page Interface), the selection and access to the main operating features (gray tabs), independent PID controllers (blue tabs) and alarm, trip and configuration pages (green tabs) is provided.

The main operating features (grey tabs) are:

The Startup Page. The selection of the prototype's operating alternatives is done among the Lab, Manual and Auto mode. Each of three alternatives provides different predefined permission and operating strategy. In Lab scale mode, all parameters can be change accordingly by the user. In manual mode, only few parameters can be changed such as pump rotational speed, 3-way valve position, etc. In auto mode the user can monitor the operating conditions through the system overview page and alarm log page but every parameter has a predefined value and nothing can be changed by the user. The marine ORC prototype will operate on board in auto mode. Furthermore, the user can set the resistor load and the generation selection mode that wishes the unit to operate. Regarding the generation selection mode, the user can select between the three alternatives of only the 1st scroll generator, only the 2nd scroll generator or both scroll generators operation. Last, the user can start or stop the system manually from this page.

The Power Bus bar Overview Page. Monitoring and /or access to the basic electrical components of the onboard Marine prototype is provided through this page. These electrical components are the scroll – generator assemblies, the ORC feed pump, the resistor bank and the motor – generator assembly. In addition, the user can select the electrical grid to which the ORC unit will be connected (land grid or ship grid). Depending on the operational mode, the user can control the operation of the pump, scroll – generator and resistor bank by altering their operating parameters.

The System Overview Page. Through this page the user can monitor only (auto mode) or monitor and control (manual or lab mode) the marine ORC prototype. The visualization and realization of the monitor and control is done through a P&ID sketch up (Figure 4.20) In addition the user, in manual or lab mode, can access all five independent PID control set and monitor pages, directly by appropriately touching on the screen of HMI.

A description of the independent PID controllers (blue tabs) is as follows.

The **five (5) independent PID controllers** can be accessed directly from the main page interface or from the system overview page. The control architecture allows the user to enable or disable any PID controller (auto or manual control mode) and to alter the desired set value. At the same time, the present value and the control valve or pump operational level is depicted in order to have an estimate of the

operating boundaries and condition of each PID controller. In addition, a timeline graph provides information on the history of the PID controller operation. Last, the user can regulate the PID controller by adjusting the gains.

A description of the alarm, trip and configuration pages (green tabs) is given below.

Main Alarm Page. All active alarms are listed in time order. A short description and the status (acknowledged or not) for each alarm is presented on the specific page. The user cannot delete or override any alarm.

Alarm Log Page. All occurred alarms are listed in time order. A short description and the status (active or not) of each alarm is presented on the specific page. The user can delete the alarm log, if all alarms have been acknowledged and password key is typed.

List Trip Page. All trip functions are presented and briefly described. The operation status is also presented (Activated, normal, de activated).

List Group Alarm Pages. This list extends to three sub pages. It contains a list with all sensors (temperature, pressure, speedometer, power meter), communication status with all three VFD and status of the ESD PLC. The user can set a Low and High Alarm set for each sensor signal, can activate or de activate each parameter on alarm list and can check on the status of each of the aforementioned parameters.

System Page. This page includes multiple sub pages where the user can perform from simple checks to comprehensive configuration tasks such as calibration of sensors or even re programming the software code of the HMI. Briefly, the user can set the system's date and time, test the buzzer, System log file back up or adjust the monitor settings (Brightness, contrast, etc). In addition, through the system configuration page option, the user can perform zero and span calibration to all temperature, pressure and flow rate sensors. In system configuration page, the user can also change the default values that actuate the PID controlling process. In example, the temperature of the hot water inlet in the evaporator, as already described, acts as a threshold to enter stand by mode. Its default value was set to 70 °C. This default value can be altered accordingly. Another configuration option is the temperature that the refrigerant exits the evaporator. The set default value of 74 °C acts as an actuator which swifts the ORC system from standby mode to normal mode operation. Finally, various transition times from one mode of operation to a next or previous can be set accordingly.

Figure 4.18: Human Machine Interface, ORC led status and control buttons.

Figure 4.19: ORC HMI main page layout.

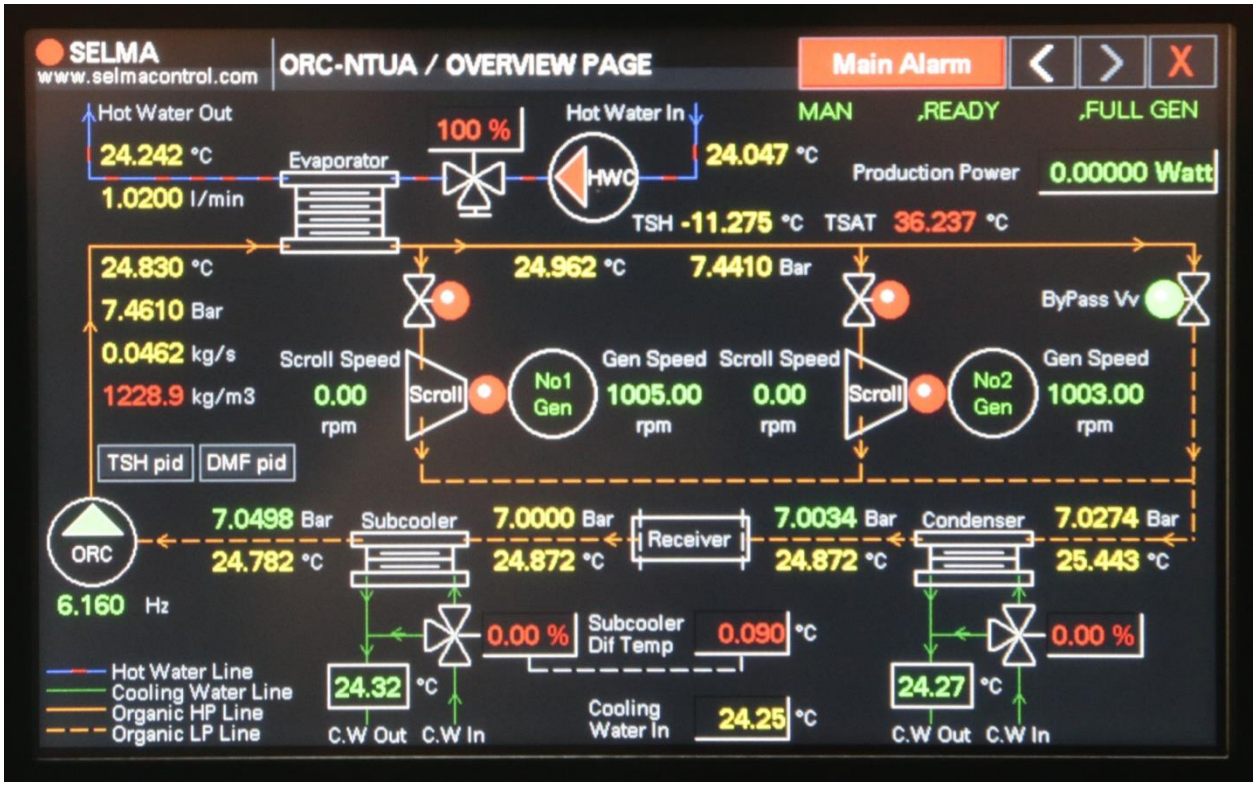

Figure 4.20: ORC overview page layout.

Figure 4.21: ORC HMI power bus bar page layout.

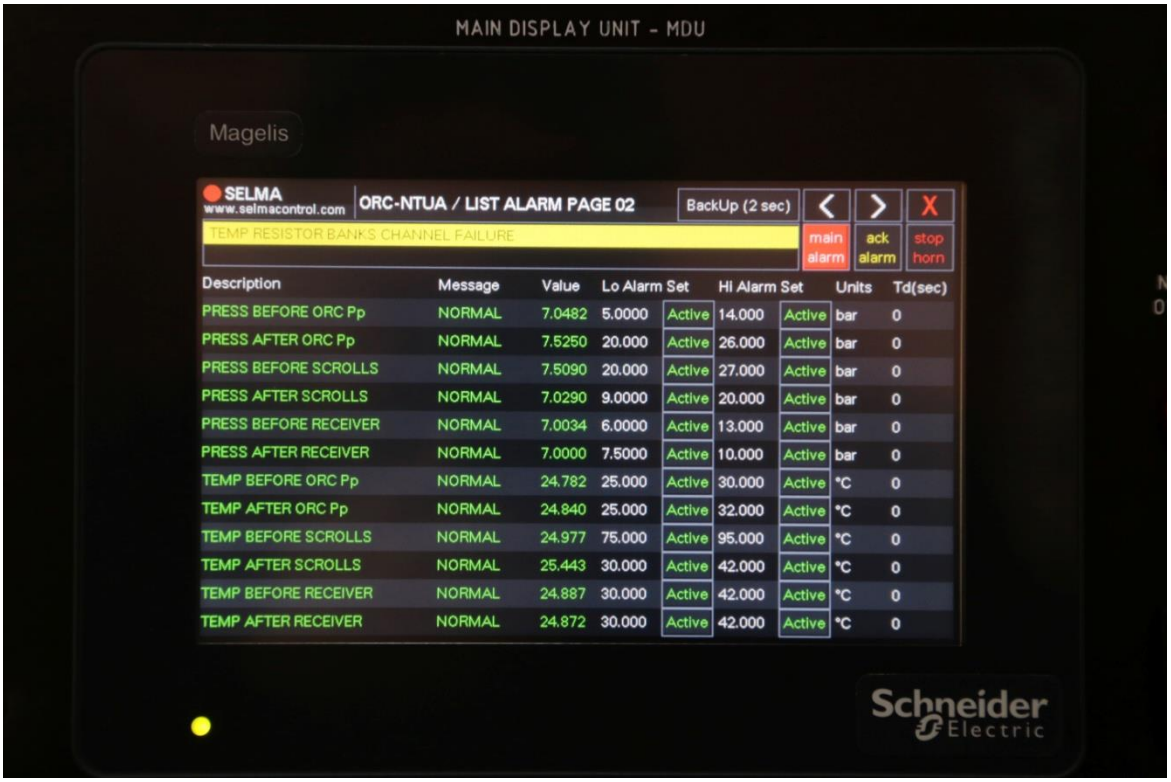

Description	Message	Value	Lo Alarm Set		Hi Alarm Set		Units	Td(sec)
PRESS BEFORE ORC Pp	NORMAL	7.0482	5.0000	Active	14.000	Active	bar	0
PRESS AFTER ORC Pp	NORMAL	7.5250	20.000	Active	26.000	Active	bar	0
PRESS BEFORE SCROLLS	NORMAL	7.5090	20.000	Active	27.000	Active	bar	0
PRESS AFTER SCROLLS	NORMAL	7.0290	9.0000	Active	20.000	Active	bar	0
PRESS BEFORE RECEIVER	NORMAL	7.0034	6.0000	Active	13.000	Active	bar	0
PRESS AFTER RECEIVER	NORMAL	7.0000	7.5000	Active	10.000	Active	bar	0
TEMP BEFORE ORC Pp	NORMAL	24.782	25.000	Active	30.000	Active	°C	0
TEMP AFTER ORC Pp	NORMAL	24.840	25.000	Active	32.000	Active	°C	0
TEMP BEFORE SCROLLS	NORMAL	24.977	75.000	Active	95.000	Active	°C	0
TEMP AFTER SCROLLS	NORMAL	25.443	30.000	Active	42.000	Active	°C	0
TEMP BEFORE RECEIVER	NORMAL	24.887	30.000	Active	42.000	Active	°C	0
TEMP AFTER RECEIVER	NORMAL	24.872	30.000	Active	42.000	Active	°C	0

Figure 4.22: ORC HMI List alarm page layout.

Figure 4.23: ORC Subcooling PID controller layout.

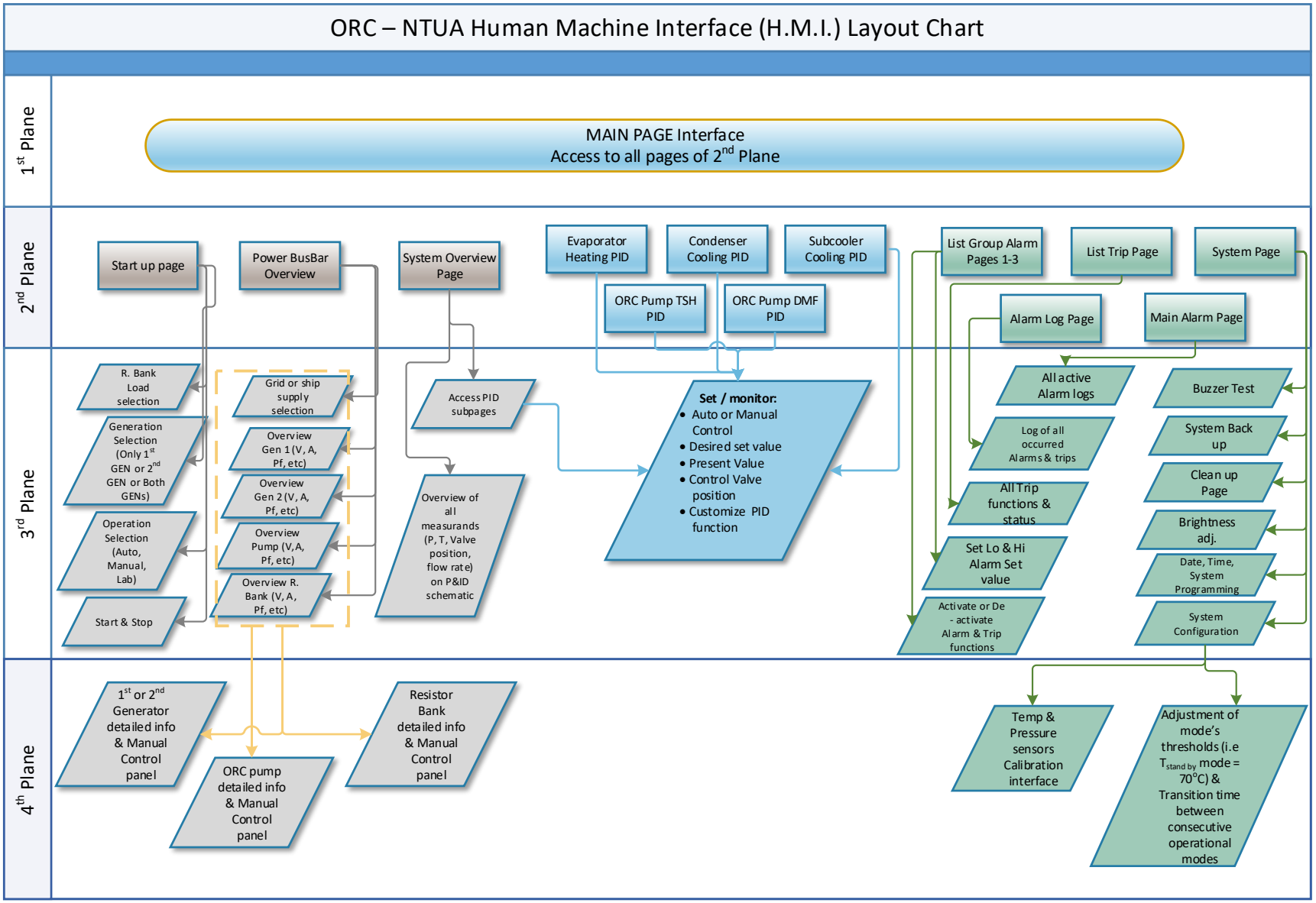

Figure 4.24: ORC- NTUA Human Machine Interface (H.M.I.) layout chart.

4.7 DNV GL rules for classification

All DNV GL rules for classification had to be met in order to be able to have the appropriate certificate of compliance and thus DNV GL approval to proceed with on board installation and operation. These rules apply to all three independent circuits of the ORC prototype:

- Refrigerant circuit
- Hot water circuit
- Sea water circuit

and therefore all requirements imposed by relevant Part 4 Systems and components Chapter 6 Piping systems were mandatory for classification approval.

In more details, the ORC prototype had to comply with general requirements such as detailed P&ID drawings, extensive equipment list with details such as certification for the intended use, maximum operating pressure and or temperature, dimensions, weight, other specific information, etc. In addition, all necessary actions specified by the risk assessment procedure had to be implemented and compliance with specific requirements that had to do with

- ✓ Appropriate materials use for each purpose (refrigeration circuits, sea water piping, soft water piping),
- ✓ Minimum thickness,
- ✓ Basic design criteria of each circuit and
- ✓ Necessary safety equipment

had to be checked and documented.

The implementation procedure of DNV GL rules revealed several mistakes that originally were made during the design and construction of the first experimental ORC. These mainly had to do with the poor selection of appropriate equipment's material that consist the sea water circuit. Surprisingly, DNV GL Part 4 Systems and components Chapter 6 Piping systems Section 2 Clause 1.1.1 dictates that "traditional stainless steels, including 316 or 316L, should not be considered suitable for use in seawater systems". This requirement resulted in a complete reconstruction of the sea water circuit, since the condenser, sub cooler and piping was constructed by 316 stainless steel material. Hence two new copper-nickel-alloy heat exchangers by Bitzer Company were installed with an appropriate certificate of conformity for sea water systems. At the same time the sea water piping was made from galvanized seamless carbon steel pipes according to International Standard ISO1461:2009. The complete arrangement of the sea water circuit is presented in section 4.5.

Finally, after the completion of the assessment and the re construction process, the marine on board ORC prototype received the desired DNV GL approval. Thus the ORC unit, since it was found to be compliant to DNVGL rules for ships Pt.4 Cp.6 piping systems (January 2017), could be fitted inside an engine room of a ship.

DNV·GL

MACROBUTTON NoName [Addressee's name - press F11 to jump to next field]

DNV GL AS Approval
LNG, Cargo Handling & Piping Systems
P.O. Box 300
1322 Høvik
Norway
Tel: +47 67 57 90 26

Date:	Our reference:	Your reference:	Job ID:
2017-02-07	MCANO385/HCKW/ P261.1S-J-7499		MCANO385-911A0334-1

PIPING, Id. No. P261.1S
FW-3D drawings of experimental ORC unit

Reference is made to your letter dated 2017-02-01. The following documents are stamped 2017-02-07 and given the status as shown below:

Document No	Rev	DNV GL No	Title	Code	Status
		2133	911A0334 - Major components description & Schematic diagrams ORC prototype 2017		For Inf.
		2134	911A0334 - ORC P& ID-ORC		Appr.w/comm
		2135	911A0334 - New ORC assembly Hot water circuit		For Inf.
		2135	911A0334 - New ORC assembly Hot water circuit		For Inf.
		2137	911A0334 - New ORC assembly SEA WATER		For Inf.

Document No. **(empty)**, "911A0334 - ORC P& ID-ORC" has been reviewed in accordance with DNV Rules Pt. 4 Ch. 6 Sec. 6, with the following comment:

196 **Scope** **Important Note**

This drawing has been reviewed and examined and found to be compliant with DNVGL Rules for Ships, Pt. 4 Ch. 6 Piping systems (January 2017).
The approval is limited to this experimental installation only. Please note that additional requirements will apply for units of a bigger size. Reference is made to Pt. 4 Ch. 6 Sec. 6 [1.1.1].
This unit is found to be compliant to be fitted inside an engine room of a ship. Please also note that the scope is limited to the unit itself. Connections to existing ship systems (cooling water, electrical systems, control and monitoring systems) have not been reviewed.
Comment is given for your information only, no follow-up is needed.

Approval Engineer for this approval is Hans-Christian Koch-Wintervoll.

4.8 Operation as marine on board ORC prototype

Finally, after almost 15 weeks, the onboard marine ORC unit was ready for testing in the laboratory facilities (Figure 4.13). A tremendous effort by LSBTP personnel and external associates was the driven force of such an accomplishment. Nevertheless, a lot of work was needed to be done, namely debugging the automation & control strategy, testing all operational modes, alarm and trip functions and demonstrate a trouble free operation for at least 24 hour and 48 hour demo operation on laboratory test rig. This last step, started around March 2017 and lasted until late May of the same year.

Hence, before operating the marine ORC prototype, it was mandatory to resolve all bugs occurred during preliminary testing of automation and control and verify all alarm and trip functions. This task was extremely important towards the final goal of the project which was a standalone actuating, operating and acting onboard marine ORC prototype. The time required to finally resolve all bugs and to prove the strategy and architecture of the automation and control was more than originally anticipated and mainly had to do with the complexity of the overall strategy in order to support a standalone operating and controlling capability. All "childhood illnesses" of the marine ORC prototype were addressed and mainly had to do with establishing and securing communication with all equipment and devices, data logging and debugging the software code. In addition, the robustness and functionality of all alarm and trip functions during "dummy operation" but also at real operating conditions was tested and documented. Finally, after almost 9 weeks and 500 hours of preliminary operation, the marine prototype was ready for its first standalone operation. This significant milestone was early May of 2017 and was achieved thanks to the effort of LSBTP personnel and external associates.

On 05 of May 2017, all trip (section 4.6.2) and several alarm functions were demonstrated to DNV GL authorized engineer. After that, the trouble free standalone continuous operation of the marine ORC prototype had to be demonstrated.

In following sections 4.8.1 & 4.8.2 a trouble free operation for at least 24hour and 48hour demo operation on laboratory test rig is presented.

4.8.1 Twenty-four hour (24h) continuous operation test

The purpose of the 24 hour continuous operation was to demonstrate the startup, uninterruptible operation and automatic shutdown of the marine ORC prototype. The test started on the 5th of May 2017 and ended on the following day. During this trial the system has started, following the procedure described in section 4.6.3.1. The time required for a cold start (from zero load to full load) did not exceed the 18 minutes in total. This time increases the flexibility of the system and demonstrates the successful control strategy and architecture. In more details, after completing all sixteen (16) steps (see section 4.6.3.1), it finally reached normal operating conditions with all five PID controllers activated. The system after operating more than twenty-four (24) hours, was forced to execute the normal shutdown procedure, as described in section 4.6.3.1. This was realized by simply shutting down the natural gas boiler supply and allowing the HT temperature supply gradually to reduce. The ORC system automation and control, as

designed, actuated on the ORC system and shutdown the marine prototype as expected, in less than 3 minutes. The following diagrams illustrate the sequence of actions imposed by the interaction of HT temperature supply value and control strategy.

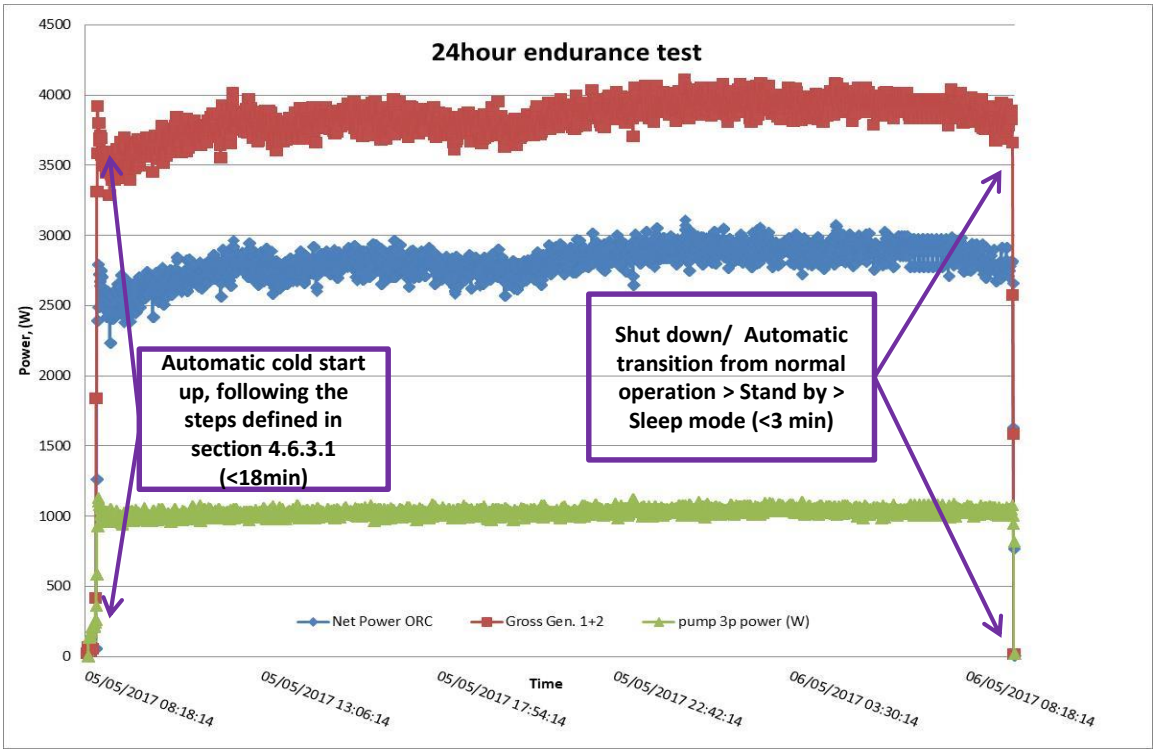

Figure 4.25: Gross, Net Power produced & pump consumption during the 24hour continuous operation test.

The basic outcomes of the 24-hour continuous operation are highlighted as follows:

- A continuous 24-hour trouble free operation.
- All PID controllers run smoothly and facilitate the stand alone operation.
- The system exhibited impressive required time from zero load to nominal load (less than 18 minutes – cold start)
- The system required less than 3 minutes to transit from nominal load to sleep mode.
- The marine ORC prototype produced nearly 75 kWh (Gross) and 55 kWh (Net) energy during its' 24 hour operation.

4.8.2 Forty-eight hour (48h) continuous operation test

As a second step, during the 48 hour in addition to previous, the marine ORC prototype responded to different simulated operating conditions of the heat source (gas boiler). In more details, during the 48hour test, the natural gas supply was changed (reduced and after a while increased) which affected the heat load and as a consequence the HT temperature supply to the evaporator. This manual alteration of the HT temperature simulates the behavior of the I.C.E. under different operating condition such as sea going, maneuvering and in port conditions. Hence, under real operating conditions, the marine ORC

prototype followed the decrease and after a period of time the increase of the HT temperature by switching between appropriate operating modes. The definition of these operating modes is provided in sections 4.6.3.1 to 4.6.3.4.

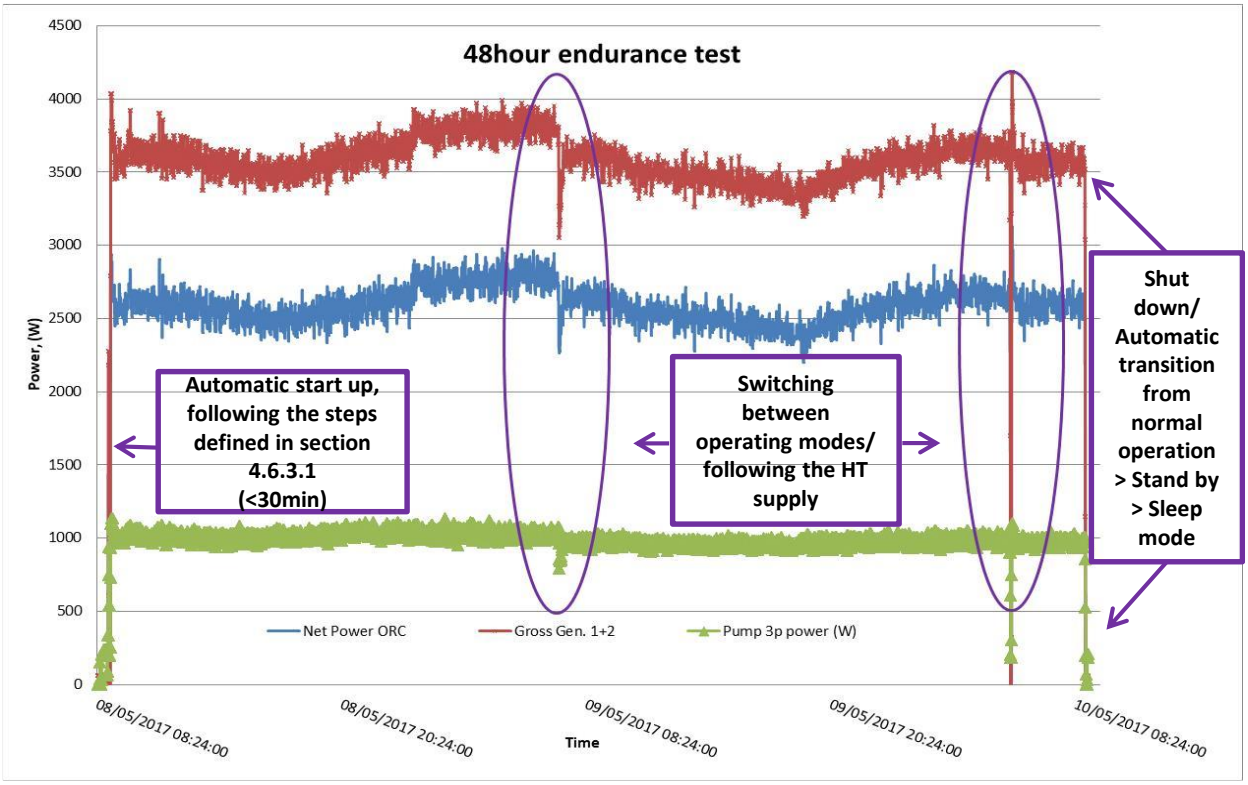

Figure 4.26: Gross, Net Power produced & pump consumption during the 48hour continuous operation test.

In Figure 4.27, the transition of the marine ORC prototype from one operational mode to another operational load, following the HT temperature variation (ICE load variation) is depicted. In more details, the system shifts from normal operation – nominal load (**Phase 1**) to partial load – rump down (**Phase 2**) to then standby mode (**Phase 3**) to again partial load -rump up (**Phase 4**) and finally again to normal operation – nominal load (**Phase 5**). This variable HT temperature cycle lasted only 9 minutes in total. This sharp temperature variation and the successful follow up by the system's automation & control demonstrates the capabilities of the marine ORC prototype in terms of flexibility and performance. Another important achievement was that the system also exhibited an impressive warm start minimum time of less than 3 minutes. This time was required for the system to switch from sleep mode to nominal load operation, which is presented in Figure 4.27 as the elapsed time of Phase 4.

In Figure 4.28, the transition of the marine ORC prototype from normal operating mode to sleep mode during shut down procedure is presented. The system responded, as expected, impressively. The rapid transition from one mode to the next was performed, ensuring the proper response of the automation & control in the event of the shutdown procedure.

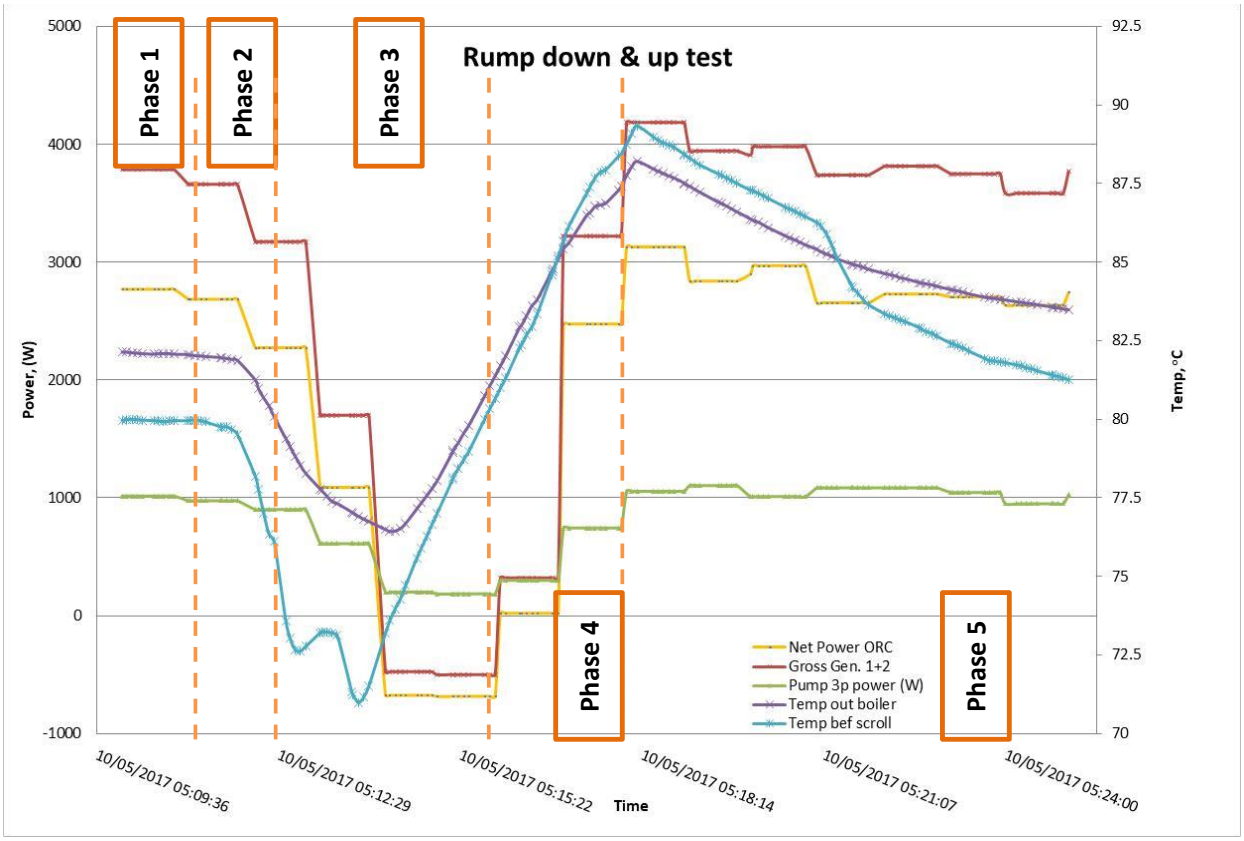

Figure 4.27: Rump down & rump up test during the 48 hour endurance test.

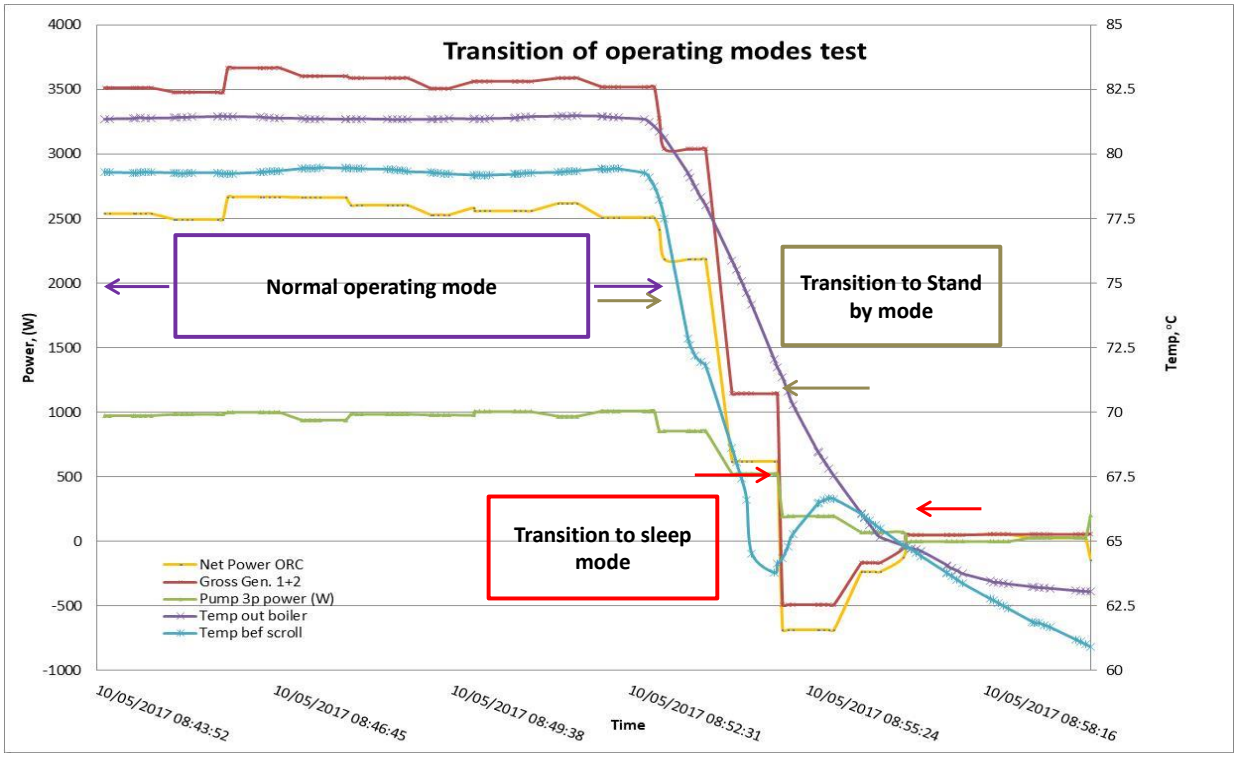

Figure 4.28: Shutdown procedure of the marine ORC prototype.

The basic outcomes of the 48-hour continuous operation are highlighted as follows:

- A continuous 48-hour trouble free operation.
- All PID controllers run smoothly and facilitate the stand alone operation.
- The system exhibited impressive required time from zero load to nominal load (less than 30 minutes – cold start).
- The system exhibited impressive required time from zero load to nominal load (less than 3 minutes – hot start).
- The system demonstrated a successful rump down and rump up behavior during the HT temperature variation (ICE load variation).
- The system required less than 4 minutes to transit from nominal load to sleep mode.
- The marine ORC prototype produced nearly 115 kWh (Gross) and 83 kWh (Net) energy during its' 48 hour operation.

4.9 Conclusions from the final development phase

The final development phase concluded after almost 6 months (December 2016 until May of 2017). During those months several tasks were performed, in parallel or in sequence, with final aim to design, develop and operate a complete autonomous experimental ORC test rig at real life conditions. This ambitious goal was met to a large extent. Unfortunately, the operation on board was never accomplished since the time required for all necessary actions was significantly greater than originally estimated. Nevertheless, this fact shouldn't and couldn't reduce the tremendous effort by all involved parties and the quantifiable accomplishments at the end of this development phase.

The major results and conclusions arisen from the final stage of development of the ORC WHR unit are summarized briefly below.

- An extensive **hazard / risk assessment** was performed in order to identify all risks, causes and consequences associated to each hazard. All major conclusions and key results from the hazard – risk assessment improved the design, safety and automation - control strategy aspects.

- **Compactness and modular design**. An extensive re construction, given the dimensional restriction imposed by ship's access ports and hatches was designed and realized under extreme time constraints. Another important requirement was that transportation process and all work carried out on board, in terms of assembly, wiring, filling, testing, tuning and finally setting in operation should be kept as short in time as possible and do not exceed the 36-hour limit. This time constraint reflects the particularities of the marine market and industry where proper planning and multi tasking are considered as a must and could be summed as "a ship never waits". Therefore, several actions needed to be performed simultaneously. Considering the fact that only refrigerant circuit's filling and leakage testing would require 8 -10 hours, assembly and wiring should be kept as short as possible. Although, this was never proved in real life conditions, a simulation under laboratory conditions was performed. According to Sellers [66], compactness and modular design should be top priority in a marine ORC unit.

- **An extensive reconstruction of the sea water circuit.** The implementation procedure of DNV GL rules revealed several mistakes that originally were made during the design and construction of the first experimental ORC. These mainly had to do with the poor selection of appropriate equipment's material that consist the sea water circuit. Surprisingly, DNV GL Part 4 Systems and components Chapter 6 Piping systems Section 2 Clause 1.1.1 dictates that "traditional stainless steels, including 316 or 316L, should not be considered suitable for use in seawater systems". This requirement resulted in a complete reconstruction of the sea water circuit, since the condenser, sub cooler and piping was originally constructed by 316 stainless steel material.

- **Sensors, PLC and other miscellaneous equipment.** An independent emergency shutdown PLC, a new master PLC and other minor equipment were installed as a consequence, mainly, to hazard identification procedure and ship owner requirements. According to Sellers [66], the robustness of the automation system will not only affect the operating availability of the ORC

system but will also provide, the proper data logs, in order to access the operating profile of the ORC system. The latter, at least in early stages of technology adoption, will highlight the performance of such systems, and probably correlate the operational profile to the type of ship or typical route.

- **A power supply motor generator module and a resistor bank were installed.** This arrangement isolates the ship power grid from that of ORC prototype without compromising the necessary external power supply to ORC unit during startup and shutdown procedure.

- Detailed **electrical, piping and ORC prototype drawings (as built)** were designed and a detailed **equipment list** with details such as certification for the intended use, maximum operating pressure and or temperature, dimensions, weight, other specific information was formulated.

- Demonstration of a successful **automation & control strategy** and operation. A state of the art automation and control sub system was realized. The marine ORC prototype is equipped with a **Human Machine Interface (H.M.I.)** which allows the parameterization and operation of the marine ORC prototype, according to the conditions and scope of operation. The use of three way and regulating valves allows the system to run completely independent. Therefore, the operation of the ORC unit is not controlled by the crew and thus maximizing the availability of the system. Hence, incidents encountered during operation like in the case of Calnetix ORC module are avoided. [66]

- Demonstration of trouble free operation at **standalone continuous operating mode**. The marine ORC prototype demonstrated impressive operational features such as autonomous startup and shut down and a successful rump down and rump up behavior during the HT temperature variation (ICE load variation). The complete autonomous operation minimizes the crew's interaction to the ORC operation and availability. Therefore, incidents encountered during operation like in the case of Calnetix ORC module are avoided. [66]

- After the completion of the assessment and the re construction process, the marine on board ORC prototype received the desired **DNV GL approval**. Thus the ORC unit, since it was found to be compliant to DNVGL rules for ships Pt.4 Cp.6 piping systems (January 2017), could be fitted inside an engine room of a ship.

4.10 Current status of ORC marine applications

Unsimilar to other mobile ORC applications, the knowledge that has been produced about the performance of ORC's in marine applications is considered scarce and limited. In most research cases, the waste heat recovery focused on exhaust gases waste heat. In several cases, safety issues are downgraded or even neglected, although some working fluids can be toxic or highly flammable making leakages very dangerous. [67] This risk is magnified in atmospheres were the ventilation and evacuation of dangerous gases is difficult such as inside the hull of a ship. It is obvious that overall efficiency, safety, environmental impact and economic viability of the plant depend on the selected working fluid and hence the selection of the working fluid is about finding the best compromise of properties. [68]

Besides of the theoretical research studies that are being performed in the field of marine ORC's, some marine equipment manufacturers and shipyards have involved themselves with the concept of ORC systems for waste heat recovery in marine applications. Regarding to existing marine ORC applications, the literature is very scarce and only few examples can be found.

Starting a decade ago, an important milestone were the positives results that Turboden has achieved, in 2010, in the field of waste heat recovery in stationary internal combustion engines. This led to the signed agreement between Turboden and Wärtsilä to develop, commercialize and distribute an ORC solution specifically applicable to the marine market. The solution consists in the Wärtsilä Marine Engine Combined Cycle (ECC) and it is based on an ORC to recover waste heat from the exhaust gases and the jacket cooling water circuit. It is claimed that the system could increase the engine power in a range from 8 to 12 % (Turboden, 2010).

Ever since, several companies followed and in more details, in 2011 the Opcon group has signed a cooperation agreement with MAN Diesel & Turbo to combine Opcon technology for energy efficiency with MAN Diesel & Turbo diesel engines for reduced fuel consumption and emissions (Opcon, 2011). The Group Opcon has mounted two of their ORC module for marine applications onboard of a Wallenius marine vessel (MV Figaro). The heat recovery units, designed to recover heat from a low grade heat sources, is powered by the hot water of the vessel's cooling system. The higher ORC unit is able to generate up to 500 kW and the fuel savings are expected to be around 4-6 %. The ORC system is coupled to an Opcon Powerbox WST system that is powered by the surplus steam available in the vessel. This system consists in a special steam turbine that generates electricity from wet or saturated steam (Opcon, 2012).

In 2015 the ORC manufacturer Enertime has received a funding from the European Union to implement its ORC technology in large ships by working in partnership with the shipyard STX France (Enertime,2015). During the last years Enertime has been developing ORC modules designed to recover heat from marine vessels and cargo ships. The modules have been downsized as much as possible to fit in the limited space onboard (down to 100 kW_e).

On April 2016, the Wärtsilä 12RTA96C main engine onboard the Arnold Maersk containership was fitted out with a 125 kW output prototype Calnetix/MHI ORC, exploiting jacket water between 85 °C-95 °C with a 264 m^3/h flow. Sellers shared a lot their experience and lesson learned during all phases of realization.[66] The most important ones were the need to engage the ship's engineer early in the planning phase, the space limitations and the need for further compactness, the robustness of the data

logging system and last but not least the ORC system should be as much autonomous as possible, since several times the crew probably didn't started and stopped the ORC, especially during short distance voyages. The later affected the running hours and ultimately the recorded and documented total kilowatt hours produced. As an obvious consequence, a reduced economic profitability is expected.

Further to the above action, Calnetix is utilising magnetic bearings. Although, it may increase the initial investment, the systems gain reliability and efficiency due to "one moving part and no physical bearing contact".

Most recently, Orcan has collaborated with refrigeration and aircon specialist, Bitzer SE on a fully enclosed screw expander which, as claimed, exhibits a flatter efficiency line, not a curve, regardless of the load point. It's also maintenance free and won't need opening before it's reached around 120,000 running hours, reducing maintenance to an absolute minimum.

On the other hand, Enogia's developed its own turbine which is optimized for the specific running condition of the application (tailor made application). The design principle followed is that temperature and therefore pressure variations can be regulated by altering the organic fluid flow rate. Further, the lubrication is provided by the working fluid itself and not by oil as a lubricant, since it can mix with the working fluid and decrease efficiency after a year or so.

Climeon's approach is somewhat different again as it utilizes direct condensation, which allows for a smaller, low-pressure design. The basic principle behind this design solution is that a small amount of the working fluid is chilled to -35°C before being sprayed back into the condensing chamber: the resulting droplets yield a huge thermal reaction surface. Climeon claims that it results in a larger power return, even taking into account the energy hived off for the extra chilling process.

Shipping has experienced a surge in environmental regulations over the past decade. Those emanating from agreements reached under the auspices of the International Maritime Organization (IMO) include the global sulphur limit on ship fuel, nitrogen oxides (NO_x) Tier III requirements in Emission Control Areas (ECAs) and the ballast water management regulation. All will impact on shipping in the next five years, while greenhouse gas (GHG) emissions will be the main challenge in the decades to 2050.

Having in mind the tight regulatory framework, Organic Rankine Cycle systems may offer more flexibility and could contributed to ships overall efficiency. As with most technology, efficiency comes at a price and developers need to be careful about which advantages are targeting. In example, an ORC tuned to higher expansion ratio may achieve a better energy conversion but it could require an expander with more stages and thus higher SIC. Another example could be the nominal output that the WHR system should have for a given source, since several design characteristics are influence by that decision, leading to a higher or lower SIC.

The following Chapter 5 of this thesis will assess the economic performance and viability of a jacket water WHR ORC unit and highlight the parameters affecting the Levelized Cost of Electricity (LCOE).

Chapter 5. – Economic assessment of a marine WHR ORC system

5.1 General scope & economic theory background

In this Chapter of the thesis the economic performance and viability of a jacket water WHR ORC unit are assessed, based on the economic theory and available literature data. Hence, a show case is presented which consists of a 13,600 TEU containership, which is powered by a two-stroke marine Diesel engine with a Maximum Continuous Rating (MCR) of a 72,240 kW. In Section 5.2, all available data concerning the ship characteristics are presented. In Section 5.3, ultimately, the Levelized Cost of Energy (LCOE) of a WHR ORC unit will be calculated and parameters affecting it, will be highlighted.

At this point, the economic theory is deployed and basic economic equations and assumptions are presented.

For the economic evaluation, the following economic indicators apply.

Net Present Value (NPV) is an indicator that reflects the current value of future cash flows generated by an investment project. The present value of a cash flow depends on the interval of time between the base period and the cash flow. It also depends on the discount rate. Thus, the formula for NPV is as follows:

$$\boldsymbol{NPV = -C_o + \sum_{t=0}^{n} \left[\frac{C_f \cdot (1+f_f)^{t-1} - C_{OM} \cdot (1+f)^{t-1}}{(1+i)^t} \right]} \quad (5.1)$$

Where: i is the interest or discount rate

t the year of a future payment

n is the assessment period in years

f the year increase in operational & maintenance expenditure

f_f the year increase of fuel price

C_o the capital cost of investment which includes all corresponding labor, components and other relative costs to WHR unit installation

C_f the year fuel avoidance cost (energy saving)

C_{OM} the year operational & maintenance cost

The Internal rate of return (IRR) is the interest rate at which the net present value of all the cash flows (both positive and negative) from a project or investment equal zero. Internal rate of return is used to evaluate the attractiveness of a project or investment. Thus, the formula for IRR is as follows:

$$-\boldsymbol{C_o} + \sum_{\boldsymbol{t=0}}^{\boldsymbol{n}} \left[\frac{\boldsymbol{C_f \cdot \left(1 + f_f\right)^{t-1} - C_{OM} \cdot (1+f)^{t-1}}}{\boldsymbol{(1 + IRR)^t}} \right] = \boldsymbol{0} \qquad (5.2)$$

Discount rate $D_{f\,(t)}$ of year t and for real interest rate i. This ratio allows the conversion of a future value into present value money during the reference year. Described by the equation (5.3):

$$\mathbf{D_{f(t)}} = \frac{\mathbf{1}}{\mathbf{(1+i)^t}} \qquad (5.3)$$

Present Value Factor $PVF_{f\,(t)}$ of annual fixed and overdue cash flows up to year t and for real interest rate i. This rate allows the conversion of a fixed annual and overdue value into monetary total present value in the reference year. Described by the following equation (5.4):

$$\mathbf{PVF_{f(t)}} = \frac{\mathbf{1 - (1+i)^{-t}}}{\mathbf{i}} \qquad (5.4)$$

Capital recovery factor $CRF_{f\,(t)}$ for year t and for real discount rate i. This ratio allows the conversion of a present value of money in the reference year to an equivalent fixed annual and overdue value from the reference year to year t. Described by the equation:

$$\mathbf{CRF_{f(t)}} = \frac{\mathbf{i}}{\mathbf{1 - (1+i)^{-t}}} = \frac{\mathbf{1}}{\boldsymbol{PVF_{f(t)}}} \qquad (5.5)$$

Specific Investment Cost is expressed in €/kW_e and is calculated as follows.

$$\boldsymbol{S.I.C.} = \frac{\boldsymbol{C_o}}{\boldsymbol{P_{net}}} \qquad (5.6)$$

Where:

P_{net} is the net electrical power of the WHR unit.

Levelized Cost of Energy (Electricity) is expressed in €/MWh_e and is calculated as follows:

$$\boldsymbol{LCOE} = \frac{\boldsymbol{C_{annual}}}{\boldsymbol{E_{annual}}} = \frac{\boldsymbol{CRF \cdot \left\{ C_o + \sum_{t=0}^{n} \left[\frac{C_{OM} \cdot (1+f)^{t-1}}{(1+i)^t} \right] \right\}}}{\boldsymbol{E_{annual}}} \qquad (5.7)$$

Where:

C_{annual} the annual cost that comprises the annuity of capital investment and operating costs.

E_{annual} the annual energy production by the WHR unit.

In Figure 5.1 the presentation of Present Value Factor $PVF_{f(t)}$ and a Capital recovery factor $CRF_{f(t)}$ is illustrated.

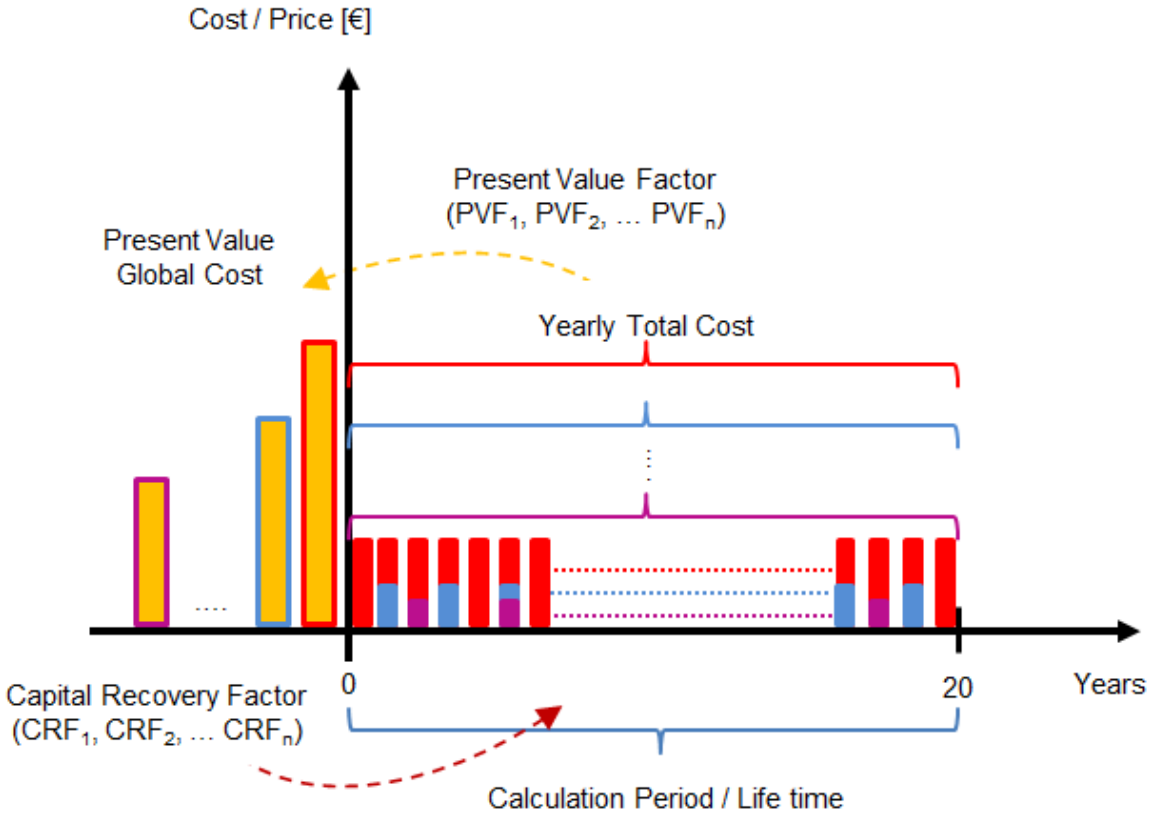

Figure 5.1: Illustration of PVF & CRF during investment assessment.

Available data for ORC Specific Investment Cost (S.I.C.) in the marine industry are scarce, since manufacturers avoid to provide indicative estimations, with the exception of Electratherm.[69] In following Figure 5.2, effort was made to gather and depict available SIC data from various sources. In most of the cases, these costs are indicative for industrial applications. In addition, since the original stated SIC was calculated on a different reference year, an appropriate "normalization" was performed with the use of the following equation.

$$SIC_{2019} = SIC_t \cdot \frac{CEPCI_{2019}}{CEPCI_t} \quad (5.8)$$

Where:

CEPCI year(t) is the general Chemical Engineering Plant Cost Index of the respective year t.

In the following Table 5.1, the average year value of CEPCI from 2010 up to 2019 (December) is presented. [70] The cost is originally in US dollar currency. To convert the values to euro, a conversion factor of 0.8929 is taken into account, which was the average exchange rate of year 2019.

Table 5.1: Average year value of Chemical Engineering Price Cost Index (CEPCI) from 2010 up to 2019 (December).

Year	CEPCI (US Dollars)	Year	CEPCI (US Dollars)
2008	575.4	2014	576.1
2009	521.9	2015	556.8
2010	550.8	2016	541.7
2011	585.7	2017	567.5
2012	584.6	2018	603.1
2013	567.3	Dec 2019	591.9

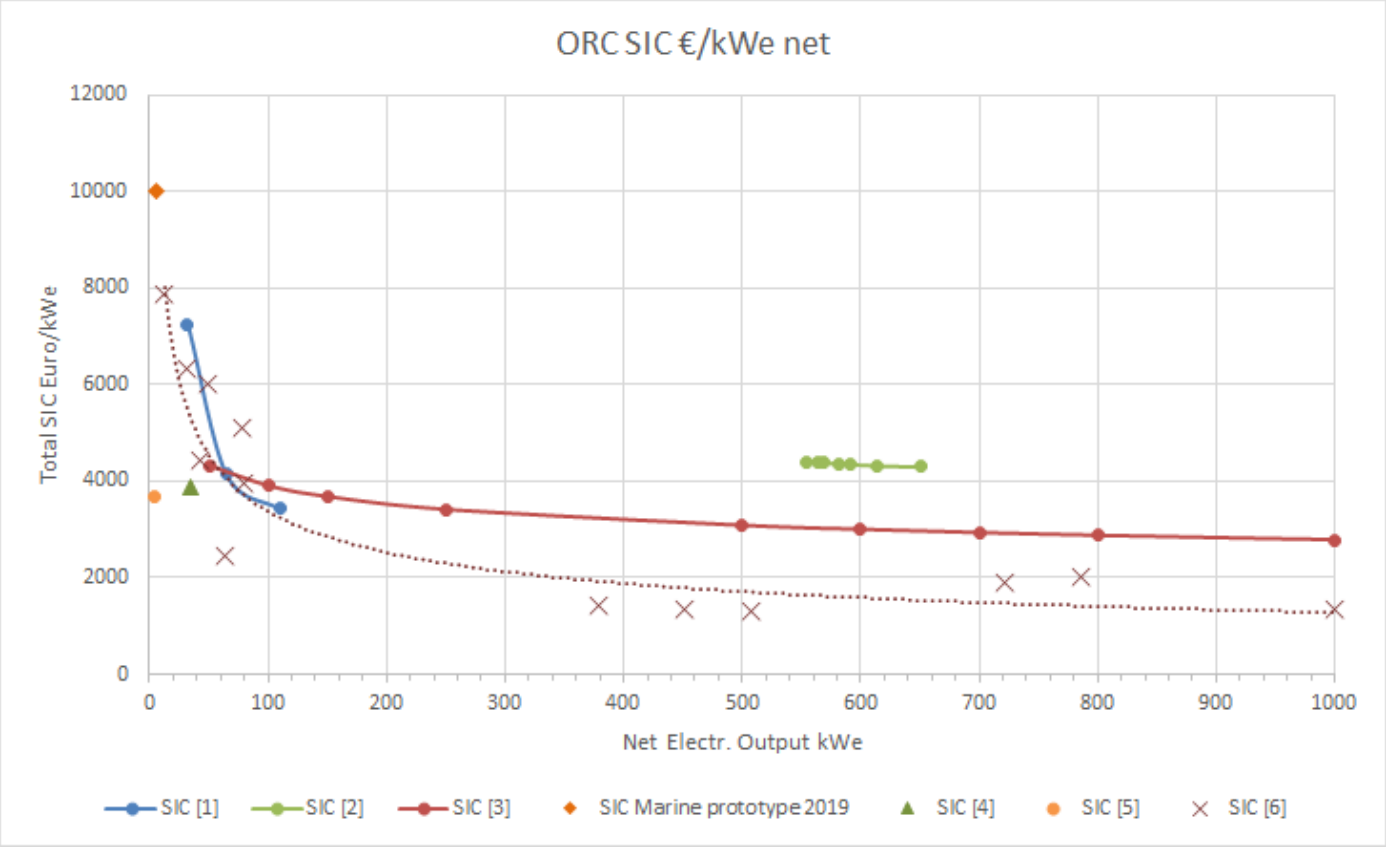

Figure 5.2: Specific Investment Cost (SIC) of various WHR ORC units according to literature review.

Where Figure 5.2 legends are briefly described below:

SIC[1]: ElektraTherm Power + Generator product line stated turnkey SIC. (Estimation Year / Reference Year: 2019 / 2019) – Working fluid:245fa.[69]

SIC [2]: S. Lecompte SIC estimation. (Estimation Year / Reference Year: 2013 / 2019) – Working fluid:245fa.[72]

SIC [3]: Gewald SIC estimation. (Estimation Year / Reference Year: 2013 / 2019) – Working fluid:N/A.[71]

SIC Marine prototype: SIC estimation of the LSBTP onboard marine prototype (Estimation Year / Reference Year: 2017 / 2019) – Working fluid:134a.

SIC [4]: Schuster et al. SIC estimation. (Estimation Year / Reference Year: 2008 / 2019) – Working fluid:245fa. [34]

SIC [5]: Quollin et al. μORC SIC estimation. (Estimation Year / Reference Year: 2010 / 2019) – Working fluid:134a. [49]

SIC [6]: Quollin et al. WHR SIC literature review. (Estimation Year / Reference Year: 2012 / 2019) – Working fluid: N/A. [53]

As basic remark, a steep reduction in SIC values from μscale (app. 3 kW_e) to medium scale application (<100 kW_e) and then to large scale application is evident. This is referred as "economy of scale" due to the fact that the SIC is sensitive to the size of the WHR plant/application. It can be mainly attributed to a combination of minimum required fixed costs and adopted technology (mainly the expander technology), as the application rated power is increased. At the threshold of 100 kW_e, two different SIC patterns can be observed. The first pattern is provided by Quollin et. al. [53] and it is based on WHR literature review and the second pattern is provided by Gewald [71] and is based on a mix of offers and literature review. It is clear that a large differentiation in estimated / calculated SIC is present. The latter pattern is based on the following equation (5.9) which is a correlation for the specific costs of ORC modules, in €/kW, depending on the ORC electrical power output. As already mentioned, the calculated pair of values are based on a compilation of offers and literature review. As indicated by Gewald [71], the calculated SIC includes only the ORC module SIC and no other investment costs (direct or indirect) such as transportation, commissioning and others. In order to calculate the overall investment costs an empirical multiplying factor is proposed of 1.47, namely "installation factor" by Gewald [71]. If only the SIC ORC module was plotted in Figure 5.2, based on equation (5.9), a good agreement between the values provided by Quollin et. al. [53] and Gewald [71] is noted. Hence, on the following economic evaluation, the overall investment SIC based on Gewald [71] will be used.

$$C_{ORCmodule} = 5000 * P_{el.ORC}^{-0.174} \tag{5.9}$$

As already mentioned, an appropriate "normalization", based on the respective Chemical Engineering Plant Cost Index, needs to be performed on the above equation (5.9) with the use of

equation (5.8). Hence, the economic evaluation is based on the ORC module SIC as calculated by the following equation (5.10).

$$C_{ORCmodule,2019} = \frac{\boldsymbol{CEPCI_{2019}}}{\boldsymbol{CEPCI_{2013}}} \cdot \mathbf{5000} * \boldsymbol{P_{el.ORC}^{-0.174}} = \mathbf{5216.6} * \boldsymbol{P_{el.ORC}^{-0.174}} \quad (5.10)$$

The overall SIC is the product of SIC ORC module, calculated with the use of the above equation (5.10), and the empirical "installation factor" of 1.47. A multiplying factor of 1.5 on the total component cost is also reported as appropriate integration cost / installation factor by Lecompte. [72]

Thus, the total (direct & indirect costs) SIC associated with the WHR ORC installation is performed with following equation (5.11).

$$C_{WHR\ ORCinstallation,2019} = \mathbf{1.47} * \mathbf{5216.6} * P_{el.ORC}^{-0.174} = \mathbf{7668.5} * P_{el.ORC}^{-0.174} \quad (5.11)$$

As an alternative approach could have been the economic analysis of the ORC based on the module costing technique (MCT). This technique is used for preliminary cost estimates and mainly it is used for larger plants (>500 kW_e). In our case, based on the available waste heat by the JWC, the nominal electrical power output will not exceed the 215 kW_e threshold, as it will be presented in the following section 5.2. Thus, the calculation of the overall SIC based on the Gewald [71] equation provides a fair estimation, appropriate for the preliminary level of the present economic assessment.

In Table 5.2, the basic assumptions used for the economic assessment are presented.

Table 5.2: Assumptions for the economic assessment.

Parameter	Value
ORC lifetime / Calculation Period (n)	20 years
Interest or discount rate (i)	8.0 %
Initial operational & maintenance expenditure (C_{OM})	2 % of initial investment (C_o)
Increase in operational & maintenance expenditure per year (f)	3.0 %/year
Increase of fuel price per year (f_f)	4.0 %/year

Own Capital	**100 %**
Loan or Subsidy	**0 %**
Running hours per year	**6252** (see Table 5.3)
SIC ORC module	**2437.0 €/kW$_e$ net** (see Table 5.5 & equation (5.10))
SIC WHR ORC installation	**3582.0 €/kW$_e$ net** (see Table 5.5 & equation (5.11))
Total initial investment cost	**758,380 €**
Fuel cost	**0.5 €/kg**
SFOC (Diesel Generator's at 75% MCR)	**181 gr/kWh**

5.2 Containership characteristics

In this Section, all available technical & operating data concerning, a show case are presented. This ship show case is a 13,600 TEU containership, which is powered by a two-stroke marine Diesel engine with a Maximum Continuous Rating (MCR) of a 72,240 kW. It is also equipped with five Diesel generators (including the emergency generator) with a nominal electric power output of 2,700 kW each, that cover the electric power needs of the vessel. This type of ship was selected since it represents a typical commercial use ship and because of easily accessible available data. [73]

The HT circuit water cools the cylinder jackets and heads of the main engine in the same way as depicted previously in Figure 4.5. A percentage of the waste heat by the jacket cooling water is used daily to produce 40 tonnes of fresh water in a fresh water generator. Hence, the available amount of waste heat is limited to nearly one third of the total rejected heat daily by the jacket cooling system. The evaluated WHR ORC module would be connected just after the exit of the ICE's jacket.

The energy demands and operating profile of the main engine are presented in the following Table 5.3. The operating profiles derived by statistical analysis of operational data for similar sized ships. Moreover, the electricity demand takes into account the number of reefer containers transported by the

vessel at different mission stages. As presented, the ship's electricity demand is considerable in most of its operating modes. [74]

Table 5.3: Operating profile, operating water temperature and energy demands.

Mode	Running hours (h/a)	$W_{pr,D}$ (MW)	$W_{el,D}$ (MW)	W_{JWC} (MW_{th})	$W_{FWG,D}$ (MW_{th})	T_{JWC} (°C)	$WTH_{available}$ (MW_{th})
A	1,661	54.25	10.3	7.60	4.85	85.29	2.74
B	2,573	57.20	6.7	7.88	5.13	85.56	2.76
C	1,451	57.20	3.3	7.88	5.13	85.56	2.76
D	567	52.60	4.9	7.43	4.69	85.15	2.74

As presented above in Table 5.3, the Waste Thermal Heat (WTH) available is the remaining waste heat by the jacket cooling system after the required thermal heat for the fresh water generator is abstracted.

In following Figure 5.3, the rejected or required thermal energy for jacket cooling and fresh water generation are illustrated in relation to main engine (ME) power output. In addition, the HT jacket temperature is also visualized in relation to main engine power output. As can be observed by presented respective values in Table 5.3 and Figure 5.3, the temperature of the water outlet from the jacket varies between 80.4 to 86.70 °C. The temperature of the water jacket outlet affects the produced electrical output of the WHR ORC module, therefore its variation is taken into account in order to estimate the electrical output and thus the energy during each Main Engine operational mode (A, B, C or D). This fact, in our case, has minor effect since the temperature variation between the four operational modes lays in the region of few decimals (approx. ±0.25 °C), as presented in Table 5.3.

Another important parameter that affects the overall performance of the WHR ORC module is the sea water temperature. The sea water temperature varies between regions and seasons and affects the low pressure of the Organic Rankine Cycle and therefore the performance of the expander and ultimately the produced electrical output of the WHR ORC module. During present evaluation the monthly mean temperatures of the North and Mediterranean Sea are used as presented in following Figure 5.4 and Table 5.4.

Table 5.4: North & Mediterranean Sea monthly average, maximum & minimum sea level water temperature values.

	North Sea monthly sea level water temperature values			Mediterranean Sea monthly sea level water temperature values		
Month	Max. Water temperature (°C)	Min. Water temperature (°C)	Aver. Water temperature (°C)	Max. Water temperature (°C)	Min. Water temperature (°C)	Aver. Water temperature (°C)
Jan	7.7	4.7	6	18.0	11.0	15.7
Feb	4.7	3.9	4.2	17.0	10.0	14.9
Mar	5.3	3.8	4.4	17.0	11.0	15.1
Apr	9.0	5.3	7.0	18.0	13.0	16.1
May	14.4	9.2	11.4	21.0	16.0	18.5
Jun	19.3	14.3	16.5	24.0	18.0	21.7
Jul	21.9	19.4	21	27.0	21.0	24.3
Aug	22.5	21.7	22.2	28.0	22.0	25.5
Sep	21.6	19.2	20.6	27.0	21.0	24.5
Oct	19.0	14.9	17.2	26.0	18.0	22.2
Nov	14.9	11.4	13.1	23.0	16.0	19.5
Dec	11.3	7.8	9.4	20.0	14.0	17.2

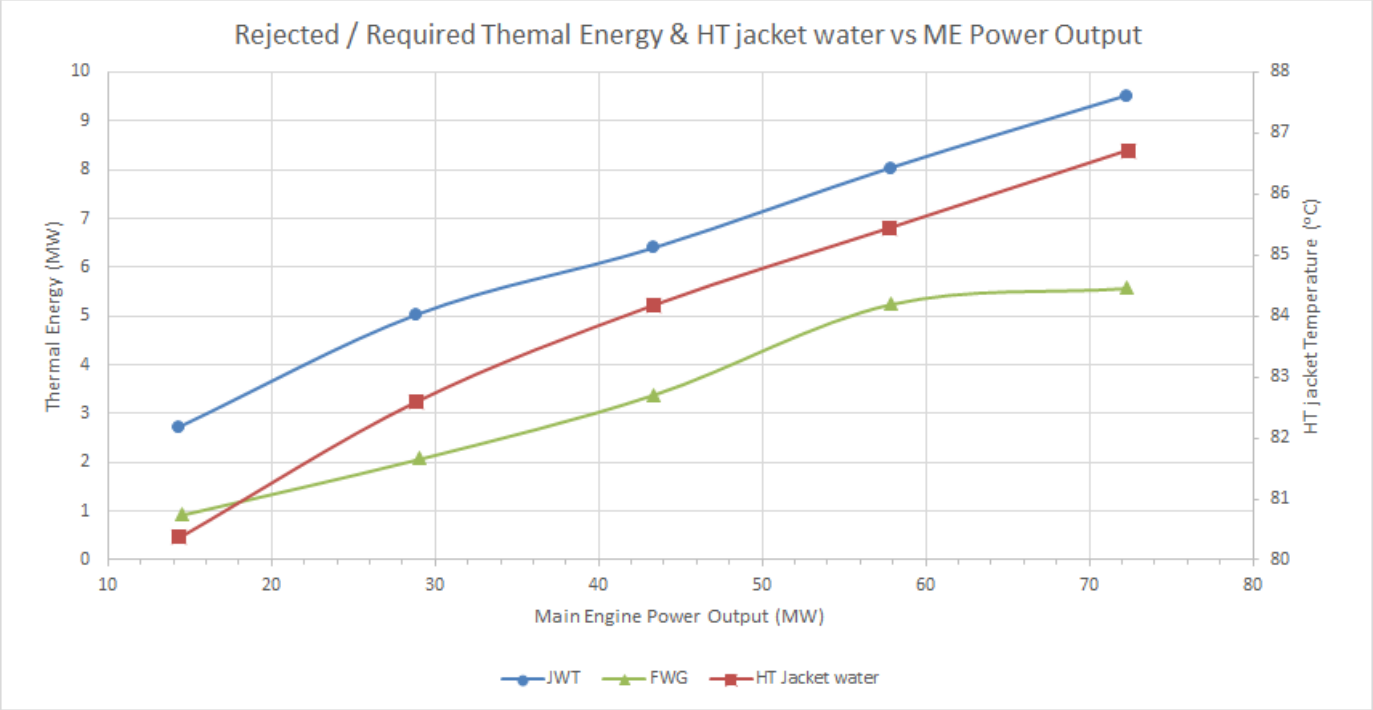

Figure 5.3: Rejected or Required Thermal Energy (MW_{th}) & HT jacket water (°C) in relation to main engine (ME) Power Output (MW_{pr}).

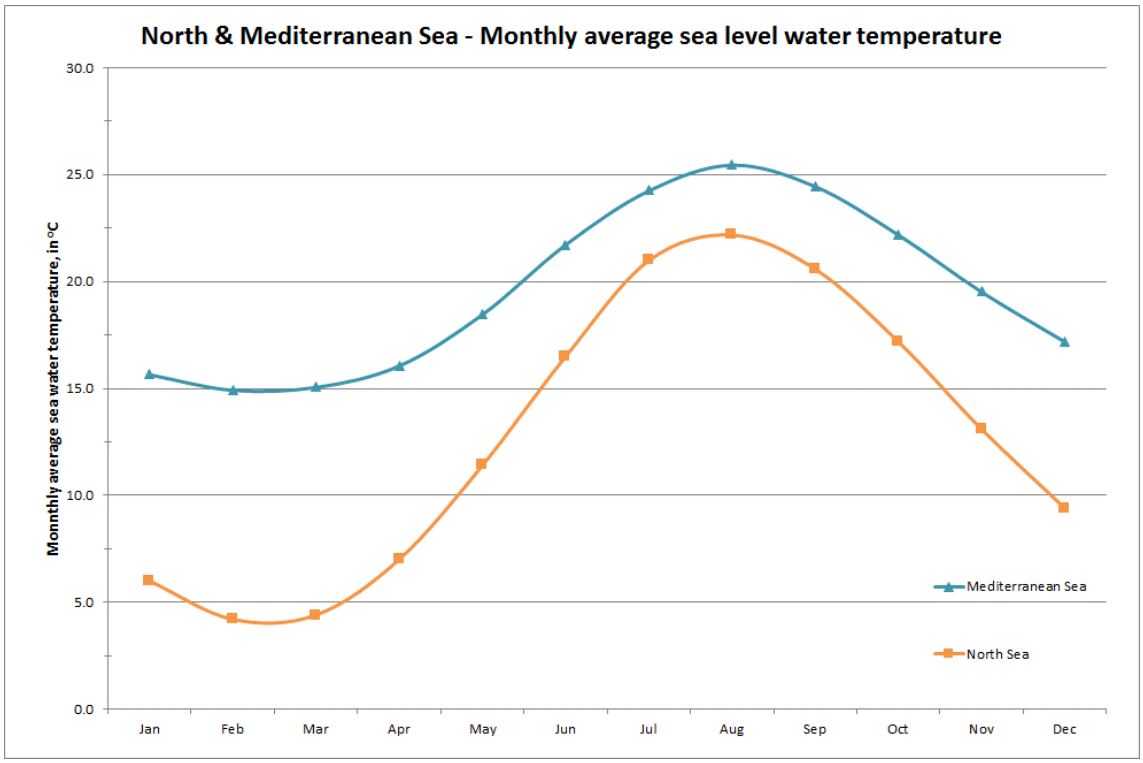

Figure 5.4: North & Mediterranean Sea monthly average sea level water temperature values.

Furthermore, it is assumed that the operational modes (A, B, C & D) of the ME are proportionally distributed over the year, on a month basis. This means that the total yearly running hours of each of the four operational modes is multiplied with the respective ratio of the respective month days divided by the total year days. Therefore, the mean produced electrical output and thus the energy are differentiated per month. Two different ship routes are considered, the first assumes that the ship is operating in the Mediterranean Sea and the second assumes that the ship is operating in North Sea. Thus, the effect on the electricity produced and the economic performance will be evaluated for the two ship routes, simultaneously.

In following Table 5.5, the details of basic assumptions and calculations made for the nominal / design point operation of the WHR ORC are presented. The thermodynamic calculations were performed in ASPEN Plus software simulator. For the economical assessment, the available thermal waste and the temperature of the water jacket outlet are considered constant, based on the information presented in previous Table 5.3. The expander is considered as radial turbine.

Table 5.5: Basic assumptions and calculations of WHR ORC nominal / design point operation for the economic assessment.

Parameter	Value
ORC working fluid	R134a
Turbine Inlet Temperature	82.0 °C
Turbine Inlet Pressure (High Pressure circuit)	25.0 bar_a
Condenser Outlet Pressure (Low Pressure circuit)	7.5 bar_a
Design Superheating working fluid (T_{sh})	5.0 °C
Design Subcooling working fluid (T_{sc})	5.0 °C
Pump electromechanical efficiency	80.0 %
Pump isentropic efficiency	65.0 %
Pump electromechanical efficiency	80.0 %

Turbine isentropic efficiency	85.0 %
Turbine electromechanical efficiency	85.0 %
Pump isentropic efficiency	65.0 %
Gross electrical efficiency at design conditions	8.5 %
Net electrical efficiency at design conditions	7.1 %
Thermal exploitation efficiency	15.5 %
Exergy efficiency	11.3 %
Thermal Energy from JWC	2500.0 kW_{th}
Water jacket inlet temperature to evaporator	85.0 ^{o}C
Jacket water mass flow rate (available) at design point	59.9 kg/s
Working fluid mass flow rate at design point	12.1 kg/s
Gross electrical output at design point	211.7 kW_e
Net electrical output at design point	177.2 kW_e

The calculated net electrical output, gross and net electrical output are in accordance with respective declared values in literature.[34], [53], [66] & [75]

Moreover, in order to estimate the performance of the WHR ORC during off design conditions the results of the off design model, developed during the experimental campaign of the WHR ORC prototype, was used [61]. Hence, the performance of the WHR ORC was estimated during monthly and yearly basis. As already, mentioned the variation of sea water temperature affects the overall performance of the WHR ORC. In following Figure 5.5, the variation of the net produced electrical output in relation to six different sea water temperatures are presented. The illustrated curve is expressed by a polynomial equation and for different temperature values than those illustrated in Figure 5.5, a correlation was performed with the use of the polynomial equation, as presented in Figure 5.5. The presented relation of the net produced

electrical output and the temperature level of the cooling water is in good agreement with other research results. [76]

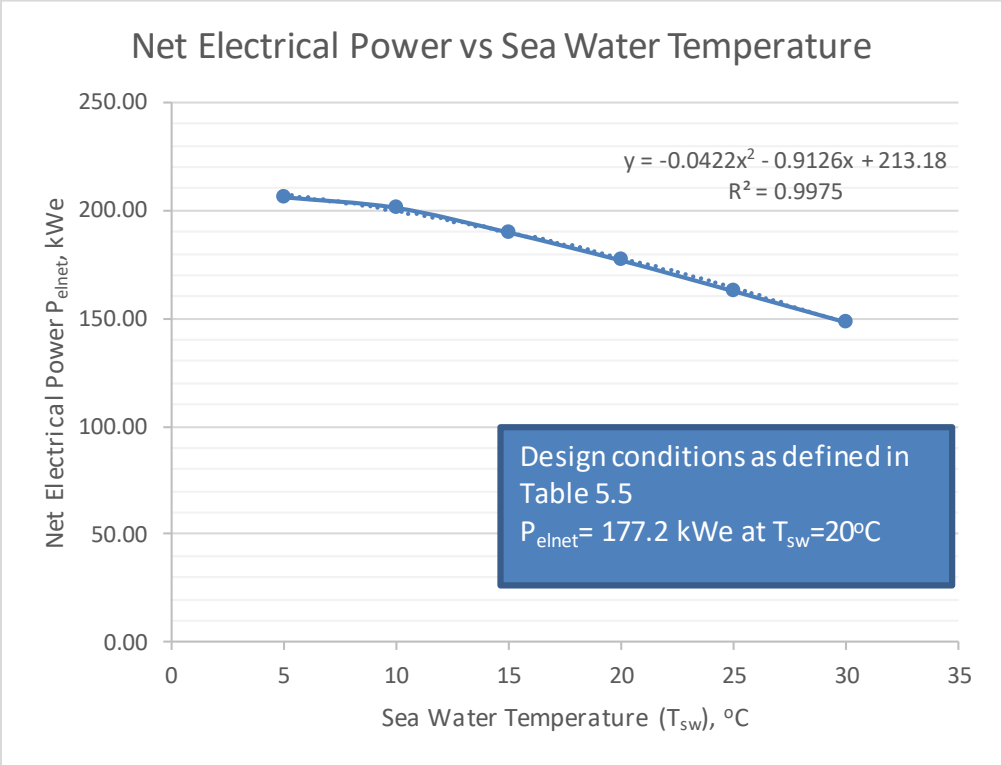

Figure 5.5: Variation of net produced electrical output in relation to different sea water temperatures. ($T_{water\ inlet\ evaporator}$= 85 °C & $\dot{m}_{R134a}$= 12.08 kg/s)

Furthermore, in Figure 5.6 and Figure 5.7 the calculated net electrical output and energy produced for the two different sea routes are presented. As expected, the North Sea route favors the WHR ORC average net electrical output and electrical energy produced, thus improving the economic performance of the WHR ORC in comparison to the results obtained by the respective Mediterranean Sea route, as it will be presented in the following section 5.3.

As a result, the WHR ORC produces 178.5 kW_e and 192.9 kW_e net electrical output on average yearly basis for the Mediterranean and North Sea route, respectively. As far now the total net electrical energy over the year, the WHR ORC on the North Sea route produces almost 1,206 MWh_e where during the Mediterranean route produces 8.1 % less, that is 1,116 MWh_e net electricity yearly production in absolute numbers.

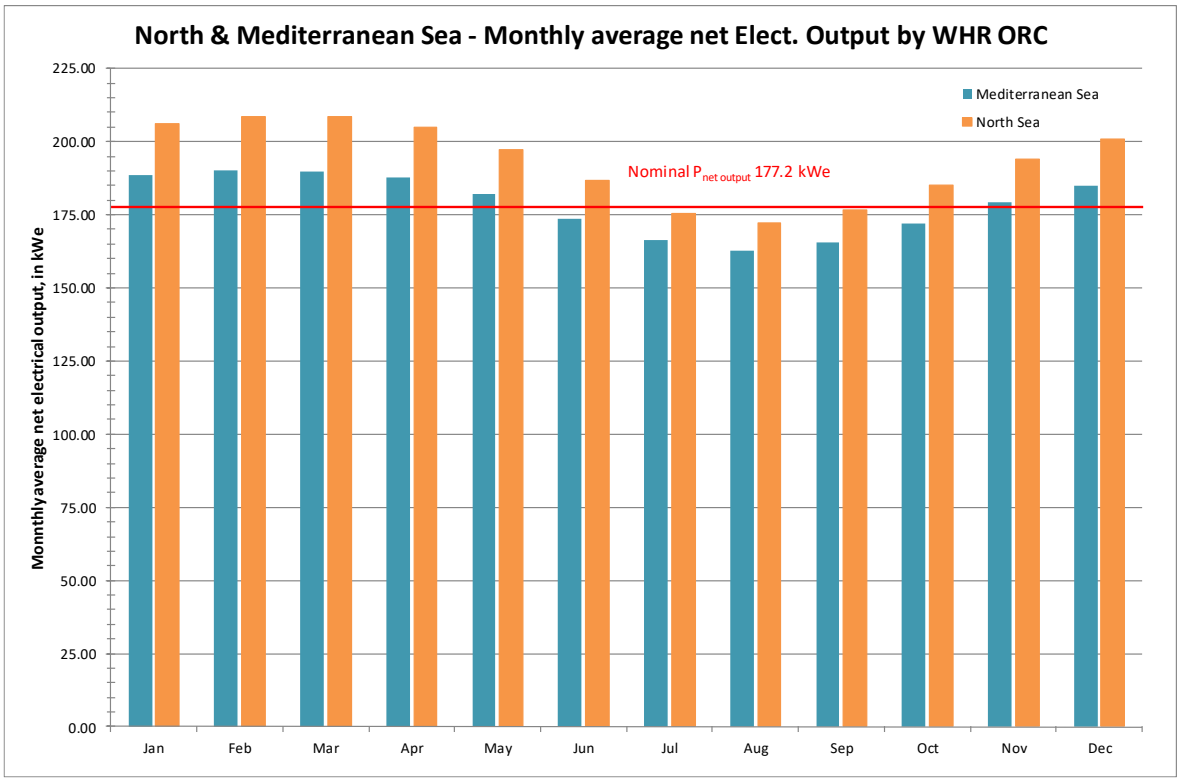

Figure 5.6: Monthly average net Electrical Output by WHR ORC for two different sea routes.

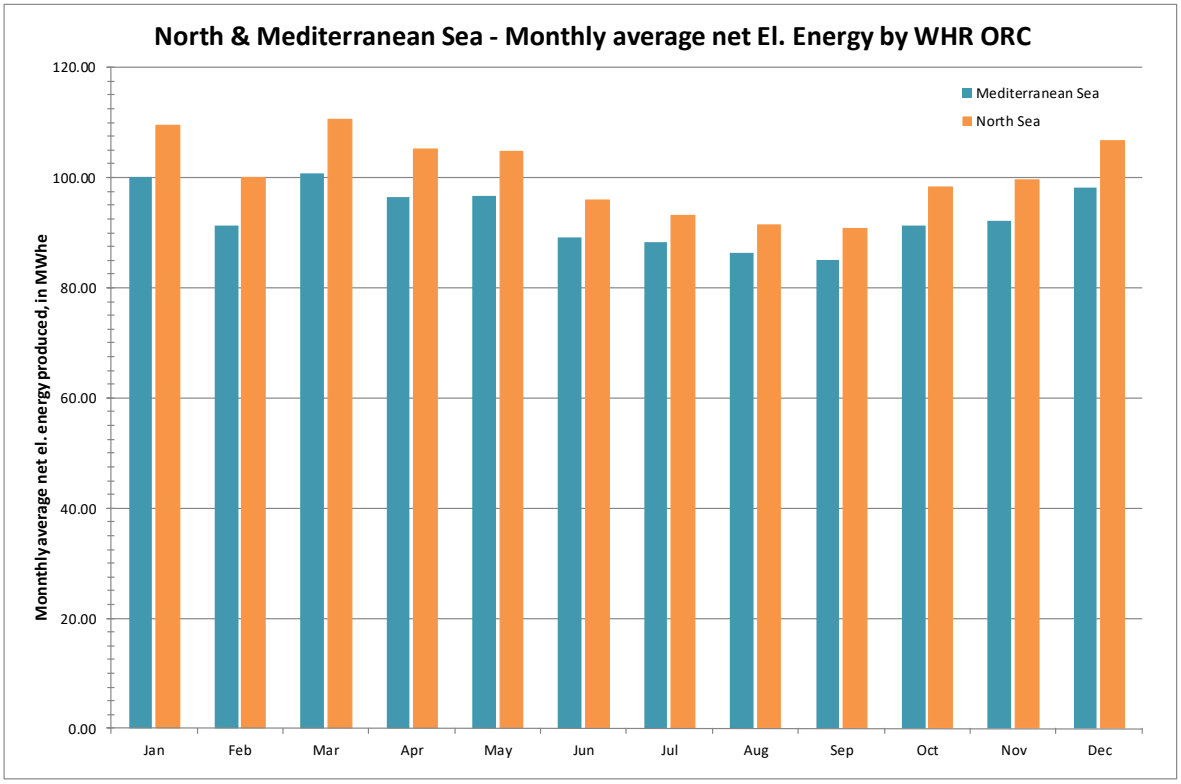

Figure 5.7: Monthly average net Electrical Energy produced by WHR ORC for two different sea routes.

5.3 Show case WHR ORC unit economic assessment

In this Section, the economic assessment results of the show case are presented for the two alternative sea routes. All assumptions, thermodynamic and energy related results presented in previous sections 5.1 and 5.2 were used during the economic assessment.

Furthermore, based on the economic assumptions presented in Table 5.2 and the energetic/ thermodynamic assumptions / results presented in Table 5.5, the WHR ORC installation exhibits the following financial results for the two alternative sea routes (North Sea & Mediterranean Sea) during its life span (20 years). In Table 5.6, the various economic indexes are presented for both sea route alternatives. As expected, the operation and economic performance of a WHR ORC is favored by the lower North Sea's water temperature profile. The better economic performance is illustated in terms of year cash flows in Figure 5.8. The North Sea operation produces more energy per year and thus greater fuel savings. That has as a result that the North Sea operation gets quicker to the economic breakeven point, that is the time in years, where the cummulatted cash flows are equal to zero. Normally in economics, the breakeven point is usually the Simple Payback Time (SPB). Unfortunately, SPB doesn't include the time value of money, like the Depreciated Payback Time (DPB), which is also calculated and differs substantially from SPB. In Table 5.6, both terms are presented.

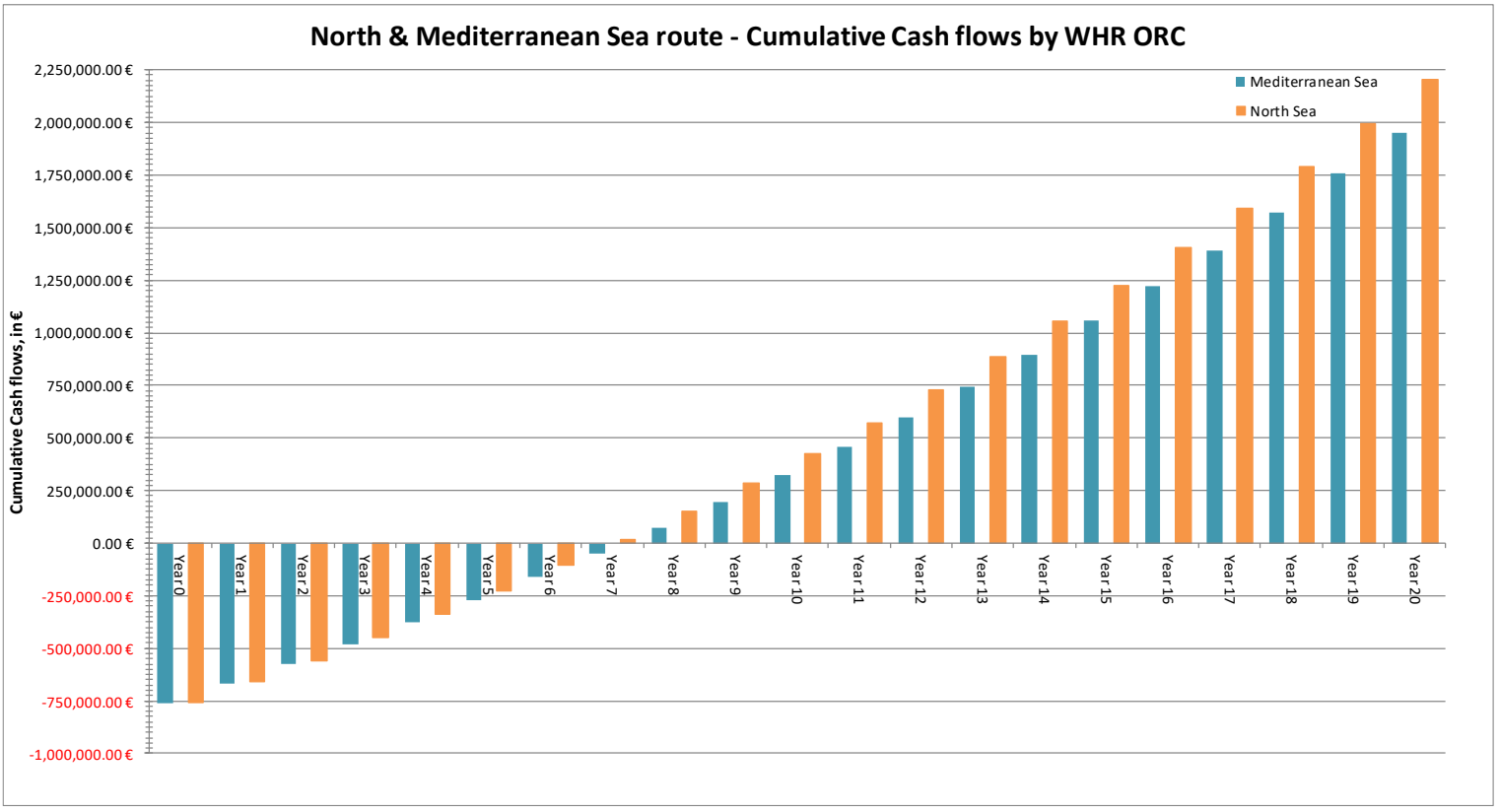

Figure 5.8: Cumulative Cash flows produced by WHR ORC operation for North Sea & Mediterranean Sea route.

Table 5.6: WHR Organic Rankine Cycle various economic indexes for both sea route alternatives.

Index	Mediterranean Sea route's WHR ORC results during lifetime	North Sea route's WHR ORC economic results during lifetime
Investment's Internal Rate of Return (I.R.R.), in %	14.04 %	15.42 %
NPV of investment cost, in €	758,380	758,380
NPV of Operation & Maintenance (OM's), in €	190,956	190,956
NPV of Energy savings, in €	1,303,558	1,407,789
NPV net Benefit (Fuel savings minus OM's), in €	1,112,601	1,216,833
Net Benefit Cost Ratio (BCR)	1.47	1.60
Simple Payback (SPB), in years	8.83	8.06
Depreciated Payback (DPB), in years	11.54	10.31
NPV of investment, in €	354,221	458,453
Levelized Cost of Electricity (LCOE), in €/MWh$_e$	86.67	80.19
Average yearly net electrical power output ($P_{el.net}$), in kW$_e$	178.52	192.97
Average yearly net electrical energy production ($E_{el.net}$), in MWh	1,115.6	1,205.8

For both sea route alternatives, the initial investment cost and the OM's are considered equals since no alteration on the WHR ORC installation are expected. As consequence, the calculated LCOE depends only on the average yearly electrical energy produced. The calculated values of LCOE, for the basic assumptions of 8 % interest rate and 6,252 running hours are in good agreement with literature. [34], [72]

As general conclusion, the investment of an Organic Rankine Cycle for waste heat recovery from a marine engine jacket cooling water proves to be economically profitable in both alternative operational sea routes. All economic indexes are attractive for the basic scenario assumptions, as presented in Table 5.2 and Table 5.5.

In order to assess the effect of various economic parameters on specific economic indexes, a sensitivity analysis was performed. This sensitivity analysis was performed only for Mediterranean Sea route since it is expected to produce equivalent qualitative remarks and conclusions for the North Sea case, as well.

In Figure 5.9, the influence of increasing or decreasing the initial capital investment on NPV of investment, Levelized Cost of Electricity and Depreciated Payback time is illustrated. As expected, an increase of initial capital investment increases the DPB and LCOE and decreases the NPV, and vice versa. In more details, in Table 5.8, it can be seen that an increase of Capital Investment creates an equivalent increase rate to LCOE and almost one and a half increase rate to DPB and vice versa. At the same time, an increase of Capital Investment creates an equivalent decrease rate to IRR and almost a double decrease rate to NPV of investment and vice versa. Thus, a poor estimation of the initial capital investment could affect greatly the economic performance of the Organic Rankine Cycle.

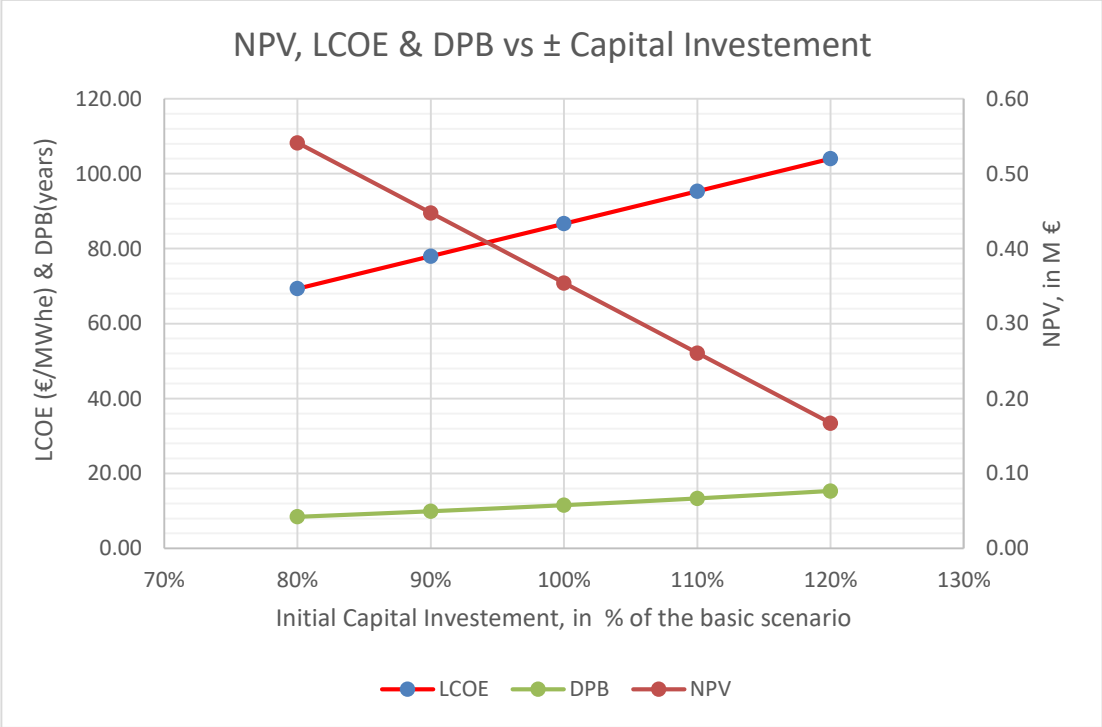

Figure 5.9: NPV (M €), LCOE (€/MWh$_e$) & DPB (years) in relation to initial capital investment variation.

In Figure 5.10, the influence of increasing or decreasing the interest rate on NPV of investment, Levelized Cost of Electricity and Depreciated Payback time is presented. As expected, an increase of interest rate increases the DPB and LCOE and decreases the NPV, and vice versa. In more details, in Table 5.8, it can be concluded that an increase of interest rate creates almost a half increase rate to LCOE and

DPB and vice versa. At the same time, an increase of interest rate creates nearly a double decrease rate to NPV of investment and vice versa. The IRR remains constant to the variation of interest rate, as was expected. Again also for this sensitivity analysis, a poor selection of interest rate's value could change an investment's decision from approval to decline.

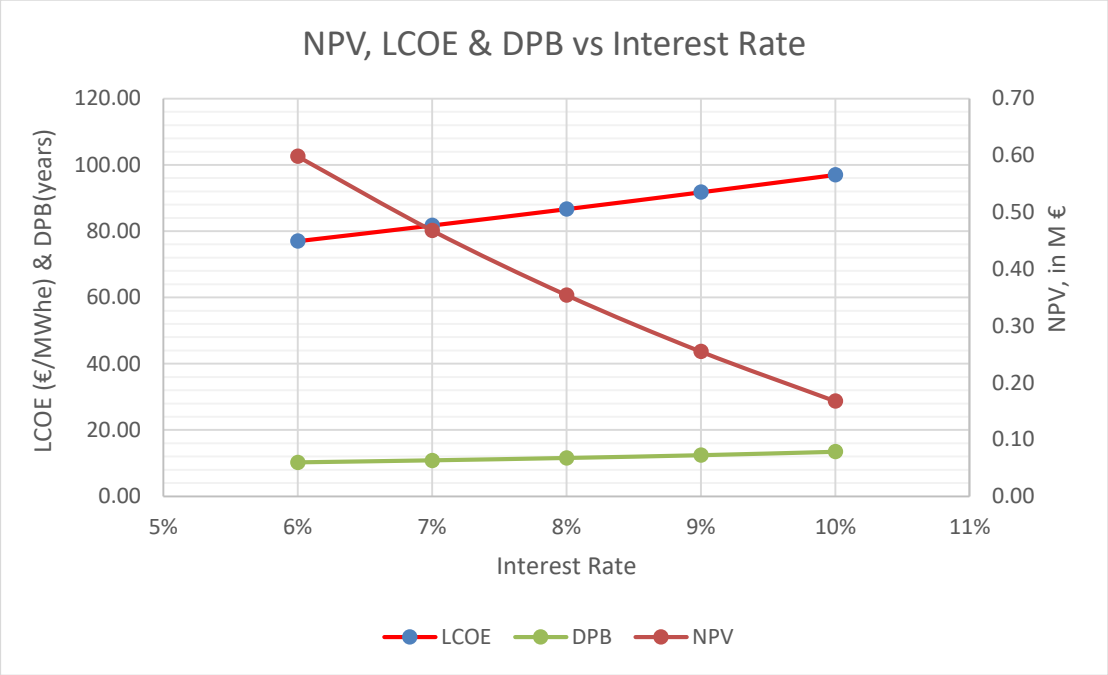

Figure 5.10: NPV (M €), LCOE (€/MWh$_e$) & DPB (years) in relation to interest rate variation.

In Figure 5.11, the influence of fuel price fluctuations on NPV of investment, Internal Rate of Return (IRR) and Depreciated Payback time is presented. As expected, an increase of fuel price has a positive effect on NPV and IRR and decreases rapidly the DPB, and vice versa. The main reason is greater or lower future cash flows that are produced due to the increase or decrease of fuel price, respectively. Furthermore, in Table 5.8, it can be concluded that an increase of fuel price creates almost a similar increase rate to IRR and a three and a half times increase rate to NPV and vice versa. At the same time, an increase of fuel price creates nearly an equivalent decrease rate to DPB and vice versa. This sensitivity analysis underlines the effect that energy price carrier has on energy investments and especially waste heat recovery investments. The fuel price trend over the life span of a WHR project is introducing a substantial risk to project economic performance and viability. Since, Levelized Cost of Electricity is independent of the fuel price value (see equation (5.7)) any fuel price fluctuations has no direct effect on LCOE.

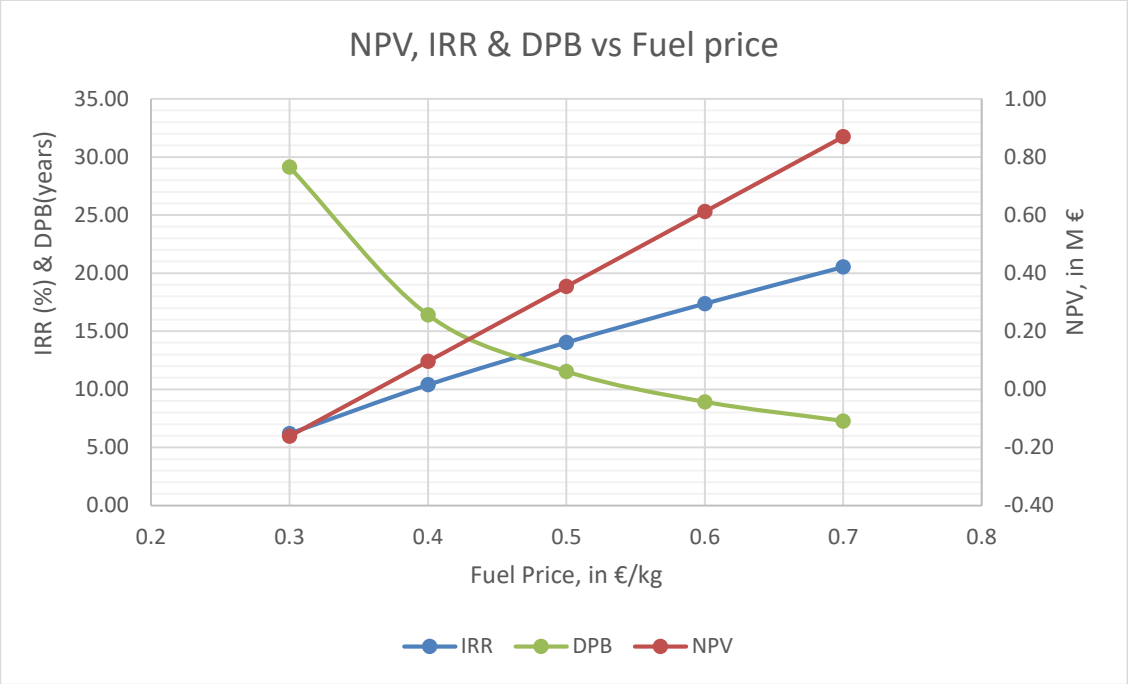

Figure 5.11: NPV (M €), IRR (%) & DPB (years) in relation to fuel price variation.

Last but not least, in Figure 5.12, the combining effect of running hours on a year basis and interest rate, on NPV of investment and Levelized Cost of Electricity, is presented. As expected, an increase of ORC running hours and a decrease of interest rate maximizes the economic profitability of the investment, since it increases the NPV of investment and at the same time minimizes the LCOE. It is also evident that a combination of less running hours and higher interest rate threatens the viability of the investment and shifts the investment decision from accept to decline. Furthermore, in following Table 5.10 it can be seen that the economic index that is greatly affected by the variation of running hours and interest rate is the NPV of investment. This affect tends to be greater as the interest rate increases. Other economic indexes (DPB, LCOE) are affected, obviously, by the combining effect of running hours and interest rate. Specifically, the relative variation of LCOE due to running hours' alteration is equal for all three interest rate alternatives, as illustrative in below Figure 5.12. The exception is the IRR, where its' absolute and relative variation are independent of interest rate, as already pointed out in Table 5.8.

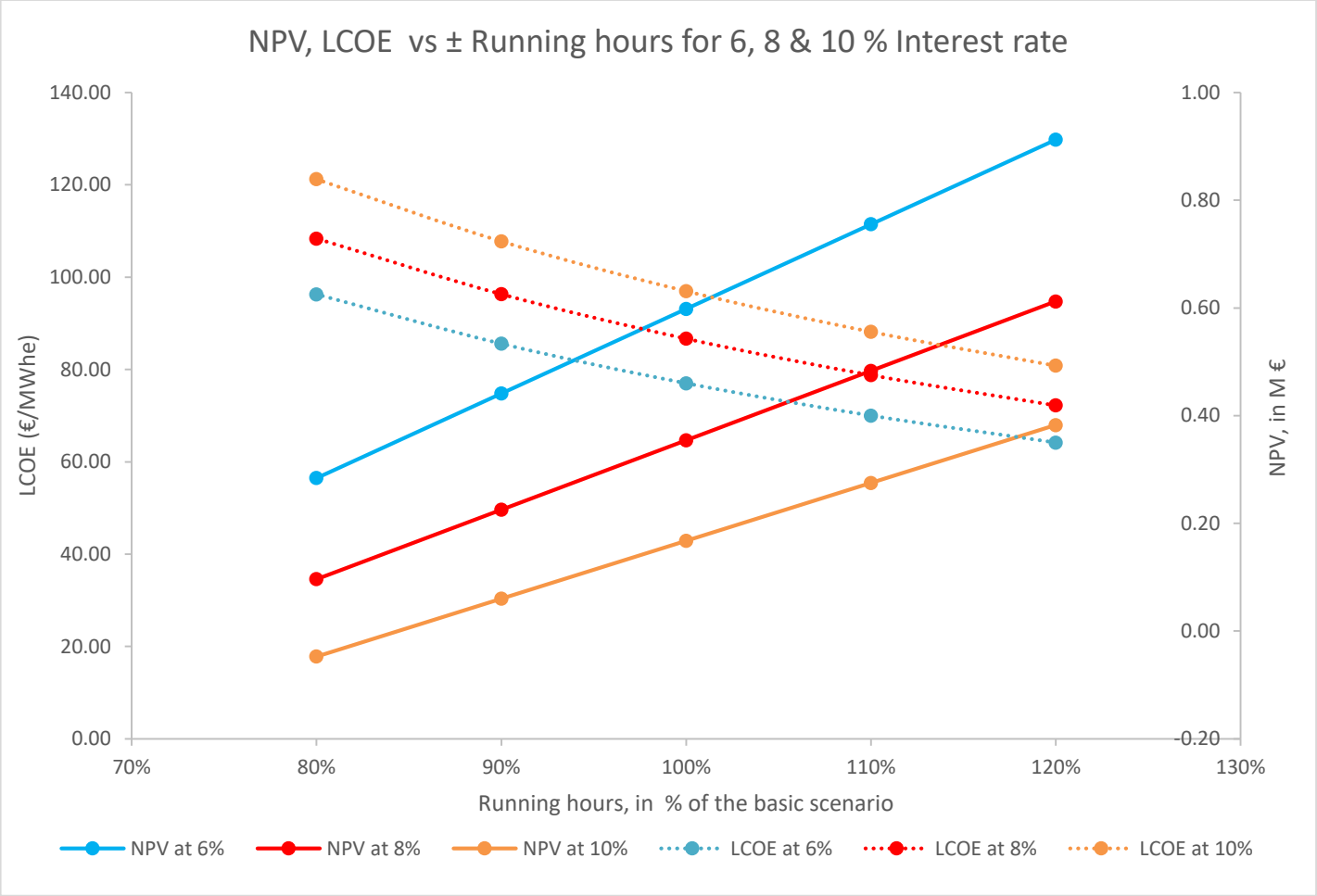

Figure 5.12: NPV (M €) & LCOE (€/MWh$_e$) in relation to ORC running hours and interest rate variation.

As already mentioned, in following Table 5.7, Table 5.8, Table 5.9 & Table 5.10 the results of the sensitivity analysis are presented, for the Mediterranean Sea route alternative. The absolute and relative values of all economic indexes under investigation are presented.

Table 5.7: NPV of investment (M €), IRR (%), DPB (years) & LCOE (€/MWh$_e$) in relation to fuel price, capital investment and interest rate variation.

Fuel Price influence, in €/kg	0.7	0.6	0.5	0.4	0.3
IRR, in %	20.54	17.39	14.04	10.39	6.19
NPV, M €	0.87	0.61	0.35	0.10	-0.16
DPB, in years	7.28	8.92	11.54	16.41	29.14
LCOE, in €/MWh$_e$	86.67	86.67	86.67	86.67	86.67

Capital Investment influence, in €	120 % 910,056	110 % 834,218	100 % 758,380	90 % 682,542	80 % 606,704
IRR, in %	11.03	12.43	14.04	15.93	18.19
NPV, M €	0.17	0.26	0.35	0.45	0.54
DPB, in years	15.33	13.33	11.54	9.92	8.44
LCOE, in €/MWh$_e$	104.00	95.34	86.67	78.00	69.34

Interest rate influence	6 %	7 %	8 %	9 %	10 %
IRR, in %	14.04	14.04	14.04	14.04	14.04
NPV, M €	0.60	0.47	0.35	0.25	0.17
DPB, in years	10.20	10.82	11.54	12.40	13.45
LCOE, in €/MWh$_e$	77.01	81.75	86.67	91.75	96.99

Table 5.8: Relative variation of NPV investment, IRR, DPB & LCOE in regards to basic scenario of fuel price, capital investment and interest rate variation.

Fuel Price influence, in €/kg	0.7	0.6	0.5 Basic Scenario	0.4	0.3
IRR, in ± % to Basic scenario	46.3	23.8	0.0	-26.0	-55.9
NPV, in ± % to Basic scenario	145.6	72.8	0.0	-72.8	-145.6
DPB, in in ± % to Basic scenario	-37.0	-22.7	0.0	42.2	152.5
LCOE, in ± % to Basic scenario	0.0	0.0	0.0	0.0	0.0

Capital Investment influence, in €	120 % 910,056	110 % 834,218	100 % 758,380 Basic Scenario	90 % 682,542	80 % 606,704
IRR, in ± % to Basic scenario	-21.5	-11.5	0.0	13.4	29.5
NPV, in ± % to Basic scenario	-52.8	-26.4	0.0	26.4	52.8
DPB, in in ± % to Basic scenario	32.8	15.5	0.0	-14.0	-26.8
LCOE, in ± % to Basic scenario	20.0	10.0	0.0	-10.0	-20.0

Interest rate influence	6 %	7 %	8 % Basic Scenario	9 %	10 %
IRR, in ± % to Basic scenario	0.0	0.0	0.0	0.0	0.0
NPV, in ± % to Basic scenario	68.9	32.1	0.0	-28.1	-52.7
DPB, in in ± % to Basic scenario	-11.6	-6.3	0.0	7.4	16.5
LCOE, in ± % to Basic scenario	-11.1	-5.7	0.0	5.9	11.9

Table 5.9: NPV of investment (M €), IRR (%), DPB (years) & LCOE (€/MWh$_e$) in relation to WHR ORC running hours and interest rate variation.

Running hours influence for 6 % interest rate	120 % 7,502 h	110 % 6,877 h	100 % 6,252 h	90 % 5,627 h	80 % 5,002 h
IRR, in %	17.39	15.75	14.04	12.27	10.39
NPV, M €	0.91	0.76	0.60	0.44	0.28
DPB, in years	8.10	9.03	10.20	11.72	13.78
LCOE, in €/MWh$_e$	64.18	70.01	77.01	85.57	96.26

Running hours influence for 8 % interest rate	120 % 7,502 h	110 % 6,877 h	100 % 6,252 h	90 % 5,627 h	80 % 5,002 h
IRR, in %	17.39	15.75	14.04	12.27	10.39
NPV, M €	0.61	0.48	0.35	0.23	0.10
DPB, in years	8.92	10.06	11.54	13.54	16.41
LCOE, in €/MWh$_e$	72.23	78.79	86.67	96.30	108.34

Running hours influence for 10 % interest rate	120 % 7,502 h	110 % 6,877 h	100 % 6,252 h	90 % 5,627 h	80 % 5,002 h
IRR, in %	17.39	15.75	14.04	12.27	10.39
NPV, M €	0.38	0.27	0.17	0.06	-0.05
DPB, in years	9.98	11.45	13.45	16.35	21.03
LCOE, in €/MWh$_e$	80.83	88.17	96.99	107.77	121.24

Table 5.10: Relative variation of NPV investment, IRR, DPB & LCOE in regards to different scenarios WHR ORC running hours and interest rate variation.

Running hours influence for 6 % interest rate	120 % 7,502 h	110 % 6,877 h	100 % 6,252 h	90 % 5,627 h	80 % 5,002 h
IRR, in ± % to Basic scenario	23.8	12.1	0.0	-12.6	-26.0
NPV, in ± % to Basic scenario	52.5	26.3	0.0	-26.3	-52.5
DPB, in in ± % Basic scenario	-20.6	-11.5	0.0	14.9	35.1
LCOE, in ± % Basic scenario	-16.7	-9.1	0.0	11.1	25.0

Running hours influence for 8 % interest rate	120 % 7,502 h	110 % 6,877 h	100 % 6,252 h	90 % 5,627 h	80 % 5,002 h
IRR, in ± % to Basic scenario	23.8	12.1	0.0	-12.6	-26.0
NPV, in ± % to Basic scenario	72.8	36.4	0.0	-36.4	-72.8
DPB, in in ± % Basic scenario	-22.7	-12.8	0.0	17.3	42.2
LCOE, in ± % Basic scenario	-16.7	-9.1	0.0	11.1	25.0

Running hours influence for 10 % interest rate	120 % 7,502 h	110 % 6,877 h	100 % 6,252 h	90 % 5,627 h	80 % 5,002 h
IRR, in ± % to Basic scenario	23.8	12.1	0.0	-12.6	-26.0
NPV, in ± % to Basic scenario	128.2	64.1	0.0	-64.1	-128.2
DPB, in in ± % Basic scenario	-25.8	-14.9	0.0	21.6	56.4
LCOE, in ± % Basic scenario	-16.7	-9.1	0.0	11.1	25.0

5.4 Conclusions on WHR ORC unit economic assessment

The economic performance and viability of a jacket water WHR ORC unit was assessed, based on the economic theory and available literature data. A show case was presented which consists of a 13,600 TEU containership, which is powered by a two-stroke marine Diesel engine with a Maximum Continuous Rating (MCR) of a 72,240 kW.

As a result, the WHR ORC utilizes 2,500kW_{th} waste thermal heat and produces 178.5 kW_e and 192.9 kW_e net electrical output on average yearly basis for the Mediterranean and North Sea route, respectively. As far now the total net electrical energy over the year, the WHR ORC on the North Sea route produces almost 1,206 MWh_e where during the Mediterranean route produces 8.1 % less, that is 1,116 MWh_e net electricity yearly production in absolute numbers.

During the economic assessment, several economic indexes were calculated and the economic performance and viability was demonstrated for the basic scenario assumptions. The economic assessment results of the show case were presented for the two alternative sea routes (Mediterranean Sea & North Sea), in Table 5.6. As general conclusion, the investment of an Organic Rankine Cycle for waste heat recovery from a marine engine jacket cooling water proves to be economically profitable in both alternative operational sea routes. It produces, approximately 355,000 and 460,000 € as NPV of investment and exhibits a 14.0 and 15.4 % IRR for the two alternative sea routes (Mediterranean Sea & North Sea), respectively.

Ultimately, the Levelized Cost of Energy (LCOE) of the WHR ORC unit was calculated. The calculated values of 86.67 and 80.19 €/MWhe for the basic assumptions of 8 % interest rate and 6,252 running hours are in good agreement with literature. In addition, in the frames of a comprehensive sensitivity analysis, parameters affecting it, such as fuel price, running hours, interest rate and capital investment, were highlighted. The fuel price fluctuation was highlighted as the most crucial parameter to the economic performance and viability during the life of investment, with running hours of the WHR Organic Rankine Cycle unit following as second most important. The variation of Capital cost and interest rate seem to have a lower but equivalent influence to the economic performance and viability. The NPV of investment is affected the most by the fluctuations of investment parameters, followed by IRR and DPB. The LCOE was least affected by the fluctuations, in relative numbers.

Chapter 6. – General Conclusions & Future work

In the first section of last Chapter, the main conclusions and achievements of the present thesis are briefly mentioned, followed by its innovative aspects. In the last section, some recommendations for future work are provided.

6.1 General conclusions & achievements

The energetic consumption of a commercial ship mainly consists of propulsion and internal consumption electricity needs, which are entirely covered by specially designed marine diesel engines (main and auxiliary respectively). This research focused on the construction, experimental evaluation and full automation of an ORC WHR system, specially designed for the jacket water of a marine auxiliary diesel engine.

An experimental ORC prototype unit was designed and constructed (**1st Achievement**)., based on a conventional low-temperature subcritical Organic Rankine Cycle using R134a as working medium. At nominal design conditions, the laboratory experimental unit produces 5kWe_{gross}, when connected to a 90kWth gas boiler unit test bench. In order to simulate the operating characteristics of JWC of a marine engine, the boiler thermal output is adjustable and thus part load operation and varying hot water supply temperature profile were simulated as well. After a long period of pitfalls, the overall goal was achieved since the stable operation of the experimental ORC WHR on laboratory conditions was accomplished. More than 1000 hours were estimated as the time required to troubleshoot and finally succeed a stable operation at various loads (**2nd Achievement**).

Two experimental campaigns were designed and concluded (**3rd Achievement**). Significant knowledge on the behavior, influencing parameters (i.e. cavitation phenomena on the ORC feed pump, the performance of the scroll expanders and the effect of superheating and subcooling) and improvements that would increase the overall performance of the unit was obtained. This experience and knowledge was capitalized, through the evolution process of the experimental test rig. The ultimate final goal was the autonomous operation of the experimental unit after all, which was achieved at the very final end of the evolution process. The importance of the feed pump performance and free cavitation operation was highlighted, especially for small scale ORC units.

During the 2nd experimental campaign, the following basic conclusions are summarized. The pump's global efficiency is an increasing function of the pressure difference. Values of the relative volumetric efficiency above 96 % were found for the multi-diaphragm pump, as confirmed by literature. Also, specific cavitation tests revealed that a $NPSH_a$ > 7 mH_2O at partial load and a $NPSH_a$ > 9 mH_2O at full load are necessary to guarantee operation stability. These values imposed the installation of a subcooler at a later stage of the evolution process and played an important role in the automation & control strategy.

As far the results and conclusions regarding the expander, in order to maximize expander's isentropic efficiency, the expander is required to operate at the highest possible rotational speeds. Of course, the

rate of increase in isentropic efficiency decreases as expander's rotational speed approaches the maximum value examined, that is, 1450 RPM. The expander's output power increases with increasing rotational speed, at the same time, a smaller increase in the electrical power output is also noticed when increasing its inlet pressure.

All experimental data derived from the second test campaign were used in parallel research activities [45], [47], [61] & [62]. The main goal was to establish models of critical components. These models were calibrated against the experimental data of the second experimental campaign.

After the completion of the experimental campaigns, a new ambitious goal was set. With the support of DNV GL, it was decided to proceed with the design and software development of a complete autonomous experimental marine on board ORC unit (**4th Achievement**).

The major results and conclusions arisen from the final stage of development of the ORC WHR unit are summarized briefly below.

- An extensive **hazard / risk assessment** was performed in order to identify all risks, causes and consequences associated to each hazard. All major conclusions and key results from the hazard – risk assessment improved the design, safety and automation - control strategy aspects.

- **Compactness and modular design**. An extensive re construction, given the dimensional restriction imposed by ship's access ports and hatches was designed and realized under extreme time constraints. Another important requirement was that transportation process and all work carried out on board, in terms of assembly, wiring, filling, testing, tuning and finally setting in operation should be kept as short in time as possible and do not exceed the 36-hour limit. This time constraint reflects the particularities of the marine market and industry where proper planning and multi tasking are considered as a must and could be summed as "a ship never waits". Therefore, several actions needed to be performed simultaneously. Considering the fact that only refrigerant circuit's filling and leakage testing would require 8 -10 hours, assembly and wiring should be kept as short as possible. Although, this was never proved in real life conditions, a simulation under laboratory conditions was performed.

- **An extensive reconstruction of the sea water circuit.** The implementation procedure of DNV GL rules revealed several mistakes that originally were made during the design and construction of the first experimental ORC. DNV GL Part 4 Systems and components Chapter 6 Piping systems Section 2 Clause 1.1.1 dictates that "traditional stainless steels, including 316 or 316L, should not be considered suitable for use in seawater systems". This requirement resulted in a complete reconstruction of the sea water circuit, since the condenser, sub cooler and piping was originally constructed by 316 stainless steel material.

- **Sensors, PLC and other miscellaneous equipment.** An independent emergency shutdown PLC, a new master PLC and other minor equipment were installed as a consequence, mainly, to hazard identification procedure and ship owner requirements. According to Sellers [66], the robustness of the automation system will not only affect the operating availability of the ORC

system but will also provide, the proper data logs, in order to access the operating profile of the ORC system. The latter, at least in early stages of technology adoption, will highlight the performance of such systems, and probably correlate the operational profile to the type of ship or typical route.

- **A power supply motor generator module and a resistor bank were installed.** This arrangement isolates the ship power grid from that of ORC prototype without compromising the necessary external power supply to ORC unit during startup and shutdown procedure.

- Detailed **electrical, piping and ORC prototype drawings (as built)** were designed and a detailed **equipment list** with details such as certification for the intended use, maximum operating pressure and or temperature, dimensions, weight, other specific information was formulated.

- Demonstration of a successful **automation & control strategy** and operation. A state of the art automation and control sub system was realized. The marine ORC prototype is equipped with a **Human Machine Interface (H.M.I.)** which allows the parameterization and operation of the marine ORC prototype, according to the conditions and scope of operation. Therefore, the operation of the ORC unit is not controlled by the crew and thus maximizing the availability of the system.

- Demonstration of trouble free operation at **standalone continuous operating mode**. The marine ORC prototype demonstrated impressive operational features such as autonomous startup and shut down and a successful rump down and rump up behavior during the HT temperature variation (ICE load variation). The complete autonomous operation minimizes the crew's interaction to the ORC operation and availability.

- After the completion of the assessment and the re construction process, the marine on board ORC prototype received the desired **DNV GL approval**. Thus the ORC unit, since it was found to be compliant to DNVGL rules for ships Pt.4 Cp.6 piping systems (January 2017), could be fitted inside an engine room of a ship.

Finally, the economic performance and viability of a jacket water WHR ORC unit was assessed, based on the economic theory and available literature data. A show case was presented which consisted of a 13,600 TEU containership, which is powered by a two-stroke marine Diesel engine with a Maximum Continuous Rating (MCR) of a 72,240 kW. Two alternative sea routes were evaluated. The WHR ORC utilizes 2,500kW_{th} waste thermal heat and produces 178.5 kW_e and 192.9 kW_e net electrical output on average yearly basis for the Mediterranean and North Sea route, respectively. As far now the total net electrical energy over the year, the WHR ORC on the North Sea route produces almost 1,206 MWh_e where during the Mediterranean route produces 8.1 % less, that is 1,116 MWh_e net electricity yearly production in absolute numbers. As general conclusion, the investment of an Organic Rankine Cycle for waste heat recovery from a marine engine jacket cooling water proves to be economically profitable in both alternative operational sea routes. It produces, approximately 355,000 and 460,000 Euro as NPV of investment and exhibits a 14.0 and 15.4 % IRR for the two alternative sea routes (Mediterranean Sea &

North Sea), respectively. Ultimately, the Levelized Cost of Energy (LCOE) of the WHR ORC unit was calculated. The calculated values of 86.67 and 80.19 €/MWhe for the basic assumptions of 8 % interest rate and 6,252 running hours are in good agreement with literature. In addition, in the frames of a comprehensive sensitivity analysis, parameters affecting it, such as running hours, interest rate and capital investment, were highlighted.

6.2 Innovative aspects

The innovative aspects of the present thesis can be summarized as follows.

Two experimental campaigns were designed and concluded. **Significant knowledge** on the behavior, influencing parameters (i.e. cavitation phenomena on the ORC feed pump, the performance of the scroll expanders and the effect of superheating and subcooling) and improvements that would increase the overall performance of the unit was obtained. This experience and knowledge was capitalized, through the evolution process of the experimental test rig.

Fully automated ORC system for marine application. The ORC prototype is the first ever designed and constructed in Hellas for low temperature marine application (90 ^{o}C) and one of the first worldwide. Its' operation has demonstrated impressive operational features such as **autonomous startup** and **shut down** and a **successful rump down and rump up behavior** during the HT temperature variation (ICE load variation).

A successful **automation & control strategy** and operation was established. A state of the art automation and control sub system was realized. The marine ORC prototype is equipped with a **Human Machine Interface (H.M.I.)** which allows the parameterization and operation of the marine ORC prototype, according to the conditions and scope of operation.

Compactness and modular design. Dimensional restriction imposed by ship's access ports and hatches demands that systems that are installed on engine room should be as compact as possible. In addition, the modular design minimizes all required actions on board such transportation process assembly, wiring, filling, testing, tuning and finally setting in operation.

DNV GL approval. The ORC system, since it was found to be **compliant to DNVGL rules for ships** Pt.4 Cp.6 piping systems (January 2017), can be fitted inside an engine room of a ship.

A large **experimental data base** was derived from the test campaigns and was used in parallel research activities. The main goal was to establish models of critical components. These models were calibrated against the experimental data of the second experimental campaign.

6.3 Future work

In this last section some future work areas are proposed.

Life Cycle Analysis. An LCA is an interesting research area since literature references are scarce. The utilization of parts of present work such as the detailed electrical, piping and ORC prototype drawings (as built) and the detailed equipment list (prices, materials, technical characteristics, etc) will assist on the formulation of the required database for the LCA. This database can be expanded to include other expander and feed pump technologies, as well as working fluids.

Replacement of working fluid. As known, the use of 1,1,1,2 – Tetrafluoroethane R-134a is being phased out because of its high global-warming potential (F-Gas regulation). Hence, the investigation and evaluation of suitable alternative working fluids such as R1234yf or 1234ze are very important future steps. The selection of an alternative working fluid will cause the reevaluation of all critical components' performance and behavior such as feed pump, scroll expanders, etc. Nevertheless, such required changes can be adopted, due to the Human Machine Interface (H.M.I.) design, where ability for parameterization and operation of the marine ORC prototype, according to the conditions and scope of operation, were set as corner stones to the automation & control strategy architecture.

Ship trials. Although envisaged during the present work, the on board continuous operation was not realized. The opportunity of such project will provide valuable feedback. The continuous operation will access the durability of such a system in specific demanding conditions. Furthermore, proper data logs, in order to access the operating profile of the ORC system will be obtained. The latter, at least in these early stages of technology adoption, will highlight the performance of such systems, and probably correlate the operational profile to the type of ship or typical route.

Alternative heat sources. Although not foreseen during the design and construction phase of the WHR ORC system, an alternative heat source could be evaluated. This heat source doesn't have to be a waste heat source, mandatorily. A Renewable Energy Source could be coupled to the ORC system, such as a geothermal or solar collector field source. The parallel arrangement of two identical expanders provides the ability to the system to operate independently each scroll expander at nominal design conditions with the half heat flux (35-45 kW_{th}). The coupling of the ORC system with a solar collector field will provided valuable information, in order to access the operating profile of the ORC system / solar collector field arrangement. Thus, in early stages of technology adoption, will highlight the performance of such systems, the inertia and probably correlate the operational profile to various parameters.

Model Predictive control strategy. Implementation of more complex optimal control strategies of the ORC system based on dynamic models. These strategies can also be tailor made for other alternative heat sources.

BIBLIOGRAGPHY Chapter 1

[1] DNV GL ETO2018 Maritime forecast to 2050.

[2] Buhaug, Ø., Corbett, JJ., Endresen, Ø, Eyring, V., Faber, J., et.al.(2009), "Second IMOGHG study 2009 update of the 2000 GHG study: Final report covering phase 1 and phase 2", London: International Maritime Organization.

[3] Façanha, C., Blumberg, K., Miller, J. (2012) "Global transportation energy and climate roadmap", International Council on Clean Transportation. Retrieved from http://www. theicct.org/global-transportation-energy-and-climate-roadmap.

[4] Boeing, 2012. World air cargo Freight Forecast: 2012-2013.

[5] International Council on Clean Transportation (ICCT) White Paper, July 2013.

[6] International Maritime Organization, "MEPC 62/22 Annex 19: 2011 Amendments to the annex of the protocol of 1997 to amend the international convention for the prevention of pollution from ships, 1973, as modified by the protocol of 1978 relating thereto (inclusion of regulations on energy for ships in MARPOL Annex VI)", available at: http://www.imo.org/MediaCentre/HotTopics/GHG/Documents/ eedi 20amendments 20RESOLUTION 20MEPC203 2062.pdf

[7] Note by the International Maritime Organization to the thirty-third session of the Subsidiary Body for Scientific and Technical Advice (SBSTA 33), 4 November 2010.

[8] ICCT Policy Update 15, October 2011, available at https://theicct.org/publications/energy-efficiency-design-index-eedi-new-ships

[9] International Maritime Organization, "MEPC 63/23 Annex 8:2012 guidelines on the method of calculation of the attained energy design index (EEDI) for new ships", availableat http://www.imo.org/KnowledgeCentre/IndexofIMOResolutions/Documents/ MEPC 20- 20Marine 20Environment 20Protection/212(63).pdf

[10] Bouman E.A. et al. (2017), "State-of-the-art technologies, measures, and potential for reducing GHG emissions from shipping — A review", Transportation Research Part D: Transport and Environment, Vol.52, Part A, May 2017, pp408–421

[11] AEA Energy & Environment (AEA) (2008). Greenhouse gas emissions from shipping: trends, projections and abatement potential. London.

[12] CE Delft.(2009). Technical support for European action to reducing greenhouse gas emissions from international maritime transport (annex). Delft, Netherlands.

[13] DNV (2010). Pathways to low carbon shipping. Available at http://www.dnv.com/binaries/position%20paper%20from%20dnv%20pathways%20to%20low%20carbon%20 shipping_tcm4-535306.pdf

[14] International Council on Clean Transportation (ICCT) (2011b). Reducing greenhouse gas emissions from ships: cost effectiveness of available options. Washington: ICCT. Available at http://www.theicct.org/reducing-ghg-emissions-ships.

[15] DNV GL ETO2019 Maritime forecast to 2050.

[16] Kat, J. O., Cerup-Simonsen, B., Jakobsen, O. G., Pedersen, l. R., Petersen, J. B., Posborg, T. (2009). "An integrated approach towards cost-effective operation of ships with reduced GHG emissions", SNAME Annual Meeting, Providence, R.I.

[17] Maersk Line, limited (2012). Maersk Line, Limited 2011 Sustainability Report. Available at http://www.namepa.net/2012/Maersk2011sustainabilityreport.pdf

[18] Smith T., et al. (2014), Third IMO GHG Study 2014; International Maritime Organization (IMO) London, UK, June 2014.

[19] Kalli, J., Karvonen, T., Makkonen, T., 2009, "Sulphur content in ships bunker fuel in 2015, Technical Report", Helsinki, Finland: Ministry of Transport and communications

[20] Jaichandar, S., Annamalai, K., 2012, "Effects of open combustion chamber geometries on the performance of pongamia biodiesel in a DI diesel engine", Fuel, vol. 98, no. 1: p.272-279.

[21] Park, S., 2012, "Optimization of combustion chamber geometry and engine operating conditions for compression ignition engines fueled with dimethyl ether", Fuel, vol. 97, no.1: p. 61-71.

[22] Gan, S., Ng, H.K., Pang. K.M., 2011, "Homogeneous Charge Compression Ignition (HCCI) combustion: implementation and effects on pollutants in direct injection diesel engines", Applied Energy, vol88, no.1: p.559-67.

[23] Yao, M., Zheng, Z., Liu, H., 2009, "Progress and recent trends in homogeneous charge compression ignition (HCCI) engines". Progress in Energy and Combustion Science 2009, vol. 35, no.1: p. 398-437.

[24] Zheng, M., Reader, G.T., 2004, "Energy efficiency analyses of active flow after treatment systems for lean burn internal combustion engines", Energy Conversion and Management, vol. 45, no1. : p. 2473-93.

[25] Park, C., Kim, S., Kim, H., Moriyoshi, Y., 2012, "Stratified lean combustion characteristics of a spray-guided combustion system in a gasoline direct injection engine", Energy, vol. 41, no. 1: p. 401-407.

[26] Lu, X., Shen, Y., Zhang, Y., Zhou, X., Ji, L., Yang, Z., 2011, "Controlled three-stage heat release of stratified charge compression ignition (SCCI) combustion with a two-stage primary reference fuel supply", Fuel, vol. 90, no. 1: p. 2026-38.

[27] Shu, G., Liang, Y., Wei, H., Tian, H., Zhao, J., Liu, L., 2013, "A review of waste heat recovery on Two-stroke IC engine aboard ships", Renewable Sustainable Energy Review 2013, vol. 19, no.0: p. 385-401.

[28] MAN, Diesel & Turbo, Denmark, 2012, Waste heat recovery systems (WHRS). URL: www.mandieselturbo.com.

[29] Larsen, U., Nguyen, T., Knudsen, T., Haglind, F., 2014b, "System analysis and optimization

of a Kalina split-cycle for waste heat recovery on large marine diesel engines", Energy, vol. 64, no. 1: p. 484-494.

[30] Bounefour, Ouadha, a., 2014, "Thermodynamic analysis and thermodynamic analysis and working fluid optimization of a combined ORC-VCC system using waste heat from a marine diesel engine", Proceedings of the ASME 2014 International Mechanical Engineering Congress and Exposition IMECE2014 November 14-20, 2014, Montreal, Quebec, Canada.

[31] Yang, M.H., Yeh, R.H., 2014, "Analyzing the optimization of an organic Rankine cycle system for recovering waste heat from a large marine engine containing a cooling water system", Energy Conversion and Management, vol. 88, no. 1:p. 999-1010.

[32] Larsen, U., Sigthorsson, O.,Haglind., F., 2014a, "A comparison of advanced heat recovery power cycles in a combined cycle for large ships", Energy, vol. 74, no.1 : p. 260-268.

[33] Bombarda, P., Invernizzi, C.M., Pietra, C., 2010, "Heat recovery from diesel engines: a thermodynamic comparison between Kalina and ORC cycles.", Applied Thermal Engineering, vol.30, no 2-3: p. 212-219.

BIBLIOGRAGPHY Chapter 2

[34] A. Schuster, S. Karellas, E. Kakaras, and H. Spliethoff, "Energetic and economic investigation of Organic Rankine Cycle applications," Appl. Therm. Eng., vol. 29, no. 8–9, pp. 1809–1817, 2009.

[35] S. Quoilin, "Sustainable energy conversion through the use of Organic Rankine Cycles for waste heat recovery and solar applications," no. October, pp. 1–183, 2011.

[36] Wanner Engineering I. Hydra-Cell® INDUSTRIAL PUMP – Installation & Service Models: D-10 and G-10, D10-991-2400B5/2004.

[37] Declaye S, Lemort V. "Improving the performance of micro-ORC systems [Phd thesis]: Universite de Liege", Liege, Belgium.; 2015.

[38] S. L. Dixon, "Radial Flow Gas Turbines," in Fluid Mechanics, Thermodynamics of Turbomachinery, no. 1992, 1992, pp. 236–276.

[39] J. G. Persson and G. Sohlenius, "Performance Evaluation of Fluid Machinery During Conceptual Design," CIRP Ann. - Manuf. Technol., vol. 39, no. 1, pp. 137–140, 1990.

[40] S. Quoilin, S. Declaye, A. Legros, and L. Guillaume, "Working fluid selection and operating maps for Organic Rankine Cycle expansion machines," Int. Compress. Eng. Conf., pp. 1–10, 2012.

[41] V. Lemort, S. Declaye, and S. Quoilin, "Experimental characterization of a hermetic scroll expander for use in a micro-scale Rankine cycle," Proc. Inst. Mech. Eng. Part A J. Power Energy, vol. 226, no. 1, pp. 126–136, 2012.

[42] Z. Wu, D. Pan, N. Gao, T. Zhu, and F. Xie, "Experimental testing and numerical simulation of scroll expander in a small scale organic Rankine cycle system," Appl. Therm. Eng., vol. 87, pp. 529–537, 2015.

[43] S. Declaye, S. Quoilin, L. Guillaume, and V. Lemort, "Experimental study on an open-drive scroll expander integrated into an ORC (Organic Rankine Cycle) system with R245fa as working fluid," Energy, vol. 55, pp. 173–183, 2013.

[44] S. Chapman, Electric Machinery Fundamentals, 4th edition. Puclication Tziola, 2010.

[45] T. Roumpedakis, S. Chapaloglou, P. Pallis, A.D. Leontaritis, K. Braimakis, S. Karellas "Experimental investigation and CFD analysis of heat transfer in Single Phase Subcooler of a Small Scale Waste Heat Recovery ORC", Energy Procedia, Volume 129, September 2017, Pages 487-494; https://doi.org/10.1016/j.egypro.2017.09.166

[46] N. Antoniou, "Remote management and control of a waste heat recovery installation with ORC technology for ship engines via Labview and PLC," N.T.U.A., 2015.

[47] F.D'Amigo, P. Pallis, A.D. Leontaritis, S. Karellas, N.M. Kakalis, S. Rech, A. Lazzaretto "Semi – Empirical model of a multi-diaphragm pump in an Organic Rankine C (ORC) experimental unit.", Energy, Volume 143, 15 January 2018, Pages 1056-1071 https://doi.org/10.1016/j.energy.2017.10.127

BIBLIOGRAGPHY Chapter 3

[48] Braimakis, K., Preißinger, M., Brüggemann, D., Karellas, S., Panopoulos, K., 2015, "Low grade waste heat recovery with subcritical and supercritical Organic Rankine Cycle based on natural refrigerants and their binary mixtures", Energy, In Press, Corrected Proof, doi: 10.1016/j.energy.2015.03.092

[49] Quoilin S., Lemort, V., 2011, "Thermo-economic optimization of waste heat recovery Organic Rankine Cycles", Applied Thermal Engineering, vol. 31, no.1: p. 2885-2893.

[50] Mago, P.J., Chamra, L.M., Srinivasan, K., Somayaji, C., 2008, "An examination of regenerative Organic Rankine Cycles using dry fluids", Applied Thermal Engineering, vol. 28, no. 1: p. 998-1007.

[51] T. Yamamoto, T., Furuhata, T., Arai, T., Mori, T., 2001, "Design and testing of the Organic Rankine Cycle, Energy", vol. 26, no. 1: 239-251.

[52] Lemort V, Quoilin S, Cuevas C, Lebrun J. "Testing and modeling a scroll expander integrated into an Organic Rankine Cycle." ApplThermEng 2009;29:3094-3102.

[53] Quoilin S, Broek MVD, Declaye S, Dewallef P, Lemort V. "Techno-economic survey of Organic Rankine Cycle (ORC) systems." Renewable and Sustainable Energy Reviews. 2013; 22:168-86.

[54] Bala EJ, O'Callaghan PW, Probert SD. "Influence of organic working fluids on the performance of a positive-displacement pump with sliding vanes." Applied Energy. 1985;20:153-9.

[55] Leontaritis AD, Pallis P, Karellas S, Papastergiou A, Antoniou N, Vourliotis P, et al. "Experimental study on a low temperature ORC unit for onboard waste heat recovery from marine diesel engines." 3rd International Seminar on ORC Power Systems. Brussels, Belgium.2015.

[56] A. Landelle, N. Tauveron, R. Revellin, P. Haberschill, S. Colasson, and V. Roussel, "Performance investigation of reciprocating pump running with organic fluid for organic Rankine cycle," Appl. Therm. Eng., vol. 113, pp. 962–969, 2017.

[57] P. Song, M. Wei, L. Shi, S. N. Danish, and C. Ma, "A review of scroll expanders for organic rankine cycle systems," *Appl. Therm. Eng.*, vol. 75, pp. 54–64, 2015.

[58] N. Ishii, M. Yamamura, S. Muramatsu, S. Yamamoto, and M. Sakai "Mechanical Efficiency of a Variable Speed Scroll Compressor," Proc. Int. Compress. Eng. Conf., no. June, pp. 192–199, 1990.

[59] F. Ayachi, E. B. Ksayer, P. Neveu, and A. Zoughaib, "Experimental investigation and modeling of a hermetic scroll expander," Appl. Energy, vol. 181, pp. 256–267, 2016.

[60] R. Zanelli and D. Favrat, "Experimental investigation of a hermetic scroll expander-generator," 12th Int. Compress. Eng. Conf. Purdue, pp. 459–464, 1994.

[61] E. Varvagiannis, "Experimental and theoretical investigation for the automatic control of

a waste heat recovery ORC unit," N.T.U.A., 2017.

[62] G. Carraro, P. Pallis, A.D. Leontaritis, S. Karellas, P. Vourliotis, S. Rech, A. Lazzaretto "Experimental performance evaluation of a multi-diaphragm pump of a micro-ORC system.", Energy Procedia, Volume 129, September 2017, Pages 1018-1025; https://doi.org/10.1016/j.egypro.2017.09.232

BIBLIOGRAGPHY Chapter 4

[63] P. Petr, C. Schröder, J. Köhler, and M. Gräber, “Paper ID : 123 Page 1 Optimal control OF waste heat recovery systems applying non linear model predictive control (NMPC). 3rd International Seminar on ORC Power Systems. Brussels, Belgium.2015, Paper ID : 123 Page 2,” pp. 1–10.

[64] A. Hernandez, V. Lemort, and R. De Keyser, “Multivariable Epsac Predictive Control for Organic Rankine Cycle Technology,” no. October, pp. 2011–2013, 2013.

[65] S. Quoilin, R. Aumann, A. Grill, A. Schuster, V. Lemort, and H. Spliethoff, “Dynamic modeling and optimal control strategy of waste heat recovery Organic Rankine Cycles,” Appl. Energy, vol. 88, no. 6, pp. 2183–2190, 2011.

[66] Sellers C., “Field operation of a 125kW ORC with ship engine jacket water”, 4th International Seminar on ORC Power Systems. Milan, Italy.2017.

[67] Bellolio S., Lemort V., Rigo P., “Organic Rankine cycle systems for waste heat recovery in marine applications.”, SCC 2015 International conference on shipping in changing climates, November 2015, Glasgow, Scotland.

[68] Kölsch B., Radulovic J. (2015) “Utilization of diesel engine waste heat by Organic Rankine Cycle”, Applied Thermal Engineering, 78, 437-448.

BIBLIOGRAGPHY Chapter 5

[69] ElectraTherm by BITZER GROUP, March 2020, available at: https://electratherm.com/

[70] Chemical Engineering Price Cost Index, available at: https://www.chemengonline.com/pci-home

[71] D. Gewald, "Waste heat recovery of stationary internal combustion engines for power generation [Phd thesis]: Technische Universität München" Munich, Germany, 2013.

[72] S. Lecompte "Performance evaluation of Organic Rankine Cycle Architectures: Application to Waste Heat Valorization [Phd thesis]: Universiteit Gent", Gent, Belgium.; 2015-2016.

[73] M. Kalikatzarakis, C. Frangopoulos, "Thermo-economic optimization of synthesis, design and operation of a marine organic Rankine cycle system", Journal of Engineering for the Maritime Environment, vol.231, pp137-152, 2016.

[74] Kakalis N., Dimopoulos G. and Stefanatos I., "Model-based techno-economic assessment and optimization of marine waste heat recovery options", International Council on Combustion Engines 2009, Paper No:183, Shangai, China, 2009.

[75] K. Braimakis, T. Roumpedakis, A. Leontaritis, S. Karellas, Book title: Advances in New Heat Transfer Fluids, Ch. 13 "Comparison of environmentally friendly working fluids for organic Rankine cycles", pp 377-426, Publisher: CRS Press, Editor: Alina Adriana Minea, year 2017.

[76] G. Tieyu, L. Changwei, "Off-Design Performance of Subcritical and Supercritical Organic Rankine Cycles in Geothermal Power Systems under an Optimal Control Strategy.", Journal of Energies, vol.10, pp1185, 2017.